Magmatic And Tectonic Evolution Of Southern Tibet And The Himalaya

Thesis

Magmatic and Tectonic Evolution of Southern Tibet and the Himalaya

A thesis presented for the degree of Doctor of Philosophy

by

Helen Myfanwy Williams

BA (Hons) Cantab., 1997

Department of Earth Sciences
The Open University

December, 2000

Acknowledgements

I'd like to start by thanking my supervisors, Simon Kelley, Simon Turner and Nigel Harris for their support, advice and tolerance of my rather haphazard style of research. My examiners, Graham Pearson and Anthony Cohen, are thanked for wading through this doorstop in an incredibly short period of time, and for coming up with helpful ideas and comments at the end of it all.

Many people at the OU have helped to fashion my approach towards geochemistry and research in the last three years. I'd like to say cheers to Ian Parkinson for his patient explanations of REE data; to Nick Rogers for talks about weird ultrapotassic rocks; to Chris Hawkesworth for looking at random geochemical plots, and to Bruce Schaefer for stoically reading and commenting on *numerous* drafts of manuscripts and chapters. Huge thanks go to the OU Himalayan crowd: Tom Argles, Christophe Prince and Gavin Foster, and to Nick Arnaud, Christine Miller, Sally Gibson and Brad Hacker who all (apparently) survived email conversations with me about Tibetan rocks.

Fieldwork in India and southern Tibet was made possible by the hard work and perseverance of many people; I'd like to thank Leonore Hoke, Bob Spicer and Professor Guo from the Tibet expedition, and Christophe for exuberant field assistance in India.

Back at the OU, huge respect goes to Janet Dryden and Alison Robinson for calm in the face of beurocratic absurdity. The downstairs crew: Kay Green and Brian Ellis are thanked for thin sections; John Watson and Andy Tindle are thanked for XRF and microprobe help, respectively. Jo Wartho for her help with Ar-Ar analyses and her tolerance of my high ^{36}Ar samples, which nearly sent the multiplier into orbit! I'm indebted to Mabs Gilmour and Jo Rhodes who endured my presence in the radiogenic labs and gave guidance in matters relating to chocolate, gossip and occasionally geochemistry. Peter van Calsteren is thanked for keeping the TIMS and plasma machines going and for tolerating my panicked phonecalls about the plasma in the middle of the night. I'm grateful to Hazel Chapman and Mike Bickle for last-minute Sr isotope analyses at Cambridge, and to Chris Ottley and Julian Pearce for ICPMS and hospitality in Durham.

There are many people who have made life at the OU enjoyable for me, and who've been there when I've needed them. I'm immensely grateful to Louise Thomas, Jo Rhodes and Sarah Sherlock for the late-night hospital vigil, and for support and friendship over the last three years. Pete Evans and Rob Hughes must be mentioned for mild abuse, excessive caffeine consumption and introducing me to the art of the teflon meltdown. Massive thanks to my fellow partner in crime, Glyn Williams-Jones, for being far more organised than me, telling me that he's far more organised than me, for putting the coffee on and always being ready for a chat. Cheers to Siobhàn McGarry, fellow DJ in the Radio Bristol experience, to Bruce Charlier and to Rhiannon George for being there. A huge thanks to all the fellow PhD'ers and the long-suffering individuals who have either shared an office or house with me.

Finally, I'd like to say thanks to my parents for their incredible support over the years; this would not have been possible without you.

Abstract

The Himalaya-Tibetan orogen has become the paradigm for continental collision and is central to deciphering continental tectonics. Neogene extension in the orogen is not predicted by plate tectonic theory, and its significance is widely debated.

In the Himalaya, north-south extension is restricted to the Southern Tibetan Detachment System (STDS), which juxtaposes the High Himalayan Crystalline Series (HHCS) against the Tibetan Sedimentary Series (TSS). ^{40}Ar-^{39}Ar ages from HHCS and TSS of the Garhwal Himalaya indicate that STDS movement initiated between 17.3 ± 0.4 to 24.3 ± 1.6 Ma (2σ), synchronous with Main Central Thrust (MCT) movement. One-dimensional thermal modelling suggests that the STDS is a reactivated thrust, implying a fundamental change in Himalayan tectonics in the early Miocene.

The onset of east-west extension in southern Tibet is constrained by north-south trending shoshonitic dykes to be 13.3 ± 0.8-18.3 ± 2.7 Ma. Trace-element modelling indicates that the shoshonitic dykes and associated lavas in southern and northern Tibet were derived by $\leq 2\%$ melting of enriched sub-continental lithospheric mantle (SCLM) at 65–85km. The northern and southern shoshonites have distinctive isotopic ($\varepsilon Nd_{(i)}$ north, -5.5 to-10.3; south –8.8 to –18.1) and major element signatures that relate to distinct SCLM sources corresponding to the tectonically accreted terranes of the plateau. The trace-element compositions of these sources, determined by inverse modelling, suggest subduction-related metasomatism. ^{40}Ar-^{39}Ar dating of xenocrystic phlogopites indicates metasomatism of the southern SCLM occurred at 62±2 Ma, synchronous with collision.

These data link Neogene extension to a thermally perturbed lithosphere. SCLM thinning following slab detachment explains magmatism, extension and uplift in southern Tibet. Episodic convective removal of the SCLM is proposed for northern Tibet. In view of these models, initiation of extension at 18.3±1.6 Ma in southern Tibet places a minimum constraint on plateau uplift. This overlaps with STDS and MCT movement, implying that changes in Himalayan tectonics are controlled by plateau uplift.

Table of Contents

List of Figures

List of Tables

1 Introduction

1.1 Continental Tectonics

The development of plate tectonic theory provided a framework by which it became possible to understand the creation of new sea floor at mid-ocean ridges and its destruction at subduction zones (Vine and Matthews, 1963; Vine, 1966). While the processes involved in the thermal evolution of the oceanic lithosphere are relatively simple and becoming increasingly well understood (Parsons and McKenzie, 1978) those that control the evolution of the continents remain less clear. Whereas plate boundaries in oceanic regions are narrow and easily defined, the continents are characterised by diffuse patterns of seismicity, faulting and magmatism that cannot be easily attributed to the localisation of deformation on discrete plate boundaries. The contrasting behaviour of the continental lithosphere is nowhere more apparent than in convergent settings, where the buoyancy of the continental crust makes deep subduction difficult. Continental collision results in the generation of a compressional stress field, shortening of continental lithosphere and the formation of mountain ranges and high plateaux. Much of our present knowledge about the thermal and mechanical properties of the continental lithosphere stems from ongoing theoretical, geophysical and geological studies of orogenic zones.

1.2 The Himalayan-Tibetan Orogen

The Himalayan-Tibetan orogen is the largest on Earth, in terms of both altitude and area, and is the result of the continent-continent collision of the Indian plate with the southern margin of Eurasia. Collision began in the early Tertiary, and is ongoing today. It is this continued convergence which sets the Himalaya, and the Tibetan plateau to the north, apart as a unique natural laboratory for the study of continental tectonics, metamorphism, and magmatism in a collisional setting.

Thickening and south-directed thrusting of the northern margin of the Indian plate followed collision, forming the Himalaya mountain belt. Such processes continue today, demonstrated by the seismicity of the region (Wesnousky et al., 1999). Crustal thickening and consequent heating produced Barrovian style metamorphism in the core of the orogen, culminating in crustal anatexis and the genesis of leucogranite magmas in the early Miocene (Le Fort, 1975). From the Early Miocene, the Himalaya have been characterised by north-south extension at the highest structural levels, broadly synchronous with thrusting at deeper levels (Burchfiel et al., 1992; Hodges et al., 1992). The observation of synchronous extension and thrusting in an active convergent setting has important implications for understanding continental dynamics, as it contrasts with the common assumption that extension in mountain belts simply reflects the gravitational collapse of the crust towards the end of orogenesis, where convergence has slowed or ceased (see Dewey, 1988 for a review).

In contrast to the narrow Himalayan belt, the Tibetan plateau covers an area of over

5×10^6 km^2, and is characterised by widespread seismicity and normal faulting, while strike-slip and thrust faulting is largely restricted to the plateau margins (Molnar and Tapponnier, 1978). Widespread extension in a dominantly compressional stress field is not predicted by plate tectonic theory, and the geodynamics of the Tibetan plateau have consequently been the subject of debate for over a quarter of a century. In an important study, England and McKenzie (1982) analysed the deformation of a thin viscous sheet as an analogue for the continental crust and underlying sub-continental lithospheric mantle (SCLM). The most significant result of their numerical experiments was that the deformation field was only weakly dependent on the geometry assigned to the plate boundaries; consequently they were able to reproduce the diffuse patterns of continental deformation. Based on this analogy, England and Houseman (1986) inferred that the penetration of India (a rigid indentor in their model) into Eurasia (approximated as a thin viscous sheet) was accommodated by widespread thickening of Asian lithosphere. They related east-west extension on the plateau to an increase in elevation and a potential energy excess following the removal of orogenically thickened SCLM beneath Tibet (Houseman et al., 1981). In this model, distributed shortening causes the SCLM to become thermally unstable with respect to the asthenosphere, triggering convective thinning at its base. The replacement of dense, cold continental lithospheric mantle with buoyant asthenosphere results in isostatic uplift, and the subsequent thermal relaxation is followed by extension, as the thickened crust can no longer support itself. This model has been applied to the evolution of other regions such as the Basin and Range (Hawkesworth et al., 1995) and the Bolivian Altiplano (Allmendinger et al., 1997) with the Tibetan plateau gaining a kind of "type locality" status in continental tectonics.

However, the development of the Tibetan plateau and its relationship to the Himalayan mountain belt to the south remain a subject of debate, in part due to numerical experiments which indicate more complex behaviour for the continental lithosphere (e.g. Pysklywec et al., 2000) and difficulties in directly testing viscous sheet models. It has been argued that the evolution of the plateau may be better described in terms of movement on rigid plates, involving intracontinental subduction (Meyer et al., 1998) and the extrusion of the Tibetan plateau to the east along major transcurrent faults, which act as oblique plate boundaries (Tapponnier et al., 1982). Intermediate models, that investigate the role of the geometry of the colliding plates and the underthrusting Indian lithosphere, have also been proposed (Chemenda et al., 2000; Pysklywec et al., 2000). In the light of the controversy surrounding the evolution of the Himalayan-Tibetan orogen and the behaviour of the continental lithosphere (e.g. Lenardic and Kaula, 1995; Kong et al., 1997; Willett, 1999; Pysklywec et al., 2000), it is important to re-assess and refine geodynamic models for the evolution of the Himalayan-Tibetan orogen. This can be achieved by integrating neotectonic and geophysical studies with geochronological constraints on post-collisional deformation, metamorphism and magmatism in the Himalaya and Tibet. Furthermore, obtaining a greater knowledge of the timing and mechanisms of orogenesis has implications for climatic models; both mountain building and plateau uplift have been implicated as major controls on atmospheric circulation and Cenozoic climate change (e.g. Kutzbach et al., 1989; Raymo and Rudiman, 1992; Molnar et al., 1993).

1.3 Thesis objectives

This thesis focuses on the post-collisional evolution of the Himalaya and Tibet. The principal aim of this work is to assess the application of the different geodynamic models to describing the evolution of the Himalayan-Tibetan orogen. The specific objectives of this research are outlined below:

1. To date the onset of north-south extension in the well-characterised Garhwal section of the Himalaya using the ^{40}Ar-^{39}Ar technique, thus to evaluate the thermal effects of extension on the evolution of this section of the metamorphic belt.

2. To constrain the onset of east-west extension in the southern Tibetan plateau by ^{40}Ar-^{39}Ar dating of north-south trending dyke swarms, and to assess temporal relationships between east-west extension, magmatism and uplift in Tibet, and north-south extension in the Himalaya.

3. To determine the conditions of melting and the sources of mafic and silicic post-collisional potassic magmatism in southern and northern Tibet by an integrated major, trace element and Sr, Nd and Pb and mineral chemistry study and thus to deduce the thermal evolution of the Tibetan SCLM and crust following collision.

4. To discuss the timing and petrogenesis of post-collisional volcanism in terms of models of continental orogenesis, and evaluate the competing geodynamic models for the development of the Tibetan plateau.

5. To assess the degree to which the post-collisional evolution of the Himalayan belt and the Tibetan plateau can be interrelated.

1.4 Chapter Layout

Chapter 2 gives an overview of the geodynamic framework of the Indian-Asian collision prior to the onset of continental collision, discusses present knowledge of the timing of collision, metamorphism and extension and reviews existing geodynamic models for the development and evolution of the Tibetan plateau.

Chapter 3 presents the results of a ^{40}Ar-^{39}Ar geochronological study on the Garhwal section of the Himalayan metamorphic belt. The ^{40}Ar-^{39}Ar ages are used to constrain the timing of extensional movement on the Malari Fault. The implications of normal faulting for the evolution of the metamorphic belt are explored by simple one-dimensional thermal modelling using the new ^{40}Ar-^{39}Ar data in conjunction with published constraints on the prograde evolution of the metamorphic belt.

Chapter 4 presents new ^{40}Ar-^{39}Ar ages and geochemical data for post-collisional dykes in southern Tibet. These data are used to constrain the onset of east-west extension in southern Tibet and, by comparison with published geochemical and geochronological data for

potassic volcanics in southern Tibet, to address the relationship of extension to post-collisional potassic magmatism.

Chapter 5 presents ^{40}Ar-^{39}Ar ages, elemental and isotopic data for Miocene to Recent post-collisional potassic volcanics from northern and southern Tibet, which are discussed in the context of published data. These data are used to identify the presence of different sub-continental lithospheric mantle (SCLM) source regions. The nature of the melting regimes, mantle source compositions and mineralogy are constrained by forward and inverse methods of trace element modelling. Petrogenetic constraints for both mafic and silicic samples are used to determine the time-averaged thermal structure of the Tibetan lithosphere, and to assess geodynamic models for the plateau's development. Preliminary ^{40}Ar-^{39}Ar dates for xenocrystic phlogopites place constraints on the timing of the most recent episode of mantle metasomatism.

Chapter 6 is a synthesis of the preceding three chapters; it summarises and discusses their findings in the broader context of the evolution of the Himalayan-Tibetan orogen as a whole. Potential areas of further research are highlighted.

Published abstracts relating to this thesis are given in Appendix F. Chapter 4 is a complete manuscript, accepted for publication in *Geology,* entitled "Age and composition of dykes in Southern Tibet: new constraints on the timing of east-west extension and its relationship to post-collisional volcanism" co-authored by Simon Turner (Bristol University), Simon Kelley (OU) and Nigel Harris (OU). Two additional papers will arise from this thesis, based on Chapters 3 and 5.

2 Background and Geological Setting: The Himalayan-Tibetan orogen

This Chapter gives an overview of the main aspects of Himalayan and Tibetan geology and of relevant geodynamic models in order to provide a framework for the discussion of the timing of normal faulting in Chapter 3, and of Tibetan post-collisional magmatism in Chapters 4 and 5. For further detail, the reader is referred to reviews by (Le Fort, 1975; Hodges, 2000; Yin and Harrison, 2000) and references therein.

2.1 Overview

The Himalaya and the Tibetan plateau are considered a classic example of orogenesis, resulting from the continent-continent collision of the Indian and Eurasian plates in the early Tertiary (Rowley, 1996). The timing of collision has been determined by several methods: i) reconstruction of the relative positions on India and Asia extrapolated from apparent polar wander paths (APWP; Klootwijk et al., 1992); ii) estimating the northward movement of India on the basis of magnetic anomalies in the Indian ocean (Patriat and Achache, 1984); iv) faunal evidence for the time when the ocean separating India from Asia ceased to be a geographical barrier (Jaegar et al., 1989); v) sedimentological evidence recording rapid subsidence and sedimentation associated with the generation of fore-deep basin (Rowley, 1996). Clearly, these methods of dating the timing of collision correspond to dating different stages in a protracted process. Logically, one would expect the APWP to give the

most accurate determination of when initial contact of the continental plates occurred. On the basis of APWP, Klootwijk et al. (1992) suggested that collision was oldest in the western Himalaya, between 60 and 65 Ma, and that suturing between the two continents was completed by 50 to 55 Ma. However, the timing of changes in the northward motion of India would relate most closely to when suturing was complete (i.e. when subduction of buoyant continental lithosphere begins). Patriat and Achache (1984) estimated that collision occurred between 48 and 50 Ma using this approach, and their ages approach the APWP ages of Klootwijk et al. (1992) for complete suture. The significance of the sedimentological estimates is less clear as the response time of the crust to thrust loading is poorly constrained, as is when such thrusting occurs. Nonetheless, these estimates supply minimum ages to collision.

Irrespective of the method used to estimate the timing of collision, it is clear that there is a general decrease in the age of collision to the east. Using APWP, Klootwijk et al. (1992) estimate that there was a delay of 5 to 15 Ma between suturing in the western extremity of the orogen and suturing in the east. In a review of stratigraphic data, Rowley, (1996) estimate the diachroneity at ~ 9 Ma, from ~ 52 Ma in the west to ~ 41 Ma in the east. Collision diachroneity is thought to be the result of a 20° to 30° counterclockwise rotation of the Indian plate with respect to Asia during the early Tertiary (Figure 2.1) (Klootwijk et al., 1985; Van der Voo et al., 1999). In this thesis, the onset of collision is taken as 60 to 65 Ma, after (Klootwijk et al., 1992), and final suturing is assumed to have been completed by 48 to 50 Ma (Patriat and Achache, 1984).

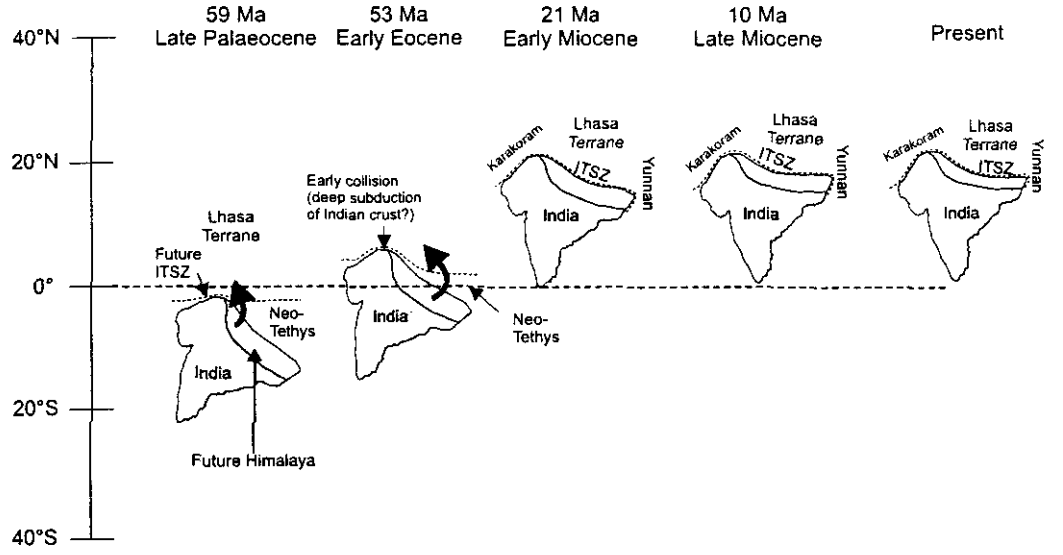

Figure 2.1 Five stage evolution of the India-Asia convergence.

During the Late Paleocene to the Eocene, the northern boundary of the Indian plate collided, from west to east, with the Asia margin. From ~ 36 Ma onwards the counterclockwise rotation of India became pronounced, and by the early Miocene actual indentation of India into Asia had ceased. Modified after Klootwijk et al. (1985).

The 2500 km long mountain belt extends from south-eastern China to northern Pakistan, and forms the eastern continuation of the Alpine-Himalayan chain (Le Fort, 1975), delineating the boundary between various fragments of Gondwana and the southern margin of Laurasia (Figure 2.2). To the north of the Himalayan belt lies the Tibetan plateau, an area of uplifted crust approximately 3500 by 1500 km with a mean elevation of ca. 5000 m (Fielding et al., 1994). It is a complex tectonic collage created by the sequential accretion, from north to south, of several microplates and ancient arc terranes to the southern margin of Eurasia since the early Paleozoic (Dewey et al., 1988). The closure of Neo-Tethys in the Cretaceous and the formation of the Himalayan mountain belt during the Tertiary represent the most recent of these events.

As shown in Figure 2.2, the plateau may be divided into four major east-west striking blocks: the Lhasa, Changtang, Songan-Ganze and Kunlun terranes. The Lhasa terrane is bounded by the Indus Tsangpo Suture Zone (ITSZ) to the south and by the Bangong-Nujiang suture to the north, which marks the locus of collision with the Changtang block in the late Jurassic (Dewey et al., 1988). It has been proposed, on the basis of biostratigraphic correlations (Yin, 1997), that peninsular India and the Lhasa terrane were both derived from Gondwana, and that the latter may represent a block that rifted early from the supercontinent. Sedimentary strata exposed in the Lhasa terrane consist predominantly of shallow marine clastic and carbonate sequences deposited intermittently from the Ordovician to the Eocene (Yin et al., 1988; Zhang et al., 1998). The basement is believed to be Mid-Proterozoic in age, as represented by the Amdo orthogneiss (Harris et al., 1988). The Changtang terrane lies between the Jinsha suture to the north and the Bangong-Nujiang suture to the south; it was accreted to the Songpan-Ganze block to the north in the Late

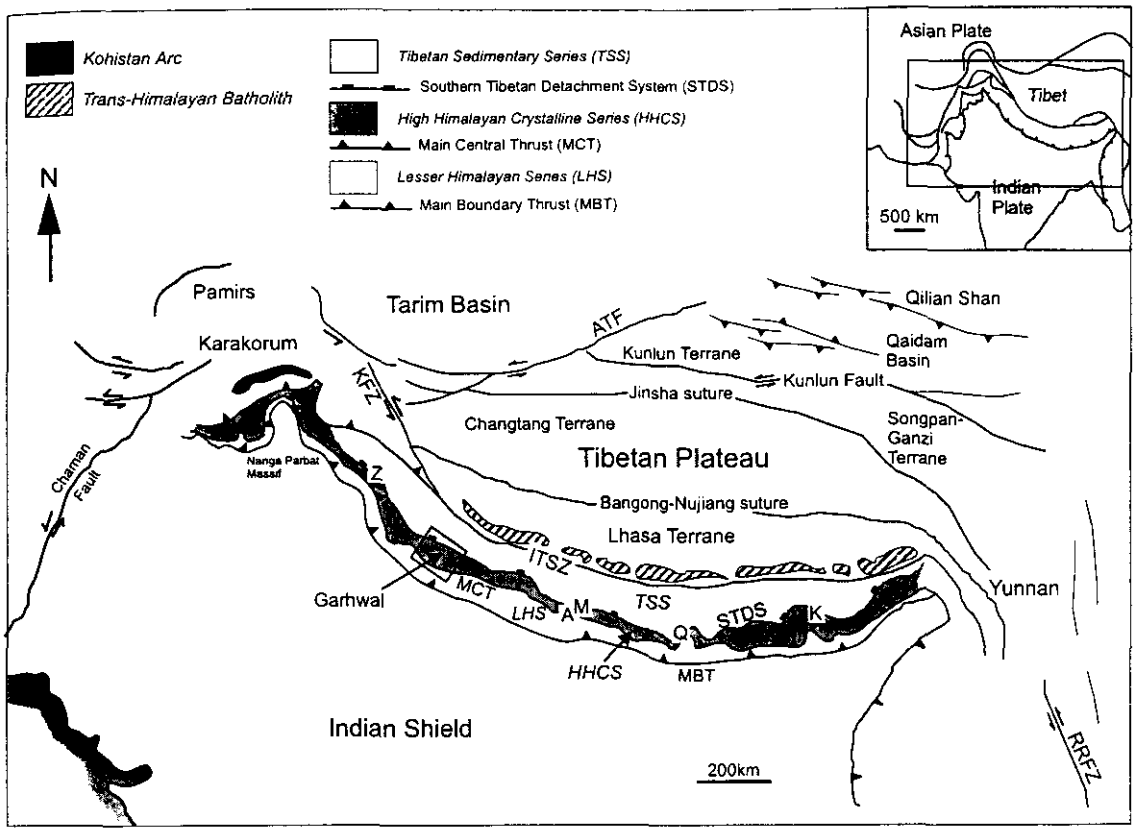

Figure 2.2 Simplified tectonic map of southern Asia and the Himalayan mountain belt.

The main tectonic units, and their bounding faults are shown. Major fault zones shown include the Karakorum Fault Zone (KFZ), the Red River Shear Zone (RRFZ) and the Altyn Tagh Fault (ATF) in Tibet, the Southern Tibetan Detachment System (STDS), Main Central Thrust (MCT) and Main Boundary Thrust (MBT) in the Himalaya. The Indus-Tsangpo-Suture Zone (ITSZ) divides the Indian from the Laurasian terranes to the north. The suture zone is further complicated in the west, where the Kohistan-Laddakh island arc terrane was sutured to Asia in the Cretaceous. The subduction of Tethys resulted in calc-alkaline Andean-type magmatism: the Trans-Himalayan Batholith, exposed to the north of the suture zone. Himalayan localities discussed: Z - Zanskar, A - Annapurna, M - Manaslu, Q - Qomolangma (Everest), K - Khula Kangri.

Triassic or earliest Jurassic (Dewey et al., 1988). It is not clear what the age and nature of the Changtang basement are, and how this block evolved prior to collision in the Tertiary. Recent studies (e.g. Hacker et al., 2000; Kapp et al., 2000) suggest that the lower crust of the Changtang terrane is composed of a series of metasedimentary mélange complexes, in contrast to the crystalline basement inferred for the Lhasa terrane. The Songpan-Ganze terrane was accreted to the Kunlun-Tarim basin along the Kunlun-Quinlin suture during the Late Permian (Dewey et al., 1988); however there is no direct information regarding either the nature or age of the crustal basement of the Songpan-Ganze block, or the Kunlun terrane.

Before collision with India, the southern margin of the Lhasa terrane was marked by a continental arc (the Trans-Himalyan Batholith and associated extrusives) that developed as a consequence of the northward subduction of Neo-Tethys oceanic crust in the Cretaceous (Dewey and Bird, 1970; Debon et al., 1985). Geochronological studies suggest that calc-alkaline magmatism pre-dated, and significantly outlasted, the docking of the Indian sub-continent with Eurasia (Schärer et al., 1984; Debon et al., 1985; Miller et al., 2000).

To the west, the Tibetan plateau narrows and is replaced by the Karakoram, which, along with the Lhasa terrane, formed the southern margin of the Asian plate prior to the collision of the Kohistan-Ladakh arc in the mid Cretaceous, and then the Indian plate in the early Tertiary (Searle et al., 1999a). The Indus Tsangpo Suture Zone (ITSZ) separates the Karakoram, Kohistan-Ladakh arc and southern Tibet from the Indian plate. Remnants of Neo-Tethys are preserved in the form of flysch, mollase and ophiolites in this zone, identifying this feature as the boundary between the Indian and Asian landmasses (Gansser, 1964). Petrologic evidence suggests that Indian continental margin was subducted to mantle depths (O'Brien et al., 1999), whereas seismic anisotropy measurements (Hirn et al., 1995)

and reflection profiles (Zhao et al., 1993) indicate shallow north directed underthrusting of Indian lithosphere south of the ITSZ. Recent seismic studies (e.g. Kosarev et al., 1999) indicate that Indian lithosphere may now underplate Tibet as far as ~33°N, > 400 km north of the ITSZ. Seismic tomography suggests that portions of the oceanic slab have now been partly overridden by penisular India (Van der Voo et al., 1999).

The Tibetan Sedimentary Series (TSS), exposed on the southern side of the ITSZ, are a ~10 to 15 m thick sequence of Cambro-Ordovician to mid-Eocene fossiliferous marine sediments (Burg et al., 1983) and are recognised as the passive margin shelf deposits of the Indian Plate (Gaetani and Garzanti, 1991). Following collision, they were deformed into a series of south directed thrust nappes (Steck et al., 1993) and metamorphosed to lower greenschist grade. As such, the TSS represents the northernmost and structurally highest unit of the Himalayan orogen, although original depositional relationships with the other lithotectonic units are unclear. The TSS has been relatively poorly studied compared to the other major units of the orogen, and it is consequently difficult to assess the lateral continuity of the unit across the range. Although it has been suggested that the TSS form an autochthonous sequence, the thinning of units and presence of imbricate thrusts precludes confirmation of this hypothesis (e.g. Steck et al., 1993).

The TSS are bound to the south by a northerly dipping, normal sense fault called the Southern Tibetan Detachment System (STDS) which separates them from the metamorphic core of the orogen, the High Himalayan Crystalline Series (HHCS). The STDS separates the weakly metamorphosed TSS from the high-grade metasediments and extends across the orogen, from Zanskar to eastern Tibet, north of Bhutan (Herren, 1987; Burchfiel et al., 1992; Edwards et al., 1996). Generally, the STDS may be described as a series of low-angle

detachments, with a footwall of mylonitised sillimanite-grade metapelites injected by leucogranite intrusions. Structural studies have shown that it is characterised by top-to-the-north shear indicating normal movement (Herren, 1987; Burchfiel et al., 1992) possibly with a dextral shear component (Pêcher, 1991). However, the study of individual sections of the fault system reveals that the character of the detachment is variable along strike, from semi-brittle normal faulting to highly ductile shear zones where the metamorphic isograds of the HHCS are compressed (Burchfiel et al., 1992; Hodges et al., 1996; Searle, 1999). This highlights the fact that the STDS is not a single fault plane, but a complex zone of north-directed extensional deformation. Different strands of the STDS are likely to have been active at different times and to have experienced several periods of reactivation (Hodges et al., 1996). The whole STDS may have once been a of series sub-parallel north dipping thrusts, analogous to the MCT and MBT (Shackleton, 1981; Patel et al., 1993; Vannay and Hodges, 1996).

The HHCS are a ~ 15 to 30 km thick sequence of Late Proterozoic/Cambro-Ordovician amphibolite grade gneisses, schists, calc silicates and amphibolites (Parrish and Hodges, 1996; Ahmad et al., 2000). They are interpreted as a thick section of accreted continental crust originally derived from the subducting Indian plate (Le Fort, 1975), which has been thickened and buried as a result of collision and southward directed thrusting, and is intruded by leucogranitic dykes and plutons at higher structural levels. The base of this sequence is marked by the Main Central Thrust Zone (MCTZ), a shear zone between 5 and 20 km thick, which separates the HHCS from the Lesser Himalayan Series (LHS) to the south (Metcalfe, 1993; McFarlane, 1995; Harrison et al., 1997b; Jain and Manickavasagam, 1997). The MCT is undoubtedly important in accommodating deformation - deep seismic reflection profiles; Hauk (1998) suggest a minimum of ~300 km of shortening of the Indian

basement across the Himalaya, most of which they attribute to shear along the MCT. The LHS is a ~20 km thick sequence of lower grade metasediments intercalated with metamorphosed volcanics and granites. Both the HHCS and LHS were largely derived from Late Proterozoic/Cambro-Ordovician sedimentary protoliths, and recent Sr and Nd isotope studies, and U-Pb analyses of detrital zircons within these units, suggest that the LHS is older that the HHCS and may represent the basement on which the HHCS was deposited (Parrish and Hodges, 1996; Ahmad et al., 2000). The LHS is in turn thrust to the south over the Siwalik foreland basin molasse sequence by the Main Boundary Thrust (MBT). The southernmost thrust in this sequence is the seismically active Main Frontal Thrust (Wesnousky et al., 1999), which thrusts the Siwalik sequence over the Indo-Gangetic plains. The MBT and MCT can be correlated with large-scale crustal reflections beneath the Himalaya and Southern Tibet, while the ultimate sole thrust is a décollement termed the Main Himalayan Thrust, interpreted as the active fault along which India is currently underthrusting southern Tibet at depth (Brown et al., 1996; Hauk, 1998).

The Himalaya are an active orogenic region - the northward movement of the Indian plate continues at a rate of 58 ± 4 mm yr^{-1} today (Bilham et al., 1997) although it has slowed since initial collision. Based on this continuing convergence, Patriat and Achache (1984) estimated that some 2500 km of shortening between the Asian and Indian cratons must have taken place since collision. The mechanisms by which the northward movement of the Indian plate has been accommodated are widely debated, and popular models include underthrusting along major faults within the Himalaya (Coward and Butler, 1985), extrusion of crustal wedges by synchronous motion on normal and reverse faults within the Himalaya (Burchfiel et al., 1992) eastward extrusion of the Tibetan plateau along strike-slip faults (Tapponier and Molnar, 1976; Wittlinger et al., 1998), continental subduction (Meyer et al.,

1998), convective removal of mantle lithosphere beneath Tibet (Houseman et al., 1981) and breakoff of the subducting Indian slab (Chemenda et al., 2000). These models and their predictions will be discussed in a later section. As a young, still-evolving mountain belt, the Himalayan-Tibetan orogen provides a unique window into the thermotectonic processes that have driven the formation of older orogenic regions.

2.2 Post-collision evolution of the Himalayan-Tibetan orogen

2.2.1 The Himalaya: metamorphism and magmatism

Crustal thickening and tectonic burial following collision resulted in increased pressures and temperatures in the crust. This is evident in the preserved metamorphic facies of the TSS, HHCS and Lesser Himalaya Series (LHS). The HHCS and LHS display folded and inverted patterns of metamorphic isograds. In the HHCS, the preserved metamorphic field gradients apparently increase up structural section from garnet + kyanite to sillimanite + K-feldspar at the top of the sequence (Le Fort, 1975). The assemblage biotite + garnet ± kyanite is present at the top of the LHS sequence close to the MCTZ, but the lower levels of this sequence appear unaffected by Tertiary metamorphism (Oliver et al., 1995). The origins and significance of the apparent inverted metamorphism in both sequences have been widely debated (e.g. Jaupart et al., 1985; Hodges and Silverberg, 1988; Harrison et al., 1997b; Jain and Manickavasagam, 1997).

Based on field and metamorphic evidence, two metamorphic "events" can be distinguished within the HHCS: an earlier ("Eo-Himalayan") kyanite-grade metamorphism and a later, sillimanite-grade "Neo-Himalayan" event (Hodges and Silverberg, 1988; Vannay and Hodges, 1996). These two metamorphic events probably represent selective preservation of certain segments of the continuous P-T path followed by the upper crust after collision, characterised by a transition from higher pressures to higher temperatures with time. Few ages constrain the timing of the earlier, M1 kyanite-grade "event", but the available data presently suggest that it is Eocene to mid-Oligocene in age with a duration of at least 10 Ma (Hodges and Silverberg, 1988; Vannay and Hodges, 1996; Prince, 1999; Vance and Harris, 1999).

The Neo-Himalayan sillimanite-grade event coincided with mid-or lower-crustal melting and formation of migmatites at ~ 21 to 20 Ma and leucogranite magmas at ~ 24 to 17 Ma with the main phase of melt generation at 24 to 19 Ma (for reviews see Harrison et al., 1997a; Searle et al., 1999b). These granites, termed the High Himalayan Leucogranites (HHL) may have formed from vapor-absent muscovite-dehydration melting of the basal, kyanite-grade HHCS triggered by isothermal decompression on the STDS (Harris and Massey, 1994). In contrast, Harrison et al. (1997a; 1999) invoked shear heating along a continuously active basal decollément to explain the formation of the HHL and a belt of younger granites, termed the North Himalayan Granites. Recently, Harrison et al. (1999) obtained detailed age data by *in-situ* dating of the Manaslu leucogranite in Nepal and suggested that magma generation occurred over a period of ~ 4 Ma, with two main pulses of melt generation. A similarly complex pattern of melt generation and emplacement occurs in the Annapurna range, where Hodges et al. (1996) observed several generations of

leucogranite generation, with U-Th-Pb data suggesting that magmatism ranged from 22.5 to ~18.5 Ma, with the peak of activity between 22.5 and 21.5 Ma.

2.2.2 The Himalaya: timing of faulting and exhumation

Establishing a geochronological timescale of deformation, metamorphism and magmatism is important in constraining thermal and tectonic processes in orogenic regions. In particular, determining the relative timing of motion on different faults or different parts of a fault is fundamental to understanding the thermal and mechanical response of the crust to continental collision. In order to provide a context for the new ^{40}Ar-^{39}Ar ages for the Malari fault presented in Chapter 3, the following sections discuss available geochronological constraints for movement on the different strands of the MCT and STDS across the orogen. All errors in the following review of literature data are quoted, where appropriate, at the 2 σ level, based on the errors assigned to the ages by the authors. In Chapters 3, 4, and 5, where new ^{40}Ar-^{39}Ar ages are presented, the calculated ages are asigned 2 σ errors, calculated from the regression of the data on the inverse diagram.

2.2.2.1 Overview: Geochronology in Metamorphic Terranes

The interpretation of the ages discussed below in terms of geological events is based - critically – on the closure temperature concept (Dodson, 1973). This is discussed in detail with respect to the ^{40}Ar-^{39}Ar system in section 3.2.8, however, the salient aspects of this concept and of its application to other isotope systems (Rb-Sr, U-Th-Pb and Sm-Nd) are outlined below. Closure temperature theory is based on the temperature dependence of solid

diffusion processes. Dodson (1973) defined the closure temperature of a geochronological system as the temperature that corresponds to the apparent age recorded by the system. The system is regarded as being theoretically closed to the migration of either parent or daughter isotope below this temperature, allowing the build-up of the radiogenic daughter isotope. Such closure temperatures may be constrained for different mineral and isotopic systems using independent geological estimation of temperatures or by calculation from the expression of (Dodson, 1973), applying experimentally determined diffusion parameters.

For example, in the Rb-Sr system, a thermal perturbation may be recorded by the movement of radiogenic ^{87}Sr (produced by decay of ^{87}Rb) from Rb rich minerals such as potassium feldspar and micas into minerals suchas as plagioclase and apatite, which have a strong affinity for Sr. The timing of such events may be determined using mineral-whole rock isochrons, and therefore used to elucidate the cooling history of metamorphic terranes. This approach was first used by Jager et al. (1967) and Jager (1973) in the central Alps. Jager et al. found that in rocks of low metamorphic grade, muscovites and biotites gave Hercynian (> 200 Ma) Rb-Sr ages, whereas on moving to a higher metamorphic grade characterised by the appearance of stipnomelane (which these authors considered equivalent to a temperature of ~ 300°C) ages of 35 to 40 Ma were preserved. Jager et al. attributed these younger ages to the resetting of the Rb-Sr system during metamorphism. On the basis of these observations, they argued that the 300°C temperature corresponded to the closure of the Rb-Sr system in biotite. Similarly, the closure temperature of white mica (muscovite and phengite) was constrained to be ~ 500°C on the basis of the first resetting of Rb-Sr ages above the staurolite-chlorotoid isograd (Purdy and Jagar, 1976).

The traditional approach to studying the chronological and high-temperature thermal histoy of metamorphic terrains has been through the U-Th-Pb chronology of accessory phases such as titanite, zircon and monazite (e.g. Spear and Parrish, 1996) which occur in both igneous and metamorphic rocks. Based on the similarity between titanite U-Pb ages to ^{40}Ar-^{39}Ar ages preserved in hornblendes within the metamorphic core of the southeastern Canadian Cordillera, Leaman and Parish (1991) inferred that the closure temperature for Pb in titanite was equivalent to that for Ar in hornblende (530°C; Harrison, 1981). By comparing the retentivity of Pb in zircon relative to titanite, Heaman and Parrish estimated that the closure temperature of Pb in unalterted zircon was > 800°C. In monazite the closure temperature of the U-Th-Pb system is constrained to be ~ 700°C (Copeland et al., 1988) based on the preservation of inherited Pb in ?metamorphic monazites. This estimate corresponds well with experimental data, which suggests that a closure temperature of ~ 750°C be assigned to monazite (Ayres et al., 1998). It should be emphasised that the Pb diffusion systematics in both zircon and monazite are complex; for example Pb loss in metamict (fractured) zircons has been documented at relatively low temperatures, below 600°C (e.g. Silver, 1963) and may be thermally induced during high grade metamorphism at temperatures above 650°C (Leaman and Parrish, 1991).

Vance and O'Nions (1990) argued that Sm-Nd garnet chronology provided a uniquely powerful tool for dating high temperature prograde metamorphism, in contrast to the Rb-Sr and ^{40}Ar-^{39}Ar systems, which record cooling events. The closure temperature for Nd in garnet ranges from 675 to 800°C, and, as highlighted in a recent study, is dependent on cooling rate, grain size and peak temperature experienced (Ganguly et al., 1998). As the compositions of garnets often record the pressure and temperature regime over which they grew, the prograde pressure-temperature evolution of the rock can be directly linked with

the Sm-Nd ages obtained, as recently demonstrated for the Zanskar Himalaya (Vance and Harris, 1998).

2.2.2.2 Main Central Thrust

Timing of southward thrusting on the MCT has been constrained by dating the main phase of tectonic burial of the Main Central Thrust Zone (MCTZ) or the Lesser Himalayan sequence, which are both in the thrust footwall. Alternatively, if thrusting propagated southwards, dating the latest high temperature prograde metamorphism (i.e. burial) of the HHCS will give an indirect maximum age constraint on the timing of MCT movment. This may be complicated or rendered invalid by out-of-sequence movements (e.g. Hodges et al., 1996).

There are relatively few geochronological studies that have focussed on the MCT, and the bulk of the data originates from the Garhwal (India; 78°30' E), Annapurna (Nepal; 84° E) and Qomolangma (Everest, Nepal, 86°40' E) sections (Figure 2.2). In Garhwal, Metcalfe (1993) related a hornblende ^{40}Ar-^{39}Ar age of 19.8 ± 2.6 Ma from the MCTZ to the latest episode of high temperature shearing (closure temperature for Ar in hornblende: 500-550°C; McDougall and Harrison, 1999) on this strand of the fault system. This age is consistent with garnet Sm-Nd and monazite U-Th-Pb data from the basal HHCS of Garhwal (Prince, 1999) which suggest that high temperature mineral growth continued until 22 ± 3 Ma and 22.5 ± 1.6 Ma, respectively. As the ages of Prince (1999) are attributed to prograde metamorphism within the hangingwall of the MCT, they represent maximum age constraints on the timing of fault movement. A younger Rb-Sr age of 13.5 ± 0.5 Ma from the Garhwal

MCTZ (Oliver et al., 1995) may relate to a later phase of reactivation. Reactivation of the MCT is also implied by *in situ* dating of monazite inclusions in garnets from the MCTZ of Garhwal, which indicate a maximum age of ~6 Ma for this event (Harrison et al., 1997b). Further east, in the Annapurna section (Figure 2.2) of Nepal Hodges et al. (1996) obtained a U-Pb age of ~22.5 Ma from a deformed migmatitic leucosome in the basal HHCS. Although this age is imprecise, compromised by discordance, Hodges et al. (1996) interpreted it in terms of migmatite crystallisation shortly before, or during thrust related deformation. Similarly, Coleman (1998) constrained the time of amphibolite-grade metamorphism, and therefore high-temperature shearing on the MCT, to be ~18 –20 Ma based on a U-Pb age from the basal HHCS in the Marsyandi Valley (84°20' E). Johnson and Rogers (1997) suggested that high temperature shearing on the MCT in the Kathmandu Valley (85° E) could be as young as 13.9 ± 0.2 Ma based on Rb-Sr data for deformed pegmatites in the basal HHCS. They interpreted their ages in terms of simple cooling following high-temperature metamorphism (unrelated to exhumation), and tentatively suggested that ductile movement on the MCT had ceased by ~ 14 Ma. It is not possible to determine whether these young ages represent fault reactivation, or out-of-sequence thrusting. Hubbard and Harrison (1989) concluded that a hornblende ^{40}Ar-^{39}Ar age of 20.9 ± 0.2 Ma from the basal HHCS of the Qomolangma section (Figure 2.2) dated metamorphism related to MCT thrusting, as the closure temperature of Ar in hornblende falls within the range of metamorphic temperatures calculated for the lower MCTZ.

2.2.2.3 Southern Tibetan Detachment System

The timing of cooling within the upper HHCS, and potentially, movement on the STDS, is somewhat better constrained than the MCT. However, few cross-cutting relationships have been observed, and the majority of ages reflect cooling events that have been related to normal faulting and exhumation. As there is a delay between fault movement and cooling (House and Hodges, 1994; Vance et al., 1998) due to thermal relaxation processes within the upper crust, cooling ages provide minimum age constraints on faulting. Furthermore, relating cooling ages to exhumation and normal fault movement can be ambiguous – for example, the well-constrained cooling of the HHCS leucogranites at ~17 to 20 Ma has been attributed to independent movement on both the MCT and the STDS (Hubbard and Harrison, 1989; Metcalfe, 1993).

The Zanskar Shear Zone (ZSZ), the western extremity of the STDS (Figure 2.2), has been studied in detail. Inger (1998) bracketed ductile movement on the shear zone to between 26.5 ± 0.7 and 22.5 ± 0.5 Ma, based on Rb-Sr mineral ages on mylonites from the shear zone. Inger (1998) related these ages to deformation, as the greenschist-facies mylonites had not been above Rb-Sr closure temperatures (~500°C; Cliff, 1985). Similarly, Vance et al. (1998) interpreted ^{40}Ar-^{39}Ar ages of 23.5 ± 1.8 Ma to 28 ± 0.7 Ma on pervasively deformed samples from the ZSZ in terms of the absolute timing of deformation, and ductile deformation in the shear zone. Younger ages (14.4 ± 2.1 to 19.8 ± 1.9 Ma) from the upper HHCS were interpreted in terms of delayed footwall cooling following normal faulting (Vance et al., 1998; Dezes et al., 1999). In this section, Inger (1998) observed that the

difference between biotite ^{40}Ar-^{39}Ar cooling ages of similar samples was considerably less than that between muscovite ^{40}Ar-^{39}Ar cooling ages. This implies several stages of fault movement and footwall reorganisation at temperatures between muscovite (400-450°C; McDougall and Harrison, 1999) and biotite (330-250°C) closure – i.e. samples were tectonically juxtaposed between 18.2 ± 0.4 Ma (^{40}Ar-^{39}Ar, muscovite) and 16.3 ± 0.3 Ma (^{40}Ar-^{39}Ar, biotite).

Structural criteria suggest that the Garhwal leucogranites were emplaced in a broadly north-south extensional tectonic regime (Scaillet et al, 1995; Searle et al, 1993), and may therefore be used to constrain the timing of extension related to STDS movement. Searle et al. (1999b) obtained a U-Pb age of 23.0 ± 0.2 Ma and a K-Ar age of 22 ± 0.1 Ma Ma for the Shivling leucogranite (79°30' E), which were interpreted in terms of emplacement and cooling, respectively. The similarity of these ages requires rapid cooling (350-400°C Ma^{-1}) between the U-Pb closure temperatures in monazite (750°C; Ayers and Miller, 1998) and the Ar closure temperature in muscovite (400 to 450°C). Th-Pb monazite ages of 21.9 ± 0.5 Ma and 22.4 ± 0.5 Ma for the Shivling and Gangotri leucogranites, respectively (Harrison et al., 1997a), are consistent with these age constraints and suggest that leucogranite generation and extension relating to STDS movement may be relatively synchronous in Garhwal. Younger cooling ages of 17.9 ± 0.1 Ma (^{40}Ar-^{39}Ar) and 18.9 ± 1.3 Ma (K-Ar) for the Gangotri and Bhagirathi leucogranites, respectively (Stern et al., 1989; Sorkhabi et al., 1996), may reflect a later phase of extension-related cooling.

Work in the Annapurna region, Nepal (Figure 2.2) demonstrates close spatial and temporal relations between extensional and contractional fault systems. Hodges et al. (1996) identified several generations of normal and thrust faulting, with the earliest extension

contemporaneous with thrusting at ~ 22.5 Ma. Coleman and Hodges (1998) obtained ^{40}Ar-^{39}Ar ages of 26.7 ± 1.2 Ma to 29.7 ± 1.2 Ma from metamorphic white micas in TSS marbles in the hangingwall of the STDS in the Marsyandi Valley of Nepal (84°10' E). These ages may be regarded as maximum age constraints on STDS movement, since normal faulting results will rapidly cool of the footwall, and will not strongly affect the thermal structure of the hangingwall. A ^{40}Ar-^{39}Ar age of 16.6 ± 0.7 Ma for an undeformed leucogranite crosscutting the hangingwall foliation provides a minimum constraint on the timing of ductile deformation (Coleman and Hodges, 1998). Younger ^{40}Ar-^{39}Ar ages of 14.9 ± 0.7 Ma to 16.6 ± 0.7 Ma for the HHCS (Coleman and Hodges, 1998) likely reflect delayed cooling in response to normal faulting. Further east, the Manaslu pluton (84°30' E; Figure 2.2) cross-cuts extensional features related to the detachment, and shows localised development of dextral, ductile normal shear. Most movement on the STDS in this region therefore considered to pre-dated emplacement of the granite, which occurred from 24.8 ± 0.8Ma, in several discrete phases (Guillot et al., 1994; Harrison et al., 1999).

In the Qomolangma region of southern Tibet (Figure 2.2), granites both pre-and post-date a strand of the STDS, although Murphy and Harrison (1999) emphasise that no direct cross-cutting relations have been observed. Amphibolite facies metamorphism within the upper HHCS footwall is constrained by a U-Pb titanite age at 20.5 ± 0.1 Ma (Hodges et al., 1992), providing a maximum constraint on STDS movement, since prograde metamorphism was effectively terminated by exhumation related to extensional faulting. The bulk of U-Pb and Th-Pb data for this section of the STDS suggests that movement occurred before ~16 Ma (e.g. Hodges and Hurtado, 1998; Murphy and Harrison, 1999). A muscovite ^{40}Ar-^{39}Ar age of 16.4 ± 0.4 Ma obtained from the Rongbuk pluton is within error of most of the Th-Pb and U-Pb ages, suggesting that cooling of the HHL and upper HHCS was extremely rapid at this

time (Hodges et al., 1998). On the basis of monazite Th-Pb ages between 16.2 ± 0.8 Ma and 16.8 ± 0.8 Ma, Murphy and Harrison (1999) argued that the Qomolangma section of the STDS had not moved significantly prior to ~17 Ma, precluding synchronous movement on the MCT and STDS. However, the ages obtained by Murphy and Harrison (1999) are potentially biased towards younger values, as individual microprobe spot ages in the range of 19.5 to 23.9 Ma are discarded on the basis of inheritance, which cannot be quantified in the Th-Pb system. Furthermore, Williams et al. (1999) emphasise that the behaviour of the Th and Pb in monazite is complex, and may not bear any relation to discrete tectonic events.

Younger cooling ages associated with the detachment system have been recorded from several localities further east. Hodges et al. (1994) suggested, on the basis of ^{40}Ar-^{39}Ar ages on muscovite and potassium feldspar, that a pulse of rapid cooling (100°C-400°C Ma^{-1}) between 13.5 ± 0.5 Ma to 16.1 ± 0.3 Ma in the Dingyyê region of southern Tibet could be related to tectonic denudation on normal faults. Leucogranite emplacement and movement on the STDS appears to young dramatically east of the Yadong cross-structure, an apparent 70 km offset of the detachment (Wu et al., 1998). Edwards and Harrison (1997) obtained a Th-Pb monazite age of 12.5 ± 0.4 Ma on the mylonitised Khula Kangri granite (Figure 2.2) in the footwall of the STDS, placing a broad constraint on the timing of deformation. This age is based on a weighted mean of a selected population of microprobe analyses, and may not fully reflect the spatial complexities of monazite growth (Williams et al., 1999). However, Wu et al. (1998) dated a leucogranite immediately to the east of the Yadong cross-structure (90°) at 11.9 ± 0.6 Ma using the U-Pb technique which lends support to the age obtained by Edwards and Harrison (1997). ^{40}Ar-^{39}Ar cooling ages from the Khula Kangri granite are 10.7 ± 0.5 Ma and 10.9 ± 0.3 Ma, for biotite and muscovite respectively (Maluski

et al., 1988). The close similarity of the Th-Pb, U-Pb and ^{40}Ar-^{39}Ar ages suggest rapid cooling (at least 150°C Ma^{-1}).

From the available data it appears that the STDS was active as early as ~26 Ma in Zanskar, and that rapid cooling related to tectonic denudation on this fault system was occurring as recently as ~11 Ma. Leucogranites, generally emplaced in the immediate footwall of the STDS, show extensional fabrics, evidence of emplacement in an extensional environment, which probably facilitated their emplacement. Cooling rates preserved in footwall rocks appear to be high (100°C-400°CMa^{-1}) for individual segments of the fault, although the available data imply that cooling is not synchronous along strike across the orogen. Ductile deformation on the MCT is constrained to be between ~19 to 22 Ma, although several phases of subsequent reactivation have been documented, the most recent being <6 Ma from *in situ* Th-Pb dating of monazite inclusions in garnet (Harrison et al., 1997b). Studies of individual fault segments from 76° to 90°E along the strike of the mountain belt demonstrate that there is considerable variation in both the timing and style of deformation. Evaluating the diachroneity of movement on these different strands of the MCT and STDS is complicated by difficulties in correlating different units and structural levels along strike, and in identifying and correlating different fault strands. Also problematic is the complex nature of the fault systems themselves, many parts of which show evidence of multiple reactivation (e.g. Harrison et al., 1997b; Catlos et al., 1999).

2.2.3 The Tibetan Plateau

Since palaeomagnetic studies by Patriat and Achache, (1984) and Lin and Watts (1988) suggest that some 2000 ± 800 km of movement has occurred between the Lhasa terrane and Asia, significant shortening over the Tibetan Plateau can be inferred. Following collision along the ITSZ, the southern Tibetan plateau was characterised by molasse deposition, extensive crustal thickening and the development of major thrust systems between 30.4 ± 0.4 Ma and 12.3 ± 0.4 Ma, as constrained by multi-diffusion domain (MDD) modelling of ^{40}Ar-^{39}Ar data obtained from potassium feldspars in upper crustal rocks (Quidelleur et al., 1997; Yin et al., 1999a). Tertiary thrusting and foreland basin development is also observed in the northern Changtang, Songpan-Ganzi and Kunlun terranes, although the exact timing of these events is unknown (Coward et al., 1988; Leeder et al., 1988). Seismic studies indicate that the crust of the Lhasa terrane is now ~80 km thick, whereas the crust of the northern terranes is ~60 km thick (Kosarev et al., 1999).

Unfortunately, it is difficult to directly determine the pre-collision elevation of the Tibetan plateau, or whether crustal thickening occurred purely as a result of the Indo-Asia collision, or whether it reflects earlier orogenic events. Murphy et al. (1997) suggested that the Lhasa terrane had already attained an elevation of ~3 km by the mid Cretaceous, as a consequence of thrusting between the Lhasa and Changtang blocks. Their estimates of the palaeoelevation of southern Tibet were based on two balanced cross sections, and it should be noted that their calculations did not account for crustal subsidence following thrusting. Moreover, the conclusions reached by Murphy et al. (1997) are not substantiated by the

widespread distribution of fossiliferous marine sediments which indicate that a substantial part of the Lhasa terrane was below sea-level until the mid-Eocene (Zhang et al., 1998). Therefore, southern Tibet can only have attained its present elevation of ~5 km following the Tertiary collision. The Changtang and Songpan-Ganzi terranes are characterised by discontinuous continental red-bed deposition from the Permian and Carboniferous, respectively (Smith and Xu, 1988); their elevation prior to collision is therefore unconstrained.

The Miocene to Recent deformation of the Tibetan plateau has been characterised by east-west extension since 14.2 ± 0.9 Ma in the south (Coleman and Hodges, 1995), and from 3.9 ± 0.4 Ma in northern Tibet, based on preliminary ^{40}Ar-^{39}Ar data from syn-kinematic fault vein muscovites (Bi et al., 1999). Strike-slip movement occurs on the major strike-slip faults bounding the plateau (Figure 2.2), and thrust faulting is prevalent at the plateau margins (Figure 2.2), in the Himalaya and to the northeast of the plateau, in the Qulian Shan (Tapponnier et al., 1990). Extension is manifest as north-south trending grabens (Armijo et al., 1986; Yin et al., 1999b), and in the development of associated Neogene-Quartenary intermontane basins. This mode of deformation continues today, evident from the seismicity in southern Tibet (Molnar and Tapponnier, 1978). Major strike-slip faults include the Karakorum Fault Zone (KFZ; Figure 2.2), active from ~18 Ma (Searle et al., 1998), the Altyn Tagh fault system and the Red River Fault Zone (RRFZ), both intermittently active from ~32 Ma (Leloup et al., 1995; Yin and Harrison, 2000). Seismic studies indicate that individual faults within the Altyn Tagh Fault System in northern Tibet remain active today (Molnar and Lyon-Caen, 1989). The Altyn Tagh fault may be either a crustal-scale transfer fault or a lithospheric-scale thrust (Wittlinger et al., 1998). Teleseismic experiments across the fault reveal a low P-wave velocity anomaly down to depths of ~ 140 km, and on this

basis, the Altyn Tagh fault was interpreted as an intracontinental plate boundary (Wittlinger et al., 1998). If this interpretation is correct, it has important implications for the accommodation of plate convergence, allowing the extrusion of large lithospheric blocks – i.e. the Tibetan plateau – to the east, and the south directed subduction of the Tarim Basin beneath the plateau (Wittlinger et al., 1998).

2.2.3.1 Post collisional magmatism

The Tibetan plateau is presently characterised by the presence of small-volume mafic potassic and dacitic magmatism, the significance of which is discussed further in Chapters 4 and 5. ^{40}Ar-^{39}Ar dating of these volcanic rocks demonstrates that they were emplaced from 25.4 ± 0.2 Ma in southern Tibet (Miller et al., 1999) and from 18.5 ± 0.6 Ma and 36 ± 0.6 Ma in northern and eastern Tibet, respectively (Turner et al., 1996; Chung et al., 1998; Hacker, pers. comm). This style of magmatism supercedes calc-alkaline, subduction related magmatism within the Lhasa terrane, which had ceased by 37.0 ± 3.5 Ma (Miller et al., 2000). Such changes in magmatism are indicative of a change in the thermal structures of mantle and crust, and therefore suggest a major change in tectonic regime. Post-collisional, mafic potassic magmatism in northern and southern Tibet is generally considered to be derived from the SCLM (Turner et al., 1993; Turner et al., 1996; Miller et al., 1999) although Hacker et al. (2000) suggested that the unusual geochemistry of these rocks could result from the interaction of mantle and lower crustal melts.

2.2.3.2 Geodynamic models for the development of the Tibetan plateau

From the above discussion, it is apparent that there have been major changes in the style of deformation and magmatism manifest on the Tibetan plateau in the Neogene. Such changes are indicative of a fundamental change in the stress regime of the orogen, yet the chronology of marine magnetic anomalies in the Indian ocean indicate that there was little change in either the rate, or the inclination of plate convergence during this time (Patriat and Achache, 1984). Therefore, the onset of extension, strike-slip faulting and the transition from calc-alkaline to potassic, shoshonitic magmatism in the Tibetan plateau must reflect the influence of other mechanisms.

The Miocene transition from a compressive to an extensional deformation regime without a cessation or decrease in plate convergence has been interpreted in several ways. McCaffrey and Nabelek (1998) related the distribution of north-south trending normal faults in southern Tibet to oblique underthrusting of the Indian plate, and suggested that the southern margin of the plateau was behaving as a series of rigid blocks, spreading to accommodate the northward movement of the curved indentor. However, this model does not explain the widespread distribution of normal faults in northern Tibet (Yin et al., 1999b), further from the collision front. An alternative interpretation is that the transition from a dominantly compressional to an extensional regime reflects an increase in the elevation and potential energy of the region to a level that cannot be sustained by the marginal stresses imposed by plate convergence. If such a marked increase occurred in the plateau's elevation during the Miocene, it would have profound consequences for the Himalayan belt to the south (Hodges,

2000), and other more distal parts of the convergent region e.g. the Karakoram and the Tien Shan (Abdrakhmatov et al., 1996).

A plethora of geodynamic models have been proposed to explain the development of the Tibetan plateau, but it is not yet clear whether any hypothesis truly meets the tests posed by its own predictions. The purpose of this section is to outline the major competing models and to discuss their respective predictions in terms of magmatism, deformation and elevation history. Geodynamic models for the uplift of the Tibetan Plateau include those which treat the lithosphere as a continuum (e.g. Houseman et al., 1981; England and McKenzie, 1982; England and Houseman, 1986), and those which describe the behaviour of the lithosphere in terms of rigid plates, relating the high elevation of the plateau to crustal thickening and eastward extrusion along major strike-slip faults (Tapponnier et al., 1982). Continental subduction of both Indian and Asian lithosphere (Willett and Beaumont, 1994; Meyer et al., 1998) and the breakoff of the oceanic part of the subducting Indian slab (Chemenda et al., 2000) have also been invoked to explain the present high elevation and extension of the plateau.

Continuum models

In the first class of models, the lithosphere is treated as a continuum and plate convergence is accommodated by the distributed deformation and thickening of the entire lithosphere which thermally destabilises the sub-continental mantle lithosphere (SCLM) with respect to the asthenosphere, resulting in subsequent removal (Houseman et al., 1981). This process has been depicted in different ways. Bird (1979) described removal of the SCLM in terms directly comparable with subduction processes: the entire SCLM is peeled off (delaminated)

as a slab and replaced by hot asthenosphere that comes into direct contact with the base of the crust. This can result in decompression melting of the asthenosphere, and the generation of considerable volumes of basaltic magmas, with associated crustal melting. In contrast, Houseman et al. (1981) proposed removal of SCLM by convective thinning at its base following instantaneous thickening of the upper conducing layer of the SCLM and the thermal boundary layer. This model, depicted in Figure 2.3 A, differs from that of Bird (1979) in that only part of the SCLM is removed, and the asthenosphere does not come into contact with the base of the crust. Furthermore, delamination models predict a migrating front of SCLM removal, while models that invoke some form of convective thinning predict a roughly symmetric geometry for the process. In any case, removal of the lower SCLM, and its replacement by asthenosphere results in uplift and an increase in the potential energy of the region. Plateau uplift is simply an isostatic response to the removal of part of the relatively cold and dense SCLM, and its replacement with more buoyant, hot asthenosphere. Furthermore, the replacement of SCLM with asthenosphere results in a transient elevation in the thermal structure of the remaining SCLM. Post-collisional magmatism in both northern and southern Tibet (Turner et al., 1993; Turner et al., 1996; Chung et al., 1998; Miller et al., 1999) has been ascribed to the melting of enriched regions within the SCLM following convective removal. The increase in potential energy and elevation resulting from convective removal cannot be supported by convergent boundary forces and, following thermal relaxation, the potential energy excess is dissipated by normal faulting (England and Houseman, 1989).

Refinements of the initial model of (Houseman et al., 1981) incorporate more realistic temperature and strain dependent rheologies for the crust and mantle lithosphere (e.g. Houseman and Molnar, 1997; Conrad and Molnar, 1999), and examine the effects of

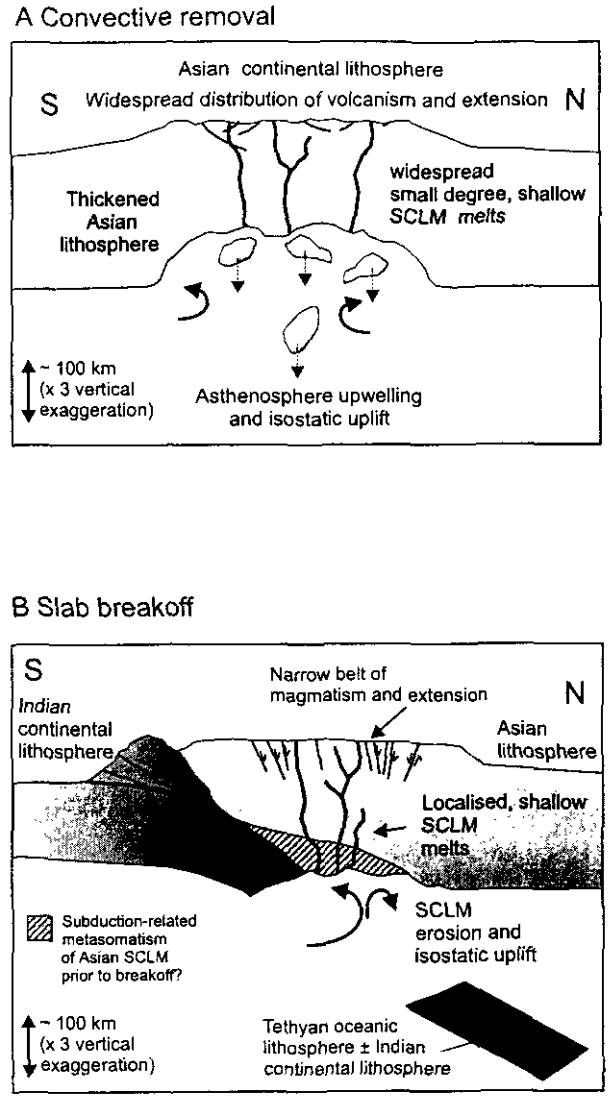

Figure 2.3 Schematic illustration of convective removal and slab breakoff models.

Modified after Platt and England, (1994); Davies and von Blanckenburg (1995). Convective removal (A) can explain genetic relationships between high elevation, extension and small degree SCLM melting. The removal of the dense, oceanic part of the subducting slab (B) and its replacement with asthenosphere will result in isostatic uplift and ultimately extension, although the length-scale of this is unclear. If slab breakoff is accompanied by localised thinning of the overriding SCLM, then small degree SCLM melting of the thinned region will occur.

time-delayed instability development (Houseman and Molnar, 1997). Clearly, the rheology of the SCLM is fundamental: it controls the resistance of the SCLM to deformation, and therefore whether or not convective removal is likely to occur. For example, Houseman and Molnar (1997) estimated that only the lower 50 to 60 % of the SCLM (i.e. the hottest part of the SCLM, > 900°C) can be removed assuming a rheology of dry olivine; for a wet olivine rheology, the fraction removed increases to > 80 %. Their model suggests that the fraction of SCLM removed was almost completely independent of the development time of the initial convective instability, and that in all conditions, convective thinning had a duration of ~10 Ma. Lenardic and Kaula (1995) considered the effects of temperature-dependent Newtonian viscosity on a stratified lithosphere, and found that this effectively strengthened the upper SCLM and reduced the fraction of SCLM which could be removed. They suggested a timescale of only ~5 Ma for this process. Conrad and Molnar (1999) suggested that the short timescales and the small fractions of the SCLM removed predicted by numerical models could be reconciled with large-scale surface uplift if episodic, multi-stage convective erosion at the base of the SCLM was invoked. They estimate that after ~10 Ma of mechanical thickening, episodic convective erosion could reduce the SCLM to ~60 % of its original value prior to thickening. Such episodic convective thinning clearly predicts a corresponding distribution of SCLM-derived magmatism coupled with a diachronous pattern of uplift and upper crustal extension. At present, the episodic process envisaged by Conrad and Molnar (1999) is likely to be the most realistic depiction of convective removal although this, and other viscous sheet models, do not yet address lateral variations in SCLM strength and composition, or pre-existing structural heterogeneities. (*c.f.* Kong et al., 1997).

Rigid Plate Models

Models which envisage the evolution of the Tibetan plateau in terms of plate boundary movements suggest that plate convergence is accommodated by the extrusion of the plateau to the east by strike-slip faulting along major shear zones (e.g. the RRFZ, KFZ and Altyn Tagh fault systems; Figure 2.2) and by thrusting within and to the north of the plateau (Tapponnier et al., 1982; Armijo et al., 1986; Meyer et al., 1998; Wittlinger et al., 1998). In these models, the crust thickens and is extruded eastwards while the Indian continental lithosphere subducts to the north at the original collision front. Meyer et al. (1998) further suggested that significant crustal thickening and elevation increase occurred as a consequence of south-directed intracontinental subduction of Tibetan lithosphere beneath the plateau on the reactivated Bangong-Nuijang and Jinsha sutures. Similarly, Wittlinger et al. (1998) suggested that the Altyn Tagh fault system extends to the base of the SCLM and behaves as an oblique plate boundary, allowing south-directed subduction of Tarim basin lithosphere beneath northern Tibet. These models predict diachronous uplift of the plateau soon after collision. In the context of these rigid plate models, the upper-crustal extension in southern Tibet is the product of forces applied to adjacent plate boundaries (Klootwijk et al., 1985; Armijo et al., 1986; McCaffrey and Nabelek, 1998) and does not reflect the elevation history of the region in any sense. Similarly, such rigid plate models do not create a mechanism for the association of magmatism with either extension or elevation change, and no temporal relationships between any of these events are predicted by these models.

Slab Breakoff

The uplift of the Tibetan plateau and the exhumation of high-grade rocks in the core of the Himalayan belt can also be explained in terms of slab breakoff (Figure 2.3 B): the buoyancy-driven detachment of subducted oceanic lithosphere from lighter continental lithosphere during continental collision (Davies and von Blanckenburg, 1995; Chemenda et al., 2000). Chemenda et al. (2000) further suggested that the evolution of the Himalayan-Tibetan orogen could be explained by two breakoff events, the first involving removal of Tethyan oceanic lithosphere in the Eocene, whereas subducted Indian SCLM is detached in the early Miocene. In this model, the second breakoff event causes failure and extrusion of the Indian crust and the formation of the STDS and MCT/MBT systems. Plateau uplift and exhumation of high grade rocks is caused by isostatic rebound following the detachment of the dense oceanic slab, and its replacement by asthenosphere at the breakoff point. At first appraisal, this model appears to be a simple modification of the rigid plate models discussed above: for slab breakoff to occur, strain localisation within the subducting Indian lithosphere is required, as opposed to the diffuse accommodation of deformation envisaged by (Houseman et al., 1981). However, this process could potentially result in the localised thermal erosion of the overriding Tibetan SCLM (e.g. Davies and von Blanckenburg, 1995; Davies and von Blanckenburg, 1997) in a manner analogous to the episodic convective erosion of the lower SCLM envisaged by Conrad and Molnar (1999). In this case, localised small-degree melting of the remaining SCLM is likely to occur above the breakoff point as the asthenosphere comes into direct contact with the base of the thinned SCLM in the area above the breakoff point (Figure 2.3 B).

The differences between models in which convective thinning of SCLM is triggered by diffuse shortening and models where it is a consequence of subduction related events are largely conceptual: they stem from assumed differences in the rheology and mechanical behaviour of continental lithosphere. Therefore, these models are best regarded as end member descriptions of lithospheric mantle behaviour during orogenesis. This point is emphasised by the recent finite-element modelling of Pysklywec et al. (2000) which demonstrates that mixed modes of lithosphere deformation, including the failure of strong lithosphere, slab breakoff and Rayleigh-Taylor type convective instabilities at the base of the SCLM, can occur beneath collisional regions. While the models of Houseman et al. (1981); Davies and von Blanckenburg (1995); Conrad and Molnar (1999); Pysklywec et al. (2000) are all strongly dependent on the rheology assumed for the continental lithosphere, they all demonstrate the potential instability of non-cratonic continental lithosphere during orogenic processes.

2.3 Summary

The Himalayan and Tibetan regions have been traditionally treated as separate systems; and the interrelationships between them are not yet fully understood (Hodges, 2000). Both systems document a history of post-collisional magmatism, crustal thickening and extensional faulting. New findings (see Hodges, 2000 for a recent review) indicate that marked changes took place in the modes of deformation and in the magmatism of the Himalaya and southern Tibet in the Early Miocene. This suggests that the evolution of the Himalaya and the Tibetan plateau are coupled in some way, and that a major change in the dynamics of the entire orogen occurred in the Early Miocene.

Geodynamic models for the uplift of the Tibetan plateau make predictions regarding the relationships between the thermal state of the continental lithosphere, crustal extension and uplift. Rigid plate models predict the localisation of deformation on the strike-slip faults which bound the modern plateau, and envisage that extension will only occur in close proximity to these faults or to the collision zone. They do not predict diffuse magmatism, but require it to be localised on fault zones as a consequence of shear heating (e.g. Leloup et al., 1995; Leloup et al., 1999), or to be associated with the Banngong-Nuijiang and Jinsha sutures (Figure 2.2) in the continental subduction model of Meyer et al. (1998).

Continuum models that invoke SCLM thinning (e.g. Houseman et al., 1981) predict diffuse extension, an elevation in the thermal structure of the Tibetan lithosphere, and the widespread distribution of crustal melts and magmas derived from shallow melting of the SCLM across the plateau. These models do not predict the spatial association of any of these features with any major sutures, strike-slip faults or the collision zone. They predict a temporal association between extension and plateau uplift, and that mantle derived magmatism – interpreted as the surface expression of SCLM thinning – will predate both extension and uplift. Localised thinning of the SCLM following slab breakoff will produce a narrow, linear belt of SCLM-derived magmatism followed by extensional faulting that mirrors the geometry of the collision zone. Slab breakoff without SCLM thinning would also produce SCLM-derived mantle melts; these would be extracted from the base of the thickened SCLM at depths of ~ 150 to 200 km.

Both slab breakoff and convective removal models predict a rapid increase in the plateau's elevation. This will result in an increased potential energy contrast at the margins of the

plateau, resulting in thrust faulting or the extrusion of fault-bounded crustal wedges at the plateau margins. These models therefore predict that the onset of SCLM-derived magmatism in Tibet will be synchronous with the development with major fault systems in the Himalaya, and possibly to the north of the plateau (Figure 2.2). In order to test such models, it is essential to establish the relative chronology of movement on major faults, magmatism, extensional deformation and uplift in both the Himalaya and Tibet, and to combine this with available constraints on the thermal structure of the lithosphere in these regions.

3 Timing of movement on the Southern Tibetan Detachment System, Malari Region from ^{40}Ar-^{39}Ar geochronology

3.1 Introduction

An apparently paradoxical feature of orogenic processes is the development of extensional structures within overall highly compressive systems. Until recently, extension and exhumation were considered to be purely late-orogenic processes, initiated after shortening had ceased, possibly triggered by potential energy excesses in the orogenic wedge (Platt and England, 1994). However, new evidence from active mountain belts such as the Alps and the Himalayas (Armijo et al., 1986; Burchfiel et al., 1992) and older orogens such as the Caledonides (Fossen and Dunlap, 1998; Braathen et al., 2000) suggests that extension is likely to have been contemporaneous with shortening and crustal thickening, and may have exerted a significant control on the thermal and topographic evolution of these regions.

In the Himalayan-Tibetan orogen, two distinct types of normal faulting are observed, and linked with geodynamic models for the evolution of the region (Chapter 2). East-west extension on north-south striking normal faults has been occurring in southern Tibet and northern Nepal since at least 14 Ma (Coleman and Hodges, 1995), possibly as early as 18 Ma (Chapter 4). In contrast, extension in the Himalayan mountain belt is north-south in

sense and largely restricted to the STDS. Movement on this normal fault system has dominated much of the unroofing across the mountain belt, and is likely to exert a control on topography.

In this chapter the results of a laser Ar-Ar study of micas from the Garhwal Himalaya are presented, with the aim of constraining the timing of movement on the Malari strand of the STDS and the thermal effects of such extension on the metamorphic belt. The ^{40}Ar-^{39}Ar system is a powerful tool in studying the timing and rates of exhumation within orogenic regions, as different minerals close to Ar diffusion at different temperatures. This provides timing information about different stages of cooling and exhumation. Furthermore, the ^{40}Ar-^{39}Ar technique can date the absolute timing of deformation events, in cases where grain size reduction or re-crystallisation occurs below the temperature at which argon can diffuse out of the mineral (Reddy and Potts, 1999). Therefore, the spatial distribution of argon ages across structures such as thrusts and normal faults provides important information about the timing of movement of these structures, and hence can provide constraints on the thermal evolution of the crust in orogenic regions. This work builds on a complementary study of prograde, high temperature metamorphism in this region (Prince, 1999), allowing the elucidation of the thermal history of this section of the mountain belt, and comparisons with the other Himalayan sections discussed in the Chapter 2.

3.2 The ^{40}Ar-^{39}Ar technique

3.2.1 Introduction and general principles

In order to form a framework for the presentation of new ^{40}Ar-^{39}Ar ages in this and subsequent chapters, this section briefly discusses the various aspects of the ^{40}Ar-^{39}Ar dating system and their role in the interpretation of ^{40}Ar-^{39}Ar ages in deformed terranes. For a more detailed background to the ^{40}Ar-^{39}Ar technique, the reader is referred to McDougall and Harrison (1999) and to Kelley (1995).

3.2.2 The ^{40}Ar-^{39}Ar dating technique

In radiogenic dating systems, based on the constant decay of a parent isotope and the accumulation of a stable daughter isotope, the age calculated reflects radiogenic ingrowth following the closure of the system to the incorporation or loss of either the parent or daughter species. The ^{40}Ar-^{39}Ar dating technique is, like the K-Ar system, based on the decay of the radiogenic parent species ^{40}K to its daughter, ^{40}Ar.

^{40}K has a half-life of 1250 Ma, 89.5% decaying to ^{40}Ca by electron (β^-) emission, and 10.5% decaying to ^{40}Ar predominantly by orbital electron capture. As both daughter products are stable, the ratios of both $^{40}Ca/^{40}K$ and $^{40}Ar/^{40}K$ could theoretically be used to obtain dates. However, ^{40}Ca is an abundant isotope in nature and distinguishing ^{40}Ca produced by decay

of ^{40}K from naturally present ^{40}Ca is only possible in the oldest, potassium-rich rocks. In contrast, ^{40}Ar is only ever present in trace amounts and dating based on the production of ^{40}Ar *from* ^{40}K *can be applied to geological problems.*

The fundamental difference between the ^{40}Ar-^{39}Ar dating technique and the K-Ar system is in the measurement of potassium. Merrihue and Turner (1966) first utilised the fact that ^{39}Ar has a comparatively long half-life (269 years) and can be treated as a stable isotope in mass spectrometry. They applied this to the development of the modern ^{40}Ar-^{39}Ar technique, where ^{39}K is transformed to ^{39}Ar by fast neutron bombardment during irradiation in a nuclear reactor. A neutron replaces a proton in the nucleus of the ^{39}K, transmuting it to ^{39}Ar with a corresponding release of energy, recoiling the atom an average of 0.08 μm (Villa et al., 1983).

Isotopes of K undergo very little fractionation in nature and, therefore, the $^{40}K/^{39}K$ ratio may be regarded as essentially constant, and is conventionally assumed to be 0.0001167 (Steiger and Jäger, 1977). Therefore, the $^{40}Ar/^{39}Ar$ ratio is proportional to the $^{40}Ar/^{40}K$ – the daughter to parent ratio - in the sample, and can be used to calculate the age. Although the ^{39}Ar produced is radioactive and ultimately decays to ^{39}K by beta emission with a half-life of 269 years, the effect is minimal between the irradiation time and the analysis, which is generally less than a year.

The amount of ^{39}Ar produced from ^{39}K during irradiation is a function of ^{39}K in the sample, proportional to a dimensionless irradiation parameter, J. The J value is specific to each sample within a given irradiation, and is calculated by including standard minerals of known age within the collection of samples to be dated. The inclusion of such standards, which

have precise ages based on numerous repeat analyses and calibration to the K-Ar dating scheme, effectively monitors the neutron flux. Each reactor has a different spectrum and level of neutron flux, and the flux varies depending on the location of the samples within the reactor. The neutron flux gradient is significant along the length and breadth of the sample containing tube, and standards are interspersed between samples in order to monitor these variations. The value of J appropriate for the samples irradiated will depend on their location relative to the standards during irradiation - small sample sizes are generally irradiated to ensure that the neutron flux across minerals from an individual sample is constant.

The apparent age of the sample is calculated as in equation 3.1 (Mitchell, 1968):

Equation 3-1

$$age = \frac{1}{\lambda} \ln \left\{ \left(\frac{^{40}Ar^{*}}{^{39}Ar} \right) J + 1 \right\}$$

The age is a function of the measured $^{40}Ar^*/^{39}Ar$ ratio of the sample (where *denotes the ^{40}Ar resulting purely from radiogenic ingrowth), the J value for the irradiation, and λ, the combined decay constant for ^{40}K, comprising the decay of ^{40}Ar to ^{40}Ca by beta emissions, the decay of ^{40}K to ^{40}Ar by electron capture and gamma emission, and the decay of ^{40}K to ^{40}Ar by electron capture. This has a value of $5.543 \times 10^{-10} yr^{-1}$.

In an "ideal" radiometric dating technique, the measured abundance of the daughter species would reflect solely its accumulation by decay of the parent species since the system first became closed to their exchange. In many isotope systems, this assumption is not strictly valid, as there is already a significant abundance of daughter species present within the system. In the ^{40}Ar-^{39}Ar dating system, the argon released from a sample during laser ablation or step heating will ideally reflect a mixture of two components: trapped argon, present initially or absorbed into the sample during preparation, and the argon which accumulated from the decay of radiogenic ^{40}K, following closure of the system. The radiogenic $^{40}Ar^*/^{39}Ar$ ratio used in Equation 3.1 can be calculated by subtracting the "initial" ^{40}Ar component, assuming that it has the same $^{40}Ar/^{36}Ar$ value as present-day air (295.5). This approach may be complicated by the presence of an initial component with a non-atmospheric $^{40}Ar/^{36}Ar$ value, or by spatial heterogenities in the composition of this component. These problems can be addressed, to some degree, by plotting the data on a $^{36}Ar/^{40}Ar$-$^{39}Ar/^{40}Ar$ inverse isochron. This is explored further in section 3.2.6.

3.2.3 Irradiation and interference reactions

The amount of ^{39}Ar produced from the transmutation of ^{39}K during irradiation is proportional to several parameters unique to the irradiation: the length of time of the irradiation, the neutron flux density at a specified energy and the neutron capture cross-section of ^{39}K for neutrons of that energy. These factors, the $^{39}K/^{40}K$ ratio, and the combined decay constant for ^{39}K define the dimensionless parameter J in Equation 3.1. The irradiation procedure induces not only the production of ^{39}Ar, but also a series of interfering reactions that result from the neutron bombardment of K, Ar, Cl and Ca. The magnitude of

the interference reactions varies with the neutron flux energy, and correction factors may be calculated for different nuclear reactors based on the irradiation of mineral salts (McDougall and Harrison, 1999) . If samples have high calcium contents, a correction must be made for the decay of ^{37}Ar (produced from ^{40}Ca) in the period between sample irradiation and analysis, as ^{37}Ar has a half-life of 35 days. In order to achieve the maximum analytical precision, the neutron flux of the irradiation must be optimised carefully so that a measurable amount of ^{39}Ar is produced while the amounts of isotopes derived from interfering reactions (which will also increase with the neutron flux) are minimised (Turner, 1971). The most important aspects to be considered in this are the sample's approximate age and K/Ca ratio. Older samples require higher irradiation fluxes to obtain low $^{40}Ar/^{39}Ar$ ratios, and higher Ca minerals such as amphibole are more prone to interference reactions.

While interference reactions generally have a detrimental effect on the precision of the ages obtained by the ^{40}Ar-^{39}Ar technique, they may also provide useful compositional information that may be related to the ages obtained. For example, neutron bombardment induces the transmutation of ^{37}Cl to ^{38}Cl, which has an extremely short half-life, ultimately decaying to ^{38}Ar. Therefore the relative amount of ^{38}Ar in an individual analysis may be correlated with the amount of chlorine (and potentially, the degree of alteration) held in similar lattice sites to Ar (Onsott et al., 1991).

3.2.4 Calculation of errors

The precision on the age obtained from a ^{40}Ar-^{39}Ar analysis depends on several factors. The magnitude of the uncertainty is frequently dependent on the sample size, or amount of argon

extracted from within the sample, as large samples are less affected by blank corrections and errors on the blanks. Young samples, with lower amounts of argon, often contain relatively high atmospheric contamination, and a larger volume of sample may have to be analysed in order to increase the precision on such analyses. The error in the calculated age (1 sigma) can be calculated using the following expression from Dalrymple et al. (1981):

Equation 3-2

$$\sigma_t^2 = \frac{J^2\sigma_R^2 + R^2\sigma_J^2}{\lambda^2(1+RJ)^2}$$

where σ_t is the final error on the age, J is the irradiation parameter discussed in sections 3.2.1 and 3.1.2, R is the $^{40}Ar^*/^{39}Ar$ ratio, λ is the combined decay constant of ^{40}K, σ_R is the error on the $^{40}Ar^*/^{39}Ar$ ratio as measured and σ_J is the error on the J value. The latter may be calculated as the error on the average J value obtained from analyses of the relevant standards included within package of irradiated samples; here a maximum "blanket value" of $\pm$ 0.5% is used.

3.2.5 Release and analysis of argon

3.2.5.1 Sample preparation and loading

Laser techniques are flexible, allowing for both the analysis of *in situ* mineral grains or groundmass/glass within a "thick" section and also of individual separated minerals. *In situ* work allows the investigation of relationships between age, the position of the analysed mineral within the rock and textural relationship to other mineral species. However, if the section is cut from only a small fragment of the rock sample that may not contain all the mineral phases of particular interest. When a rock is crushed and separated, individual minerals of a given species are hand-picked to produce a pure separate without altered or damaged grains. The nature of the research and the limitations imposed by the available samples determine the approach adopted.

In the following study both "thick" sections and mineral separates were prepared. The "thick" section preparation technique is similar to that of a thin section except the resultant section is 100-150 μm thick and is attached to its glass slide by *Canada Balsam* rather than epoxy resin. The sections were subsequently heated to soften the *Canada Balsam* and removed from their glass slide. Each section was then cleaned to remove the resin (see below) and broken into smaller pieces suitable for packing into irradiation cylinders

Mineral separates were prepared by first crushing and sieving the samples, retaining the 250 μm – 1000 μm fraction. The fractions were then washed in de-ionised water to remove

dust particles, and dried overnight. Mica grains were then hand-picked using a low powered binocular microscope. Clear grains that appeared to have unbroken and unaltered edges were selected preferentially in an attempt to reduce the possibility of analysing grains with edges damaged by the preparation process or natural alteration.

Both section and separate samples need to be cleaned prior to irradiation and analysis, as the presence of grease from the preparation stage potentially adds hydrocarbons to the analysis, which can interfere with the argon measurements. Cleaning also removes contaminants, some of which may contain potassium that potentially affects the $^{40}Ar/^{39}Ar$ ratio. Samples were cleaned twice in methanol in an ultrasonic bath for 5 minutes, and then for a further 5 minutes in de-ionised water to remove the methanol. They were left to dry overnight before packing in aluminum foil for irradiation. Mineral standards (e.g biotite standard GA1550 in this case) were packed similarly, and spaced regularly between samples in the irradiation cylinders. Following irradiation, samples remained at the reactor until their radiation levels fall to a safe level. Samples were irradiated at the McMaster Reactor, Canada.

After irradiation the samples and standards were loaded into an ultra high vacuum laser port and baked overnight at 120 °C using a 250 W heat lamp to remove any absorbed atmospheric argon and water vapour from the sample surface.

3.2.5.2 Laser techniques

Bulk mineral techniques for the extraction of argon from irradiated samples are based around incrementally heating a relatively large volume of crushed sample with a vacuum

furnace, resulting in a series of ages being obtained for each "step" of the heating process. The use of lasers, for both step heating and total fusion of either separated or in situ minerals has subsequently improved this technique, allowing analysis of single mineral grains (Kelley, 1995).

Currently there are two main types of lasers: continuous wave (CW) and pulsed systems. Continuous wave systems are the most common and operate by the continuous pumping of lamps within the laser cavity to achieve a continuous coherent beam. They are versatile and can be used for both slow heating and instantaneous melting and produce pit sizes varying from 50-250 μm diameter. The disadvantage of these lasers is that local heating of the surrounding material may occur, and in some cases, the analysis may reflect a mixture of gas from different minerals, and possibly, a mixture of ages. Pulsed laser systems produce high power densities for as little as a few nanoseconds, which cause instantaneous ablation and melting. However, the pulsed delivery of power makes it difficult to heat a large quantity of sample quickly, which is problematic for young samples, which have low quantities of ^{40}Ar. For young samples, a CW laser technique is preferred for argon extraction.

In this study, a CW laser was used due to the generally young ages of Himalayan samples. The laser source was a *Spectron Laser Systems SL902* CW Nd YAG, producing a continuous infrared (IR) laser beam with a wavelength of 1064 nm. The beam was directed into a customised *Leica Metallux 3* microscope using high reflectance, oxide coated mirrors, and focussed at the sample surface via the objective lens, resulting in spot sizes of ~ 100 μm. The sample was observed using a CCD camera, coaxial with the laser beam. Argon was extracted from individual minerals using short pulses (10-30 seconds) from the laser. The

power of the beam was increased gradually (typical range 8-18 W) on the individual grains until they began to melt. The IR laser was also used in the analysis of "thick" sections, where the power was increased to 15-17 W and the pulse length reduced to 2-3 msec. This had the effect of reducing and focussing the laser spot, so that spatial precision was optimised and heating of the surrounding area was minimised.

3.2.5.3 Mass spectrometry

Isotopic analysis was carried out using a *MAP 215-50* noble gas spectrometer with a secondary electron multiplier detector. The gas mixture released by laser ablation of the sample was cleaned using 2 *SAES AP 10* getters, with one operated at 400 °C and one at room temperature. These getters were outgassed at the beginning of every day at 800°C for five minutes. In order to perform analyses, the valves were shut, the laser fired at the selected spot and after 5 minutes the gas was equilibrated via automated valves into the mass spectrometer. The mass spectrometer scanned peaks at masses 35, 36, 37, 38, 39, 40 and 41. Peaks at 36-40 are argon and 35 and 41 peaks were analysed so that build-up of chlorine and hydrocarbons in spectrometer could be measured, respectively. Peaks were measured ten times during one analysis, and peak intensities were extrapolated back to the inlet time to correct for argon adsorption onto the spectrometer walls.

Blank levels in the system were determined by running the system in the same way as for a sample analysis but not operating the laser. Blanks were run after every second sample run, and blank corrections were made by averaging the pair of blanks that bracketed each sample run, and then subtracting the blank value from that of the sample. A correction for mass

spectrometer discrimination is also required. Discrimination can cause the atmospheric $^{40}Ar/^{36}Ar$ ratio to be measured as a different value to the accepted 295.5. Discrimination varies with time and between spectrometers, and may be determined by the analysis of glasses known to contain air only. For the *MAP 215-50* noble gas spectrometer of this study a discrimination value of 283 was used, based on measurements of air-rich samples.

3.2.6 Correlation diagrams and interpretation of argon data

The conventional means of determining both the accumulation and the initial amount of the daughter isotope relative to the parent isotope is to use an isochron plot, where the parent and daughter isotopes are both normalised to a stable, non-radiogenic isotope (c.f. Rb-Sr and Sm-Nd systems). This has been applied to the ^{40}Ar-^{39}Ar system, where ^{40}Ar is used as a normalising isotope in the $^{36}Ar/^{40}Ar$-$^{39}Ar/^{40}Ar$ inverse isochron diagram (Roddick, 1978). Inverse isochrons have several advantages: they allow geological or analytical scatter in the data to be assessed quantitatively, and may be used to identify the presence of an initial argon component with a non-atmospheric $^{36}Ar/^{40}Ar$ composition. Least-squares regression is used to plot a line through the analysed data points (York, 1969). The slope of the line is proportional to the age of the sample, and the x-intercept is the reciprocal of the radiogenic $^{40}Ar^*/^{39}Ar$ composition, the y intercept the reciprocal of the initial $^{36}Ar/^{40}Ar$. The basic geometry of the plot is shown in Figure 3.1. The radiogenic component determined from the x-intercept corresponds directly to the "real" age of the sample, according to Equation 3.1.

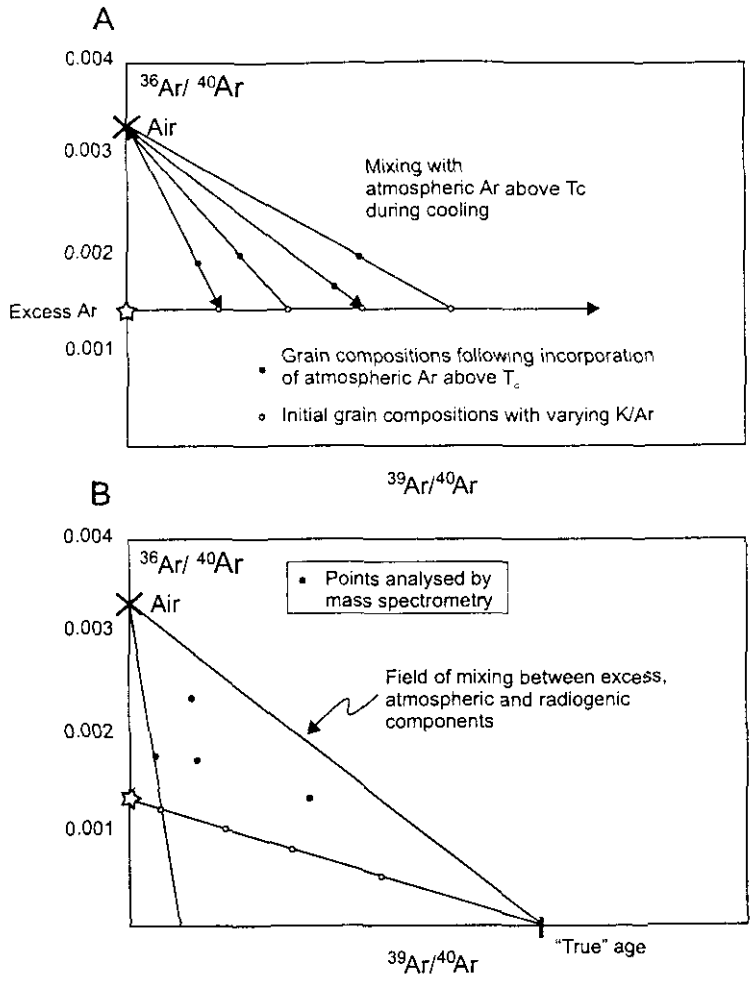

Figure 3.1 Interpretation of inverse correlation diagrams with excess argon

Modified after Roddick (1978); Arnaud and Kelley (1995)

A Situation during cooling above the closure temperature where an initial amount of argon with a non-atmospheric composition is present. At this point there is no radiogenic argon accumulation. During cooling, atmospheric argon may be incorporated into the crystal structure, displacing points upward towards the y-axis (mixing lines).

B Situation at time of analysis. Radiogenic ingrowth results in the clockwise rotation of the data array, so that it becomes steeper with increasing age and the data array more tightly clustered. Analysed points reflect mixtures of three separate argon components: air, initial excess argon and argon present due to radiogenic ingrowth. The data now occupy a triangular field on the isochron diagram. Due to the incorporation of atmospheric argon during cooling, the analysed points may define a spurious trend towards atmospheric argon and it may not be possible to determine the presence, or composition of, excess components. This may result in the calculation of erroneous older ages. The equivalent situation is shown for a sample with no excess argon.

3.2.6.1 Excess argon

The use of isochrons in geochronological systems assumes, fundamentally, that samples formed with an initial isotopic composition identical to modern air and that no later disturbance in the isotopic system followed radiogenic ingrowth. Ideally, the initial $^{36}Ar/^{40}Ar$ calculated from the y-intercept will have the same value as the determined atmospheric argon ratio ($^{40}Ar/^{36}Ar = 295.5$) and data points will define a binary mixing trend between radiogenic and atmospheric components. However, y-intercepts of lower $^{36}Ar/^{40}Ar$ than atmospheric are frequently observed, implying the presence of an initial component with a different $^{36}Ar/^{40}Ar$ signature. This phenomenon is called "excess argon" and the data array may indicate simple mixing between such a component and radiogenic argon, even allowing the "excess" ratio to be constrained. In this case the x-intercept calculated would still reflect the amount of radiogenic argon present from the decay of ^{40}K since closure, and the "real" age can be calculated.

In many cases, data do not define a clear mixing array with a single contaminating component. This may occur when argon with a different isotopic composition to that of the mineral's initial argon is incorporated. This may happen during slow cooling, when the system is above closure. Such a scenario is illustrated in Figure 3.1A. In this case, atmospheric argon is incorporated into a system with a low ("excess") initial argon isotopic composition. Radiogenic ingrowth of ^{40}Ar results in the clockwise rotation of the data array, so that it becomes steeper and more tightly clustered with time (Figure 3.1 B). At the time of analysis, the data array occupies a field on the inverse isochron diagram, with radiogenic

$^{40}Ar^{*}/^{39}Ar$/, "excess" $^{36}Ar/^{40}Ar$ and atmospheric $^{36}Ar/^{40}Ar$ forming three end-members (Figure 3.1B). If the presence of an excess component is not recognised and the array forced through atmospheric argon then an erroneously old age may be calculated. If the ages obtained using such an approach appear anomalously old for the geological setting, then excess argon may be suspected. As it may not be possible to determine the composition of the initial excess component, the youngest "apparent" (assuming an atmospheric initial composition) age calculated for a point provides a maximum constraint on the age of the sample. Horizontal arrays or clusters of data on the inverse isochron diagram may also be observed, and it is difficult to determine whether they reflect an excess component or argon loss. Argon loss and an increase in the relative proportion of the atmospheric component due to alteration may result in positive trends of $^{39}Ar/^{40}Ar$ vs. $^{36}Ar/^{40}Ar$, and the ages obtained may represent underestimates of the "true" age.

3.2.7 Calculation of sample ages

In section 3.2.3 and 3.2.4, equations for calculating ages and corresponding errors were presented. These equations are formulated for a single analysis, as opposed to an overall age and error for the bulk of analytical data collected for a particular sample. This section is concerned with the calculation of ages and errors, based on inverse isochrons and averages of ages calculated from individual analyses, and the assessment of the quality of data obtained.

When the data form an array with a negative slope on the inverse isochron diagram, an age may be calculated from the x-intercept, which defines the overall radiogenic $^{40}Ar^{*}/^{39}Ar$ of

the sample. However, before an age can be calculated, the degree to which the data form a straight mixing line must be evaluated. If the data appear scattered, but with no clear excess component, then the line may have to be forced through air. The MSWD (Mean Square Weighted Deviate) is a statistical test that evaluates the degree of scatter in the regressed data (York, 1969). Generally, an MSWD of 1 (perfect fit, within experimental errors) to 2.5 is considered acceptable (McDougall and Harrison, 1999), while an MSWD of less than one indicates that experimental errors may have been overestimated. If the MSWD calculated is greater than 2.5, this implies that there is more scatter than might be expected from experimental errors alone. Reasons for large amounts of scatter on the inverse ischron diagram include: non-homogenous incorporation of excess argon, incorporation of several initial components with different isotopic compositions, incorporation of older detrital grains. The errors on ages obtained using the $^{40}Ar^*/^{39}Ar$ x-intercept are a function of errors on the linear-least-squares-fit line to the data and its intercepts, as this will take into account the analytical errors on the individual points. This is shown below, after McDougall and Harrison (1999), where the positive and negative errors on an isochron age are calculated:

Equation 3-3

$$\pm error_{age} = age - \frac{1}{\lambda}\ln\left\{\left(\frac{^{40}Ar^*}{^{39}Ar} \pm error_x\right) J + 1\right\}$$

where the $^{40}Ar^*/^{39}Ar$ ratio is equivalent to the reciprocal of the x-intercept of the fitted line and the $error_x$ is the 1 sigma error on that x-intercept, and J and λ are the irradiation parameters and combined decay constants, respectively. The reciprocal of the y-intercept gives the $^{40}Ar/^{36}Ar$ ratio (atmospheric value is 295.5) and the errors on this value may be calculated using the error on that intercept. This expression does not take into account errors on the calculated J value, but these are negligible compared to errors on the x and y intercepts.

Alternatively, the age of the sample may be calculated by a weighted mean of the ages of individual analyses, although this approach assumes that any initial argon present has an atmospheric composition, and may only give a maximum age.

3.2.8 The closure temperature concept

3.2.8.1 Volume diffusion

Closure temperature theory is based on the temperature dependence of solid diffusion processes. The closure temperature of a geochronological system may be defined as the temperature which corresponds to the apparent age recorded by the system (Dodson, 1973). Figure 3.2 shows how these apparent, calculated ages relate to the cooling history of a radiogenic system such as ^{40}Ar-^{39}Ar. At high temperatures, there is open exchange between the system and its environment – the daughter isotope is escaping as fast as it is formed as there is no radiogenic accumulation. At low temperatures, such escape is negligible and the daughter isotope accumulates. There is a transition between these extremes during cooling,

due to the partial closure of the system. Apparent ages are calculated by extrapolating the low temperature part of the accumulation curve back to the time axis (Figure 3.2).

Although the exact closure temperature of a mineral grain is dependent on factors such as grain size, different mineral species have different closure temperatures. For example, amphibole has a higher closure temperature than muscovite, whereas muscovite has a higher closure temperature compared to biotite (Hames and Bowring, 1994; Grove and Harrison, 1996). Therefore different minerals within a given sample preserve different ^{40}Ar-^{39}Ar cooling ages that can be used to estimate the cooling rate. Furthermore, ^{40}Ar-^{39}Ar data can be combined with that from other isotopic dating systems, with different closure or resetting temperatures (Figure 3.3). Closure temperatures for different mineral systems may be constrained from geological estimates or calculated using the expression of (Dodson, 1973) and experimentally determined diffusion parameters. Equation 3.4 (Dodson, 1973) relates closure temperature to volume diffusion during linear cooling for different geometrical diffusion pathways

Equation 3-4

$$T_c = \frac{E/R}{\ln\left\{\left(ART_c^2 D_0/a^2\right)/EdT/dt\right\}}$$

Where T_c is the closure temperature (K), E the activation energy per mole for diffusion, R the universal gas constant, A is a geometrical constant (e.g. for slab, cylinder or sphere models of diffusion). D_o the diffusion coefficient at infinite temperature, a the effective

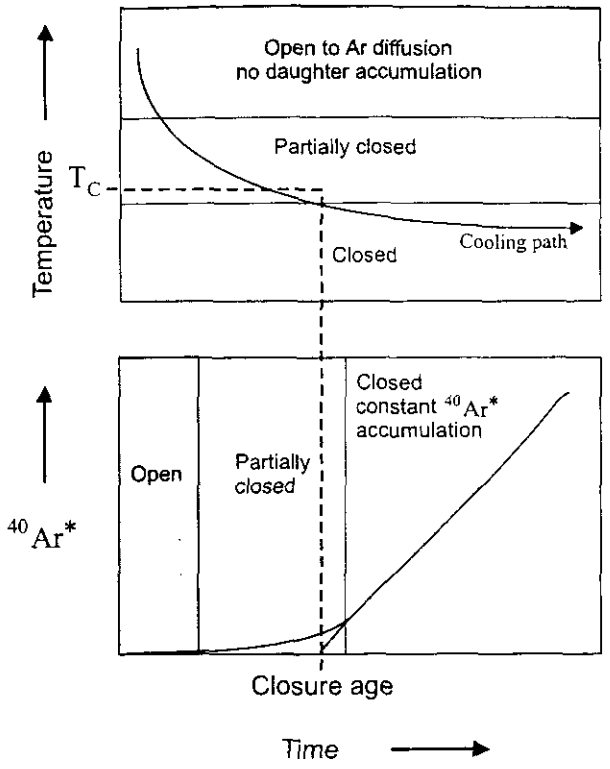

Figure 3.2 Illustration of the volume-diffusion closure temperature concept

After Dodson (1973). The age calculated from radiogenic ingrowth reflects the time at which argon diffusion had almost ceased.

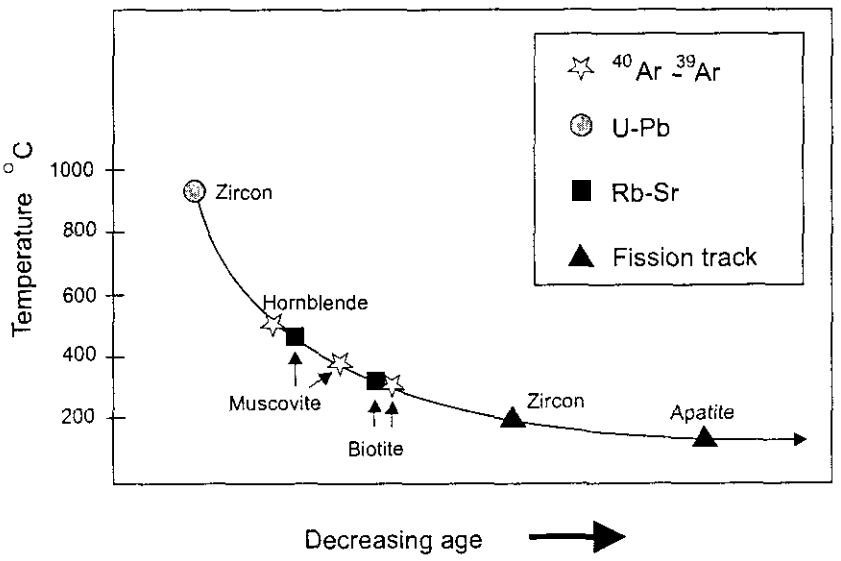

Figure 3.3 Closure temperatures in different mineral and isotopic systems

Schematic diagram modified after Cliff, (1985).

diffusion distance and dT/dt the cooling rate. D_o and E may be determined experimentally and a range of data exist for different systems.

Calculation of closure temperatures is dependent on selection of appropriate values for the diffusion parameters D_o and E, and on geological factors. The latter include the diffusion distance a, which may be estimated from crystal radii, and cooling rate. Variation in T_c with these factors is illustrated in Table 3.1, which lists closure temperatures calculated using the expression of Dodson (1973) and the diffusion parameters of Hames and Bowring (1994) for muscovite and of Grove and Harrison (1996) for biotite. Two-fold increases in grain radius and cooling rate produce corresponding increases in Tc of about 6 % and 3 %, respectively. The relative magnitude of these increases illustrates that while changes in cooling rate have only a small effect on T_c, large grain size changes, which may result from deformation, neocrystallisation and formation of grain sub-boundaries, may potentially be significant. Application of the volume-diffusion concept may also be complicated if samples have spent a long period of time at temperatures close to their closure interval. Furthermore, compositional solid-solution within mineral species has been shown to have considerable effect on diffusion parameters (Dahl, 1996; Grove and Harrison, 1996).

Table 3.1 Volume diffusion closure temperatures (Dodson, 1973) for biotite and muscovite

muscovite			biotite		
Grain radius (μm)	cooling rate (°CMa^{-1})	Tc (°C)	Grain radius (μm)	cooling rate (°CMa^{-1})	Tc (°C)
600	10	426	600	10	352
600	20	439	600	20	363
600	50	456	600	50	378
600	100	470	600	100	390
400	10	412	400	10	340
400	20	425	400	20	350
400	50	440	400	50	365
400	100	454	400	100	376
200	10	389	200	10	319
200	20	401	200	20	329
200	50	416	200	50	343
200	100	428	200	100	354
100	10	368	100	10	300
100	20	378	100	20	309
100	50	393	100	50	323
100	100	404	100	100	332

Calculated using the diffusion parameters of Hames and Bowring (1994) for muscovite and Grove and Harrison (1996) for biotite

The closure temperature concept is critically dependent on the assumption that volume diffusion is the dominant process governing the mobility of argon within the studied system. The concept of volume diffusion involves the migration of solute atoms or ions (such as Ar) via lattice point defects through a crystal and assumes structural and compositional homogeneity in the crystal. Argon may preferentially locate within structural defects (e.g. lattice dislocations, microfractures, and cleavage traces) which are larger than lattice sites. In these sites the argon will have lower potential energy and/or higher binding energy than lattice sites (Lee, 1995) and such defects may form sites of argon localisation and pathways for faster diffusion and argon loss. Such defect-enhanced "fast" diffusion (Lee, 1995) may have a significant impact on the overall distribution of elements within a mineral and therefore, the apparent ages obtained. Moreover, the vulume diffusion closure concept does not take into accounts the effects of ^{39}Ar recoil during irradiation, which serves to re-locate the distribution of Ar in the mineral, generally towards the rim of the crystal (Turner and Cadogan, 1974). Turner and Cadogan were nonetheless able to demonstrate that this problem was most severe for the smallest crystal size fractions ($<< 100\ \mu$m) in authigenic sedimentary minerals such as glauconite.

3.2.9 Interpretation and application of ^{40}Ar*/^{39}Ar ages

In the previous section the concepts and assumptions of isotopic "closure" were outlined, and it is apparent that the ages obtained are related to models of diffusive exchange and not *necessarily* to specific geological events. Further constraints on the geological setting of the samples analysed are required to place any cooling ages in a geological context.

In volcanic rocks $^{40}Ar^*/^{39}Ar$ ages are generally considered to date timing of emplacement or eruption. This is a function of rapid cooling from emplacement to closure temperatures, so that the time at which the rock cooled below the closure temperature is virtually coincident with initial emplacement, within the errors of age determination. In more slowly cooled igneous rocks this interpretation cannot be taken for granted, as there may have been subsequent cooling (or re-heating) events. Similarly, a given metamorphic event may heat minerals to temperatures above the closure temperature, resetting the isotopic clock. Any information about the previous history of the mineral is lost, and the system will only close when the mineral cools back below the closure temperature. A mild re-heating event may only partially reset the isotopic system, and the resultant age potentially reflects a mixture of two events. In general, the age obtained for a metamorphic mineral will be the last time that the mineral passed through its closure temperature, and does not necessarily record the thermal "peak" of metamorphism. An exception to this may occur when the peak metamorphic temperatures, as inferred from mineral assemblages, are within ~ 100°C of the calculated closure temperature. In these cases, calculated "cooling" ages may be within error of the timing of peak metamorphism (Cliff, 1985).

It has been argued that grain-size reduction due to deformation and neocrystallisation may reduce the effective volume diffusion closure temperature (Dunlap et al., 1991; Dunlap, 1997; Reddy and Potts, 1999). As discussed in the previous section, reduction in grain size by deformation or neocrystallisation without subsequent re-annealing will reduce the closure temperature for the system. This effect may be substantial, as shown by comparison of closure temperatures calculated for grains of differing radius in Table 3.1. For example, a reduction in grain radius from 600 μm to 100 μm reduces the calculated closure temperature

by about 16 %. For slowly cooling rocks, such a decrease in closure temperature may result in a significantly younger age being obtained. Deformation will also induce formation of lattice defects and microfractures within minerals, potentially allowing multipath diffusion. If this is the case, then the apparent ages recorded may be interpreted to reflect the absolute timing of deformation or recrystallisation. However, such highly deformed zones are also likely to be affected by excess argon, as faulting and shearing will enhance the passage of metamorphic fluids and hence the introduction of excess argon, rendering the interpretation of such "deformation ages" difficult.

3.3 Regional Geology of the Garhwal region: Overview and Previous Work

3.3.1 Introduction

This section summarises general features of the Garhwal Himalaya in order to provide a framework for this study, and is based primarily on previous studies and fieldwork carried out by the author and C. Prince. Geochronological constraints on magmatism and faulting within this region have been summarised in the previous section. For more detailed field observations and discussion of the lithology and structure of the Dhauli river valley, the reader is referred to Prince (1999).

The geology of the Garhwal region resembles other sections of the mountain belt, with the main litho-tectonic units and faults continuous east-west along strike across the orogen

(Figure 3.4 and Figure 2.2). As in other sections of the Himalaya, work in the Garhwal region has concentrated on the issues of: structural relations and definitions of lithotectonic units; metamorphism in the Lesser Himalayan Sequence and the HHC (e.g. Hodges and Silverberg, 1988; Johnson and Rogers, 1997); emplacement and cooling of the leucogranites exposed at the top of the HHCS (e.g. Stern et al., 1989; Sorkhabi et al., 1996; Searle et al., 1999b) and the timing of thrusting and normal faulting (Metcalfe, 1993).

3.3.2 Petrography of the major units

As in other areas, the litho-tectonic units of the HHCS, TSS and lesser Himalaya dominate the geology of the Garhwal Himalaya. The Lesser Himalayan nappe sequence consists of weakly metamorphosed metasediments (Valdiya, 1980; Virdi, 1986; Valdiya, 1988; Srivastava and Mitra, 1994). Much of this metamorphism appears to pre-date collision although resetting relating to south-directed thrust movement can be demonstrated (Johnson and Rogers, 1997). The HHCS is a complex sequence that includes amphibolite facies psammitic and pelitic schists, calc-silicate gneisses, augen gneisses and quartzites. In the Dhauli and the Alaknanda valleys, the HHCS can be separated into three principal units, though the boundaries between each unit are gradational (Prince, 1999). In general, the basal HHCS consists of kyanite-grade, segregated biotite-gneiss. This unit gradually becomes more quartz-rich and psammitic, eventually grading into the massive dirty quartzites of the middle unit of the HHCS. Thin calc-silicate bands can be found near the top of the basal-HHCS and throughout the rest of the HHCS. The upper HHCS consists of sillimanite-grade schists and gneisses, with pegmatitic intrusions that become increasingly common up structural section. The HHCS display the inverted metamorphism and

isothermal profiles seen elsewhere in the orogen (Le Fort, 1975; Hodges and Silverberg, 1988; Metcalfe, 1993; Prince, 1999). Leucogranite plutons, and abundant related dykes and sills, occur in the structurally higher parts of the HHCS sequence and generally yield early Miocene crystallisation and cooling ages (Stern et al., 1989; Sorkhabi et al., 1996; Searle et al., 1999b).

No fossils have been preserved within the HHCS, but the majority of workers interpret this sequence as the basement upon which the continental margin sequences of the TSS were deposited (Valdiya, 1988). Because most of the TSS outcrops north of Garhwal, in an inaccessible area of southern Tibet, little is known about the sequence in this area. Consequently, it is difficult to assess the extent to which the TSS exposed in Garhwal can be correlated with other TSS sections along strike. The TSS to the northeast of Malari range from Precambrian to Cretaceous in age (Shah and Sinha, 1974), consisting of shales, green quartzites, fossilliferous limestones and conglomerates. The sequence is pervasively deformed, and disrupted by numerous small faults. Cross bedding and grading criteria indicate that many of the beds have been overturned while shear indicators indicate at least two phases of deformation, the first of which was associated with low-grade, prograde metamorphism.

The three major units of Garhwal are separated by a series of sub-parallel, north-dipping faults or ductile shear zones. The nature of these faults is discussed in the following two sections.

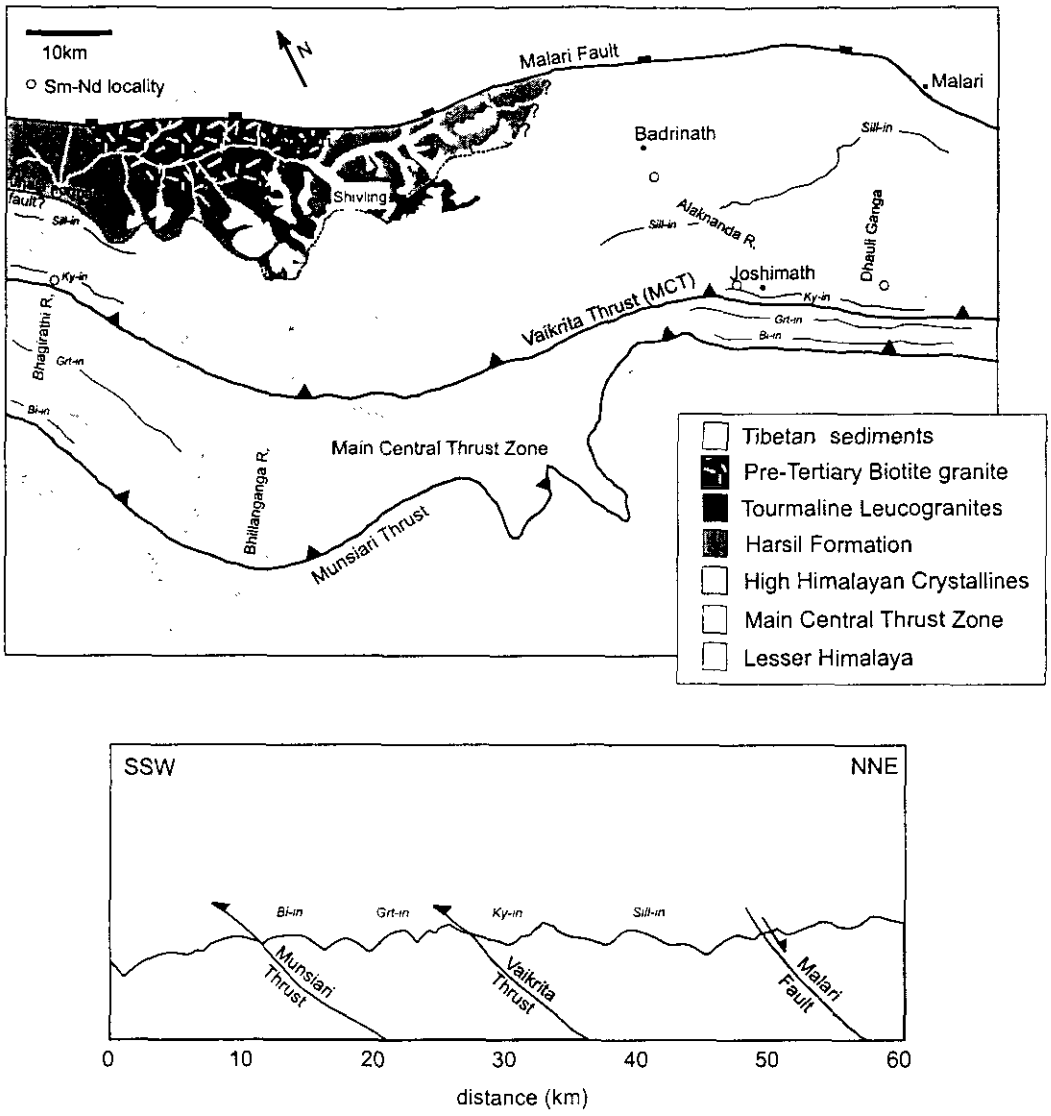

Figure 3.4 Sketch map and cross section through the Garhwal Himalaya.

Modified after Prince (1999), Metcalfe (1993) and Valdiya (1988). Despite problems in correlating different structural units across the orogen, the Vaikrita Thrust here is taken to be the equivalent of the MCT exposed in Nepal (Metcalfe, 1993; Ahmad et al., 2000), and the mylonitic zone between the Vaikrita Thrust and the Munsiari Thrust has been correlated with the MCTZ elsewhere. The Harsil Formation exposed in the Bhagirathi River area has been tentatively correlated with the upper HHCS of the Dhauli Valley, following Prince (1999) who observed relatively high grade cordierite assemblages in the sequence. The approximate position of metamorphic isograds within the MCTZ and HHCS is shown, although the dips of the isograds are poorly constrained. The areas north of Badrinath and Malari are politically sensitive, with restricted access, so the correlation of the STDS and TSS in the north of Garhwal is approximate. Localities of samples dated by Sm-Nd garnet chronometry (Prince, 1999) are shown.

3.3.3 Main Central Thrust and Main Central Thrust Zone

While Garhwal shows broad-scale similarities with other regions, there are considerable complexities and variations in detail. Most problematic has been the definition of the MCT, which in Nepal forms the lower boundary of the HHCS with the Lesser Himalayan Series (LHS) (Le Fort, 1975). As in many other sections, the MCT does not form a discrete thrust plane but marks the upper boundary of a high-strain zone of pervasive deformation related to southward-directed thrusting. This zone is bounded by two shallowly north-dipping thrusts (Figure 3.4): the Vaikrita and Munsiari Thrusts (Metcalfe, 1993). Valdiya, (1980; 1988) proposed that the Vaikrita thrust, which defines the contact between a zone of highly sheared metamorphics and granitoids and kyanite-grade orthogneisses, is the lateral equivalent of the MCT exposed in Nepal (Hubbard and Harrison, 1989). This is supported by Nd isotope data, which indicates that the metamorphic rocks above the Vaikrita Thrust correlate closely with the HHCS of other regions (Ahmad et al., 2000). Metcalfe (1993) referred to the highly sheared, mylonitic region between the two faults as the Main Central Thrust Zone (MCTZ), based on studies in the Bhagirathi Valley of Garhwal. At the base of the MCTZ, the Munisiari Thrust forms the tectonic boundary with the LHS metasediments (Metcalfe, 1993; Oliver et al., 1995). These thrust surfaces may represent the concentration of strain into relatively narrow zones at higher crustal levels during continued deformation and crustal shortening, while more ductile shear zones developed at depth (Jain and Anand, 1988).

3.3.4 Extension and normal faulting

3.3.4.1 The Gangotri region and the Jhala normal fault

At the structural top of the HHCS, the boundary with the overlying TSS has generally been interpreted as a normal fault or normal-sense shear zone (Shah and Sinha, 1974; Searle et al., 1993; Scaillet et al., 1995) although Valdiya (1988) interpreted it as a thrust. The normal movement of the Gangotri area appears ductile in nature with a roughly northwest-southeast orientation, and is mostly constrained by the geometry of the Gangotri leucogranite and sheared leucogranite dykes (Searle et al., 1993; Scaillet et al., 1995). The leucogranite intrudes metasediments with open, north-vergent folds that Scaillet et al. (1995) interpreted as "collapse structures", possibly formed as a result of gravity-controlled extension. Scaillet et al. (1995) related the *en-echelon* emplacement of the vertical feeder dykes of the Gangotri leucogranite into the underlying metasediments to magma ascent by fracture propagation, and therefore, north-south extension in this region.

The Gangotri leucogranite intrudes the Harsil formation, which Metcalfe (1993) correlated with the TSS. Based on this relationship, Metcalfe (1993) suggested that the Jhala normal fault, which separates the Harsil formation from the HHCS, was a continuation of the STDS exposed in other regions. However, the correlation of the Harsil formation with the TSS of other regions is contentious (Prince, 1999) and therefore the relationship of the Jhala normal fault to the STDS questionable. Prince (1999) tentatively proposed that the Harsil formation be correlated with the upper levels of the HHCS exposed elsewhere in Garhwal, based observations of cordierite ± staurolite metamorphic assemblages. If this correlation of the

Harsil Formation is accepted, then the implication is that the lateral continuation of the STDS in the Gangotri area must lie above the Gangotri pluton. The Jhala normal fault may therefore represent the localisation of extensional strain at lower levels in the footwall. This is consistent with the presence of extensional fabrics at structural levels above the Jhala normal fault, at the margin of the Gangotri pluton (Scaillet et al., 1995).

3.3.4.2 The Dhauli Valley and the Malari normal fault

In contrast, the position of the normal fault, locally termed the Malari Fault, at the top of the Dhauli valley is extremely clear – here the fault is a steeply dipping semi-brittle structure that trends at ~330°N, separating the HHCS from TSS to the north (Valdiya, 1988). The fault zone itself is narrow, < 0.5 km. The structural style and metamorphic grade change in the Malari region is striking, from sillimanite zone HHCS to sub-greenschist facies TSS with brittle deformation restricted to a narrow zone. The grade change in this section is similar to that found in most of the Nepalese STDS sections (Burchfiel et al., 1992) and to the Zanskar shear zone (Herren, 1987). The HHCS in the footwall of this fault show evidence of ductile deformation and normal movement to the ENE related to extension, - primarily top-to-the-northeast extensional fabrics and the rotation of fibrolite sillimanite lineations to an orientation perpendicular to the fault (Prince, 1999). Mapping of the TSS further east in Garhwal indicates that movement on the Malari fault may have also attenuated and even eliminated lithostratigraphic units of the TSS in Garhwal (Valdiya, 1988).

A major limitation in the study of the upper HHCS and TSS within the Garhwal region is the inaccessibility of many localities and problems of access to politically restricted areas. Therefore, it is difficult to assess the lateral continuity and nature of the boundary between the TSS and HHCS between the different valleys of Garhwal. For example, Valdiya (1988) suggested that there is a continuous sequence, as opposed to a tectonic contact, from HHCS to the TSS, supported by mapping of the area to the east of the Dhauli Valley. In this region, the Malari fault is shown to cut E-W through the Tethyan sediments, and does not cut the HHCS. The generality of this relationship remains to be tested.

3.4 ^{40}Ar-^{39}Ar geochronology

3.4.1 Sample selection strategy and sample locations

Samples were collected along the Dhauli Valley in order to obtain a NE-SW transect through the upper HHCS and TSS, approximately perpendicular to the strike of the fault exposed at Malari (sample localities in Figure 3.5). The objectives of this traverse were to test for differential cooling of the lithologies on either side of the normal fault, and to compare times of cooling and uplift in the upper HHCS, complementing geochronological data obtained by Metcalfe (1993) and Oliver et al. (1995). Representative samples of HHCS and TSS lithologies were collected, as well as samples from the leucogranite pluton exposed E of Malari and associated dykes intruding the upper HHCS. Petrographic descriptions of the samples collected are detailed in Appendix A, and summarised in Table 3.2.

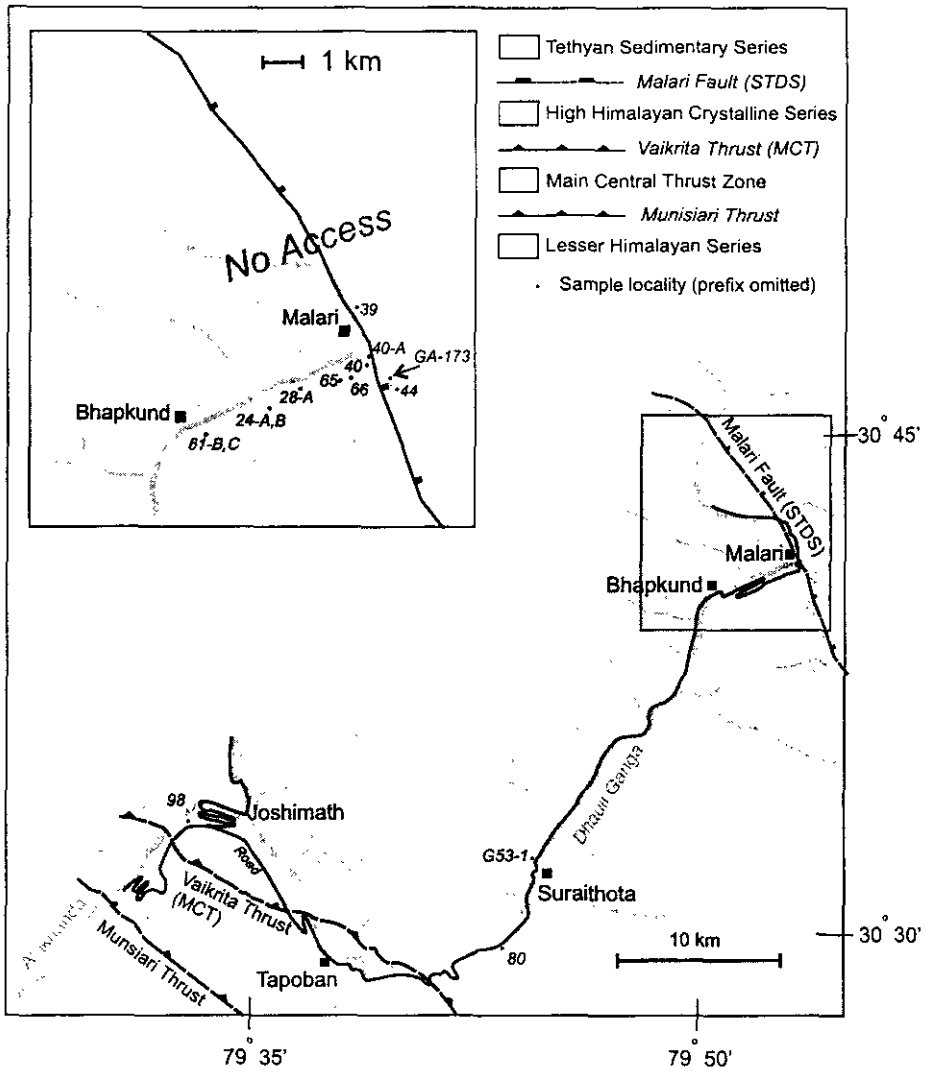

Figure 3.5 Sample localities, Malari region, Garhwal Himalaya

Samples were collected from the HHCS along the Alaknanda and Dhauli Valleys, and from the TSS and HHCS around the Malari Fault zone.

Table 3.2 Summary decriptions of analysed samples from the Malari region, Garhwal
Sample details are in Appendix A.

sample	phases analysed	grain size (μm)	unit	lithology	assemblage	metamorphic grade	deformation	alteration	comments
HW 80	bi	1000	HHCS	bi gneiss	bi-gt-qz-fsp	amphibolite	C-S micas, ductile	none - well equilibriated fabric	
HW 98	mu	400-1250	HHCS	bi gneiss	bi-gt-ky-qz-mu	amphibolite	C-S micas, ductile	slight - well equilibriated fabric	
HW 98	bi	250-1000	"	"	"	"	"	"	
HW 98	sercite matrix	<20	"	"	"	"	"	"	
HW 24-B	mu	250	HHCS	bi mu gneiss	mu-bi-qz-fsp-(sill)	upper amphibolite	C-S micas, ductile	sericitisation fsp	late fibrolitic sill
HW 65	mu	250	HHCS	metagranitoid	gt-mu-bi-sill-(chl)	upper amphibolite	sheared, late veins	chloritised biotites	
G 53 1	mu	250	HHCS	mica schist	fsp-bi-mu-qz	amphibolite	bi-fsp shear fabric	none	
HW 40-A	mu	250	HHL	leuc pluton	mu-fsp-qz	upper amphibolite	highly sheared	sericitisation fsp	
HW 66	mu	250	HHL	leuc vein	mu-fsp-qz-(chl)	upper amphibolite	sheared	sericitisation fsp and late chl	
HW 24-A	mu	800	HHL	mu schist	mu-fsp-qz	upper amphibolite	sheared, ductile	sericitisation fsp	
HW 28-A	mu	400	HHL	bi granite	bi-mu-fsp-qz-(sill)	upper amphibolite	sheared	sericitisation fsp,fluid alteration	late fibrolitic sill
HW 61-B	mu	800	HHL	leuc vein	bi-mu-fsp-qz-(sill)	upper amphibolite	slighly deformed	sericitisation fsp	
HW 61-C	mu	1200	HHL	pegmatite	mu-fsp-qz-tour	upper amphibolite	not deformed	sericitisation fsp	
HW 44	mu	<20	TSS	psammite	mu-qz-fsp-cc	low greenschist	slight	sericitisation fsp, later cc veins	
GA -173	mu	250	TSS	psammite	mu-qz-fsp	low greenschist	well-developed foliation	sericitisation fsp, some late chl	
HW39	mu	250	TSS	psammite	mu-qa-fsp-ox	low greenschist	feldspar boudinaged, relict bedding	sericitisation fsp	

mu, muscovite; bi, biotite; gt, garnet; qz, quartz; fsp, feldspar; sill, silliminite; chl, chlorite; tour, tourmaline; cc, calcite; ox, oxide and opaque phases

3.4.2 Data presentation and interpretation

This section summarises the overall approach to data presentation and interpretation adopted in this study, and data obtained for individual samples are discussed in following sections. ^{40}Ar-^{39}Ar ages are summarised in Table 3.3, and the corrected dataset presented in Appendix B. Errors are quoted at the 2 σ level and were calculated from equation 3.3; where the MSWD was > 2.5 the errors were then multiplied by $\sqrt{MSWD}$. Note that the eror bars on individual points on the inverse isochron diagrams are 1 σ. Most samples were prepared as mineral separates and analysed by fusing individual minerals. The IR laser was also used to analyse "spot" traverses across large individual crystals. Several "thick" sections were also analysed using this technique in order to constrain spatial-textural relations. The samples were irradiated in a single batch, and the *J* value assigned is 0.0122 ± 0.00006, based on analysis of the biotite standard GA1550 (97.9 ± 0.9 Ma; (McDougall and Harrison, 1999)).

The majority of the results obtained in this study are interpreted using inverse isochron/correlation diagrams, the principals of which were discussed in section 3.2.6. They incorporate relative analytical errors in the individual data points and allow assessment of the coherence of the dataset and the quality of fit of the regressed line to the data array. Furthermore, the composition of the initial $^{36}Ar/^{40}Ar$ can be calculated. The ages, initial $^{36}Ar/^{40}Ar$ compositions (where appropriate) and associated errors of the samples calculated using the isochron approach are summarised in Table 3.3, and individual isochrons and age calculations are presented and discussed further in Sections 3.4.3 to 3.4.5.

Interpretation of the isochron arrays is complicated in several cases by a low degree of variation in the $^{39}Ar/^{40}Ar$ and $^{36}Ar/^{40}Ar$ compositions of individual analyses. This is exacerbated by low argon abundances in the samples, resulting in relatively large errors in the blank-corrected values of ^{36}Ar and $^{36}Ar/^{40}Ar$. In certain cases, these factors preclude definition of clear mixing relationships with air or excess components. For samples where no excess component was apparent from the data array, the y-intercept of the least-squares-regression was fixed at an atmospheric $^{36}Ar/^{40}Ar$ composition. This gives an apparent age that effectively corresponds to a weighted mean of individual apparent ages. Such an age may be a slight overestimate, as individual analyses may still be affected by excess argon. The "forced" ages obtained from regressions carried out in this way are presented with the equivalent age, calculated without a fixed intercept, for purposes of comparison. If an age with an acceptable error and fit to a mixing line can be calculated from the data without setting an intercept, then this age is preferred as the best estimate of the "true" age of the sample. However, if the y-intercept calculated from such a regression gives a $^{40}Ar/^{36}Ar$ composition of less than 295.5, then the age based on this regression is rejected, as $^{40}Ar/^{36}Ar$ compositions of less than 295.5 are rarely observed in nature.

Ages for individual samples may also be calculated as a mean of the individual "apparent" ages obtained from each sample, or as a "total gas" age analogous to the K-Ar technique, based on the summed quantities of ^{40}Ar, ^{39}Ar and ^{36}Ar. These approaches have been avoided here where possible, as they do not provide a means of assessing the composition of the initial $^{36}Ar/^{40}Ar$, or the overall coherence of the dataset.

Table 3.3 ^{40}Ar-^{39}Ar ages for the Malari region, Garhwal

Sample	rock type	min	No. of points	MSWD	Age (Ma)	± 2σ	$^{40}Ar/^{36}Ar$	± 2σ
HHCS								
HW 80*	augen gneiss	bi	11 of 12	2.2	28.8	0.8	295.5	-
HW 80	augen gneiss	**bi**	**11 of 12**	**2.1**	**27.6**	**1.3**	**312.9**	**15.1**
HW 98*	augen gneiss	bi	5 of 5	2.4	40.9	1.5	295.5	-
HW 98	augen gneiss	**bi**	**5 of 5**	**1.7**	**34.0**	**6.5**	**485**	**166.8**
HW 98*	augen gneiss	**gms**	**10 of 10**	**13.0**	**40.1**	**1.3**	**295.5**	
*HW 98**	*augen gneiss*	*mu*	*6 of 7*	*1.4*	*40.3*	*1.1*	*295.5*	-
HW 98	augen gneiss	**mu**	**6 of 7**	**1.3**	**37.2**	**4.4**	**391**	**134.6**
HW 24-B*	**gneiss**	**mu**	**11 of 14**	**2.0**	**14.4**	**0.06**	**295.5**	-
HW 24-B		mu	11 of 14	2.0	12.3	3.5	413	201.2
HW 65*	**gneiss**	**mu**	**8 of 9**	**1.5**	**16.0**	**0.3**	**295.5**	-
HW 65	**gneiss**	mu	8 of 9	1.4	16.4	0.5	249	49.2
G 53 1*	**schist**	**mu**	**13 of 21**	**4.6**	**12.6**	**0.7**	**295.5**	
HHL								
HW 40-A*	**granite**	**mu**	**6 of 10**	**1.0**	**17.3**	**0.4**	**295.5**	
HW 40-A		mu	6 of 10	0.4	18.2	0.7	204.7	64.9
HW 66*	**granite**	**mu**	**8 of 8**	**8.6**	**19.9**	**0.9**	**295.5**	
HW 66	**granite**	mu	8 of 8	1.0	10.8	2.6	860	145
HW 24-A*	**granite**	mu	11 of 16	3.0	14.9	0.2	295.5	
HW 24-A	**granite**	**mu**	**11 of 16**	**3.1**	**14.4**	**0.4**	**332**	**111**
HW 28-A*	**granite**	**mu**	**4 of 6**	**15.0**	**19.9**	**0.5**	**295.5**	
HW 28-A	**granite**	mu	4 of 6	2.0	13.5	1.6	900	141
HW 61-B*	**granite**	mu	8 of 12	2.3	14.7	0.2	295.5	-
HW 61-B	**granite**	**mu**	**8 of 12**	**1.7**	**13.7**	**0.7**	**478**	**103**
HW 61-C*	**granite**	mu	10 of 20	3.3	16.1	0.4	295.5	
HW 61-C	**granite**	**mu**	**10 of 20**	**1.5**	**15.3**	**0.5**	**484**	**67**
TSS								
HW 44*	**psammite**	**mu**	**3 of 9**	**3.9**	**41.5**	**1.9**	**295.5**	
HW 44	**psammite**	mu	3 of 9	2.9	44.6	2.4	224	41
HW 44	**psammite**	mu	5 of 9	1.6	39.2	6.9	3973	625
GA -173*	**psammite**	**mu**	**4 of 6**	**2.0**	**24.3**	**1.6**	**205**	**92**
GA -173	**psammite**	mu	4 of 6	wt mean	26.9	6.2		
HW39	**shale**	**mu**	**7 of 10**	**wt mean**	**599**	**82**		

Summary of cooling age results. The full dataset is in Appendix B.
mu, muscovite; bi, biotite; gms, groundmass

Bold text indicates the age that is the most appropriate to attribute to the sample

** regression forced through atmospheric argon*

In the case of isochron ages, the errors are calculated from equation 3.3, and are multiplied by the square root of the MSWD, where the latter is greater than 2.5
The standard deviation of weighted means is multiplied by 2 to give the error on samples GA-173 and HW39

3.4.3 The High Himalayan Crystalline Series

Five samples were analysed from the HHCS exposed in the Dhauli Valley. Two samples, HW98 and HW80, were selected from the basal, kyanite-grade HHCS exposed in the south of the valley. Samples G531, HW24-B, HW65 and HW66 were collected from the mid to upper structural levels of the HHCS. Correlation diagrams for these samples are shown in Figures 3.6 (basal HHCS) and 3.7 (upper HHCS).

3.4.3.1 The lower HHCS – HW98 and HW80

Spot analyses of *in situ* biotite grains of HW80 gave an isochron age of 27.6 ± 1.3 Ma (Figure 3.6 A). The corresponding age, with a set atmospheric intercept is 28.8 ± 0.8 Ma, almost within error of the unforced regression.

Biotites from HW98 were also analysed *in situ*, resulting in isochron ages of 34.0 ± 6.5 Ma and 40.9 ± 1.5 Ma for unforced and forced isochrons, respectively (Figure 3.6 B).

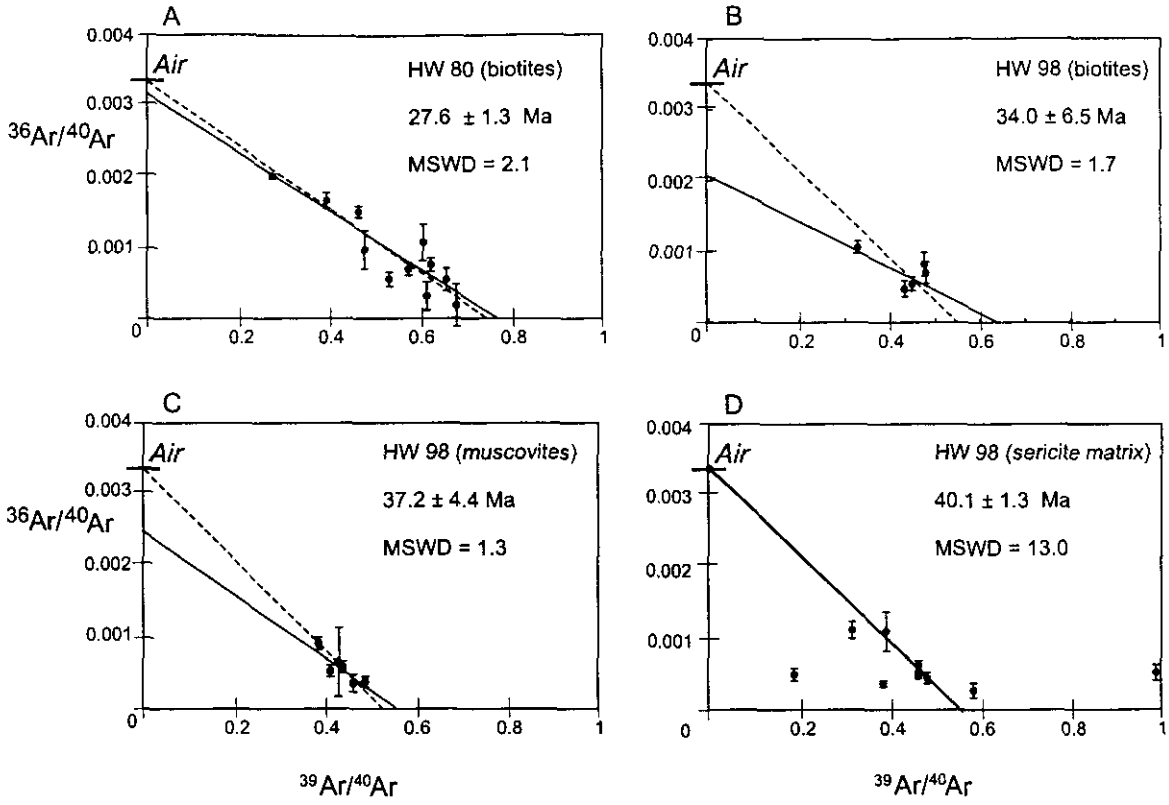

Figure 3.6 Correlation diagrams for HW 80 and HW 98, gneisses from the basal HHCS of the Dhauli valley.

The ages shown correspond to the regressions indicated by solid lines, and to the preferred ages given in Table 3.3.

The marked difference in ages obtained by regressing through an atmospheric intercept suggests that the assumption of an atmospheric composition for the initial argon in this sample is inappropriate. This is reflected in the initial $^{40}Ar/^{36}Ar$ value of 485 ± 167 calculated. The age of 34.0 ± 6.5 Ma is therefore taken as being the best estimate of the "true" biotite cooling age.

In situ analysis of muscovite crystals from the same sample give older isochron ages of 40.3 ± 1.1 Ma (forced) and 37.2 ± 4.4 Ma (Figure 3.6 C). This is consistent with higher closure temperatures for argon in muscovite. The latter age is taken as being the best estimate of the muscovite cooling age of HW98. A slightly older age of 40.1 ± 1.3 Ma with a set atmospheric intercept was obtained for the sericite matrix of HW98 (Figure 3.6 D). This age is probably a maximum, as the presence of excess argon could not be quantified due to scatter in the data (MSWD = 13). However, the similarity of the muscovite and biotite ages suggests that they are robust.

3.4.3.2 Mid to upper HHCS – G53-1, HW24-B and HW65

Muscovites were analysed *in situ* in G53-1, and gave an age of 12.6 ± 0.7 Ma, for a forced regression (Figure 3.7 A). The data are scattered (MSWD = 4.6) and the age is probably a maximum, due to the presence of unconstrained excess argon.

Muscovite analyses from HW24-B (Figure 3.7 B) form a scattered pattern on the isochron diagram, giving an age of 14.4 ± 0.06 Ma with a forced atmospheric intercept.

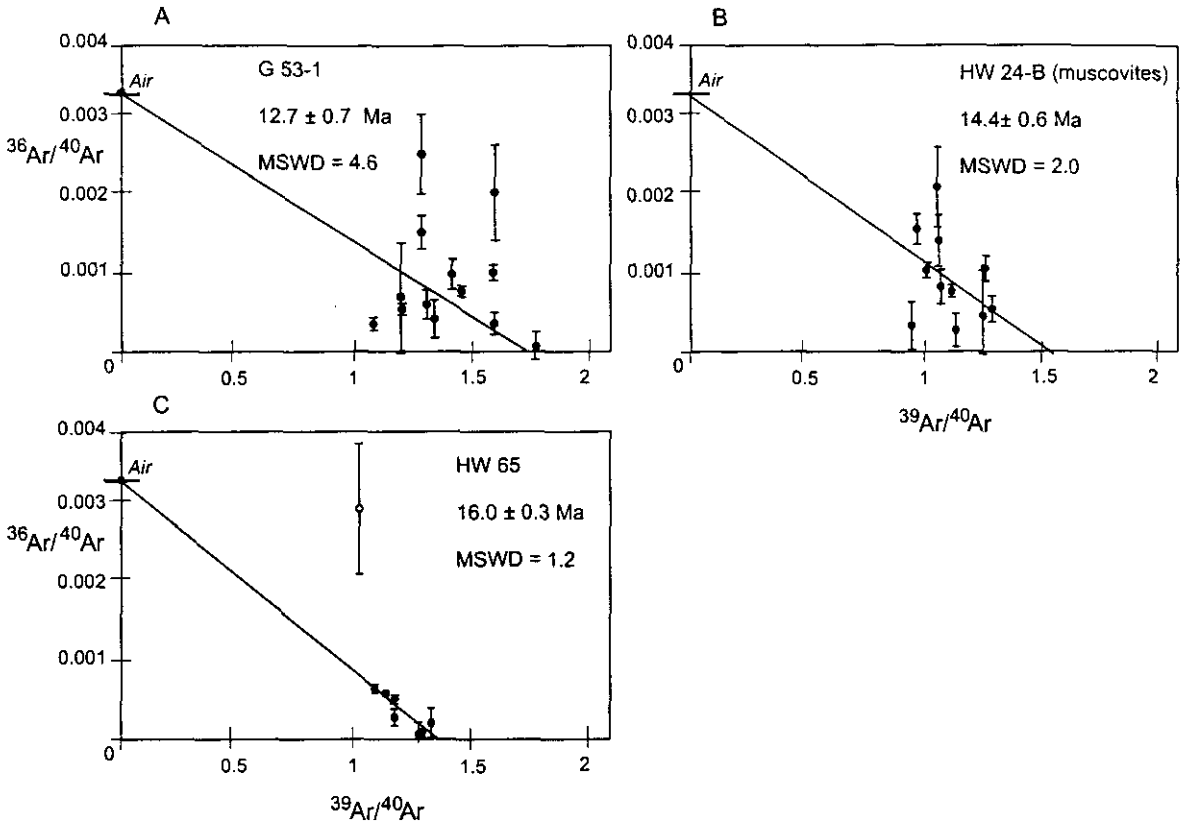

Figure 3.7 Correlation diagrams for G 53-1, HW 24-B and HW 65, from the middle to upper HHCS of the Dhauli valley

Solid data points are those used in least-squares regressions, open points have not. All regressions were forced

Muscovites from HW65 gave ages of 16.0 ± 0.3 Ma and 16.4 ± 0.5 Ma from forced and unforced regressions, respectively (Figure 3.7 C). The latter regression gave a $^{40}Ar/^{36}Ar$ value of 249 ± 50. This is not within error of the atmospheric $^{40}Ar/^{36}Ar$ value and, therefore, the age from the regression forced through atmospheric argon, 16.0 ± 0.3 Ma is the preferred as the best estimate of the "true" age of this sample.

3.4.4 High Himalayan Leucogranites

Six leucogranite samples were selected from the upper HHCS in the Dhauli Valley. Muscovites were separated from all samples, and two orthogonal traverses of 100 micron laser spots were analysed across the (*001*) surfaces of the larger crystals (HW 24-A, HW 28, HW 61-B and HW 61-C) in order to obtain first-order constraints on spatial variations in age within the crystal.

3.4.4.1 Single fusion isochron ages- HW66 and HW40-A

Individual muscovites from HW66 (Figure 3.8 A) gave isochron ages of 19.9 ± 0.9 Ma (forced) and 10.8 ± 2.6 Ma (unforced). However, the latter age is dependent on a single point (Figure 3.8 A). The positive array formed by the majority of points may be a result of alteration of the sample. The age of this sample is poorly constrained – at best it is likely to be younger than 19.9 ± 0.9 Ma. This age is not discussed further in the interpretation section.

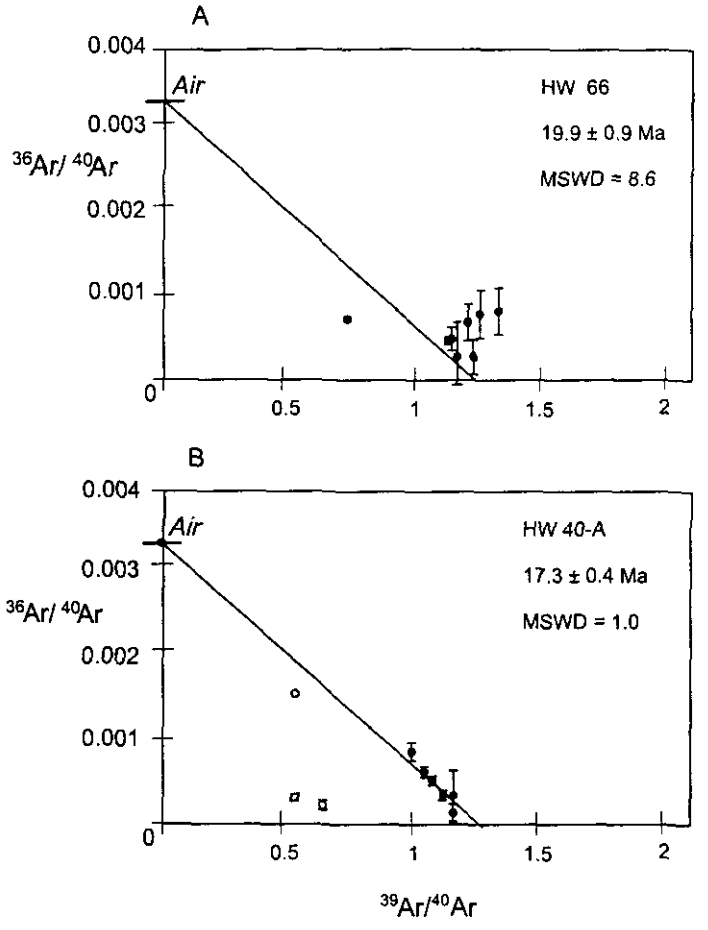

Figure 3.8 Correlation diagrams for HW 66 and HW 40-A, leucogranite intrusions in the upper HHCS, close to the Malari Fault.

Solid data points are those used in least-squares regressions, open points have not. The positive array on the correlation diagram for HW 66 suggests that some individual analyses may be affected by alteration, which may result in a younger age. In HW40-A the two open points close to the x-axis may be attributed to the presence of heterogeneous excess argon. The third open point was omitted because its relatively low error distorted the fit of the line to the remaining data array.

Single muscovite fusions of HW40-A (Figure 3.8 B) gave isochron ages of 21.7 ± 0.2 Ma (forced) and 17.0 ± 0.6 Ma (unforced). For both of these regressions, the fit of the data to the regressed line appears poor with MSWD values of 14.6 and 13.0, respectively. The majority of points form an array with a negative slope, and three points with low values of $^{36}Ar/^{40}Ar$ and $^{39}Ar/^{40}Ar$ lie off this array. As most of the data form a clear negative array, this suggests that the sample has not experienced significant argon loss due to alteration (which would result in increasing $^{36}Ar/^{40}Ar$ and $^{39}Ar/^{40}Ar$), and that these three points are dominated by an excess argon component. This observation implies that excess argon is distributed heterogeneously within the mineral. The relatively low errors on these points distort the data regression of the negative array and removal of these points improves the fit, resulting in ages of 17.3 ± 0.4 Ma (forced, MSWD of 0.95) and 18.2 ± 0.6 Ma (unforced, MSWD 0.39). The intercept of the unforced array gives a $^{40}Ar/^{36}Ar$ value of 205 ± 66. As this is lower than generally observed in nature, the age from this intercept is rejected and the age from the forced intercept, 17.3 ± 0.4 Ma, is taken as the most reasonable cooling age.

3.4.4.2 Single crystal traverses – HW24-A, HW28-A, HW61-B and HW61-C

Apparent ages in the range of 13.0 ± 1.8 Ma to 22.1 ± 0.2 Ma (2σ; note that the error bars in the diagram are for 1σ errors) were obtained from two traverses across a 1mm muscovite crystal from HW24-A (Figure 3.9 A and B). Ages were calculated from individual laser analyses, although, for some individual analyses, the ^{36}Ar peak was below the analysed blank level and no initial argon correction was made. Ages do not vary significantly with distance from rim to core across the crystal. There is no relationship with $^{38}Ar/^{39}Ar$, suggesting that alteration does not significantly affect $^{38}Ar/^{39}Ar$ and does not correlate with distance from the grain boundary.

The single-crystal laser analyses of HW24-A define a negative linear array on the isochron/correlation diagram (Figure 3.9 C), and a least-squares fit to this data gives ages of 14.9 ± 0.2 Ma (forced) and 14.4 ± 0.4 Ma (unforced), which agree within error.

Profiles across a 600 μm muscovite from HW28 yielded apparent ages ranging from 14.9 ± 1.8 Ma to 20.9 ± 0.4 Ma (Figure 3.10 A, note that the error bars in the diagram are for 1σ errors although the errors discussed in this paragraph are 2σ). There does not appear to be any spatial variation in age, but the available data define an isochron array (Figure 3.10 B) giving ages of 19.9 ± 0.5 Ma and 13.5 ± 1.6 Ma, for regressions with and without set atmospheric intercepts, respectively. The unforced age is compromised as it is tied by one point. Therefore, only a maximum age of 19.9 ± 0.1 Ma can be assigned to this sample.

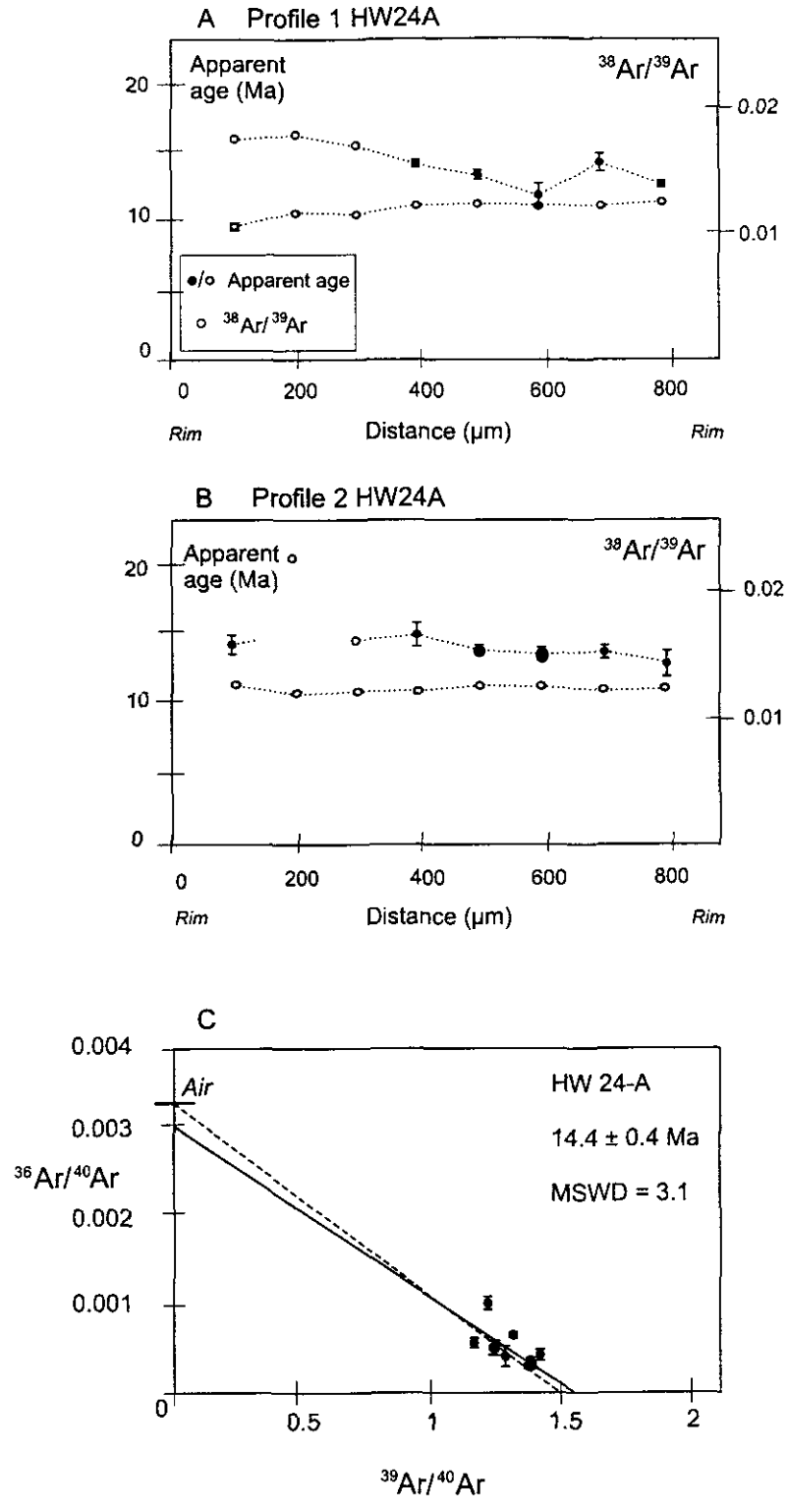

Figure 3.9 Apparent age profiles and correlation diagram for HW 24-A, a leucogranite ~ 2km south of the Malari Faul, intruding the upper HHCS

Apparent ages where the ^{36}Ar peak measured was within error of the blank are indicated by open circles. Note that the errors on the individual points are 1 sigma. These ages were calculated assuming all the ^{40}Ar measured was radiogenic. These points were omitted from the correlation diagram. The inverse isochron age corresponds to the regression shown with a solid line.

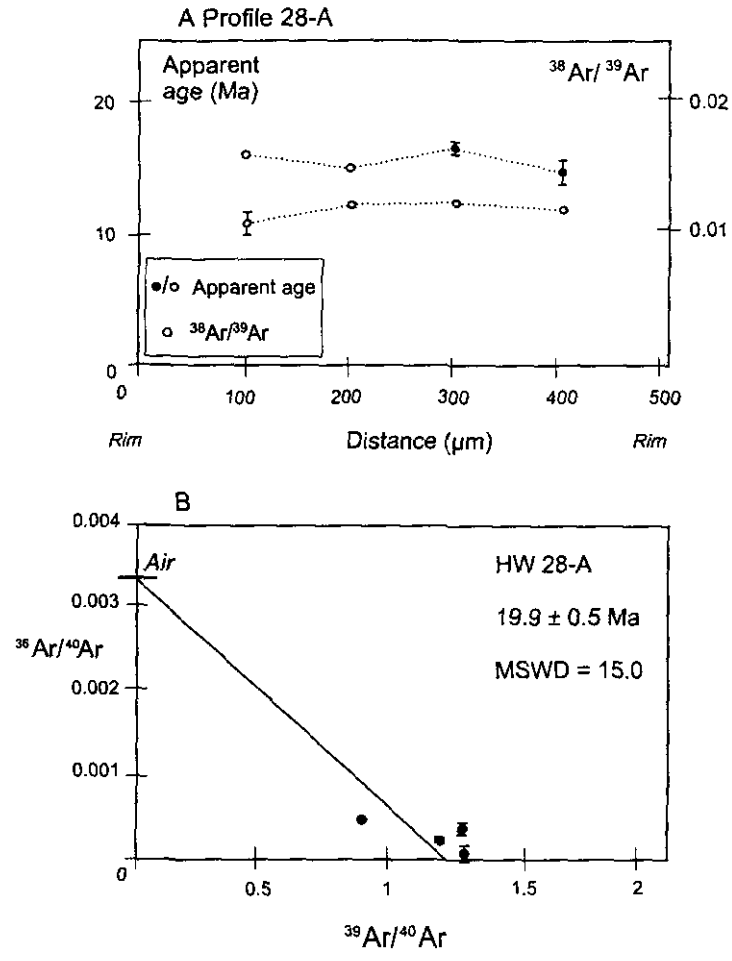

Figure 3.10 Apparent age profile and correlation diagram for HW 28, a leucogranite ~ 1.5 km south of the Malari Fault, intruding the HHCS

A single age-distance profile is shown, as there were insufficient analysed points to construct a second profile.Errors on the individual points are 1 sigma. Apparent ages where the ^{36}Ar peak measured was within error of the blank are indicated by open circles. These ages were calculated assuming all the ^{40}Ar measured was radiogenic. These points were omitted from the correlation diagram (B). The correlation diagram shows additional analyses that were not part of the first profile.

In HW61-B, apparent ages range from 14.0 ± 1.4 Ma to 19.7 ± 1.0 Ma and there appears to be variation in age with spatial position in the first profile (Figure 3.11 A). There is no clear relationship with $^{38}Ar/^{39}Ar$. In the second traverse (Figure 3.11 B) there is no apparent age variation, despite variation in $^{38}Ar/^{39}Ar$. This implies that alteration has not significantly affected the argon systematics in this case. Plotted on an isochron diagram (Figure 3.11 C), the data yield ages of 14.7 ± 0.2 Ma (forced) and 13.7 ± 0.7 Ma (unforced). The unforced regression indicates a significant initial excess argon component in the crystal and is taken as the appropriate cooling age for this sample.

In the pegmatite HW61-C apparent ages range from 13.75 ± 3.5 Ma to 27.6 ± 2.1 Ma (Figure 3.12). Both traverses show (Figure 3.12 A, B) little variation in apparent age or $^{38}Ar/^{39}Ar$. The analyses define an array on the inverse isochron diagram (Figure 3.12 C), with ages of 16.1 ± 0.4 Ma and 15.3 ± 0.5 Ma for forced and unforced atmospheric intercepts, respectively. The unforced age of 15.3 ± 0.5 Ma is preferred. The initial $^{40}Ar/^{36}Ar$ value calculated for HW61-C, 484 ± 67 is within error of the value calculated for HW61-B, which is 478 ± 103. This is unsurprising as these HHL samples are closely associated with each other and may have experienced similar events of early argon incorporation. More unexpected are the differences in the cooling ages obtained for HW61-B and HW61-C.

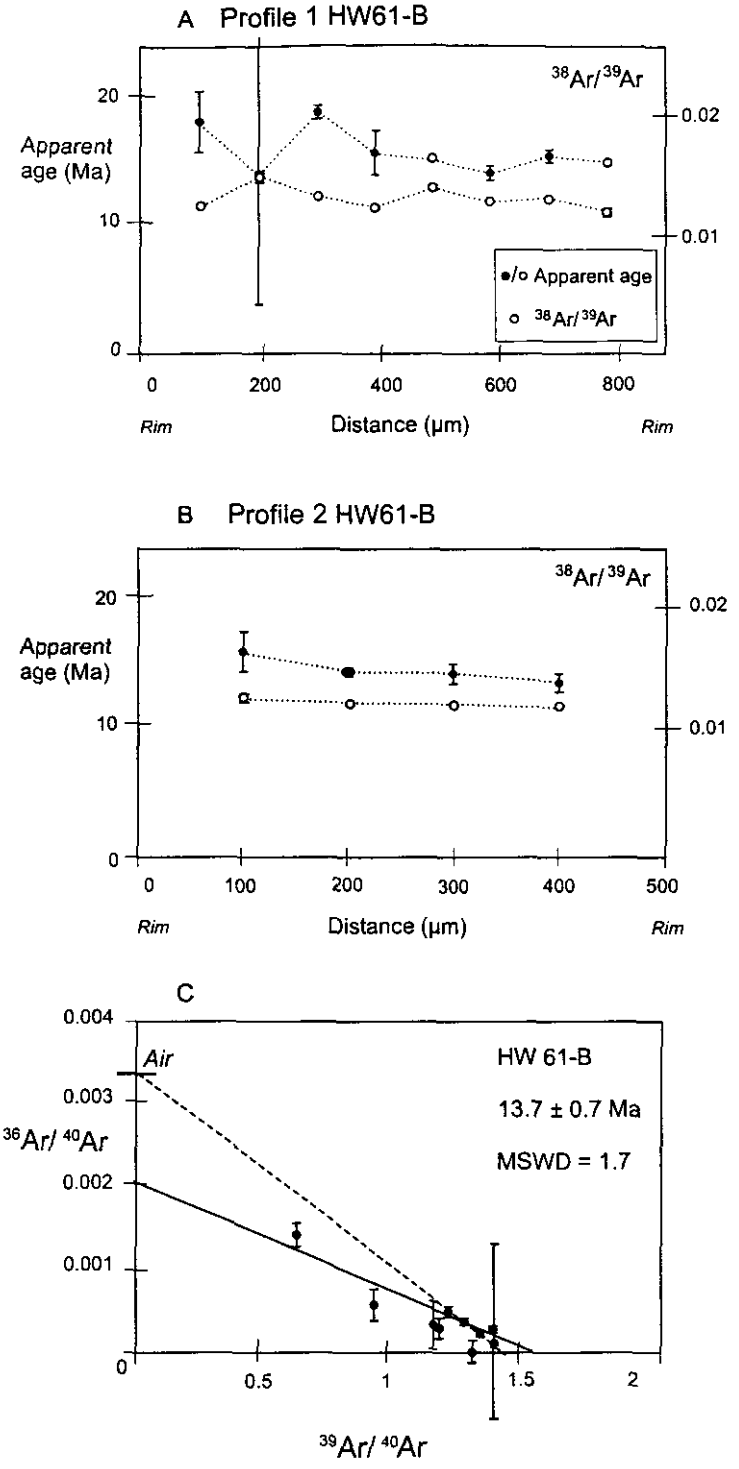

Figure 3.11 Apparent age profiles and correlation diagram for HW 61-B, a leucogranite intruding the upper HHCS in the Bhap Kund area, ~ 3.5 km south of the Malari fault

Apparent ages where the ^{36}Ar peak measured was within error of the blank are indicated by open circles. Errors on points are 1 sigma. These ages were calculated assuming all the ^{40}Ar measured was radiogenic. These points were omitted from the correlation diagram. The inverse isochron age corresponds to the solid regression line.

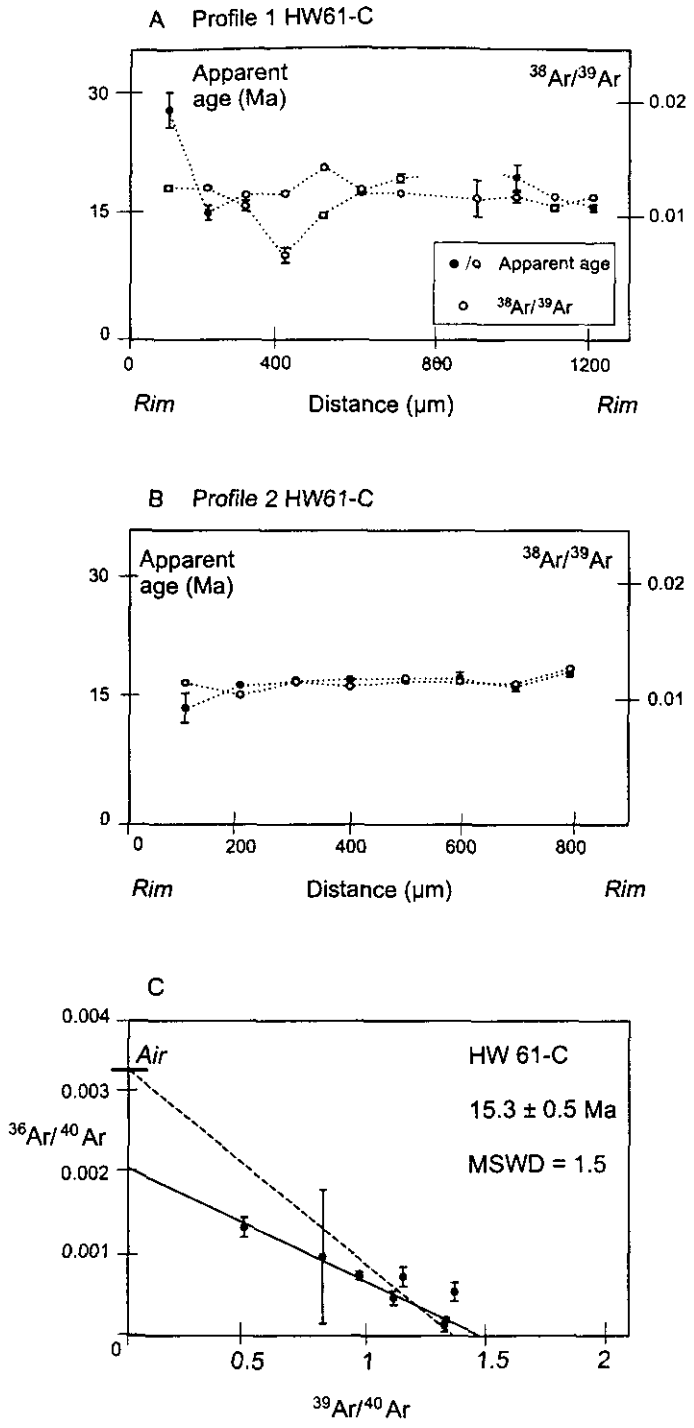

Figure 3.12 Apparent age profiles and correlation diagram for pegmatite HW 61-C, intruding the upper HHCS in the Bhap Kund locality, ~ 3.5 km south of the Malari Fault.

Apparent ages where the ^{36}Ar peak measured was within error of the blank are indicated by open circles. Errors on points are 1 sigma. These ages were calculated assuming all the ^{40}Ar measured was radiogenic. These points were omitted from the correlation diagram. The inverse isochron age corresponds to the solid regression line.

3.4.5 The Tibetan Sedimentary Series and the Malari Fault Zone

Muscovites from four samples from the region north of the inferred trace of the Malari Fault (Figure 3.5) were analysed. Two samples, HW39 and HW40, are highly sheared, low grade metasediments from the fault zone.

Single fusion muscovite analyses from HW39 did not define an isochron. A weighted mean of individual apparent ages gives an age of 599 ± 82 Ma (analyses where the ^{36}Ar peak was less than the blank level were omitted). Individual apparent ages range from 422 ± 4 Ma to 868.0 ± 16Ma. As these samples are both low grade schists, they my suffer from problems of incomplete resetting i.e. individual micas may preserve detrital, a opposed to metamorphic, ages. If this is the case, then the ages obtained constrain the maximum age of the source(s) only. A possible source may be the protolith of the HHCS which, based on U-Pb zircon ages, was probably deposited in the Late Proterozoic (Parrish and Hodges, 1996) and then metamorphosed at ~550 Ma, based on $^{87}Sr/^{86}Sr$ errorchrons (Ahmad et al., 2000).

Muscovites from HW40 gave extremely scattered apparent ages, from 74 ± 18 Ma to 659 ± 6 Ma. The data could not be used to construct an isochron as ^{36}Ar was below detection limits for the majority of analyses. Therefore, no realistic cooling age can be assigned to this sample. As with HW39, a substantial proportion of micas may be detrital, possibly derived from protolith of the HHCS.

In situ analyses of muscovite from HW44 show a dichotomy on the inverse isochron diagram (Figure 3.13 A), with three out of seven points forming a negative array and the remaining points forming a horizontal trend close to the x-axis. The most reasonable explanation for the horizontal array is that a significant proportion of the muscovites do not have strongly reset Ar systematics, and preserve detrital ages. The individual ages of these points range from 55.6 ± 1.7 Ma to 219.3± 2.6 Ma, the majority being ~ 60 Ma. The ~ 60 Ma ages may reflect partial resetting in response to early, collision related thermal events, but this cannot be directly determined. The ages from the negative array are 41.5 ± 1.9 Ma (forced) and 44.6 ± 2.4 Ma (unforced). The unforced age obtained from the negative array is associated with a $^{40}Ar/^{36}Ar$ intercept of less than 295.5, and discarded on this basis. The muscovite closure age for HW44 is therefore taken as 41.5 ± 1.9 Ma.

Individual muscovite fusions from GA-173 form a flat array on the inverse isochron diagram (Figure 3.13 B). It is not clear whether this array results from incorporation of excess argon, or whether it results from loss of ^{40}Ar by alteration processes. The "age" resulting from a regression forced through atmospheric argon is 24.3 ± 1.6 Ma, within error of the age of 27 ± 8 Ma calculated as a weighted mean of the same individual apparent ages. If the horizontal slope on the isochron diagram is taken as indicating argon loss, the oldest individual age, 48 ± 10 Ma, may be the closest estimate of the "true" closure age possible with the available data.

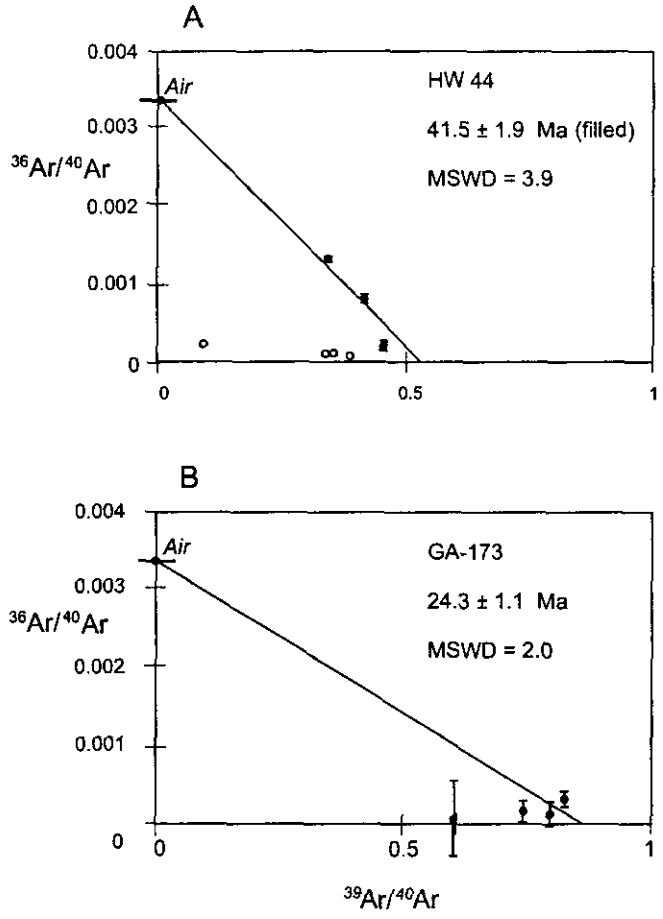

Figure 3.13 Correlation diagrams for HW 44 and GA-173, Tibetan sediments < 1 km north of the Malari Fault Open points excluded from regressions Error bars 1 sigma..

3.5 Interpretation and Discussion

3.5.1 Prograde metamorphism and cooling of the Tibetan Sedimentary Sequence

The ages of 41.5 ± 1.9 Ma and 24.3 ± 1.6 Ma obtained for TSS samples HW44 and GA-173, respectively, are interpreted in terms of cooling below muscovite closure temperatures for two reasons. Both HW44 and GA-173 are low-grade greenschist facies rocks (Figure 3.14 A, B and C), implying that prograde temperatures were 350-450°C, approaching muscovite closure temperatures. Secondly, there is no evidence for significant deformation of the samples below the closure temperature. In contrast, muscovites from samples HW39 and HW40, < 2 km away from GA-173 and HW44, preserve older ages, suggestive of detrital input rather than resetting of the Ar systematics of these rocks. One explanation is that these samples experienced different thermal histories to GA-173 and HW44, and that they were tectonically juxtaposed at a later stage. Alternatively, peak prograde temperatures may have been only marginally above muscovite closure, so that micas from HW39 and HW40 may not have been reset due to differences in chemistry or grain size. The latter hypothesis is supported by the greenschist facies assemblages preserved, and the partial resetting and preservation of detrital components in these samples.

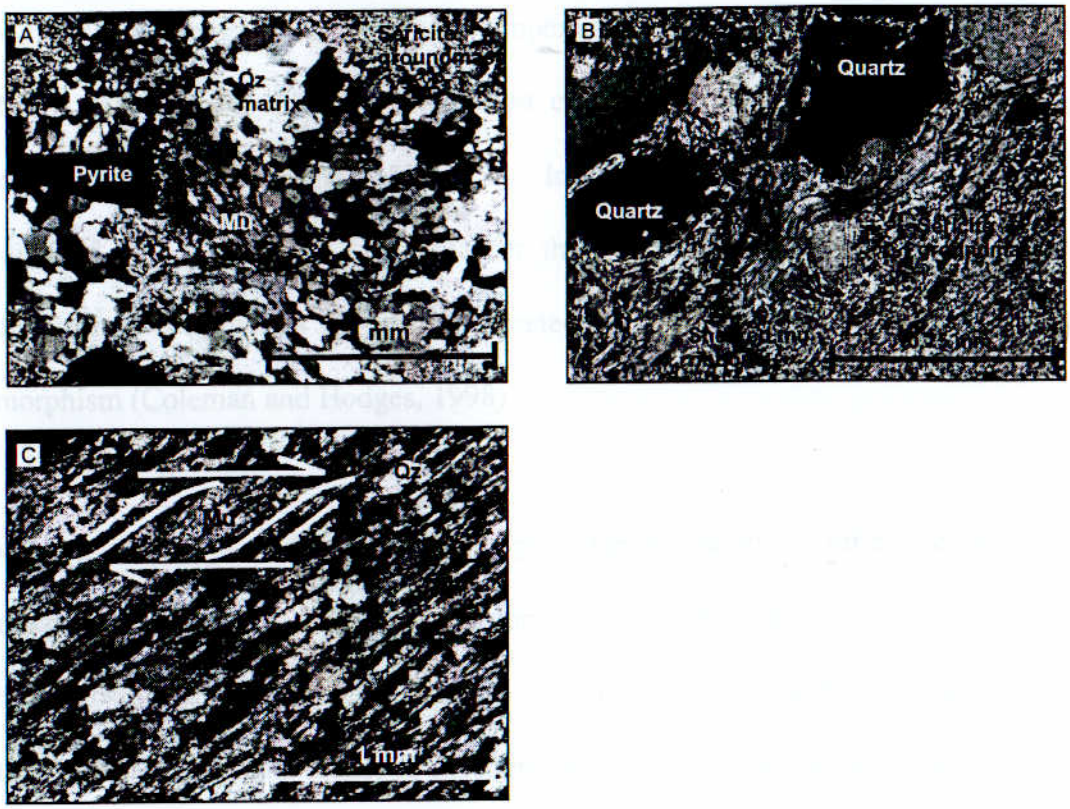

Figure 3.14 Photomicrographs of samples HW44 and GA-173.

The mineral assemblage of HW-44 (A, B) is mu + qz ± chl. The quartz matrix of this sample has completely recrystallised, and no relict bedding is preserved. White micas form ribbons, in some case developing a crenulation cleavage (B). They appear to have accommodated most of the deformation. The large size of these ribbons (B) indicates that they may be prograde in origin. GA-173 (C) has an assemblage of mu+chl+qz. Micas accommodate deformation, developing south vergent structures. The main shear direction shown trends to 250°.

Given reasonable greenschist prograde temperatures and moderate cooling rates (20-30°CMa^{-1}), the ages for GA-173 and HW44 correspond, within error, to the timing of prograde regional metamorphism of the TSS. Interestingly, these ages are similar to ^{40}Ar-^{39}Ar ages of 26.7 ± 1.4 to 29.7 ±1.2 Ma for the TSS (muscovites from metamorphosed limestones) in Nepal, which are also interpreted in terms of cooling following prograde metamorphism (Coleman and Hodges, 1998).

The cooling of HW44 and GA-173 from prograde temperatures reflects either thermal relaxation following burial and peak metamorphism, or exhumation-related cooling, driven by either erosion or tectonic processes. It is not possible to distinguish between these hypotheses using these data alone, as independent constraints on the prograde paths of the samples and cooling rates are required. The difference in age between GA-173 and HW44, at least 13 Ma for samples <1 km apart, is problematic. The older age obtained for HW44 compared to GA-173 is not consistent with the relative size of the muscovites analysed, as the smaller crystals of HW44 would be expected to have lower closure temperatures and preserve a younger age if the two samples cooled synchronously. There are two possible interpretations for the age difference- it may reflect the presence of unconstrained excess argon or detrital components in HW44, or a real difference in the thermal histories of the samples. Separation of finer grained muscovites (i.e. with lower inherent closure temperatures) from these samples could potentially resolve whether there is a significant detrital imput. Similar abrupt variations in cooling age from samples associated with the STDS have been observed, notably by Inger and Harris (1998), who related differences in age retained over very short spatial distances within the Zanskar Shear zone to the tectonic

juxtaposition of units during cooling. If this hypothesis is correct, then the implication is that there was considerable reorganisation within the hangingwall of the Malari fault between 41.5 ± 1.9 Ma and 24.3 ± 1.6 Ma.

3.5.2 Timing of movement on the Malari fault

Constraints on the timing of extension and movement on the Malari fault can be obtained from evaluating the difference in ages between the TSS, discussed above, and the upper HHCS and HHL (collectively referred to as the HHCS in the ensuing discussion). The jump in ^{40}Ar-^{39}Ar ages from 13.7 ± 0.7 to 16.0 ± 0.3 Ma in the immediate footwall of the fault (the ~ 19 Ma ages of HW66 and HW28 are excluded from the discussion here, as they are almost undoubltedly affected by excess argon) to 24.3 ±1.9 to 41.5 ± 1.9 Ma in the hanging wall demonstrates that the rocks on either side of the Malari Fault preserve distinct thermal histories. Moreover, the preservation of old detrital ages (598 ± 82 Ma) in the hangingwall suggests that the TSS did not experience the Miocene overprint so prevalent in the HHCS. This is evident in the contrasting greenschist facies assemblages of the TSS (Figure 3.14 A, B and C) and the silliminite-grade metamorphism of the upper HHCS (Figure 3.15 A, B and C). This pattern is similar to that observed in the Annapurna region by Coleman and Hodges (1998), where cooling ages in muscovites from the footwall HHCS are 15.6 ± 1.1 to 16.6 ± 0.7 Ma, in contrast to ages of 26.7 ± 1.4 to 29.7 ± 1.2 Ma preserved in muscovites of TSS in the hangingwall.

Clearly, the TSS and HHCS are units with different thermal histories, subsequently juxtaposed by movement on the Malari Fault. Therefore, the Malari Fault must have been

active between the times at which the rocks in the footwall and hangingwall of the fault cooled through muscovite closure, i.e. between 16.0 ± 0.3 and 24.3 ±1.6 Ma. As discussed in the previous section, cooling ages recorded by the TSS effectively record the time at which the thermal peak was attained. Extension and normal faulting is likely to post-date crustal thickening and prograde metamorphism, as the continental lithosphere returns to a state of isostatic equilibrium (England and Thompson, 1984). Therefore, the youngest cooling age recorded for the TSS (24.3 ± 1.6 Ma) may be regarded as an upper age bracket for the timing of normal movement on the Malari Fault.

The ages recorded by the HHCS and HHL are most readily interpreted as cooling ages since prograde temperatures determined for the upper HHCS (630-640°C) (Prince, 1999), are well above argon closure temperatures and there is little evidence for post-metamorphic shearing (Figure 3.15). Ages for the HHCS-HHL range from 13.7 ± 0.7 to 16.0 ± 0.3 Ma, excluding samples HW28-A and HW66, which are probably affected by excess argon, and HW 40-A, which lies in the fault zone itself. The exhumation and cooling of the upper HHCS through 380-400°C at 13.7 ± 0.7 to 16.0 ± 0.3 Ma may reflect erosion-related uplift or unroofing on the Malari Fault. In either case, movement on the fault, which juxtaposes the HHCS against units preserving considerably older ^{40}Ar-^{39}Ar ages, must pre-date the oldest footwall cooling age, 16.0 ± 0.3 Ma. Variation in footwall ages may reflect the different initial positions of samples with respect to the fault plane, the post-cooling tectonic juxtaposition of different units, different initial temperatures of the samples or minor spatial variations in cooling history.

HW40-A, a strongly sheared leucogranite exposed in the shear zone itself (Figure 3.15 A and B), preserves an age of 17.3 ± 0.4 Ma, older than those obtained from the footwall. One

explanation is that HW40-A cooled earlier in response to unroofing, due to its proximity to the fault plane. However, HW40-A shows evidence of low temperature deformation, with feldspars, fractured by micro-cracks (Figure 3.15 A) strained muscovites and local muscovite recrystallisation at the margins of larger, sheared muscovites (Figure 3.15 B). Empirical and experimental studies indicate that micro-cracking of feldspar generally occurs at temperatures < 300°C (Tullis and Yund, 1987; Gapais, 1989; Pryer, 1993). Combined with evidence for muscovite recrystallisation, this implies that the age of 17.3 ± 0.4 Ma represents resetting of Ar systematics due to muscovite recrystallisation or neocrystallisation below the closure temperature. Although it was not possible to directly determine sense of shear for this sample, it is likely that deformation and muscovite recrystallisation were both responses to normal movement on the Malari Fault. The implication of either process, i.e. cooling or deformation induced resetting of Ar systematics is that the age of 17.3 ± 0.4 Ma preserved by HW40-A is the most robust minimum age for normal movement on the Malari Fault. This age is almost within error of K-Ar (muscovite) and ^{40}Ar-^{39}Ar (muscovite) ages for the Gangotri and Bhagirathi leucogranites which are 18.9 ± 1.3 Ma and 17.9 ± 0.1 Ma, respectively (Stern et al., 1989; Sorkhabi et al., 1996). The upper bracket of 24.3 ± 1.1 Ma for movement on the Malari Fault is also broadly consistent with U-Pb (monazite) and K-Ar (muscovite) evidence for a pulse of rapid (200-300°C Ma^{-1}) cooling at 23-21 Ma (Searle et al., 1999b). However, cooling rates inferred in this way must be treated with caution: the closure of the U-Th-Pb system in zircon and monazite may reflect cooling from the crystallisation temperature of the injected granitic magma, and probably does not provide information about the thermal state of the rocks into which the magmas intrude.

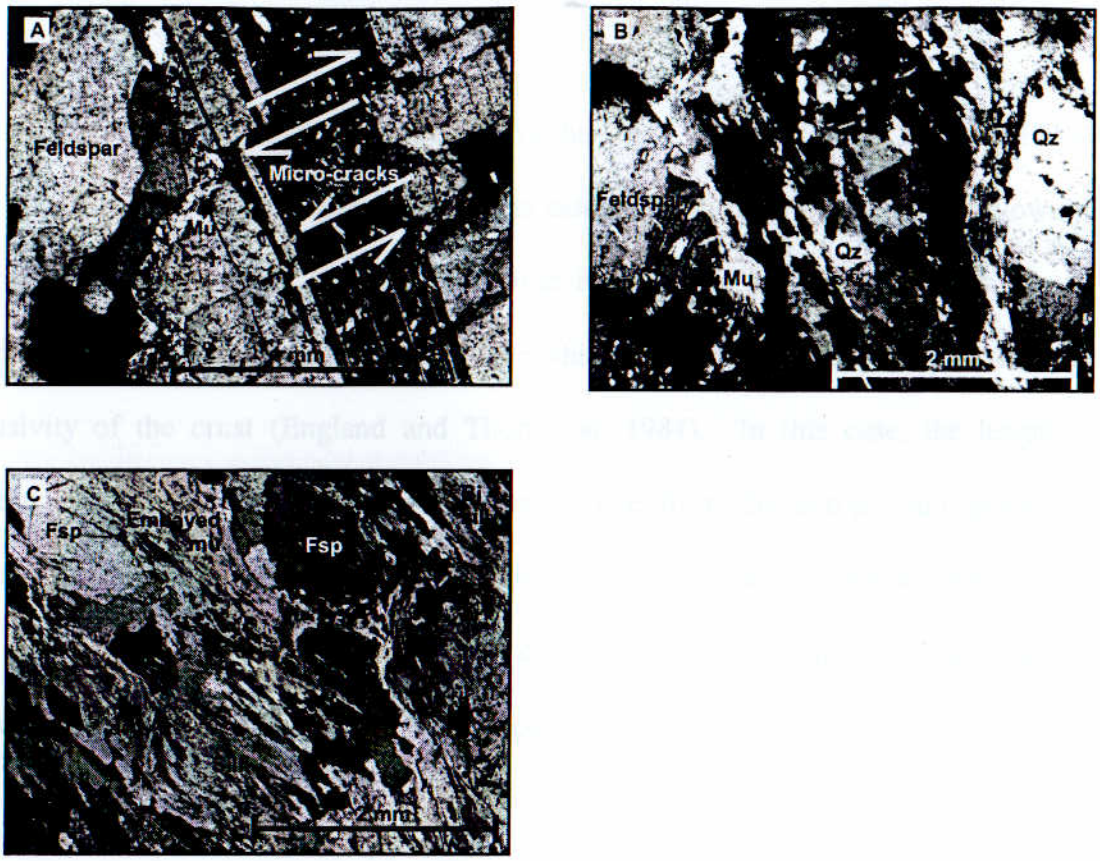

Figure 3.15 Photomicrographs of HW40A and HW61A.

HW40A (A, B) shows evidence for semi-brittle deformation: feldspar micro-cracks (A) and migration recrystallisation (B), with deformation accommodated predominantly by grain boundary sliding (B). HW61A (sill+mu+bi+ksp+qz) has large, embayed muscovites, with silliminite growing at the grain margins (C). These observations indicate that muscovites grew during prograde metamorphism, 600-700°C, well above the Ar closure temperature.

3.5.2.1 Quantifying displacement on the Malari Fault

The brackets on fault movement provided by the ^{40}Ar-^{39}Ar data for the TSS and HW40-A may be used to quantify vertical displacement associated with the Malari Fault following the approach of Vance et al. (1998). The time it takes for a thermal perturbation to be conducted is related to the length scale over which conduction propagates and the thermal diffusivity of the crust (England and Thompson, 1984). In this case, the length scale corresponds to the vertical distance of the sample from the active fault plane. This characteristic response time (effectively a thermal time constant) is independent of internal heat production and fault geometry and can be expressed using the one-dimensional equation for conduction (England and Thompson, 1984):

Equation 3-5

$$\tau = \frac{L^2}{\kappa}$$

where τ is the time taken for the conduction of a thermal perturbation over length scale L and k is the thermal diffusivity. Thermal diffusivity is a function of the conductivity and heat capacity of the material concerned; estimates of k for the upper crust range from 6×10^{-7} to $1.2 \times 10^{-6} m^2 s^{-1}$ (England and Thompson, 1984). In the following calculations, a value of $1 \times 10^{-6} m^2 s^{-1}$ is adopted for simplicity. The uncertainty in k outweighs other sources of error in these calculations, and the sensitivity of the results to this is addressed later. Instantaneous faulting, while unrealistic, is assumed here for purposes of simplicity.

Assuming that the cooling of the footwall is a direct response to unroofing on the fault, τ, the delay between the initiation of movement on the Malari Fault and the thermal response of the upper HHCS may be estimated as the difference between the cooling ages for upper HHCS and 1) the age recorded by HW40-A (17.3 ± 0.4 Ma) or 2) the youngest cooling age for the TSS (GA-173; 24.3 ± 1.6 Ma). τ is the time that it takes the sample to cool from prograde temperatures to the temperature of the fault plane at the time when the fault moved. At 24.3 ± 1.6 Ma, the temperature of the fault plane must have approached the closure temperatures for Ar in muscovite, as GA-173 preserves a cooling age. By 17.3 ± 0.4 Ma, the fault plane must have attained temperatures of 300-380°C, inferred from the semi-brittle deformation textures of HW40A (Figure 3.15 A, B). As prograde thermobarometry suggests an isothermal temperature profile across the HHCS (Prince, 1999), the values of τ calculated for different samples are comparable. Furthermore, the temperatures inferred for the fault plane at the two ages taken for fault movement are similar, allowing the thermal effects of faulting at these times to be directly compared. The model is therefore independent of fault geometry and the thermal history of individual samples prior to extension i.e. the different ages recorded by samples can be related purely to their structural distance beneath the fault, and the time at which the fault is assumed to have moved.

The range of vertical displacement, calculated for individual samples, is 6.5-10.7 km (using HW40-A) and 17.7-20.7 km (using GA-173). The error on these estimates is ~16%, and is dominated by uncertainty in *k*. Vertical displacement may be converted into the amount of

slip on the fault plane. Using the present day orientation of the Malari Fault (~ 60°), slip is 8.1-13.5 km, assuming movement at 17.3 ± 0.4 Ma and 20.5-23.1 km, for movement at 24.3 ± 1.1 Ma. If the current orientation of the fault is a result of rotation of a shallower fault plane, then these may be considerable underestimates. For example, assuming an original angle of ~30° for the fault dip increases the net slip by ~ 40%. Estimating rates of fault movement is more equivocal, as there are no direct constraints for the cessation of fault activity. Assuming movement on the Malari Fault occurred between 24.3 ± 1.6 and 17.3 ± 0.4 Ma, rates of movement on the fault range from 2.8-3.2 km Ma^{-1}, using the present day orientation of the fault to 4.9-5.6 km Ma^{-1}, assuming a dip of 30°. Similar rates of movement are obtained if movement on the fault began at 17.3 ± 0.4 Ma and ceased by the latest cooling of the upper HHCS through muscovite closure temperatures (13.7 ± 0.7 Ma; for sample HW61-B). The effects of erosion in reducing the length scale L are not taken into account, however, minimum rates of fault movement are at least twice as fast as erosion rates, which are ~1 km Ma^{-1} for rapidly eroding regions (Burbank et al., 1996). This implies that thermal re-equilibration in response to the perturbation imposed by the detachment occurs before erosion can shorten the length scale significantly.

3.6 Cooling history of the High Himalayan Crystalline Series

The data obtained here for the upper HHCS and HHL complements published K-Ar and ^{40}Ar-^{39}Ar studies on the lower HHCS and MCTZ within Garhwal (Metcalfe, 1993; Oliver et al., 1995). Muscovite cooling ages from this study and literature data (Metcalfe, 1993;

Oliver et al., 1995) are plotted against relative distance from the MCT (Vaikrita Thrust) in Figure 3.16. There are two first-order observations: firstly, the apparent cooling ages of the central HHCS are generally older than those obtained here for the upper HHCS, forming a convex array on Figure 3.16, and secondly, the apparent ages young sharply towards the MCT, and are youngest within the MCTZ. The progression of cooling ages from 20 Ma to <10 Ma towards the MCT has been interpreted in terms of the southward propagation of deformation in the mountain belt (Metcalfe, 1993) followed by subsequent reactivation (Harrison et al., 1997b; Catlos et al., 1999). The young K-Ar and ^{40}Ar-^{39}Ar ages obtained from the basal HHCS are consistent with reactivation of the MCT and resetting of the ^{40}Ar-^{39}Ar system by hydrothermal activity related to the dehydration of footwall rocks (e.g. Copeland et al, 1991). These ages are similar to Th-Pb ages of 5.7 ± 0.1 to 8.3 ± 0.1 Ma on monazite inclusions within garnets in the MCTZ (Catlos et al., 1999) which were also interpreted in terms of MCT reactivation.

While the young ages from the basal HHCS and MCTZ are readily interpreted in terms of fault reactivation, the trend to older apparent ages in the central HHCS and the metamorphic core of the orogen is harder to explain. The implication from the data is that the rocks of the upper HHCS remained hot, above muscovite closure temperatures, while the rocks of the middle- and lower-HHCS were cooling. This in turn suggests that the middle- HHCS cooled much more quickly than either the upper or basal HHCS. This is counter-intuitive, as it would be expected that the rocks closest to the detachment or to the MCT thrust front would experience the most rapid cooling (Harrison et al., 1997b; Vance et al., 1998).

Closer examination of Figure 3.16 shows that the convex age-distance curve is dependent on K-Ar data for the middle-HHCS (Metcalfe, 1993). However, the oldest K-Ar dates of Metcalfe (1993) were obtained from analyses with low amounts (< 50%) of radiogenic ^{40}Ar which implies that the data are compromised by atmospheric contamination. With these analyses omitted, the age-distance profile on Figure 3.16 is essentially flat, suggesting that, within error, the HHCS cooled synchronously. Cooling rates may be calculated using the ^{40}Ar-^{39}Ar data and Ar closure temperatures for muscovite (Table 3.1) in combination with prograde temperature constraints and Sm-Nd garnet ages obtained by Prince (1999). The following calculations assume that garnet growth and resetting of the Sm-Nd system occurred at the prograde thermal peak, as estimated by Prince (1999) on the basis of metamophic mineral assemblages. Sm-Nd ages are, necessarily, taken from both Bhagirathi (upper HHCS) and Dhauli (basal) sections. The youngest ages for the attainment of the thermal peak are used for both the basal and upper HHCS. The resulting time-averaged cooling rates are 39 ± 20 °C Ma^{-1} and 23 ± 8 °C Ma^{-1} for the basal and upper HHCS, respectively. These are approximate as prograde and cooling age constraints were not obtained from the same samples, and there may have been imbrication and reorganisation within the crustal wedge during cooling between prograde and muscovite closure temperatures. Interestingly, the cooling rates obtained for the upper HHCS are considerably lower than the rates of 75-200°C Ma^{-1} estimated for the footwall of the Zanskar Shear Zone (Vance et al., 1998). The slower cooling of the Garhwal section relative to Zanskar probably reflects differences in fault activity along strike in the orogen, although the Zanskar cooling rates are based on U-Pb closure and leucogranite emplacement in conjunction with ^{40}Ar-^{39}Ar ages, and may be overestimates, for reasons outlined earlier. However, at face value, the slower cooling of the Garhwal section may explain why the cooling ages preserved in the footwall are considerably younger than those in the Zanskar

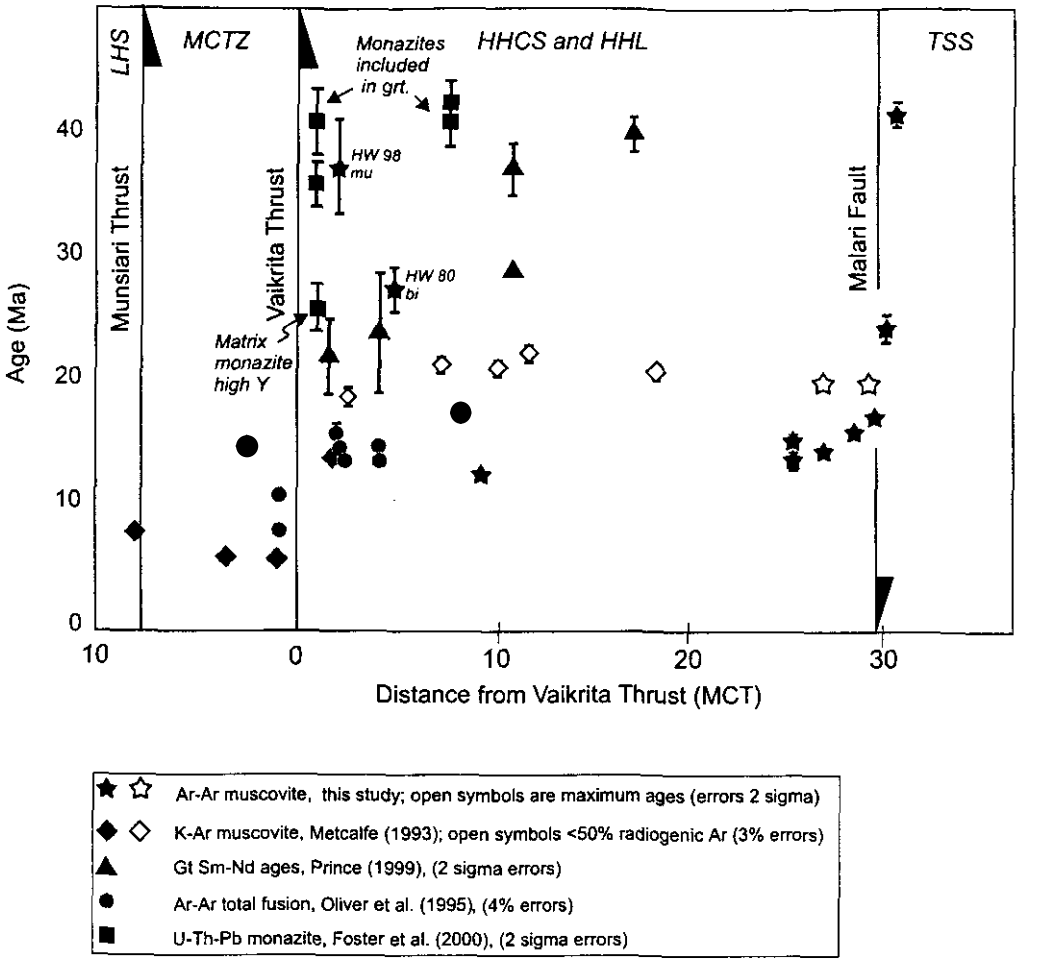

Figure 3.16 Cooling ages plotted against distance from the Vaikrita Thust (MCT). Mu, muscovite; bi, biotite; gt garnet

Samples from the Dhauli and Bhagirathi Valleys. Where not shown, error bars are smaller than symbol size.

Shear Zone, which range from 19.5 ± 1.7 to 28.0 ± 0.7 Ma (Vance et al., 1998). Given the above cooling rates, the errors of 0.4-0.7 Ma that are obtained for the majority of ^{40}Ar-^{39}Ar ages (excluding HW80 and HW98) translate to temperature differences of 7 to 20°C between samples. This implies that while variations in the timing of cooling may not be detected by regional ^{40}Ar-^{39}Ar cooling age profiles, the cooling of the HHCS slab is still remarkably synchronous.

Considerably older muscovite and biotite ages are recorded by two samples from the basal HHCS: HW80 and HW98. These ages fall into the range of Sm-Nd ages obtained for garnet growth from this lithology (Prince, 1999) and considerably predate the timing of earliest ductile movement on the MCT (Hubbard and Harrison, 1989; Metcalfe, 1993). Although similar ^{40}Ar-^{39}Ar ages have been recorded in the upper HHCS and attributed to relict "Eo-Himalayan" metamorphism that had not experienced resetting (Coleman and Hodges, 1998), it is difficult to explain the preservation of old cooling ages at the greater depths (and higher temperatures) of the basal HHCS. Since the muscovite and biotite ages for HW98 are within error of each other, one interpretation is that the sample experienced extremely rapid cooling. Both HW98 and HW80 display top-to-the-south vergent structures (Figure 3.17 A and B), which have been related to south directed thrusting. Although thrusting is not generally associated with exhumation, if sufficient topography is created the exposed part of the thrust ramp may be rapidly eroded (Harrison et al., 1997b). Therefore, a possible explanation for the similarity between these mica cooling ages and garnet prograde ages (Prince, 1999) could be early south-directed thrusting and prograde metamorphism followed by rapid exhumation due to erosion of the exposed part of the thrust ramp. However, there is little or no evidence for such an early thrusting event in other sections through the HHCS slab, and such an explanation is therefore considered unlikely. As there is currently no other

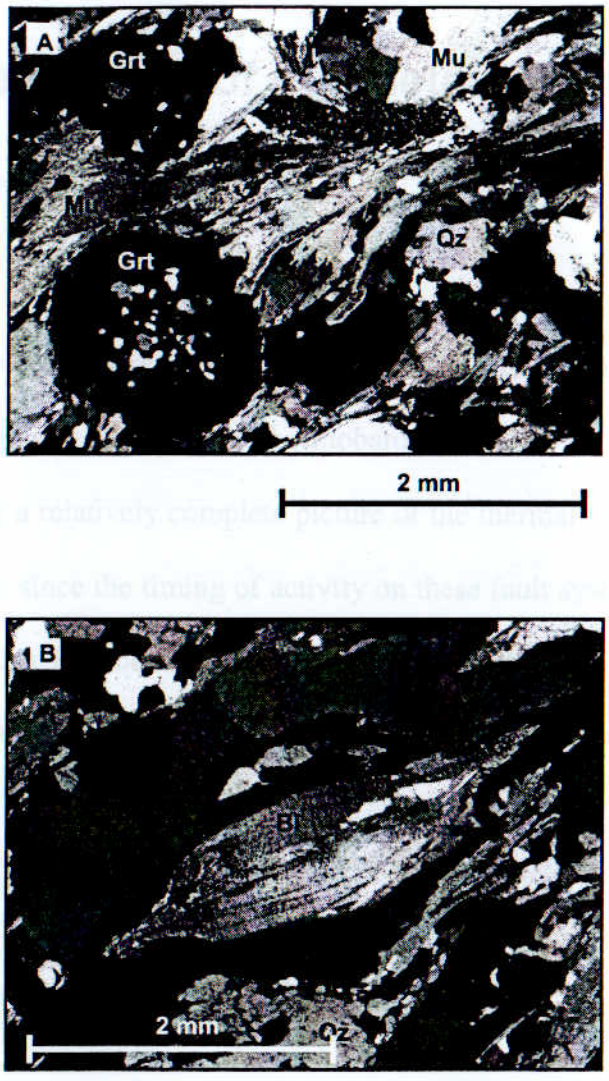

Figure 3.17 Photomicrographs of HW98 (A) and HW80 (B).

In HW98 (gt+qz+mu+bi±ky) large micas are clearly prograde, in HW80 (gt+bi+ky+qz) large prograde biotites define south-vergent structures

explanation for the preservation of near-prograde ^{40}Ar-^{39}Ar ages in groundmass micas, these ages are attributed to the presence of an unconstrained excess argon component.

3.7 Thermal evolution of the metamorphic belt in the Garhwal region

The ^{40}Ar-^{39}Ar ages obtained here for the HHCS and the TSS complement the presently available geochronological, structural and thermobarometric data for the metamorphic belt in this region, allowing a relatively complete picture of the thermal history of the belt to be constructed. Moreover, since the timing of activity on these fault systems is consistent with studies from several other Himalayan sections (discussed in chapter 2) these constraints on the evolution of the Garhwal region are likely to have implications for the evolution of the orogen as a whole.

3.7.1 Thrusting and prograde metamorphism

The early history of the mountain belt in the Garhwal region was dominated by thrusting, burial and subsequent heating. This has been studied in detail by Prince (1999) but the main points relevant to this work are summarised below. Garnet growth related to tectonic burial is constrained by Sm-Nd garnet ages and Th-U-Pb ages on monazite micro-inclusions within garnets to be from 41 to 22 Ma in the basal HHCS, and 41 to 26 Ma in the higher structural levels (Figure 3.18), ~10 Ma after final suturing (Patriat and Achache, 1984). Prince (1999) used the internally consistent thermobarometric database of Holland and Powell (1998) and

mineral composition data to constrain the PT paths experienced by the basal and upper HHCS in the Dhauli and Bhagirathi sections. Using this approach, relatively shallow PT paths for both upper and basal HHCS were obtained, implying thermal re-equilibration following burial to depths of ~ 25 to 28 km (basal HHCS 1.06 ± 0.15 to 1.20 ± 0.13 GPa, upper HHCS 0.95 ± 0.12 to 1.04 ± 0.15 GPa). Thermal re-equilibration following burial is supported by the growth of matrix monazites at 30-26 Ma in the upper HHCS of Garhwal (Foster et al., 2000). Their low Y contents suggest that monazite growth occurred after garnet had cystallised. This implies that temperatures of ~ 550°C, sufficient for monazite growth (Smith and Barreiro, 1990), were maintained from 30-26 Ma. These are overgrown by a second generation of monazite at < 25 Ma. Significantly, this generation of monazites is characterised by higher Y concentrations, suggesting growth during garnet breakdown, and by implication, decompression. This compares well with Sm-Nd constraints, which suggest garnet resorbtion and termination of prograde metamorphism by ~ 26 and 22 Ma in the basal and upper HHCS, respectively.

The constraints on the prograde evolution of the HHCS discussed above are complemented by the ^{40}Ar-^{39}Ar ages for the TSS north of the Malari fault, which imply that the timing of prograde metamorphism in the TSS was similar to the HHCS, from at least 41.5 ± 1.9 to 24.3 ± 1.6 Ma. Top-to-the-southwest trending (250°) fabrics in GA-173 (Fig 2.15) suggest that prograde mica and chlorite growth was synchronous with south directed thrusting and burial by reverse faults to the north of the present exposures. The presence of dextral, late brittle micro-fractures cross-cutting the main fabric (Figure 3.14) suggests that top-to-the-south shear continued after prograde metamorphism, at temperatures below that for Ar closure in muscovite i.e. later than 24.3 ± 1.6 Ma. The latter interpretation assumes that GA-173 had not significantly changed in orientation during development of these textures.

While there are few ^{40}Ar-^{39}Ar ages available for the TSS, the age of 24.3 ± 1.1 Ma for GA-173 is not inconsistent with ages of 26.7 ± 1.4 and 29.7 ± 1.2 Ma for the TSS in the Annapurna region (Coleman and Hodges, 1998). The implication is that the Oligocene Eo-Himalayan event documented in the HHCS across the orogen is equally prevalent in the TSS, and that the TSS also appear to have cooled relatively synchronously across the orogen. Further work is necessary to confirm the generality of these observations.

While prograde metamorphism within the HHCS and TSS may both have resulted from continued thrusting on the presently exposed suture zone (ITSZ), there are several lines of evidence which imply that garnet growth in the HHCS was triggered by renewed thrusting further south of the suture zone. As prograde PT data suggests that the upper HHCS were buried 25-28 km, a plausible scenario would be south directed thrusting of the sequence now known as the TSS over the HHCS. Given that the restored thickness of the TSS is only ~10 km (Schneider and Masch, 1993; Searle et al., 1997), thickening of the TSS must have occurred shortly after collision. Taking this logic a step further, it is reasonable to suggest that the proposed south directed thrusting of the TSS over the HHCS occurred by reverse movement on the Malari Fault, prior to extension. This is consistent with the evidence from GA-173, that prograde muscovite and chlorite grew during south directed thrusting shortly before closure of muscovite to Ar at 24.3 ± 1.6 Ma. Furthermore, the presence of brittle shears with the same orientation in this sample suggests that south directed thrusting continued after this time, and was probably the mechanism for the cooling of the TSS below closure of Ar in muscovite. These observations suggest that thrusting on the Malari Fault initiated prior to 24.3 ± 1.6 Ma. Tectonic burial in response to this thrusting is likely to have produced the metamorphic conditions corresponding to garnet growth in the HHCS until ~26-22 Ma. However, there is minimal structural evidence for reverse activity on the Malari

Fault, hindering testing of such a hypothesis. Therefore, the approach used in section 3.5.2.1 to quantify vertical movement in response to faulting is applied to this problem to i) determine whether prograde metamorphism of the TSS and HHCS can be explained by burial on the same thrusts and ii) whether the timing of prograde metamorphism of the HHCS is compatible with burial by the TSS and thrusting on the Malari Fault prior to 24.3 ± 1.6 Ma.

3.7.1.1 Quantifying early tectonic burial of the HHCS and TSS

The burial of the HHCS and the TSS by south directed thrusting is investigated using the one-dimensional expression for conduction of a thermal perturbation, where L corresponds to the vertical distance of the samples beneath the hypothetical fault plane and τ represents the time between thrusting and prograde metamorphism. In order to address the questions posed at the end of the previous section, the time of thrusting used to calculate τ is taken to be either 50 Ma, the approximate age of final suturing (Patriat and Achache, 1984) or 41.5 ± 1.9 Ma (the oldest age for prograde metamorphism of the TSS). The assumptions relevant to this model are discussed in section 3.5.2.1. Similarly, κ is taken as 1 x $10^{-6}m^2s^{-1}$, and errors on calculated depths are ~16%.

Assuming that both the HHCS and TSS were buried shortly after collision at 50 Ma, the ^{40}Ar-^{39}Ar ages of the TSS require a thrust to be 16.4 km above HW44 and 28.5 km above GA-173. As these samples are now separated by < 1 km, this confirms that the samples were juxtaposed following thrusting, or that the ages reflect other events, or detrital input in the case of HW44 (section 3.4.5). Interestingly, thrusting at 50 Ma requires a similar

magnitude of vertical displacement for the HHCS, 17.9-28.7 km, using the oldest prograde garnet and monazite inclusion ages in the upper HHCS. These depths of burial approach the depths of 25.7-28.1 km inferred from thermobarometry on the same samples. However, the thermal peak of metamorphism, recorded by garnet growth, does not directly correlate with the attainment of peak pressure, as is frequently demonstrated by clockwise PT paths for regionally metamorphosed samples. Furthermore, these calculations constrain the position of the sample vertically beneath the thrust plane only, and do not take into account the lithostatic pressure of the overlying TSS. Nonetheless, the similar depths of burial inferred for the TSS, which are 12-18 km north of the upper HHCS samples dated implies that, even with later disruption of the TSS sequence, these units could not have been buried synchronously at ~50 Ma by the same thrust. Using 41.5 ± 1.0 Ma for the onset of thrusting further emphasises this point: GA-173 is required to have been buried 23.3 km, yet unfeasibly low vertical displacements of 4.0-11.8 km are obtained for the early prograde metamorphism of the upper HHCS. Therefore, the early (~ 41 Ma) prograde metamorphism of the upper HHCS requires tectonic burial shortly after collision, and this burial probably occurred on reverse faults south of the suture zone. This does not prove in itself that burial occurred in response to thrusting on the Malari Fault, but it is likely that a major extensional fault will develop by reactivation of a pre-existing suture. It is not possible to constrain when the TSS was buried, as there are no constraints on the prograde pressures attained by these samples. However, it is clear that the TSS cannot have been buried by the same thrust as the HHCS.

Therefore, the pattern suggested here, of southward thrusting, transferral and progressive younging of deformation from collision and thrusting on the suture zone (45-55 Ma) and the proto-STDS (41.5 to 24.3 Ma), the MCT (~19 Ma) and the Main Boundary Thrust and Main

Frontal Thrust (Wesnousky et al., 1999) is consistent with the idea of a foreland-propagating thrust system (Searle et al., 1987; Metcalfe, 1993). The observation of progressive southward transfer of deformation and continual re-organisation of the crustal wedge further in Garhwal is similar to that observed elsewhere, and suggests that it may be a general feature of the deformation and thermal evolution of the orogen. This process ultimately results in more material and heat being moved into the orogenic belt (Jamieson et al., 1998), and may explain why the upper crust retained elevated temperatures, from collision in the early Tertiary until the early Miocene.

3.7.2 Extension on the Malari Fault: Implications for tectonic models

As argued in the previous section, it is probable that the Malari Fault was reverse in sense before later, normal reactivation. Based on observations of both ductile and brittle south vergent fabrics in GA-173, it is likely that reverse movement on the Malari Fault persisted (possibly intermittantly) until some time after 24.3 ± 1.6 Ma. By 17.3 ± 0.4 Ma, extension on the Malari Fault had begun. The onset of extension after 24.3 ± 1.6 Ma is consistent with termination of garnet growth at 22 ± 3 Ma (Prince, 1999) and garnet resorbtion at < 25 Ma (Foster et al., 2000). Decompression may have facilitated melting of the basal HHCS (Harris and Massey, 1994) which, as shown in Figure 3.18 attained sufficiently high prograde temperatures for decompression melting to be effective. This may have ultimately culminated in emplacement of leucogranite plutons at 23 to 18 Ma (Stern et al., 1989; Sorkhabi et al., 1996; Searle et al., 1999b).

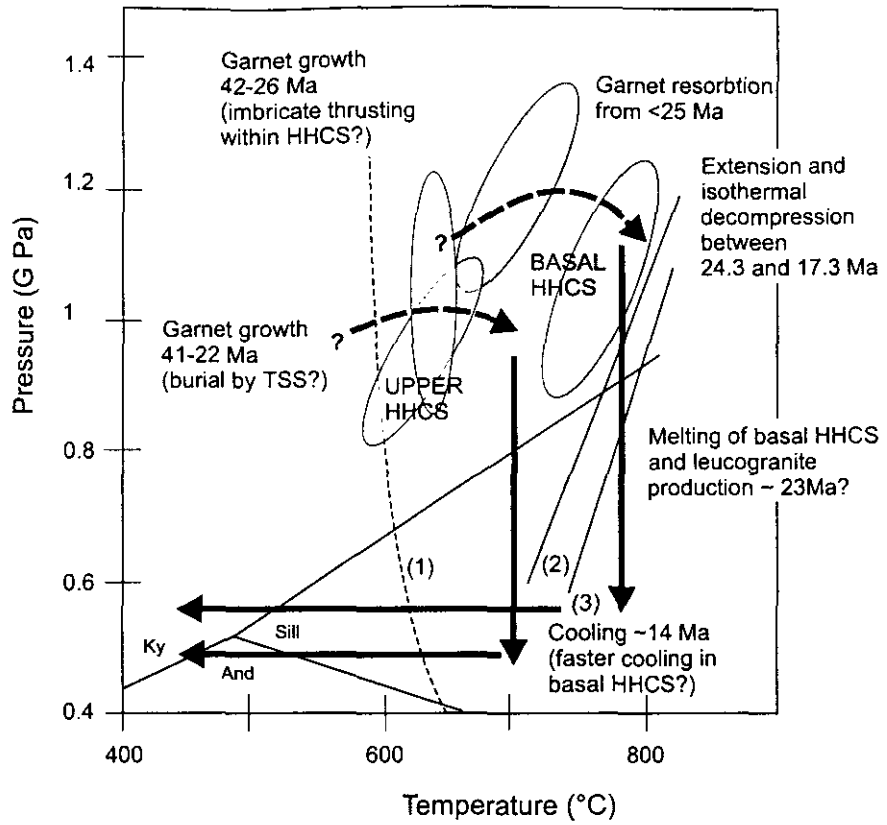

Figure 3.18 Thermal history of high grade rocks within the Garhwal Himalaya

The dashed curve (1) is the wet pelite melting curve (Le Breton and Thompson, 1988) and the two solid curves are fluid-absent melting curves of Himalayan muscovite-biotite and muscovite schists, respectively (Patiño Douce and Harris, 1998). Two schematic (heavy dashed lines) P-T paths are shown for the upper and basal HHCS. These are based on thermobarometric constraints (Prince, 2000) and cooling data. The prograde P-T constraints of Prince (2000) are shown as ellipses with 2 sigma correlated errors. Timing of garnet growth and resorbtion from Foster et al. (2000); Prince (2000), leucogranite emplacement (Stern et al., 1989; Sorkhabi et al., 1996; Searle et al., 1999b). The magnitude of decompression is based on the calculations presented in Section 3.5.2.1., assuming an original fault dip of 30°. Clearly this is an approximation, as the majority of age data is from the the upper HHCS, and individual sample paths are not determined. The implication is that isothermal decompression is a plausible mechanism for causing muscovite dehydration melting of the lower migmatitic HHCS and leucogranite formation. The rapid near-isobaric cooling part of the P-T path is not well constrained due to a lack of direct information regarding the depths at which this cooling began. Time-averaged cooling rates based on prograde and cooling temperatures do not resolve this. The implication is that the basal HHCS must have cooled faster than the upper HHCS to maintain the relatively synchronous pattern of cooling ages. Note that garnet growth from 41 to 22 Ma (Prince, 1999) requires that the upper HHCS be above the wet pelite solidus at ~40 Ma. This is consistent with small volume leucogranite generation in Garhwal at 39 ± 3 Ma, which Prince et al. (in press) related to fluid enhanced anatexis of the HHCS.

The hornblende ^{40}Ar-^{39}Ar age of 19.8 ± 2.6 Ma (Metcalfe, 1993) just below the Vaikrita Thrust (MCT) is almost within error of constraints for extension on the Malari Fault, indicating that movement on the STDS and MCT in Garhwal was relatively synchronous. This pattern is similar to that seen in other sections of the metamorphic belt (Hodges et al., 1992). Faster cooling of the basal HHCS relative to the higher structural levels (discussed in 6.3) supports models in which the STDS is essentially a passive structure, its initiation a response to the gravity-driven decollément of the TSS following MCT movement (Burg et al., 1984). This would imply a reduction in the basal shear strength of the wedge, resulting in a decrease in the ability of the wedge to support the potential energy of the thickened crust (England and Molnar, 1993). It has been suggested that such a process could be facilitated by melting of the basal HHCS (Hollister, 1993; Harris and Massey, 1994). This is certainly plausible, given the prograde temperatures attained by the basal HHCS (Figure 3.18), geochemical and isotopic evidence which relates the formation of the HHL to anatexis of the basal, kyanite-grade HHCS (Harris and Massey, 1994; Patiño Douce and Harris, 1998). However, the data presented here do not differentiate between models of leucogranite generation that invoke decompression following normal faulting (Harris and Massey, 1994), or melting by shear heating on the MCT or a basal decollement (Harrison et al., 1997a). In both cases, there is the potential for development of a self-supporting cycle consisting of melting of the basal HHCS, MCT and STDS movement and further melting (due to either shear heating or decompression). Such a cycle could potentially have been maintained until the basal HHCS cooled – by tectonic exhumation or erosion – out of the melting window. Interestingly, Hodges et al. (1996) identified alternating episodes of extension and compression in the Annapurna region, which they interpreted in terms of

"dynamic compensation" - the stabilisation of the orogenic wedge in response to changes topographic profile and erosion rates.

Nelson et al. (1996) pointed out that the MCT and STDS were not parallel at depth, but tapered together into a basal decollement. Several authors have suggested, based on these observations, that the near-synchronous movement on the MCT and STDS has resulted in the extrusion of a crustal wedge from the orogenic region (Hodges et al., 1992; Harris and Massey, 1994; Grujic et al., 1996). Burg et al. (1984) suggested that the mechanism for simultaneous movement on the MCT and STDS was the gravitational collapse of the Tethyan sedimentary pile due to the attainment of critical topography. Recent physical modelling (Chemenda et al., 2000) has shown that exhumation of underthrusted material can occur during convergence due to the failure of the subducting slab. Such a process also has the potential to cause uplift of southern Tibet, due to isostatic rebound following removal of part of the relatively cold, dense oceanic lithosphere slab (Davies and von Blanckenburg, 1995; Davies and von Blanckenburg, 1997). Irrespective of the mechanisms of plateau uplift, an increase in the elevation of the southern margin of the Tibetan plateau would result in increased potential energy gradients at the plateau margins. Platt and England (1994) suggested that thrusting prevalent at the margins of the Tibetan plateau represents a response to such a potential energy excess, and clearly, the extrusion of a wedge from the orogenic region is consistent with such a scenario. This latter hypothesis is intrinsically attractive, but difficult to prove without reliable constraints on the timing and mechanisms for the uplift of southern Tibet. Obtaining such constraints is therefore a priority in any attempt to further understand the potential interdependence and evolution of the Himalayan and Tibetan systems. This will be addressed further in Chapter 4.

3.8 Summary

The new ^{40}Ar-^{39}Ar ages for the HHCS and TSS indicate that these units cooled through muscovite closure temperatures between 12.6 ± 0.7 Ma to 16.0 ± 0.3 Ma, and 24.3 ±1.6 to 41.5 ± 1.9 Ma respectively. Older ages obtained for the basal HHCS (27.6 ± 1.3 to 40.1 ± 1.3 Ma) are attributed to the presence of an excess argon component. The data demonstrate that the upper HHCS and the HHL experienced similar cooling histories, and that the HHCS cooled relatively synchronously at ~ 14 Ma. To explain this pattern, the basal HHCS must have cooled substantially faster than the upper HHCS. In contrast, the older Ar-Ar ages of the TSS indicate that this unit must have experienced a very different thermal history to the HHCS. The juxtaposition of these units by the Malari Fault indicates that the fault represents an important tectonic discontinuity. Normal movement on the Malari Fault is constrained to be between 17.3 ± 0.4 and 24.3 ± 1.6 Ma, broadly synchronous with MCT movement. One-dimensional thermal modelling demonstrates that the synchronous cooling of the HHCS can be plausibly explained by normal movement on the STDS between 17.3 ± 0.4 and 24.3 ± 1.6 Ma.

The Tertiary ^{40}Ar-^{39}Ar ages of the TSS reflect cooling either due to thermal relaxation or due to thrusting on the Malari Fault. South-vergent shear fabrics in the TSS lend support to the latter hypothesis. The preservation of detrital ages indicates that the peak prograde temperatures experienced by the TSS approached muscovite closure temperatures. Therefore, the timing of prograde metamorphism in the TSS is constrained from ^{40}Ar-^{39}Ar data to be at least 41.5 ± 1.9 Ma, within error of prograde ages for the HHCS. Simple one-dimensional thermal modelling using ^{40}Ar-^{39}Ar data, Sm-Nd garnet ages and U-Th-Pb

monazite inclusion ages indicates that prograde metamorphism of the HHCS resulted from burial to depths of 17.9 to 28.7 km, while the TSS were buried 16.4 to 28.5 km. The main conclusion from this is that the HHCS and the TSS cannot have been buried by the same thrust. Interestingly, the burial depths calculated for the HHCS are consistent with thrusting in the position of the normal-sense Malari Fault. Early reverse activity on the Malari Fault is supported by shear criteria and probably occurred between 41.5 ± 1.9 to 24.3 ± 1.6 Ma. Thrusting on the Malari Fault is consistent with the progressive transferral of deformation to the south over a period of ~ 55 Ma, from the ITSZ to the Main Boundary Thrust and ultimately the Main Frontal Thrust.

A switch from a compressive to an extensional styles of deformation in the Malari region between 24.3 ± 1.6 and 17.3 ± 0.4 Ma must reflect a major change in the stress balance of the orogen at this time. The faster cooling of the basal HHCS relative to the higher structural levels below the detachment indicates that normal movement on the Malari Fault is likely to have been driven by MCT movement. Movement on these two fault systems is broadly synchronous, and is most easily explained in terms of the southward extrusion of a crustal wedge from the orogenic region. This could have been triggered by a change in the elevation of the Tibetan plateau at ~ 24 Ma. Age constraints for plateau uplift are required to confirm these inferences.

4 Age and composition of dykes in Southern Tibet: new constraints on the timing of east-west extension and its relationship to post-collisional volcanism

This chapter is a manuscript in its entirety, titled as above and accepted for publication in *Geology*. The manuscript is co-authored by Simon Turner (Bristol University), Simon Kelley (OU) and Nigel Harris (OU). In order to maintain consistency throughout this thesis, minor typographical modifications have been made to the original manuscript.

This chapter evaluates new constraints on the timing and tectonic significance of east-west extension in southern Tibet obtained from post-collisional north south trending dykes. It complements the discussion on the timing of north-south extension within the Himalaya in Chapter 3, and also relates to Chapter 5, which considers the geochemistry of post-collisional magmatism in north and south Tibet and its geodynamic implications.

4.1 Abstract

Controversy exists over whether east-west extension in southern Tibet is related to the dissipation of excess potential energy following plateau uplift or, alternatively, to the local

accommodation of plate boundary forces. Critical to this debate is the relationship between the onset of extension, plateau uplift and the corresponding thermal state of the lithosphere. This study discusses new ^{40}Ar-^{39}Ar ages obtained for post-collisional, north-south trending dykes in southern Tibet. Their ages range from 18.3 ± 2.7 Ma to 13.3 ± 0.8 Ma, and constrain the onset of regional east-west extension in southern Tibet. Compositionally, dykes are indistinguishable from post-collisional lavas, being either shoshonitic with a source in the sub-continental lithospheric mantle (SCLM), or calc-alkaline with a dominantly crustal origin. Ultrapotassic dykes reflect melting of the southern Tibetan SCLM and demonstrate unequivocally that regional east-west extension and SCLM derived magmatism were temporally and spatially linked, supporting models that relate the latest phase of plateau uplift to convective removal of part of the SCLM. The onset of extension at 18.3 ± 2.7 Ma therefore represents the time at which the plateau attained excess potential energy, and places a minimum age constraint on the attainment of high elevation in southern Tibet. This has fundamental implications for models that relate monsoon intensification in the Cenozoic to the uplift of high plateaus.

Here new ^{40}Ar-^{39}Ar ages and geochemical data for north-south trending dykes in south Tibet are presented. Sub-parallel dyke emplacement is unambiguously associated with fracture propagation and extension of the upper crust, perpendicular to the trend of the dykes. Therefore, the presence of north-south trending dykes provides an opportunity to constrain the onset of east-west extension independently of assumptions about crustal cooling processes, and to determine the relationship of extension to post-collisional magmatism. Combined with data on isolated dykes from Yin et al. (1994) and Miller et al. (1999), this paper presents a systematic analysis of the timing and composition of north-south dykes in

south Tibet, and shows that east-west extension and magmatism are both temporally and spatially linked.

4.2 Introduction

The geodynamic processes responsible for the uplift and ongoing extension of Tibet following collision of the Indian and Asian plates have been the focus of much interest and contention in recent years. The Himalayan-Tibetan region is regarded as the archetype of a continent-continent collision, and constraining the processes which drive the evolution of this active orogen is of fundamental importance to our understanding of continental tectonics as a whole. Furthermore, the uplift of the Tibetan Plateau has been implicated as a major control on Cenozoic climate (Kutzbach et al., 1989; Raymo and Rudiman, 1992; Molnar et al., 1993) and constraints on the timing, rates and mechanisms of plateau uplift are essential in order to test such models.

The Neogene tectonics of southern Tibet are dominated by east-west extension, which is orthogonal to ongoing plate convergence - a paradox not easily explained by plate tectonic theory. Extension, manifested by normal faulting (Figure 4.1), is restricted to the highest parts of the plateau while thrust faulting is prevalent within the lower plateau margins, to both the north and south (Molnar and Tapponnier, 1978; Molnar et al., 1993). Therefore, it has been proposed that extension reflects dissipation of excess potential energy following an increase in elevation above the levels which can be supported by convergent forces (Houseman et al., 1981; England and Houseman, 1989), Chapter 2). In contrast, McCaffrey and Nabelek (1998) have argued that extension is unrelated to uplift and is a direct response

to local plate boundary conditions. As discussed in Chapter 2, these geodynamic models for the uplift of the Tibetan plateau predict relationships between extension, uplift and the thermal state of the lithosphere (Houseman et al., 1981; England and Houseman, 1986; England and Houseman, 1989). Therefore, precise constraints for the onset of extension on the plateau itself are of fundamental importance in testing and refining such models. Unfortunately, the majority of ages obtained date upper crustal cooling events, interpreted in terms of exhumation following normal faulting (Pan and Kidd, 1992; Harrison et al., 1995). Such ages, based on thermal relaxation processes, are model dependent and may underestimate the timing of fault movement and extension (House and Hodges, 1994). Furthermore, many of these studies have been restricted to more accessible localities in northern Nepal (e.g. Coleman and Hodges, 1995), which may be influenced by Himalayan tectonics rather than plateau uplift.

Thinning of the SCLM following distributed shortening has been invoked as a mechanism for the plateau's uplift and subsequent extension (Houseman et al., 1981; England and Houseman, 1986; England and Houseman, 1989). Potassic volcanism derived from melting of the SCLM has been interpreted as the surface expression of such mantle processes (Turner et al., 1993). Models that invoke a component of SCLM thinning or erosion to explain plateau uplift and extension predict that SCLM derived volcanism should be coincident with or slightly pre-date extension. There has now been extensive research into post-collisional volcanism in Tibet, showing that the onset of volcanism is diachronous across the plateau (e.g. Coulon et al., 1986; Arnaud et al., 1992; Turner et al., 1993; Turner et al., 1996; Chung et al., 1998; Miller et al., 1999). However, the prevailing stress regimes at the time of volcanism remain – critically - unconstrained.

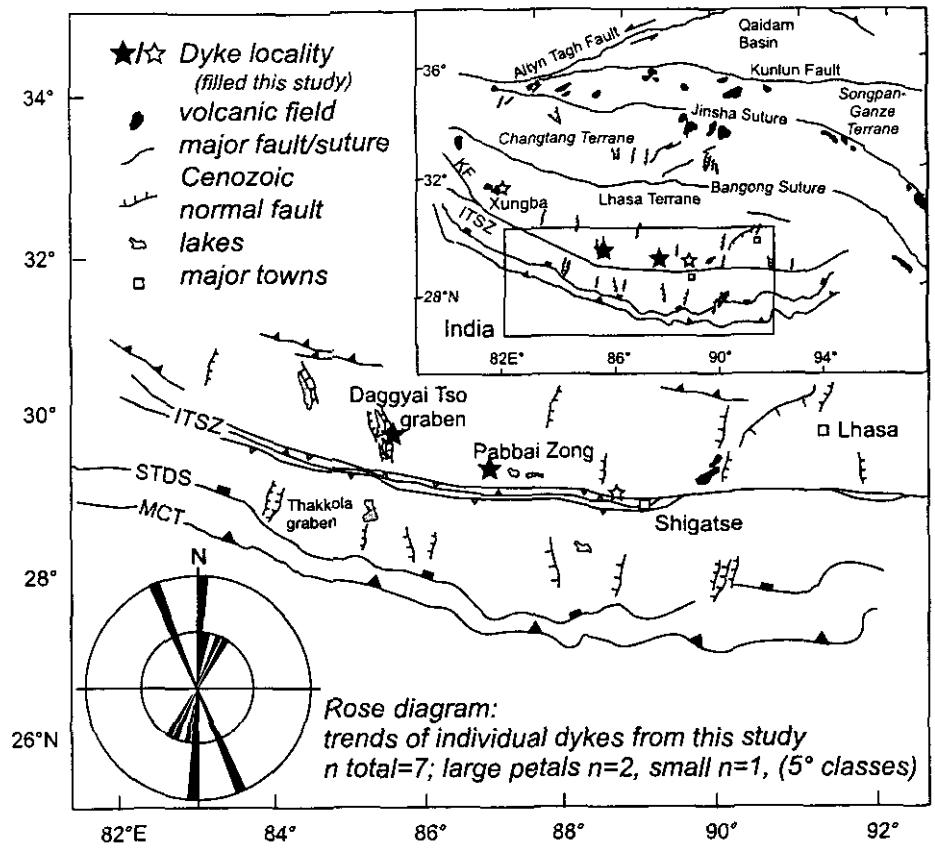

Figure 4.1 General tectonic map of Tibet

Locations of dykes collected from the Xungba and Shigatse areas by Miller et al., 1999 and Yin et al., 1994, respectively, shown by open stars. Filled stars correspond to samples analysed in this study. Major fault systems and sutures: ITSZ, Indus-Tsangpo Suture Zone; KF, Karakorum Fault, STDS, Southern Tibetan Detachment System; MCT, Main Central Thrust. Only major north-south trending faults and grabens are depicted. The major volcanic localities in north and southern Tibet are shown as black fields.

4.3 Results

Two series of north-south trending dykes from Pabbai Zong and the Daggyai Tso graben in southern Tibet are investigated (Figure 4.1; dyke orientations displayed in inset). The Pabbai Zong dyke swarm has an east-west extent of < 5 km and consists of a series of undeformed sub-parallel dykes, 2 to 5 m thick, intruding folded shales. Four dykes from this series were sampled, all are glimmerites, consisting of >40% modal phlogopite, subordinate clinopyroxene, alkali feldspar, apatite, Fe-Ti oxides and zircon. Additionally, garnet is present in sample T3B. Two dykes < 3 m thick were collected from within the Daggyai Tso graben, where they intrude evolved lavas. It was not possible to directly determine their relationship to normal faulting. The Daggyai Tso dykes are evolved, with phenocrysts of quartz, K-feldspar plagioclase, hornblende and minor Fe-Ti oxides in a glassy matrix. The petrography of the Daggyai Tso and Pabbai Zong dykes is discussed further in Chapter 5. Sample localities and descriptions are detailed in Appendix A.

The ^{40}Ar-^{39}Ar isotope analyses were performed following techniques outlined by Kelley (1995), summarised in Chapter 3. Results are presented in Table 4.1, tabulated Ar isotopic data are given in Appendix B. All ages, with the exception of JPT 14.2, were calculated using standard inverse isochron linear least-squares regression techniques, the interpretation of which is discussed in Chapter 3. The data for sample JPT 14.2 are complex, suggestive of excess argon, and for this sample a maximum age based on an individual

Table 4.1 ^{40}Ar-^{39}Ar ages for southern Tibetan dykes

Sample	rock type	min	No. of points	MSWD	Age (Ma)	± 2σ	$^{40}Ar/^{36}Ar$	± 2σ
Pabbai Zong								
JPT 7*	shoshonite	phl	8	10.9	27.2	-32.2	295.5	
JPT 7	**shoshonite**	**phl**	**8**	**2.98**	**18.3**	**2.7**	**613**	**88**
T2A*	shoshonite	phl	12	3.24	26.1	0.5	295.5	
T2A	**shoshonite**	**phl**	**15**	**2.41**	**13.8**	**3.5**	**362**	**19**
T3B[(1)]*	**shoshonite**	**phl**	**8**	**1.8**	**13.8**	**0.3**	**295.5**	
T3B[(1)]	shoshonite	phl	8	1.56	14.1	0.3	289	5
T5A*	shoshonite	phl	10	1.63	13.4	0.2	295.5	
T5A	**shoshonite**	**phl**	**10**	**1.73**	**13.3**	**0.8**	**300**	**229.6**
Daggyai Tso								
JPT14.2	**dacite**	**hbl**	**minimum from 8**		**19.3**	**1.5**	**295.5**	
T11B	**dacite**	**WR**	**5**	**1**	**17.3**	**1.9**	**976**	**364**

phl, phlogopite; hbl, hornblende; WR, whole-rock

bold typeface indicates the age most appropriate to attribute to the sample

**regression forced through atmospheric argon*

In the case of isochron ages, the errors are calculated from equation 3.3, and are multiplied by the square root of the MSWD, where the latter is greater than 2.5
The standard deviation of weighted means is multiplied by 2 to give the error on samples JPT14.2 and T11B

[(1)] a volcanic xenolith entrained in sample T3B was dated. The age reflects the resetting of Ar Ar systematics following entrainment within the dyke, and therefore gives the emplacement age of the dyke

minimum individual fusion ages assume that all non-radiogenic argon is atmospheric in composition

crystal fusion is presented. Trace element abundances were determined by inductively coupled plasma mass spectrometry (ICP-MS) at Durham University; mineral analyses were carried out at the Open University on a Cameca SX100 electron microprobe. Sr-Nd isotope analyses were performed by TIMS and inductively coupled multi-collector mass spectrometry (ICP-MC-MS) on a Nu Instruments machine at the Open University. Analytical procedures are detailed in Appendix D, full tabulated results in Appendix C. The new geochemical data for the Pabbai Zong and Daggyai Tso dykes are briefly evaluated here, and in more detail in Chapter 5.

The dykes range in age from 19.3 ± 1.5 Ma to 13.3 ± 0.8 Ma. The two Daggyai Tso dykes give ages within error of each other, implying relatively synchronous emplacement. As the 19.3 ± 1.5 Ma age for JPT 14.2 is a maximum estimate, the best constraint on emplacement of both dykes is from sample T11B, which is 17.3 ± 1.9 Ma. The data obtained for JPT 14.2 is complex, and will not be discussed further. Pabbai Zong dykes range from 18.3 ± 2.7 Ma to 13.3 ± 0.8 Ma. Compositionally, they are shoshonitic (K_2O/Na_2O 2.5-6.7; K_2O 5.0-7.7 wt %), relatively primitive (Mg# 64.4-80.5; SiO_2 51.3-56.9 wt %) and have high incompatible trace-element concentrations (Ba 1593-4220, La, 56-146 ppm). In contrast, the Daggyai Tso dykes are dacitic (Mg# 55.4-56.8; SiO_2 61.5-62.6 wt%), and calc-alkaline (K_2O/Na_2O 0.61-0.65; K_2O 2.7-2.8 wt %) with lower incompatible trace element concentrations (Ba 734-740, La 26.8-28.5 ppm). The Pabbai Zong dykes are characterised by high $^{87}Sr/^{86}Sr_{(i)}$ (0.7123-0.739) and low $\varepsilon Nd_{(i)}$ (-13.2 to-19.2) (Figure 4.3 A and B), while Daggyai Tso dykes have less enriched signatures ($^{87}Sr/^{86}Sr_{(i)}$ 0.7071-0.7073; $\varepsilon Nd_{(i)}$ -5.4 to-11.2).

4.4 Discussion

4.4.1 Timing and extent of east-west extension

The ^{40}Ar-^{39}Ar data presented here show that shoshonitic and calc-alkaline dykes were emplaced from 18.3 ± 2.7 Ma to 13.3 ± 0.8 Ma and at 17.3 ± 1.9 Ma, respectively. The occurrence of dykes > 600 km apart along strike (from Xungba to Pabbai Zong, Figure 4.1) demonstrates that emplacement is not a local phenomenon, as suggested by Yin et al. (1994), but has a wider regional significance. Although the majority of dykes trend north-south (Figure 4.1), two dykes collected by Miller et al. (1999) trend approximately east-west. This may reflect the local influence of dextral, strike-slip movement on the Karakorum Fault on the strain field at that time (Murphy et al., 2000). Given that most dykes trend north-south, it appears that they were emplaced in a dominantly east-west extensional strain field, similar to the present-day tectonic regime indicated by both field observations (Armijo et al., 1986) and earthquake fault plane solutions (Molnar and Tapponnier, 1978). The magnitude of extension, estimated from the Pabbai Zong dyke series, is < 1 % (ß = 1.003), independently verifying estimates based on normal fault distribution within southern Tibet (Armijo et al., 1986). Therefore, the earliest phase of dyke emplacement constrains the initiation of east-west extension in southern Tibet to be at least 18.3 ± 2.7 Ma. Dyke emplacement overlaps with the latest phases of upper-crustal shortening and the earliest normal faulting, the earliest dykes pre-dating existing constraints on east-west extension by about 4 to 8 Ma (Figure 4.2). This is unsurprising, as published

constraints for extension are, almost without exception, based on crustal cooling which is generally delayed with respect to faulting and exhumation (House and Hodges, 1994). Therefore, the new ^{40}Ar-^{39}Ar data presented here provide the unambiguous age constraints for the onset of extension within south Tibet. Relationships between extension and magmatism, and their implications with respect to geodynamic models for the evolution of the southern Tibetan Plateau, can now be addressed.

4.4.2 Relationship to post collisional volcanism

As illustrated in Figure 4.3 A, mafic and evolved dykes are compositionally similar to S. Tibetan shoshonitic and dacitic lava flows, respectively, emphasising their regional significance. Dykes do not predate the oldest lava flows (Figure 4.2), although the possibility of older dykes at deeper structural levels cannot be excluded. The enriched isotopic and trace element signatures of the Pabbai Zong group (Figure 4.3 A, B) are strikingly similar to those of the 18.5 ± 0.4 to 25.4 ± 0.2 Ma shoshonite flows studied by Miller et al. (1999) which have been attributed to small-degree melting of enriched regions within the SCLM. A similar origin for the Pabbai Zong dykes is supported by the presence of phlogopite xenoliths in some samples, whose high Mg#'s (93.7 to 94.3), and Ni contents (~3000 to 4000 ppm) suggests that they are derived from a refractory SCLM source re-enriched in volatiles and incompatible elements.

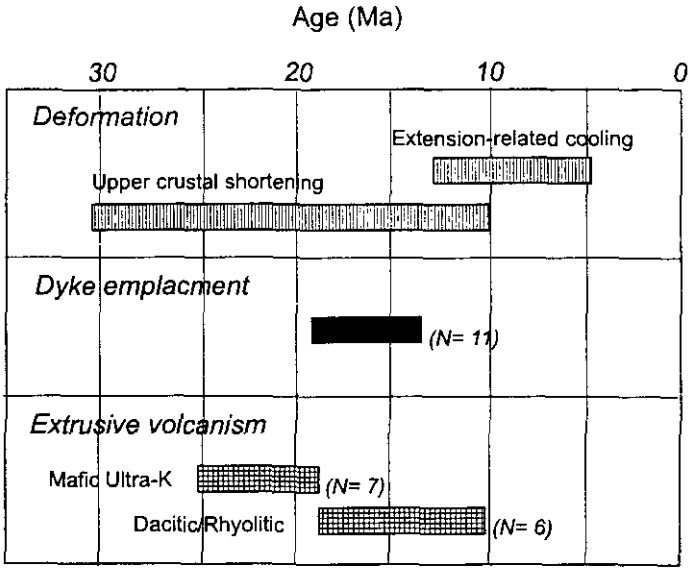

Figure 4.2 Age ranges of main post-collisional deformation and magmatic events in southern Tibet

Based on available Ar-Ar ages for post-collisional magmatism in southern Tibet (Coulon et al., 1986; Arnaud et al., 1992; Yin et al., 1994; Turner et al., 1996; Miller et al., 1999; this study), upper-crustal shortening (Ratschbacher et al., 1994; Yin et al., 1994; Quidelleur et al., 1997; Yin et al., 1999a) and extension-related cooling events (Mercier et al., 1987; Pan and Kidd, 1992; Coleman and Hodges, 1995; Harrison et al., 1995) Four mafic dykes and two dacitic dykes were dated in this study (data in Table 4.1, full details in Appendix B) and combined with ages obtained for four mafic dykes in the Xungba area (Miller et al., 1999) and an evolved dyke in the Shigatse area (Yin et al., 1994).

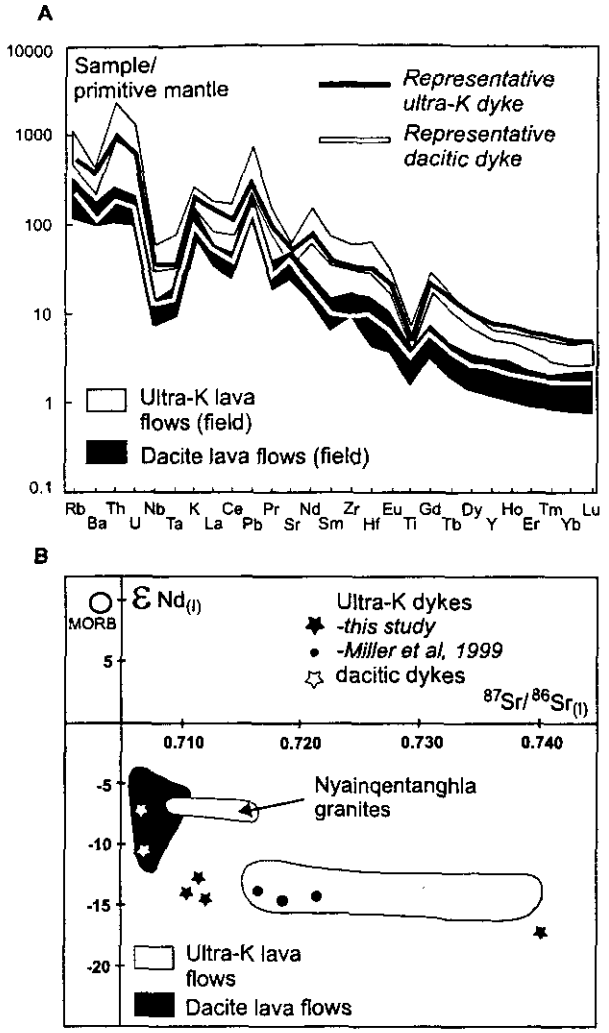

Figure 4.3 Primitive mantle normalised multi-element plot and 87Sr/86Sr(i) - eNd(i) plot for southern Tibetan dykes

(A) Incompatible element variation diagram, normalised to primitive mantle (Sun and McDonough, 1989). Compositions of S. Tibetan shoshonitic and dacitic flows (Miller et al., 1999) are shown as separate fields. Pabbai Zong dykes are characterised by incompatible element and LREE enrichment, negative Nb, Ta, Ti and positive Pb anomalies. The Daggyai Tso series mirrors this trend, although trace element abundances are lower. Both series of dykes (representative compositions shown) overlap the fields for ultrapotassic and evolved flows (Miller et al., 1999). B) Initial Nd and Sr isotope compositions for S. Tibetan dacitic and ultrapotassic flows (fields) and dykes. Data from this study, (Miller et al., 1999). The Nyainqentanghla granites (Harris et al., 1988) are used a proxy for time-averaged isotopic composition of the south Tibetan (Lhasa terrane) crust.

The evolved Daggyai Tso dykes have lower incompatible element concentrations than mafic lavas and dykes (Figure 4.3). This precludes an origin by fractionation of the mafic melts, suggesting a more complex, dominantly crustal origin, as has been invoked for dacitic flows from the Xungba area (Figure 4.1) of southern Tibet (Miller et al., 1999).

4.4.3 Implications for geodynamic models

Dykes are unambiguous indicators of extension and demonstrate that regional east-west extension and mantle magmatism in southern Tibet were genetically related. In agreement with previous work on the chemistry of post collisional lavas in southern Tibet (Miller et al., 1999), the dykes are inferred to be derived from small degree melting of an incompatible element enriched source within the SCLM. Such small-degree melts may migrate from source depths of ~ 100 to 150 km to the surface in << 1 Ma (Spera, 1987; Asmerom et al., 2000; Kelley and Wartho, 2000) and therefore mafic dyke emplacement from 18.3 ± 2.7 Ma to 13.3 ± 0.8 Ma effectively records the time of lithospheric mantle melting.

Decompression melting (McKenzie and Bickle, 1988) is commonly invoked to explain magmatism in extensional settings. However, the magnitude of extension in south Tibet, discussed above, is insufficient to cause melting of normal potential temperature mantle (McKenzie and Bickle, 1988) and another model for melt generation is required. (Kincaid and Silver (1996) suggested viscous shear heating as a means for generating small degree SCLM melts. However, heating and melting reduce viscosity and shear stress, limiting the

effectiveness of viscous heating to periods > 5 ka (Kameyama et al., 1999). As mantle magmatism spans > 12 Ma in S. Tibet (Figure 4.2) this mechanism is thought unlikely.

One plausible mechanism for attaining a thermally perturbed SCLM is the thinning and removal of lower SCLM following orogenic thickening (Houseman et al., 1981), or, as discussed in Chapter 5, following slab breakoff (Davies and von Blanckenburg, 1995). If the earliest phase of volcanism constrains thinning to be at least ~ 25 Ma within S. Tibet (Miller et al., 1999), then dyke emplacement ~ 8 Ma later suggests a delay between SCLM thinning and the onset of observable surface extension. Such a delay is consistent with the short timescales of melt migration (Spera, 1987; Asmerom et al., 2000) relative to those of isostatic and thermal re-equilibration of the lithosphere. Therefore, it is plausible that the onset of extension, constrained by the oldest dykes to be 18.3 ± 2.7 Ma, equals or post-dates the time at which southern Tibet achieved excess potential energy and high elevation. If the emplacement of northwest-southeast trending shoshonitic dykes in the northern Karakoram at 22 ±1.0 to 24.0 ± 1.0 Ma (Rex et al., 1988; Pognante, 1990) is related to the same strain field as the southern Tibetan dykes, then the onset of east-west extension may have been even earlier. Excess potential energy relating to plateau uplift may even have been achieved before 25 Ma in S. Tibet, when the first mafic lavas appeared (Figure 4.2).

The significance of spatial-temporal variations in magmatism across the entire plateau is more equivocal, as the prevailing stress regime at the time of volcanism in these regions is generally unknown. If volcanism and extension in northern and eastern Tibet (Turner et al., 1996; Chung et al., 1998, Bi et al., 1999; Yin et al., 1999) is interpreted in similar terms, the implication is that SCLM thinning beneath Tibet was a more diachronous and localised process than previously envisaged, conceivably triggered by different events at different

times. The processes that trigger SCLM thinning are still poorly understood, and extensive re-assessment of existing geodynamic models may be necessary.

While relating extension to uplift is controversial, the timing of dyke emplacement in southern Tibet is consistent with $\delta^{18}O$ data for sediments in the Thakkola graben of Nepal (Figure 4.1), which show that significant elevation was attained prior to extension (Garzione et al., 2000). The exhumation of the Gangdese Batholith between 17 and 20 Ma (Copeland et al., 1987) and molasse deposition following enhanced denudation from 19 to 20 Ma (Harrison et al., 1993) support the attainment of significant elevation in southern Tibet prior to 18.3 ± 2.7 Ma. Near synchronous movement on the main Himalayan fault systems at ~ 17-25 Ma, is consistent with the southward extrusion of a crustal wedge from the orogenic region in response to an increased potential energy contrast at the southern margin of the plateau (Platt and England, 1994; Grujic et al., 1996; Hodges, 2000).

Moreover, uplift of the southern margin of the plateau may have intensified the Asian monsoon (Kutzbach et al., 1989), enhancing silicate weathering rates resulting in the elevation of seawater $^{87}Sr/^{86}Sr$ (Palmer and Elderfield, 1985). Hence the increase in marine $^{87}Sr/^{86}Sr$ at 15-20 Ma (Richter et al., 1992) is also consistent with uplift of S. Tibet by 18.3 ± 2.7 Ma. Later intensification of the monsoon at 6 to 8 Ma (Molnar et al., 1993) may reflect diachronous and/or episodic increases in the elevation of the Himalayan-Tibetan region. If so, modification of models which link Cenozoic climate change to the uplift of high plateaus (Harrison et al., 1993; Molnar et al., 1993) may be required.

4.5 Summary

Post-collisional, shoshonitic dykes in the Lhasa Terrane reflect melting of Tibetan SCLM and crustal extension, probably following localised thinning and removal of the lower SCLM. These observations are inconsistent with models that relate the extension and uplift of S. Tibet purely to plate boundary forces. The initiation of extension is constrained by the earliest phase of dyke emplacement at to be at least 18.3 ± 2.7 Ma. Although the data does not shed light on more recent changes in plateau elevation, they do suggest that by the Early Miocene, southern Tibet had been elevated to a level unsustainable by convergent boundary forces.

5 Geochemistry of Post-collisional, High K magmatism in Tibet: Lithospheric mantle evolution during orogenesis

Potassic magmatism can be regarded as the surface expression of changes in the thermal state of the SCLM. This chapter presents new geochronological, geochemical and petrographic data obtained for post-collisional magmatism in northern and southern Tibet, which is discussed in the context of available literature data. The data are examined in terms of identifying and comparing the nature of the different melting regimes, mineralogy, composition and evolution of the mantle source regions beneath the Tibetan plateau. This Chapter builds on the issues introduced in Chapters 2 and 4, and aims to provide constraints on the evolution and stability of the Tibetan SCLM during subduction and orogenesis.

5.1 Introduction

Mafic potassic magmas generally show enriched incompatible element signatures compared to basalts derived from melting of anhydrous peridotite sources, and have isotopic signatures that indicate the ancient isolation of their source regions from the depleted mantle reservoir. While these isotopic signatures can be broadly similar to those of average continental crust (Taylor and McLennan, 1985), the absolute abundances of incompatible elements in potassic magmas are several orders of magnitude greater than crustal values. Therefore, crustal

melting, or the mixing of asthenosphere and crustally derived melts, cannot easily explain the chemical and isotopic compositions of ultrapotassic magmas. Xenoliths of metasomatised sub-continental lithospheric mantle (SCLM) sampled by ultrapotassic magmas and kimberlites (Group II) have enriched Sr-Nd-Pb isotopic and trace element signatures, distinct from both the convecting mantle and average continental crust (Menzies et al., 1987). Consequently, potassic magmas are largely considered to reflect small-degree melting of enriched, previously metasomatised regions within the sub-continental lithospheric mantle (SCLM).

The parameterisation of McKenzie and Bickle (1988) demonstrates that the decompression melting of the asthenosphere will only occur in rare circumstances, under conditions of major extension ($\beta>2$), where the crustal lid is < 50 km thick, for potential temperatures >1280°C. Therefore, other processes and geodynamic situations have been invoked to explain the petrogenesis of small-volume potassic volcanism and the melting of the SCLM. These include active subduction settings such as Fiji (Rogers and Setterfield, 1994) where high-K magmatism has been related directly to subduction processes and/or to back-arc extension. Potassic and ultrapotassic magmas may be produced in intracontinental rift settings such as the Virunga province of eastern Africa (Rogers et al., 1998) and southeast Brazil (Gibson et al., 1995) where the impact of the mantle plume with the base of the SCLM results in conductive heating and small degree melting. Small-volume potassic magmatism is also found in continental collision settings following ocean-basin closure. Much of the Neogene-Quartenary potassic volcanism of the Mediterranean region, including the Roman province of Italy (Keller, 1983) and the lamproites of southeast Spain (Venturelli et al., 1984a), are attributed to such a setting. In the Basin and Range province of the western USA, small-volume potassic and ultrapotassic magmatism pre-dates regional

extension (Hawkesworth et al., 1995). The genesis of the high-K magmas and their association with later extension and asthenosphere-derived magmatism in the Basin and Range were explained in terms of the convective removal of part of the SCLM (Houseman et al., 1981). This association of high-K magmatism and extension typifies the late magmatic history of many high plateaus formed as a result of continental collision. These include the Basin and Range province, the Bolivian Altiplano (Allmendinger et al., 1997), the Betic Cordillera (Turner et al., 1998), and the Tibetan Plateau (Turner et al., 1993; Turner et al., 1996; Miller et al., 1999). The common occurrence of high-K magmatism in these settings suggests that SCLM melting is an integral consequence of the geodynamic processes that produce high plateaus. Detailed geochemical studies of high-K magma suites from these setting therefore have the potential to place constraints on the nature, evolution, and role of the SCLM in the geodynamic processes which drive plateau formation.

5.2 Samples and petrography

Eruptive centres and volcanic units across Tibet (Figure 5.1) show variable morphology, ranging from cinder cones and pyroclastic deposits in the northwestern regions of the plateau (Liu and Maimaiti, 1989; Wanming, 1991; Arnaud et al., 1992) to complex sequences of flows, pyroclastic deposits and dykes (Coulon et al., 1986; Arnaud, 1992; Turner et al., 1996; Miller et al., 1999) in the southern regions. Volcanics are undeformed and, in some localities (such as the Neogene Namling basin), intercalated with clastic sediments. The total volume of post-collisional magmatism across the plateau is unknown, but appears surprisingly large in individual localities, ranging from 200 to 300 km^3 for centres in northwest Tibet (Liu and Maimaiti, 1989; Wanming, 1991; Tait, pers comm) and

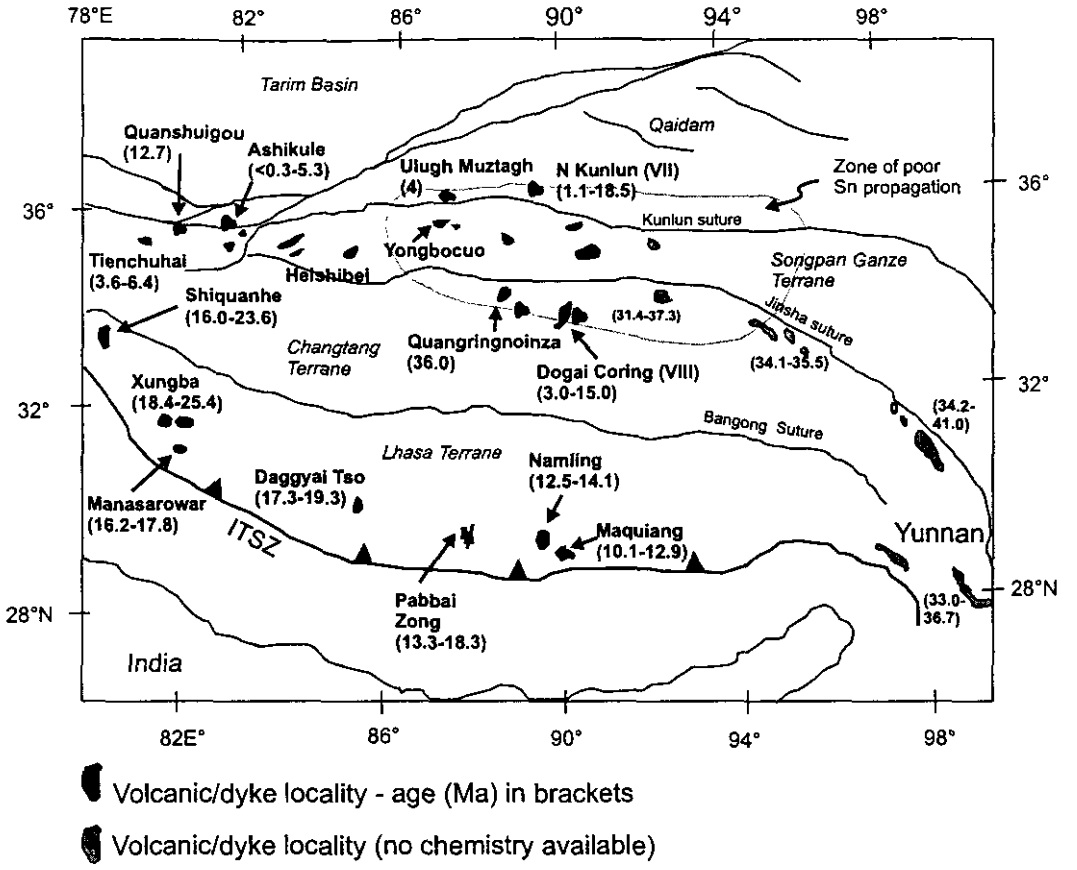

Figure 5.1 Volcanic rock and xenolith localities on the Tibetan Plateau

Presently know volcanic localities with Ar-Ar ages in brackets (Coulon et al., 1986; Liu and Maimaiti, 1989; Wanming, 1991; Arnaud, 1992; Arnaud et al., 1992; Turner et al., 1993; Turner et al., 1996; Wanming, 1997; Chung et al., 1998; Miller et al., 1999). Also shown are the positions of the major sutures that divide the plateau into its composite lithospheric terranes (Dewey et al., 1988), discussed in Chapter 2 and the region of poor Sn attenuation and elevated Poisson's ratio (McNamura et al., 1997; Owens, 1997).

80 to 120 km^3 for individual localitites in southwest Tibet (Schuster, pers comm.). Most samples are Miocene in age, ranging from 10.1 ± 0.2 to 25.4 ± 0.2 Ma in the south and 36.7 ± 0.3 Ma to the present day in the north (Figure 5.1; data sources in caption). The oldest known magmas are in the eastern regions of the plateau, where ^{40}Ar-^{39}Ar ages of 30.0 ± 1.1 to 36.7 ± 0.3 Ma have been obtained (Chung et al., 1998). While the petrogenesis of potassic magmas in northern and southern regions of the plateau has been discussed by Turner et al. (1996) and Miller et al. (1999), respectively, no systematic comparisons of the geochemical characteristics of the northern and southern magma suites presently exist in the literature.

In this chapter, new ^{40}Ar-^{39}Ar ages (Table 5.1), isotope and geochemical data (whole rock major and trace element compositions, electron microprobe data) are presented for northern and southern Tibetan samples. The full datasets are given in in Appendices B (^{40}Ar-^{39}Ar data) and C (geochemical data); additional sample descriptions and location information is given in Appendix A. Southern Tibetan samples were collected by the author in 1998 and by J. Platt in 1995 and include the Pabbai Zong and Daggyai Tso dykes discussed in Chapter 4. Samples from the collections of Arnaud (1992); Arnaud et al., (1992) and Turner et al. (1996) were re-analysed for trace element and REE concentrations by ICPMS, and additional Sr, Nd and Pb isotope analyses were carried out on selected samples. New isotope data are presented for samples from the collections of Pearce and Houjun (1988) and Wanming (1991) which were also re-analysed for trace element compositions by ICPMS at the University of Durham (J. Pearce, pers. comm.). Samples from the volcanic suites discussed in (Hacker et al., 2000) were analysed for Sr and Nd isotopes and for trace elements by ICPMS; the major element compositions of these samples were determined by XRF at the University of Bern (E. Gnos, pers. comm.). Sample petrography and localities

are detailed in Appendix A. Combined with the data of Miller et al. (1999) for southwest Tibet, the sample collection discussed here, which includes samples derived from the three major lithospheric terranes (Lhasa, Changtang and Songpan-Ganze) of Tibet (Figure 4.1), is probably one of the most comprehensive currently in existence.

Mafic lavas from the northern regions of the plateau (Figure 5.1) display variable mineralogical and textural characteristics (Wanming, 1991; Turner et al., 1996; Hacker et al., 2000) but nonetheless show some common features. The more mafic samples include the Tienchuhai lavas (Arnaud et al., 1992) and the less evolved lavas from the Dogai Coring area (zone VIII; Turner et al., 1996) are characterised by the presence of olivine, orthopyroxene, clinopyroxene and rare biotite phenocysts in a microcrystalline matrix consisting primarily of feldspar and opaques (Figure 5.2 A). More silicic samples have phenocrysts of alkali feldspar and biotite, and in some cases flourinated phlogopite and hornblende (Hacker et al., 2000). Phlogopites from all the northern samples all show signs of extensive resorbtion: embayed margins and thick oxide rims. The 36 Ma Quangringnoinza suite (^{40}Ar-^{39}Ar age on sanidine, Hacker pers. comm.) contains phenocrysts of biotite, hornblende, quartz and sanidine in a microcrystalline matrix (Figure 5.2 B).

The petrography of the southern volcanics and dykes (Chapter 4, localities in Figure 5.1) is variable, (e.g. Coulon et al., 1986; Miller et al., 1999). Mafic lava flows exposed at Shiquanhe (JPT24A-C) show similar mineralogical and textural features to the ultrapotassic lavas of Miller et al. (1999). The Shiquanhe lavas contain abundant megacrysts of phlogopite and aggregates of clinopyroxene and rarer orthopyroxene within a microcrystalline (sanidine, titanian-phlogopite, Fe-Ti oxides, apatite, glass) groundmass

Table 5.1 ^{40}Ar-^{39}Ar ages for southern and northern Tibetan lavas

Sample	lithology	rock type	min	No. of points	MSWD	Age (Ma)	± 2σ	$^{40}Ar/^{36}Ar$	± 2σ
SOUTHERN TIBET									
Namling Basin									
JPT 3*	**flow**	**dacite**	**bi**	**9 of 9**	**1.34**	**13.9**	**0.1**	**295.5**	-
JPT 3	flow	dacite	bi	9 of 9	1.39	14.0	0.2	289	0
JPT 5.2*	**flow**	**dacite**	**bi**	**8 of 8**	**2.52**	**12.5**	**0.3**	**295.5**	-
JPT 5.2		dacite	bi	8 of 8	2.58	10.7	7.4	756	3895
JPT 8	**flow**	**rhyolite**	**bi**	**10 of 10**	**5.41**	**13.8**	**4.6**	**1178**	**144.2318**
Daggyai Tso									
JPT 14.1*	***flow***	***dacite***	***phl***	***14 of 14***	***5.91***	***18.8***	***0.5***	***295.5***	-
JPT 14.1		dacite	phl	14 of 14	5.27	14.6	4.6	738	472
Shiquanhe									
JPT 24C*	flow	shoshonite	phl	12 of 12	1.41	24.6	0.1	295.5	-
JPT24C		**shoshonite**	**phl**	12 of 12	**1.39**	**24.0**	**1.0**	**369**	**116.8**
JPT24B*	flow	shoshonite	phl	9 of 9	1.30	25.0	0.6	295.5	-
JPT24B		**shoshonite**	**phl**	**9 of 9**	**1.25**	**22.3**	**4.7**	**408**	**205.3**
JPT 23	**agglomerate**	**shoshonite**	**phl**	**minimum of 7**		**21.2**	**0.6**	**295.5**	-
NORTHERN TIBET									
Quianshuigou									
Bb124*	lava flow	shoshonite	phl	7 of 7	0.7	12.4	2.3	295.5	-
Bb124			**phl**	**7 of 7**	**0.8**	**12.8**	**2.2**	**289**	127
Ashikule									
Norin 1105			**WR**	**minimum of 8**	**1.2**	**5.0**	**0.5**	**295.5**	
Norin 912			**WR**	**minimum of 10**	**1.2**	**2.7**	**1.8**	**295.5**	

phl, phlogopite; bi, biotite; WR, whole-rock

bold typeface indicates the age most appropriate to attribute to the sample

* *regression forced through atmospheric argon*

In the case of isochron ages, the errors are calculated from equation 3.3, and are multiplied by the square root of the MSWD, where the latter is greater than 2.5
For samples Norin 1105 and Norin 912, a minimum age from the individual crystal fusions is presented. This age is calculated assuming that any initial argon present was atmospheric in composition; the errors on the ages were calculated using equation 3.2.

(Figure 5.2 C and D). Phlogopites are mantled by thick rims of Fe-Ti oxide and microcrystalline clinopyroxene, and contain rare inclusions of apatite, zircon and Fe-Ti oxides. Some of the phlogopite megacrysts show undulose extinction and kink banding. Phlogopites show a wide range in compositions; they have Mg#'s of 72-89, F contents of 0.1 to 5.2 wt%, and Ni contents of 53 to 163 ppm. Clinopyroxene-orthopyroxene aggregates are similarly magnesian, with Mg#'s of 79-89 (clinopyroxene) and 79-91 (orthopyroxene) and are rimmed by a second generation of microcrystalline clinopyroxene (Figure 5.2 D). The latter observation indicates that these aggregates are not in equilibrium with the groundmass, implying a xenocrystic origin. Phlogopite and Fe-Ti oxides (ilmentite-titanian-magnetite) are occasionally observed within these aggregates; phlogopites contained within the pyroxene aggregates are largely unaltered and do not display the prominent reaction rims of the groundmass phlogopites (Figure 5.2 D). Olivine is present only in a highly resorbed state, where it has been replaced by serpentinite and carbonate-rich alteration products. The Pabbai Zong glimmerite dykes (discussed in Chapter 4) have > 40 modal % phlogopite phenocrysts (Mg#'s 68 to 94; F 0.1 to 0.8 wt%; Ni 10 to 479 ppm), subordinate clinopyoxene within a microcrystalline matrix consisting of phlogopite, alkali feldspar, Fe-Ti oxides, apatite, secondary chlorite and clay mineral alteration products (Figure 5.2 E). Note that all estimates of mineral modal abundance are based on visual counting. Phlogopites contain inclusions of ilmentite and titanian-magnetite, clinopyroxene (Mg#'s 87 to 88), Na-amphibole (magnesian riebeckite; Mg#'s 52 to 63; Na/Na+Ca, 0.81 to 0.85) rare zircon and F-apatite. Sample T3B contains abundant euhedral garnet megacrysts. Dacitic and rhyolitic lavas and dykes at Daggyai Tso and Namling contain phenocrysts of K-feldspar, plagioclase, quartz ± hornblende ± biotite, in either a glass or a microcrystalline matrix of quartz and feldspar with minor Fe-Ti oxides (Figure 5.2 F).

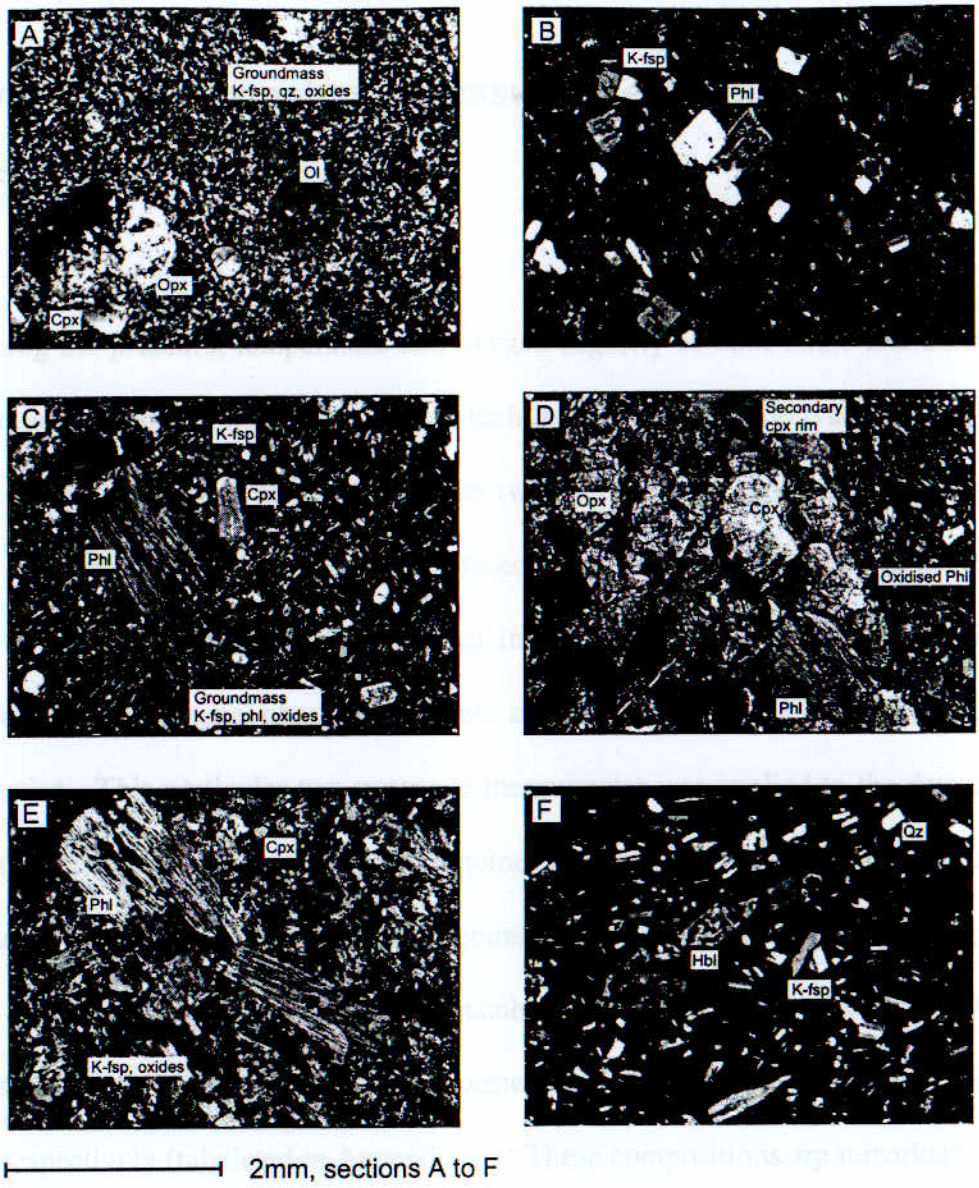

Figure 5.2 Photomicrographs of selected northern and southern Tibetan samples

A) mafic lava from the Tienchuhai locality (sample K89G187), the rock contains phenocrysts of orthopyroxene, clinopyroxene and olivine in a microcrystalline matric consisting predominantly of feldspar, quartz and opaques. B) Dacitic lava flow (11H10-4) from Dogai Coring containing phenocrysts of biotite and K-feldspar in a microcrystalline matrix of feldspar, biotite, quartz and opaques C) JPT24A has phenocrysts and megacrysts of phlogopite, clinopyroxene and orthopyroxnene (megacrysts of opx and cpx are not seen in this field of view); D) Aggregate of clinopyroxene, orthopyroxene in JPT24C. Phlogopites included in these aggregates are markedly less oxidised that groundmass phlogopites; E) glimmerite dyke T4A consists of > 40 % modal phlogopite, with subordinate K-feldspar, clinopyroxene, apatite and opaques; F) Dacite dyke JPT14.2 has phenocrysts of hornblende, K-feldspar, and quartz with minor Fe-Ti oxides in a glassy matrix.

5.2.1 Intensive parameters: Pressure, Temperature and Oxygen Fugacity

Determining the pressure, temperature and oxygen fugacity of both mafic and silicic melts can potentially constrain the sources from which these melts were derived, and the thermal structure of the lithosphere at that time. The two pyroxene thermometer (Lindsley, 1983; Lindsley and Andersen, 1983) may be used to constrain the temperature range at which co-existing ortho- and clinopyroxenes were last in equilibrium with each other, or in cases where only one pyroxene phase is present, a minimum temperature for the onset of crystallisation. This particular two-pyroxene thermometer was applied to the data obtained in this study as the calibration of the thermometer takes the effects of pressure and non-quadrilateral pyroxene components into account (i.e. the thermometer is not restricted to pure Ca-Mg-Fe pyroxenes). For the Shiquanhe lavas (JPT24A-C) the compositions of megacrystic clinopyroxenes and orthopyroxenes are $En_{36-54}Fs_{6-19}Wo_{39-47}$ and $En_{67-90}Fs_{9-31}Wo_{1-7}$, respectively (tabulated in Appendix C). These compositions are remarkably similar to those obtained for pyroxene megacrysts in ultrapotassic volcanics from the Xungba area of southwest Tibet (Miller et al., 1999), and give minimum (based on the calibration of this geothermometer at 1 atm pressure; temperature estimates increase with the pressure of equilibriation assumed) equilibration temperatures of 800 to 1275°C (details in Appendix C). The lowest temperatures correspond to the most iron-rich compositions. Assumption of higher pressures correspondingly increases the estimated temperatures to 1050-1400°C (1.5 GPa); the majority of temperatures cluster around 1100-1150°C. The very high temperatures were obtained from unusually calcium-rich orthopyroxenes. However, the two

pyroxene thermometer (Lindsley and Andersen, 1983) is extremely sensitive to the calcium contents of orthopyroxene: a 2 % increase in the value of the Wo endmember can increase the estimated temperature by 1000°C. Therefore, the uncertainties on the estimated temperatures are likely to be in considerable excess of the blanket error value of 50°C quoted by (Lindsley and Andersen, 1983). Nonetheless, the majority of clinopyroxene-orthopyroxene temperatures are either on, or well above the hydrated peridotite solidus (Wallace and Green, 1991). Pabbai Zong dykes have similar clinopyroxene compositions: $En_{49-51}Fs_7Wo_{42-45}$ (sample T2A) and $En_{48-54}Fs_{6-9}Wo_{41-45}$ (T4C), which in the absence of co-existing orthopyroxene suggest broadly similar temperatures. Pyroxene compositions and calculated temperatures are given in Appendix C. Pyroxenes from the Dogai Coring samples are more iron-rich, implying lower temperatures of 1000°C (0.1 GPa) to 1100°C (1.5 GPa) (Turner et al., 1996). Given the high degree of uncerainty on temperature estimates, which is likely to be in excess of 100°C, it appears that the different volcanic suites were emplaced at broadly similar temperature ranges. The higher temperatures obtained for some orthopyroxene megacrysts could indicate a xenolithic origin for these crystals, where their major element chemistry was not "reset" (or rehomogenised) by the later melting event which ultimately resulted in surface volcanism.

Constraints on the temperature and oxygen fugacity of emplaced lavas and dykes can be obtained using co-existing Fe-Ti oxides and the thermodynamic formulation of Ghiorso and Sack (1991). Calculated temperatures range from 830 to 1000°C for the Shiquanhe lavas (4 oxide pairs) and Pabbai Zong dykes (T3B, 2 pairs), 800 to 1050°C for the Dogai Coring lavas (K9032, 6 pairs), and 830 to 900°C for a silicic dyke (T11B, 3 pairs) exposed in the Daggyai Tso graben. Fe-Ti oxide compositions, calculated temperatures and fugacities are given in Appendix C. The discrepancy between pyroxene and Fe-Ti temperature constraints

in the Shiquanhe samples is consistent with textural criteria that suggest a xenocrystic origin for the pyroxenes.

The corresponding Fe-Ti oxygen fugacities for these samples, quoted in log units relative to the QFM buffer are: - 0.4 to + 0.5 for Shiquanhe, - 4.1 to – 0.3 for Dogai Coring and + 2.1 to + 2.9 for Daggyai Tso. Fe-Ti oxide pairs included within phlogopite megacrysts in the Pabbai Zong glimmerites give much higher oxygen fugacites: + 9.7 relative to QFM. Fe-Ti oxide temperature estimates calculated for T11B are somewhat lower than the minimum melting temperatures calculated for this sample (680 to 730°C) using zircon and monazite saturation thermometers (Watson and Harrison, 1983; Montel, 1993). This may reflect late re-equilibration of Fe-Ti oxide phases. Zircon and monazite saturation temperatures for silicic volcanics at Namling, Daggyai Tso and Manassarowar (calculated from the data in (Miller et al., 1999)) are 700 to 800°C.

Obtaining unambiguous constraints on the pressures of melt generation and/or the onset of crystallisation using mineral chemistry is difficult as the lack of glass data precludes the use of mineral-melt equilibria. The aluminium in horneblende barometer (Johnson and Rutherford, 1989; Schmidt, 1992) calibrated for rhyolitic to dacitic systems: for the Daggyai Tso samples (T11B, JPT14.2), this gives pressures of 0.6 to 0.8 GPa using the calibration of Schmidt (1992), and slightly lower pressures of 0.4 to 0.7 GPa with that of Johnson and Rutherford (1989). The implications of these constraints on for the thermal structure of the Tibetan lithosphere are discussed further in Section 5.6.2.

5.3 Whole rock Geochemistry

New major and trace element data for northern and southern samples are presented and discussed in the context of existing published data (Turner et al., 1996 and references therein; Miller et al., 1999). Samples were analysed for major and trace element abundances by XRF spectrometry at the Open University, and at the University of Bern by E. Gnos. ICP-MS trace element data are presented for the majority of samples studied; this was undertaken at Durham University with C. Ottley and J. Pearce. Sr, Nd and Pb isotope analyses were carried out at the Open University. Full datasets are presented in Appendix C, analytical details in Appendix D.

5.3.1 Major element chemistry and classification

The samples analysed in this study have SiO_2 contents ranging from 51.7 to 78.3 wt% for the southern groups and 45.3 to 75.5 wt% for the northern sub-groups, excluding the 20-26 Ma Quangringnoinza lavas, which are considerably older than the other samples discussed here. MgO abundances for the northern and southern sub-groups range from 0.04 to 7.9 wt% and 0.3 to 11.5 wt%, respectively; corresponding Mg #'s range from 27 to 78 for the south (mean 54, n = 44) and 22 to 81 in the north (mean 43, n=65). Given that partial melts in equilibrium with mantle olivine (Fo_{90}) are characterised by Mg#'s of ~73, it is clear that only the least evolved rocks approach primary mantle melts. Two classification diagrams show the general nature of the post-collisional magmatism in the northern and southern regions of the plateau: on total alkalis-silica plots (Le Maitre et al., 1989) the

majority of samples from the both northern and southern sub-groups plot above the alkali-tholeiite divide (Figure 5.3, A and B). Northern samples plot in the basaltic trachyandesite, trachyandesite and trachyte fields; the southern sub-groups show a similar trend, although they are displaced to higher SiO_2. On the plots of K_2O against SiO_2 (Figure 5.4, A and B), it is apparent that the majority of the northern and southern sub-groups are shoshonitic, with the southern sub-groups consistently elevated to higher K_2O contents for a given SiO_2 content. The relatively flat arrays of samples with $SiO_2 < 62$ wt% suggests buffering of K_2O by either melting of fractionation of a K-bearing phase such as amphibole or phlogopite. If the flat arrays are interpreted in terms of melting, then they imply the presence of residual K phases in the mantle source region itself (e.g. Turner et al., 1996). Evolved samples in both northern and southern sub-groups generally have lower K_2O contents and fall in the high-K calc alkaline field.

Major element variations against MgO suggest broad differences between the northern and southern groups, as shown in Figure 5.5 A to D, for Fe_2O_3 and TiO_2. Fe_2O_3 correlates positively with MgO in both the northern and southern groups (Figure 5.5, A and B), however, the southern sub-groups have lower F_2O_3 contents at a given value of MgO (1.1 to 7.5wt %) compared to the northern groups (wt % Fe_2O_3 1.0 to 10.9 wt %). Similarly, TiO_2 (Figure 5.5, C and D) correlates positively with MgO in both groups, although the southern groups are displaced to low TiO_2 (0.1 to 1.4 wt %) compared to the northern samples (0.1 to 2.3 wt %). Interestingly, the older Quangringnoinza lavas have lower Fe_2O_3 and TiO_2 contents than the other northern samples. In all sub-groups, Al_2O_3 is negatively correlated with MgO and there are no clear relationships between Na_2O and MgO. P_2O_5 is positively correlated with MgO in the southern samples, implying apatite fractionation.

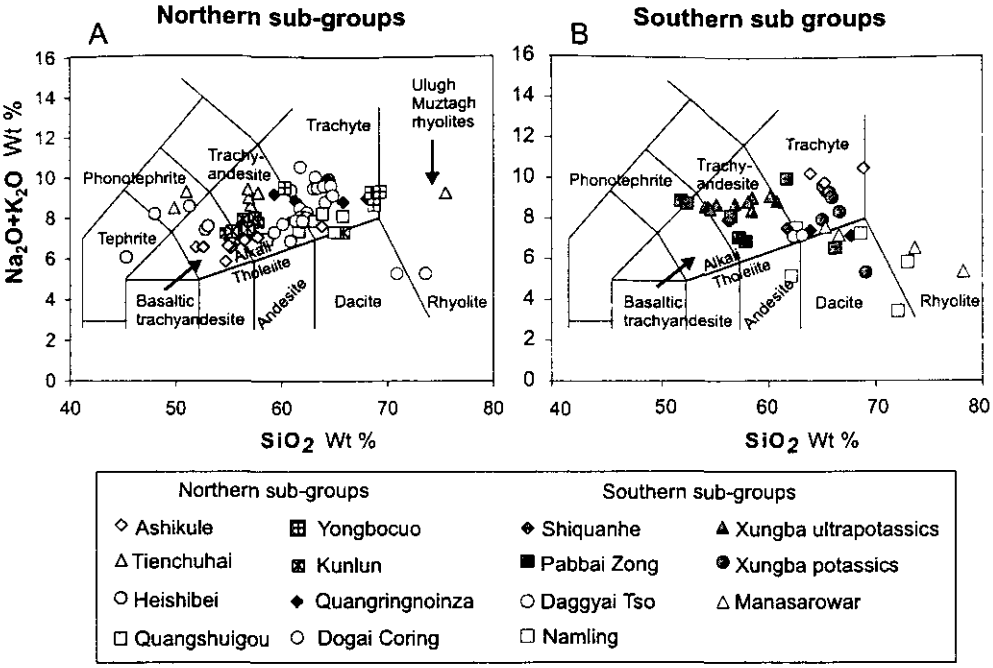

Figure 5.3 Classification the northern and southern Tibetan volcanic subgroups using the total alkalis-silica system (Le Maitre et al., 1989).

Sub-group names correspond to localities in Figure 5.1. The majority of samples may be described as trachyandesites or trachytes on this basis, although there is considerable scatter. Data: this study, Turner et al. (1996); Miller et al. (1999); Gnos (pers comm).

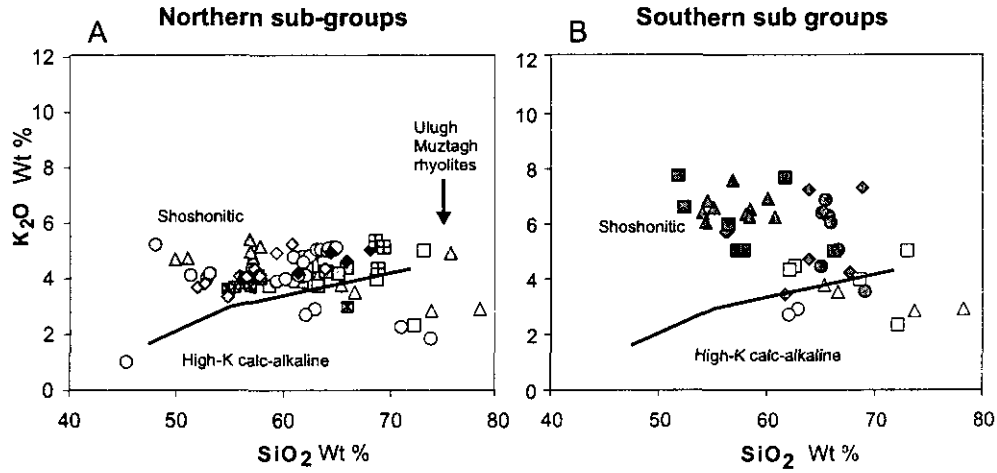

Figure 5.4 K_2O - SiO_2 for northern and southern Tibetan volcanic subgroups

Key as for Figure 5.3. K_2O is nearly invariant both within and between subgroups from the northern (A) and southern regions (B) of the plateau, although the more silicic southern sub groups (Manasarowar, Daggyai Tso and Namling) have lower K_2O contents. On this basis, the silicic magmas are best termed high K calc alkaline, the less evolved northern and southern samples shoshonitic. Data: this study, Turner et al. (1996); Miller et al. (1999); Gnos (pers comm).

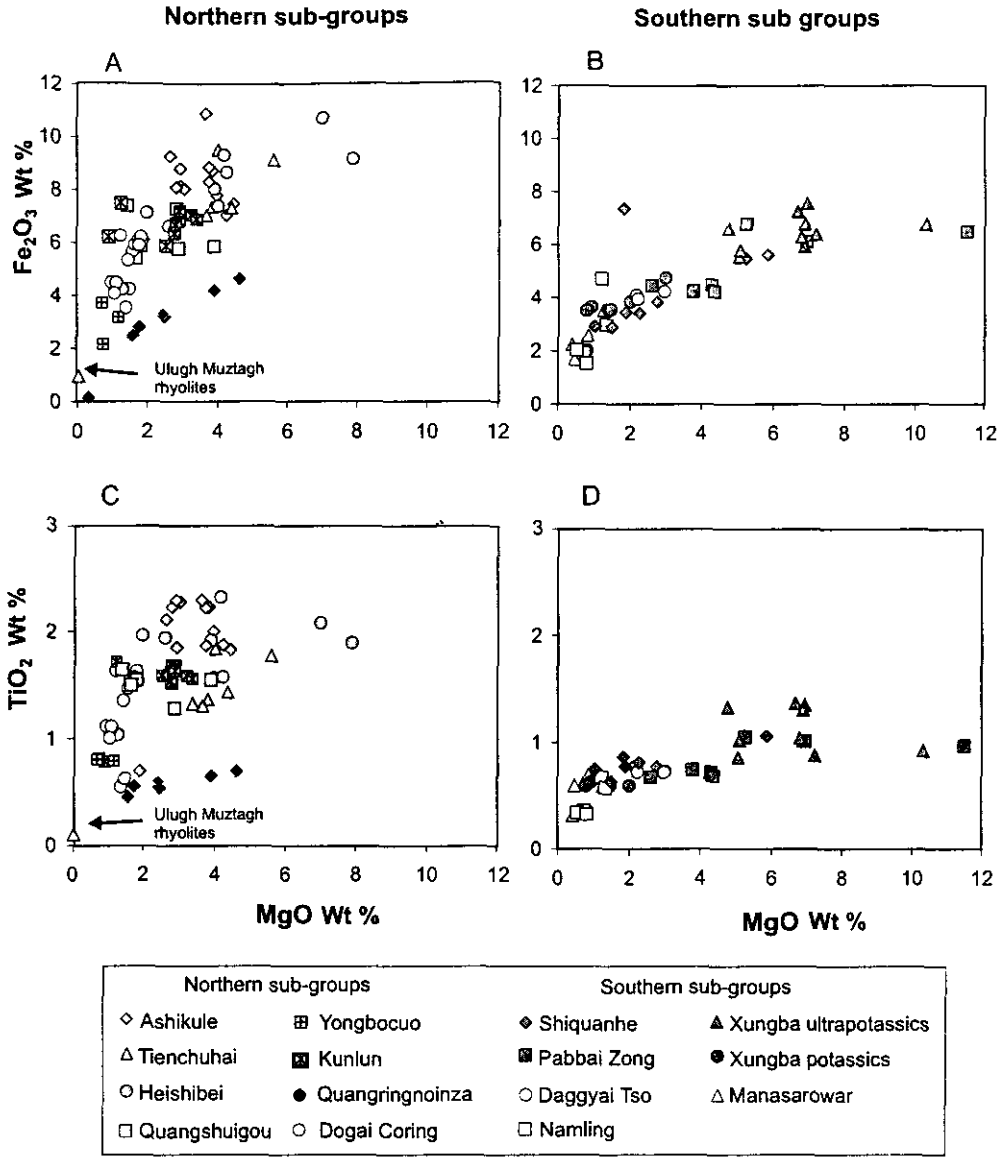

Figure 5.5 Variation of Fe_2O_3 and TiO_2 against MgO for the northern and southern volcanic subgroups

Note the high Fe_2O_3 and TiO_2 concentrations of the northern samples (A and C) relative to southern samples (B and D) at comparable MgO values. Subgroup names and locations as in Figure 5.1. Data: this study, Turner et al. (1996); Miller et al. (1999); Gnos (pers comm).

The southern lavas have lower concentrations of CaO compared to the north (south 0.4 to 7.5 wt %; north 0.6 to 10.7 wt %), higher MgO (south 0.3 to 11.5 wt %; north 0.04 to 7.9 wt %), SiO_2 (south, 51.7 to 78.3 wt %; north 45.3 to 75.5 wt %) and higher concentrations of elements compatible in mafic phases (e.g. olivine, clinopyroxene and phlogopite): Ni (south 0.4 to 649 ppm; 1 to 126 ppm), Cr (south 0.8 to 466 ppm; north 3.4 to 258 ppm). Large-scale variations between the northern and southern volcanic series dominate minor variations between individual sub-groups; the latter probably reflect compositional variation in source composition, differences in conditions and timescales of magma residence, or fractionation and assimilation of local basement. The broad contrasts in major element chemistry between the northern and southern shoshonite series suggest fundamental differences in melting regime and source region between the two groups. In order to further elucidate contrasts in the petrogensis of the northern and southern Tibetan shoshonites, the following duscussion focusses largely on geochemical variations between, as opposed to within, these two major groups.

5.3.2 Trace element and Rare Earth Element Variations

Incompatible element concentrations of both northern and southern shoshonite suites are several orders of magnitude greater than average upper or lower continental crust (Taylor and McLennan, 1985) or melts of upper crustal pelites such as the Ulugh Muztagh rhyolites in northern Tibet (McKenna and Walker, 1990). In contrast, the more silicic southern series (Daggyai Tso, Namling and Manassarowar) have much lower incompatible element concentrations, approaching crustal values. In both northern and southern shoshonite groups, Sr and Ba are positively correlated with MgO (Figure 5.6 A, B). These arrays are

most easily interpreted in terms of alkali feldspar and mica fractionation. Both shoshonite series show little correlation between Nb and MgO (Figure 5.6 C), and between Ce, Nd and MgO in the case of the northern shoshonites (Figure 5.6 D and E). More surprising are the positive correlations of Ce and Nd (and the other LREE, not shown)with MgO (Figure 5.6 D and E) in the southern shoshonites. These trends cannot be easily explained by the assimilation of local basement as the arrays with MgO are, for the most part, elevated well above the compositions of possible assimilants. These positive arrays can be interpreted in terms of fractionation and melting processes, alternatively they may represent binary mixing between melts derived from compositionally distinct source regions. Comparing the behaviour of Ce and Cr in the southern shoshonites can test these hypothesis, as Cr also shows a positive relationship with MgO (Figure 5.6 F), yet is extremely compatible in mafic phases, in contrast to Ce. In Figure 5.7 A, Ce is not correlated with Cr, precluding simple binary mixing relationships. Therefore, the positive relationship of Ce (and Cr) with MgO must have originated through fractionation or melting, or some combination of these processes. In Figure 5.7 B, the influence of melting and AFC (Assimilation and Fractional

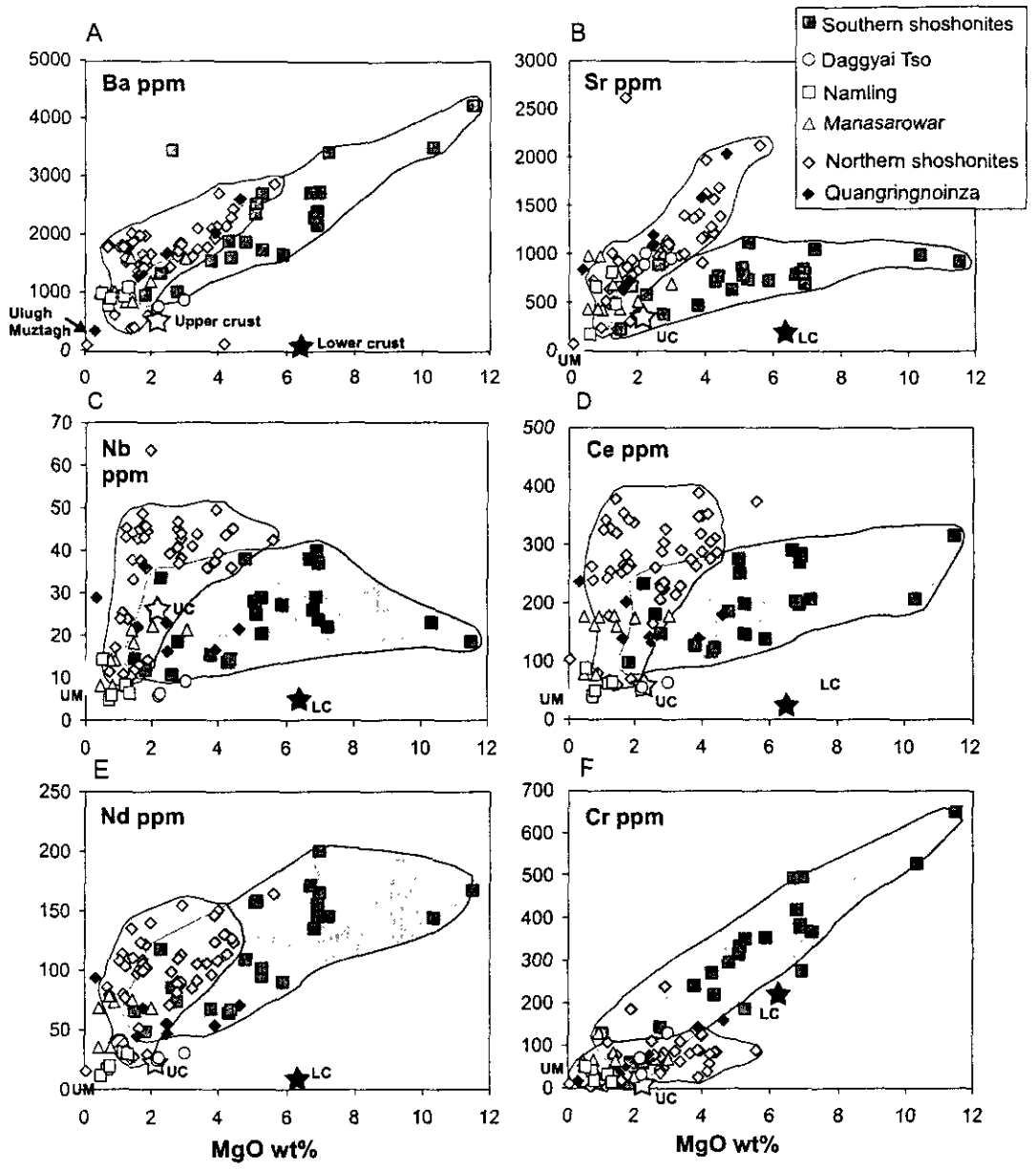

Figure 5.6 Trace element variations with MgO for the northern and southern volcanic subgroups

UC = average upper crust; LC = average lower crust (Taylor and McLennan, 1985); UM = Ulugh Mustagh rhyolites. For simplicity, magmas from the different northern and southern subgroups have been combined into two groups, with the exception of the 36 Ma Quangringnoinza samples and the silicic southern subgroups (Daggyai Tso, Namling, Manasarowar). Although data are scattered, clear trends can be distinguished for both northern and southern groups on these diagrams, with the southern group showing considerably more compositional variation. Data: this study, Turner et al. (1996); Miller et al. (1999); Gnos (pers comm).

Crystallisation (DePaolo, 1981) processes on Cr behaviour is investigated using simple models. For simplicity, Mg is treated as a trace element in these models, following Pearce and Parkinson (1993) who calculated partition coefficients for MgO based on the compositions of mineral phases and glass produced in peridotite melting experiments. The D values of Pearce and Parkinson (1993) for MgO and Cr are used here, D values for Ce are taken from Halliday et al. (1995). Although the behaviour of MgO is controlled by phase relationships, and undoubtedly more complex than allowed for in these models, its treatment here is simply for illustrative purposes, and not intended to be a rigorous description of its behaviour.

Figure 5.7 B demonstrates that the variation in Cr and MgO compositions of the southern shoshonites are most easily explained in terms of fractional crystallisation, as melting trends are essentially vertical, for small degrees of melting. The effects of assimilation are negligible, as can been seen from similarity of model curves using $R = 0.2$ and $R = 0.8$. This is a reflection of the high concentrations of this element in the mafic magmas, and its low abundance in the crust. Interestingly, the AFC curves indicate that a mafic endmember with Cr concentrations greater than either the glimmerite T2A or a small degree fertile peridotite melt is required to explain the Cr contents of the magmas. In Figure 5.7 C, AFC curves are essentially flat, except where $F > 0.4$. This is largely a function of the extremely high Ce concentrations in the magmas, and the low concentration of Ce in the assimilant. Given the short timescales of potassic melt emplacement (Spera, 1987; Kelley and Wartho, 2000), it is unlikely that the southern shoshonite magmas had such protracted fractionation histories in the crust. Therefore, AFC processes produce near horizontal trends on this diagram, explaining the variation in MgO, but not in Ce. However, variably small degrees of partial melting can easily generate considerable variation in the Ce compositions of the

resulting magmas, apparent in the near vertical trends of the model melt curves in Figure 5.7. The effects of melting processes in generating variation in Ce will be intensified for a heterogeneous source region. Therefore, while neither melting nor fractionation processes can generate the positive array of Ce with MgO, a combination of these processes can.

In order to address the nature of the source regions and melting regimes of both southern and northern shoshonites, the effects of fractionation on the major and trace element compositions of the magmas need to be distinguished from melting effects, and then removed as far as is possible. Fortunately, the near orthogonal relationships between fractionation and melting curves on incompatible element versus MgO plots (e.g. Figure 5.7 C) allow these two processes to be easily distinguished. In order to correct for fractionation, which has a relatively shallow slope, the trace element compositions of the more mafic lavas (MgO >3wt%) were normalised, where a linear trend was apparent, to 6wt% MgO. This approach is modified after that of Klein and Langmuir (1987) and Turner and Hawkesworth (1995) and involves extrapolating the concentrations of the element of interest back to 6wt % MgO by fitting linear least-squares regression lines to the northern and southern data arrays and using the slope of the regressed line to correct the data. A "model 3 fit" (McIntyre et al., 1966; Ludwig, 1999) was used – this assumes that the observed scatter is due to a combination of the assigned errors and an unknown, but normally distributed initial variation in their Y-values. As the melting trends are nearly vertical, this correction does not overprint differences in trace element concentrations arising from melting processes, or from

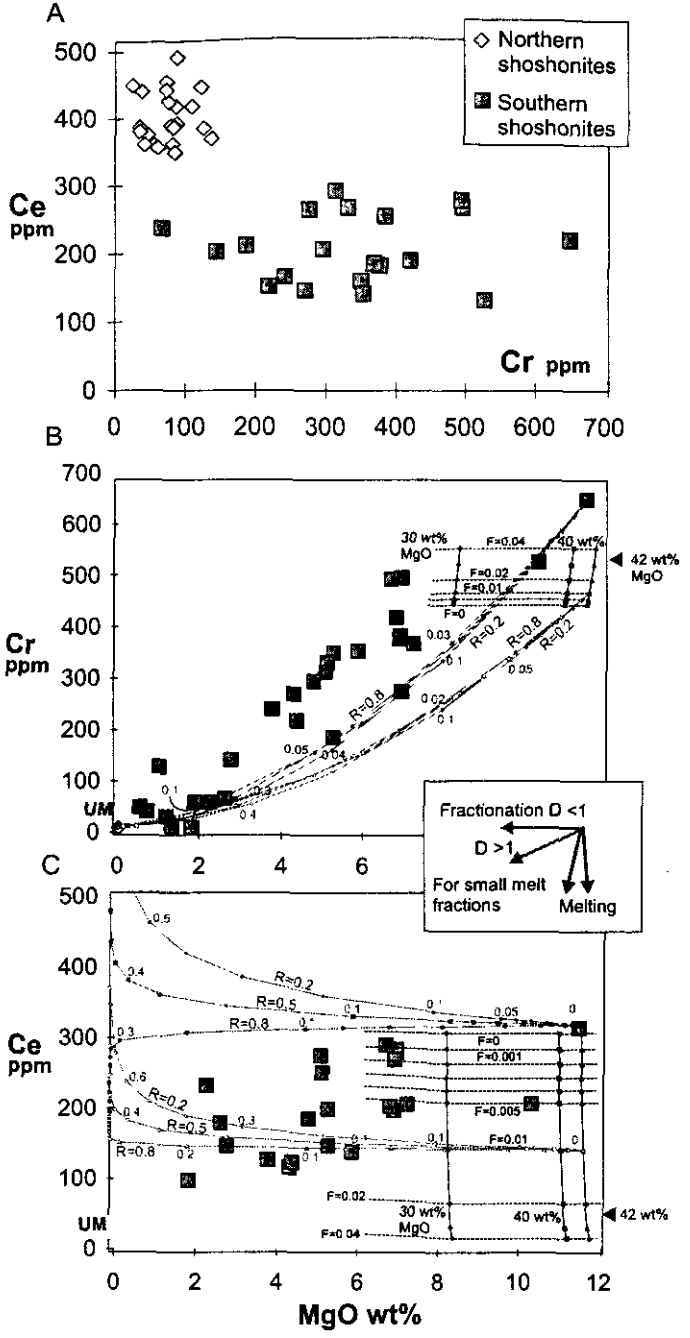

Figure 5.7 Behaviour of Ce and Cr with MgO in the southern and northern volcanic subgroups

A) variation of Ce with Cr in the southern and northern Tibetan shoshonites; the more evolved samples are not plotted. There is no evidence to support binary mixing in either group. B) Cr vs. MgO for the southern shoshonites. Non-modal modal fractional melting curves are shown for fertile peridotite sources with variable initial MgO contents, tick marks are degrees of melting, given the highly potassic nature of these rocks, only low degrees of meling are shown. AFC curves (pale grey lines) are shown using the glimmerite dyke T2A and a 1% melt of a fertile peridotite source (MgO = 42 wt%) as the mafic endmembers, in both cases the average composition of the Ulugh Muztagh rhyolites was taken as a proxy for the crustal assimilant. The AFC curves use three different values of R (the ratio of assimilation to crystal fractionation): 0.2, 0.5 and 0.8, to explore the effect of varying crustal assimilation. C) Ce vs. MgO, melting and AFC curves as for B). Note that for highly incompatible elements such as the LREE, the AFC curves are essentially flat, only showing large positive or negative deflections when there are very small fractions of remaining melt.

source heterogeneity. Only samples with MgO > 3 wt % were used in order to minimise errors resulting from over-extrapolation and to avoid problems associated with highly evolved samples which may have assimilated large amounts of crustal material. Although 6 wt % MgO is too low for the calculated compositions to be representative of primary magmas, this value is appropriate for the range shown by the available data, corrects for the majority of fractionation effects, and provides a common point for comparison of samples between, and within, the two magma groups. Given that crustal contamination is likely to accompany fractionation processes (DePaolo, 1981) it is reasonable to assume that extrapolation to 6 wt % MgO will also remove much of the effects of crustal assimilation.

The general incompatible element characteristics of the northern and southern magma sub-groups are illustrated in primitive mantle normalised (values from Sun and McDonough, 1989) multi-element diagrams and chondrite normalised (values from Nakamura, 1974) REE plots in Figure 5.8 (A, B) and Figure 5.8 (C, D), respectively. Trace element compositions were corrected to 6 wt% MgO (samples with > 3 wt% MgO only). Also shown are the more silicic magmas, with MgO < 3 wt%, which were excluded from the least-squares regressions. The patterns shown in Figures 5.8 re-iterate the LILE and REE enrichment of the northern and southern magmas relative to primitive mantle and chondritic values. HREE are less enriched: Yb is 6 to 14 times chondrite for the northern magmas, 6 to 12 for the southern group. The preferential enrichment in LREE and incompatible elements relative to the HREE in both groups is apparent in the steep slopes on the multi element diagrams and the sigmoidal patterns on the chondrite normalised plots. La_N/Yb_N (primitive mantle) ranges from 49 to 133 for the north and 18 to 63 for the south. Silicic southern sub-groups (Manasarowar, Daggyai Tso, Namling) have markedly lower incompatible element concentrations than the more magnesian samples. Mafic samples from both groups have

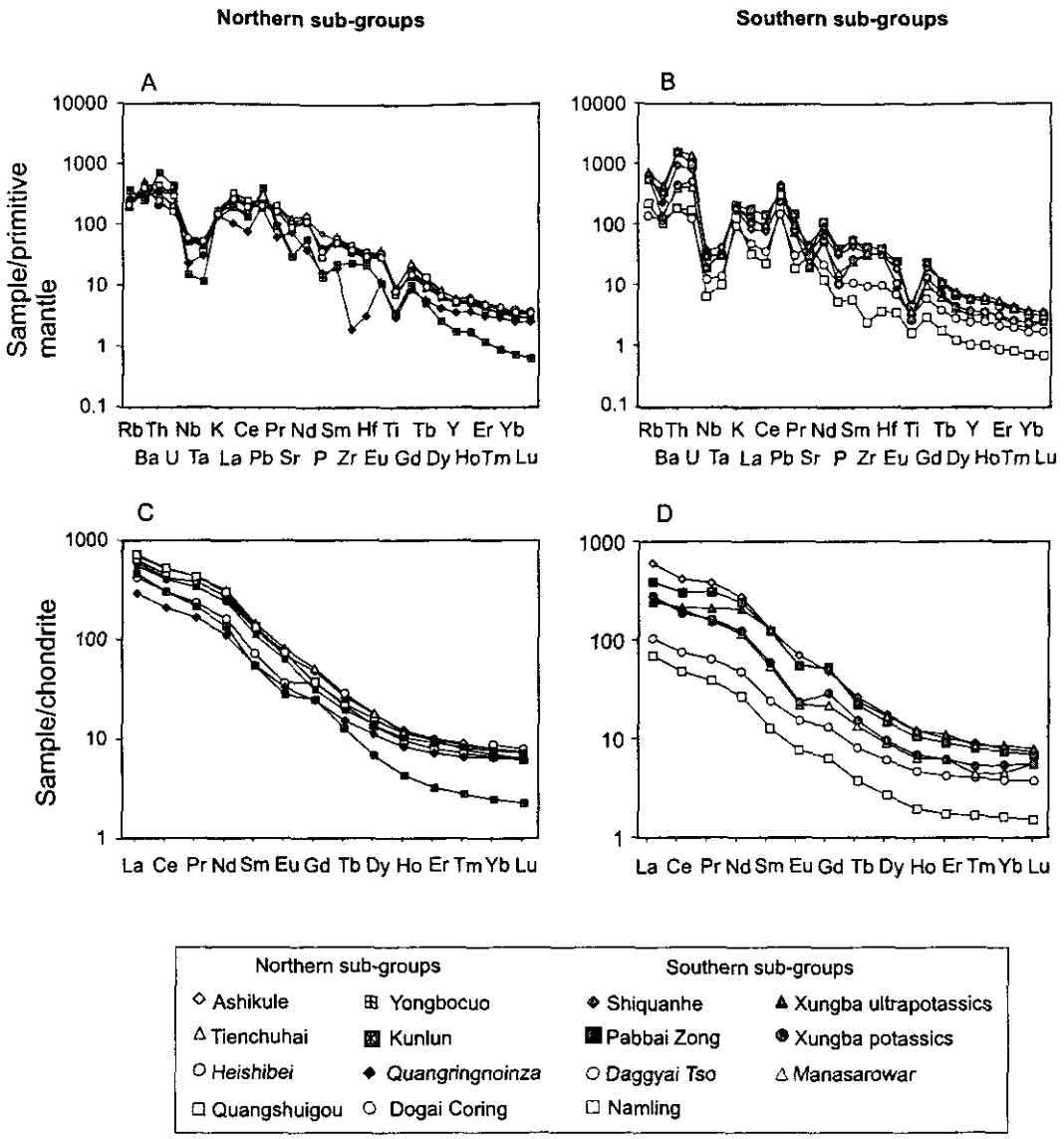

Figure 5.8 Primitive mantle normalised multi-element plots (A, B) and chondrite normalised REE plots (C, D) for representative samples from the southern and northern volcanic subgroups

Northern (A, C) and southern (B, D) sample names correspond to the sample sub groups in Figure 5.1. Data: this study, Miller et al. (1999); J. Pearce (pers. comm). Primitive mantle values from Sun and McDonough (1989) and chondritic values from Nakamura, (1974).

negative Nb, Ta and Ti anomalies – most pronounced in the southern magmas. The trace element variations of the northern and southern groups are similar; both groups have slight negative P and Sr anomalies and the southern magmas are further characterised by negative Ba and positive Pb anomalies. Negative Eu anomalies, commonly interpreted in terms of plagioclase fractionation, are not prominent. As trace element abundances are fractionation-corrected, anomalies are likely to represent either melting processes and residual source mineralogy, or the chemical signature of the source itself, which may have been preferentially depleted or enriched in certain elements during its evolution. The main differences in trace element signatures appear to be between the general north south subdivision, as opposed to individual sub-groups within them.

5.3.3 Radiogenic Isotopes

5.3.3.1 Sr and Nd isotopes

Sr and Nd isotope analyses of selected Tibetan samples were undertaken in order to assess the nature of the source regions from which they were derived, and to evaluate potential contrasts in source region. All of the Tibetan magmatic rocks discussed here plot in the enriched quadrant of the classical Sr-Nd diagram, shown in Figure 5.9 A, with radiogenic initial Sr isotopic compositions at unradiogenic initial εNd values. A distinction is made between the southern dacites and rhyolites (Daggyai Tso, Namling and Manasarowar) and shoshonitic magmas, which have MgO > 3wt%. The northern lavas are plotted as a single group, with the exception of the ~36 Ma Quangringnoinza magmas. The southern shoshonites display considerable variation in $^{87}Sr/^{86}Sr_{(i)}$ (0.7116-0.7394) and $\varepsilon Nd_{(i)}$ (-8.8 to –

18.1), whereas the northern samples show more limited variation in $^{87}Sr/^{86}Sr_{(i)}$ (0.7078 to 0.7157) compared to $\varepsilon Nd_{(i)}$ (-5.0 to –14.6). Interestingly, the Quangringnoinza magmas have isotopic signatures that are distinct from the other northern lavas ($^{87}Sr/^{86}Sr_{(i)}$ 0.7070-0.7077; $\varepsilon Nd_{(i)}$: -7.3 to –14.8) and form a near-vertical trend on the Sr-Nd isotope diagram. The more silicic southern magmas have more "primitive" $^{87}Sr/^{86}Sr_{(i)}$ (0.7066 to 0.7098) at a wide range of $\varepsilon Nd_{(i)}$ (-5.3 to –17.5). The Sr and Nd isotopic compositions of the sample groups show either flat, or no correlations with SiO_2. Nd model ages for the southern and northern shoshonite series range from 1.5 to 3.0 Ga and 1.0 to 1.3 Ga, respectively. These model ages must be regarded as hypothetical estimates, as the Sm/Nd of magmas is likely to be considerably fractionated relative to the source, and model age calculations do not take metasomatism by components with – potentially – ancient Nd isotope signatures into account.

5.3.3.2 Pb isotopes

Determinations of Pb isotope ratios for the mafic samples used in this study and available data from the literature are shown in Figure 5.10 A and B. The new data confirms the variation in Pb isotope compositions of the northern and southern shoshonites observed by Turner et al., (1996) and Miller et al. (1999). On both plots, the arrays for the northern and southern sub-groups plot above the Northern Hemisphere Reference Line (NHRL) (Hart, 1984). Northern lavas display near vertical trends, extending to high $^{207}Pb/^{204}Pb_{(i)}$ (15.61-15.72) and $^{208}Pb/^{204}Pb_{(i)}$ (38.85-39.26) at relatively invariant $^{206}Pb/^{204}Pb_{(i)}$ (18.62-18.72). Southern samples form shallower arrays due to greater variation in $^{206}Pb/^{204}Pb_{(i)}$ (18.16-19.15); $^{207}Pb/^{204}Pb_{(i)}$ (15.67-15.84) and $^{208}Pb/^{204}Pb_{(i)}$ (39.12-41.28) and are more radiogenic

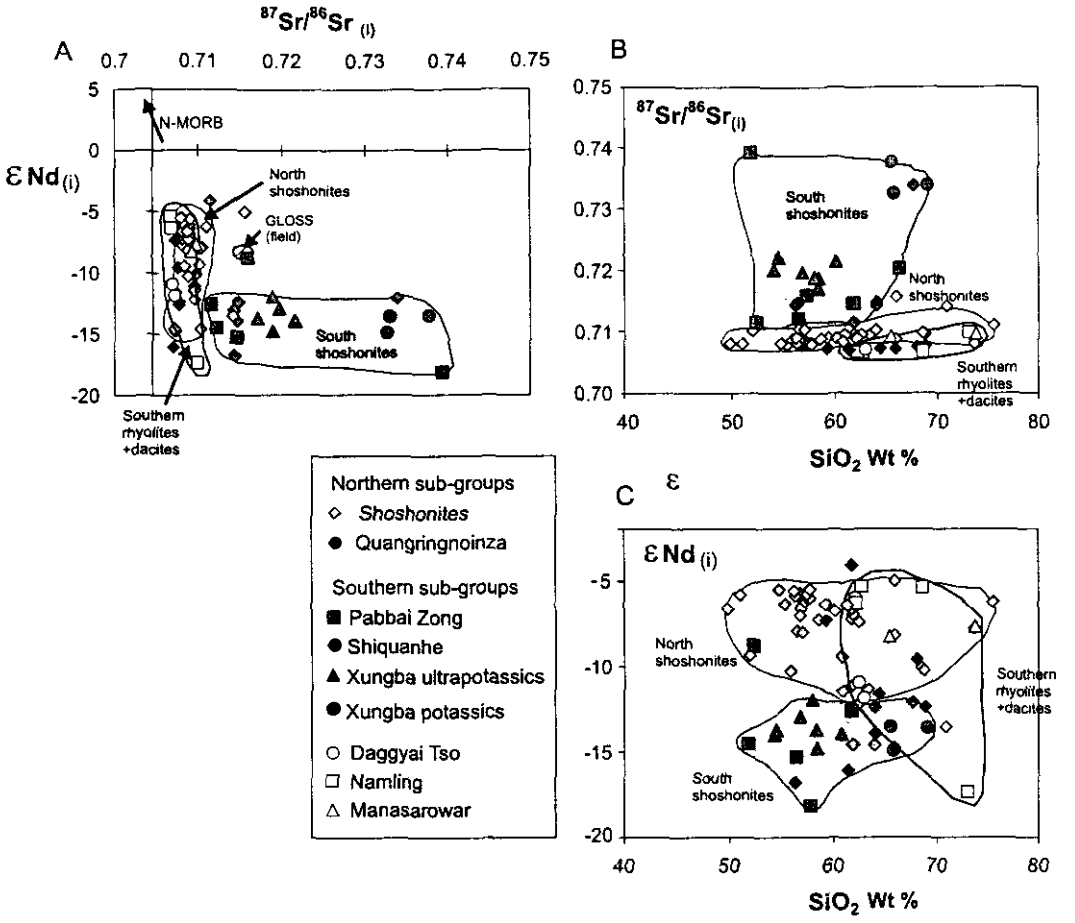

Figure 5.9 $\varepsilon Nd_{(i)}$ - $^{87}Sr/^{86}Sr_{(i)}$ and variation of $^{87}Sr/^{86}Sr_{(i)}$ and $\varepsilon Nd_{(i)}$ against SiO_2 for northern and southern volcanic subgroups

A) $\varepsilon Nd_{(i)}$ vs. $^{87}Sr/^{86}Sr_{(i)}$ for northern and southern shoshonite groups, the southern dacites and rhyolites and the Quangringnoinza series. Data: this study, Turner et al. (1996); Miller et al.(1999). The composition of globally averaged subducted sediment (GLOSS) Plank and Langmuir (1998) is shown. B) Variation of $^{87}Sr/^{86}Sr_{(i)}$ against SiO_2. Although scattered, the Sr isotope compositions of the southern magmas do not correlate with SiO_2 - the high SiO_2 samples generally having more "primitive" isotope ratios. C) Inital $\varepsilon Nd_{(i)}$ against SiO_2. There are no clear relationships between SiO_2 and Nd isotope signatures.

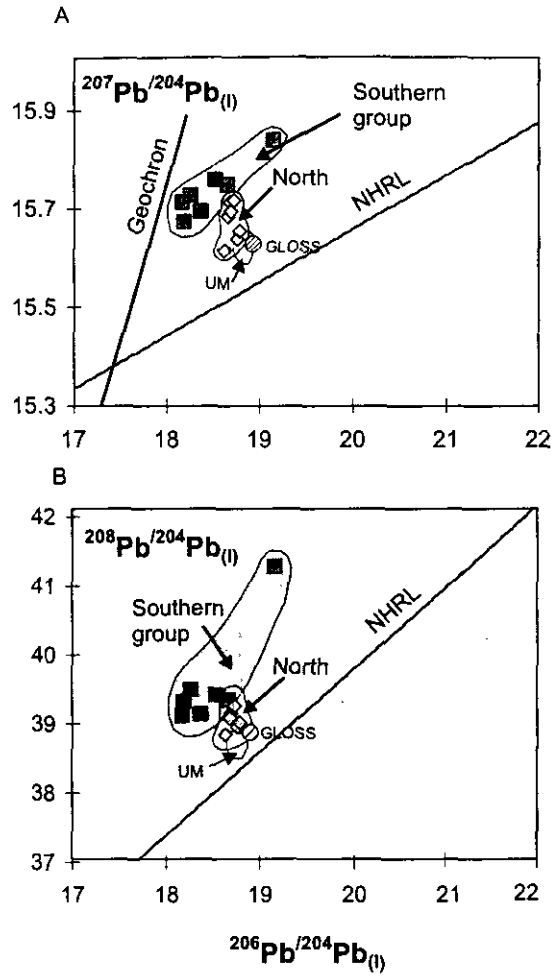

Figure 5.10 Pb isotope data for the southern and northern shoshonites . Isotope data has been corrected to the age of emplacement (method detailed in Appendix E).

The data presented for shoshonitic samples is from this study, Turner et al. (1996); Miller et al. (1999). GLOSS and the Ulugh Muztagh rhyolites (UM) of northern Tibet are shown for reference.

than the northern lavas. Both groups have more radiogenic $^{207}Pb/^{204}Pb$ and $^{208}Pb/^{204}Pb$ compositions than the Ulugh Muztagh rhyolites of northern Tibet (McKenna and Walker, 1990). $^{207}Pb/^{206}Pb$ model ages, calculated for individual samples by drawing secondary isochrons from the data points to the intersection of the geochron and the NHRL (Silver et al., 1988) are 2.8 to 3.3 Ga (north), and 3.3 to 4.1 Ga (south). These are hypothetical estimates for the time at which the sample's source region separated from the depleted mantle reservoir. The model of Silver et al. (1988) assumes that the Th/U of the source region is changed only twice, by partial melting following i) extraction of the depleted mantle from bulk silicate earth and ii) following extraction of the magma source region from the depleted mantle reservoir. Therefore, this model assumes that the Pb isotope compositions of the resulting magmas reflect purely radiogenic ingrowth, and does not allow for the incorporation of metasomatic components with ancient Pb isotope signatures, such as subducted sediment. Interestingly, the $^{207}Pb/^{206}Pb$ age of 2.3 Ga defined by the slope of southern array is considerably younger than the individual sample model ages, although it is admittedly dependent on the most radiogenic sample. An equivalent age could not be calculated for the northern array.

5.4 Discussion 1: Evidence for contrasting mantle source regions

In this section, major, trace element and isotopic constraints on the source regions of the northern and southern magmas are discussed, and evidence for two distinct source regions located within the SCLM presented. This discusssion forms a framework for the inverse

trace element modelling and discussion of melting regimes presented in the following sections.

5.4.1 Comparison of major element data at 6 wt% MgO

The relatively high Mg#'s of the more mafic samples in both northern and southern groups imply a mantle origin. This is supported by the presence of high Mg# pyroxene and phlogopite megacrysts in the southern samples. The extreme incompatible element concentrations of the shoshonites (Figure 5.8) cannot be easily resolved with models of crustal assimilation (Figure 5.7), and must therefore reflect the nature of the source region and the melting processes. High K_2O contents in both northern and southern suites implies phlogopite or K-amphibole saturation (Mengel and Green, 1989) and therefore the presence of these phases within the source region. Southern samples have higher K_2O and lower Fe_2O_3 and TiO_2 concentrations than northern samples for given MgO or SiO_2 (Figure 5.4, Figure 5.5), indicating differences in source mineralogy and/or composition. Sr, Nd and Pb isotope data indicates contrasting time-integrated source histories for the northern and southern shoshonites, lending support to this hypothesis (Figure 5.9, Figure 5.10). Source region contrasts can be further investigated by comparison of major element data at 6w t% MgO, following methods outlined in section 5.3.2. As extrapolations were only applied to magmas with MgO> 3 wt%, the petrogenesis of the southern rhyolitic and dacitic melts is not addressed here, but will be dealt with in a separate section. From Figure 5.11, A to D it is apparent that the southern samples are displaced to higher $Si_{(6)}$, lower $Fe_{(6)}$, $Ti_{(6)}$ and $Ca_{(6)}$ compared to the northern group. These data may be compared with the results of melting experiments on both fertile (e.g. HK66) and depleted natural peridotites (e.g. KLB-1,

Tinaquillo Lherzolite). The lower $Fe_{(6)}$, $Ti_{(6)}$ and $Ca_{(6)}$ of the southern group relative to the northern group echoes the displacement of the experimental data on (corrected to 6 wt % MgO by addition of Fo_{90}) for the peridotite KLB-1 and the Tinaquillo Lherzolite relative to the more fertile peridotite HK 66 (fields in Figure 5.11 A to D). The fields for KLB-1, HK 66 and the Tinaquillo Lherzolite define published data for melting experiments carried out on these starting materials at conditions ranging from 0.2 to 3 GPa, 1100 to 1600°C, with and without a free vapour phase (Falloon and Green, 1988; Hirose and Kushiro, 1993; Hirose and Kawamoto, 1995). Such experimental studies have been used to constrain the major element systematics of peridotite melting, for example SiO_2, MgO and CaO increase with temperature and degree of melting, whereas Fe_2O_3 is relatively insensitive to temperature, but increases strongly with pressure, as shown by the contours on Figure 5.11 C. *Melting under hydrous conditions at invariant pressure and temperature produces* magmas with higher SiO_2, lower TiO_2, Fe_2O_3 and CaO than those generated under anyhydrous conditions (Hirose and Kawamoto, 1995; Hirose, 1997).

If the compositions of the southern shoshonites are related directly to experimental data for the peridotite KLB-1, then polybaric melting, from ~2.3 to ~1 GPa, is required to generate the range of $Fe_{(6)}$-$Si_{(6)}$ compositions. However, such an approach is flawed in this case, as *the major element compositions of magmas cannot be directly related to the major element* systematics of peridotite melting without ambiguity, as the experimentally studied peridotite compositions may not provide sufficiently close analogues of the shoshonite source regions. This problem is illustrated in Figure 5.11 B, where both southern and northern shoshonite arrays are displaced to markedly lower $Ca_{(6)}$ contents compared to all of the experimentally studied peridotites. Given that CaO will increase in mantle melts until clinopyroxene is consumed (at F~0.25) (McKenzie and Bickle, 1988) and the low degrees of melting required

for potassic magma generation (F <0.03), the low $Ca_{(6)}$ of the shoshonites implies low modal proportions of clinopyroxene in their source regions relative to the peridotite starting materials (~ 15 % clinopyroxene). Therefore, the composition and mineralogy of the source region will also exert a strong control on the major element compositions of the magmas produced, and magmas derived from contrasting source regions will have correspondingly different major element signatures. Distinguishing the effects of source composition/mineralogy and melting regime on major element systematics is not straightforward. For example, the displacement of the southern shoshonites to lower $Fe_{(6)}$ and $Ti_{(6)}$ relative to the northern group could be a reflection of larger degrees of melting (as TiO_2 behaves incompatibly in peridotite melting experiments) at lower pressures. However, the separation of the southern and northern series on this plot argues against this hypothesis, as the displacement of the southern shoshonites to lower $Fe_{(6)}$ and $Ti_{(6)}$ is greater than can be explained by partial melting of a homogenous peridotite source at a wide range of conditions (fields define melts from experiments carried out at 0.2 to 3 GPa, and 1100 to 1600°C with variable water content). This implies that the major element compositions between the two sample groups are dominated by differences in source region composition and mineralogy, as opposed to variations in melting regimes or the vapour phases present (phlogopite xenocrysts in the southern shoshonites imply a hydrous source). The fact that the experimental fields for the different peridotite compositions overlap the other plots (Figure 5.6 A to C), whereas there is considerable separation between the northern and southern lavas is consistent with this hypothesis. Therefore, the higher $Si_{(6)}$, lower $Fe_{(6)}$, $Ti_{(6)}$ and $Ca_{(6)}$ of the southern group relative to the northern group suggests that their source region has lower modal proportions of clinopyroxene and had experienced a greater degree of depletion. A refractory source for the southern shoshonites is consistent with their high Cr

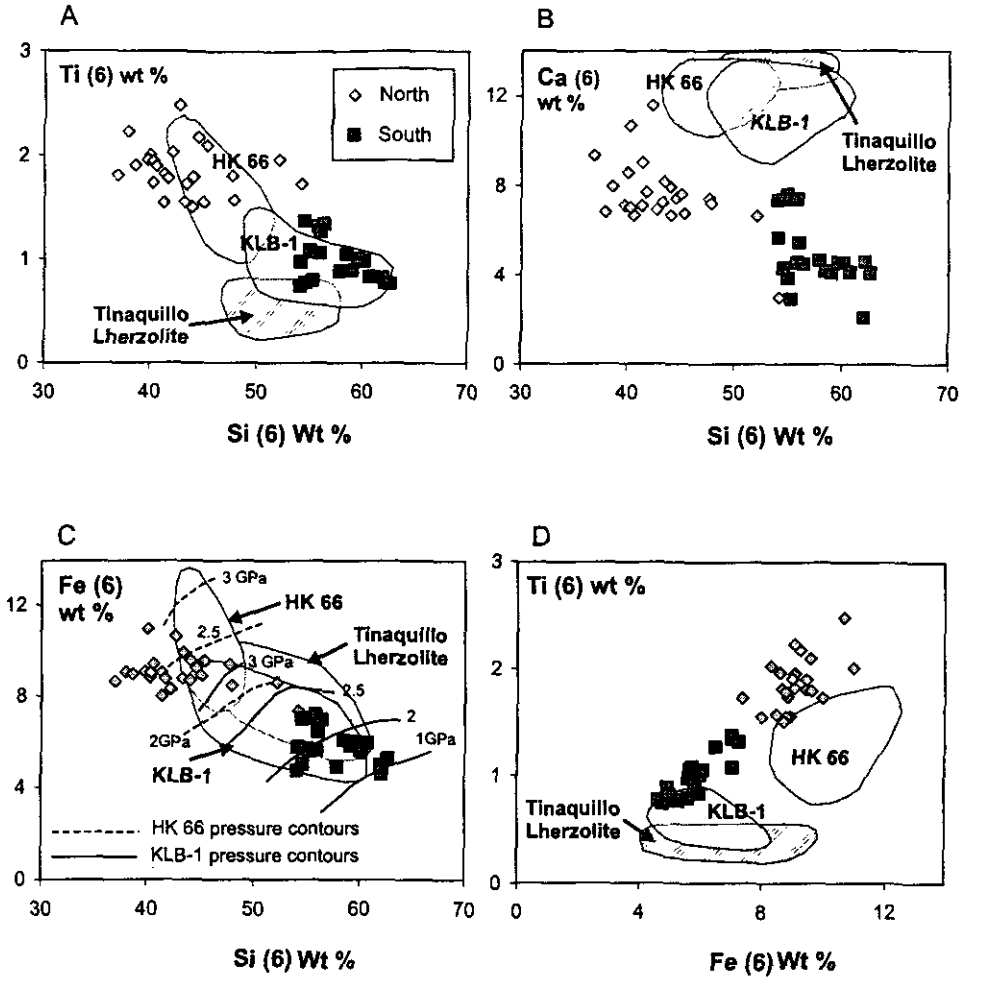

Figure 5.11 Major element data variations in the southern and northern shoshonites, normalised to 6wt% MgO

In plots A to D, the southern and northern magmas form distinct, separate groups with little to no overlap. Northern magmas show more affinity to HK66 in terms of $Fe_{(6)}$, $Si_{(6)}$ and $Ti_{(6)}$ compositions; southern samples show more similarity to KLB-1. $Ca_{(6)}$ compositions of both groups are lower than experimental peridotite melts.

concentrations, which cannot be explained by melting a primitive mantle (Sun and McDonough, 1989) source (Figure 5.7 C).

5.4.2 Trace Elements and Rare Earth Elements

As shown in Figures 5.6 and 5.8 the concentrations of incompatible elements and LREE (normalised to 6 % MgO, where appropriate) are elevated relative to average continental crust (Taylor and McLennan, 1985) and primitive mantle (Sun and McDonough, 1989). Therefore the trace element characteristics of these magmas cannot be explained in terms of mixing crustal and asthenospheric melts, and crustal assimilation would in fact dilute the LREE and LILE of the shoshonites. Instead, the origin of the enriched signatures of the northern and southern magmas must be sought in the context of the composition and mineralogy of their mantle source regions and the nature of the melting processes.

On the plots of Dy/Yb versus La/Yb (Figure 5.12 A) and La/Yb versus La (Figure 5.12 B), both northern and southern groups form broadly linear positive arrays. Major, trace and isotope data indicates that binary mixing does not produce the compositional variations within and between the southern and northern shoshonite series. As trace element data are corrected for fractional crystallisation and the assimilation of crustal material by normalisation to 6 wt% MgO, the arrays shown in Figure 5.12 A and B are unlikely to be the result of AFC processes, or the presence of cumulates. Therefore, the most reasonable interpretation of the data arrays is that they broadly define partial melting arrays. Both groups have elevated Dy/Yb and La/Yb relative to primitive mantle; the southern magmas characterised by lower abundances of La (52-127 ppm) than the northern lavas (180-254

ppm) and a wide range of Dy/Yb at more restricted La/Yb (Figure 5.12 A). In contrast, the northern magmas show greater variation in La/Yb compared to Dy/Yb. While the trends of the data arrays roughly mirror fractional melting curves (non-modal fractional melting with residual melt, see figure caption for mineralogy and melt modes), comparison with these melting models demonstrates that the compositions of the northern and southern magmas cannot be produced by melting a primitive mantle source, further supporting a SCLM origin for both groups. Moreover, the compositional gap between northern and southern data arrays cannot be explained in terms of derivation from a single source region. This implies the presence of distinct source regions with contrasting REE signatures. Fractional melting curves provide an indication of the maximum range in Dy/Yb and La/Yb obtainable by melting, and demonstrate that melting completely homogenous sources cannot generate the range in trace element compositions shown by the two groups. This is consistent with current models for potassic magmatism that invoke the preferential melting of distributed metasomatic mineral veins within the mantle lithosphere (e.g. Foley, 1992). The difference in the slopes of the northern and southern arrays may reflect differences in melting regime or source heterogeneity; the behaviour of the REE is investigated further in the following sections. The absence of correlations between indices of partial melting e.g. La/Yb and Sr or Nd isotopes (not shown) implies that melting processes, as opposed to source heterogeneity, exert a dominant control on trace element variations *within* groups, whereas the compositional differences *between* the two groups are reflection of the composition and mineralogy of their respective source regions.

The contrasting incompatible element chemistry of the northern and southern shoshonites is investigated further in Figure 5.12 C, Ti/Y against Rb/Ba. The differences between the two groups are striking, with the northern lavas forming a vertical array at high Ti/Y and low

Figure 5.12 Trace element variations of the southern and northern shoshonites; Dy/Yb vs. La/Yb, La/Yb vs. La, Ti/Y vs Rb/Ba, Rb/Ba vs Rb, Ti/Y vs Ti. Nb/Ta vs Nb.

Trace element abundances have been normalised to MgO = 6 wt%, except where the elements of interest either showed a flat array with MgO, or no correlation at all. In the southern group, Nb, Ta, U, Th, Tm, Yb and Lu were not corrected for these reasons. Similarly in the northern series, elements Nb, Ta, U, Th and Gd to Lu are not fractionation corrected. A) Dy/Yb vs. La/Yb. Primitive mantle Sun and McDonough1989) non-modal factional melting curve with residual melt (Pearce and Parkinson, 1993) shown for comparison. Modal mineralogy, with mineral modes entering the melt in brackets. garnet facies ol 0.66(0.2); opx 0.21(0.3); cpx 0.07 (0.38); grt 0.05 (0.1); residual melt 0.01 (0.01). spinel facies ol 0.69 (0.2); opx 0.21 (0.3); cpx 0.07 (0.38); sp 0.02 (0.1); residual melt 0.01 (0.01). B) La/Yb vs. La. Both northern and southern groups form steep arrays, indicative of small degrees of partial melting. The arrays are inconsistent with mixing between them. C) Ti/Y vs Rb/Ba. D) Rb/Ba vs Rb with melting vectors. Melting vector models (non-modal fractional, residual melt present): Model 1 ol 0.69 (0.08); opx 0.115 (0.08); cpx 0.03 (0.23); amph 0.13 (0.3); rutile 0.05 (0.2); phl 0.005 (0.1); grt 0.01 (0); sp 0.01 (0); residual melt 0.01 (0.01). Model 2: ol 0.69 (0.08); opx 0.115 (0.08); cpx 0.03 (0.23); amph 0.08 (0.3); phl 0.005 (0.3); grt 0.01 (0); sp 0.01 (0); residual melt 0.01 (0.01). Model 3: ol 0.69 (0.14); opx 0.115 (0.15); cpx 0.03 (0.23); phl 0.13 (0.4); grt 0.01 (0); sp 0.01 (0); residual melt 0.01 (0.01). E) Ti/Y vs Ti. F) Nb/Ta vs Nb. Note that the southern array extends to subchondritic values. D values: ol, opx, cpx, grt (Halliday et al., 1995); phl (Foley et al., 1996; Schmidt et al., 1999); amph (Dalpe and Baker, 1994); rutile (Jenner et al., 1994; Foley, 2000); residual melt D=1 (Pearce and Parkinson, 1993).

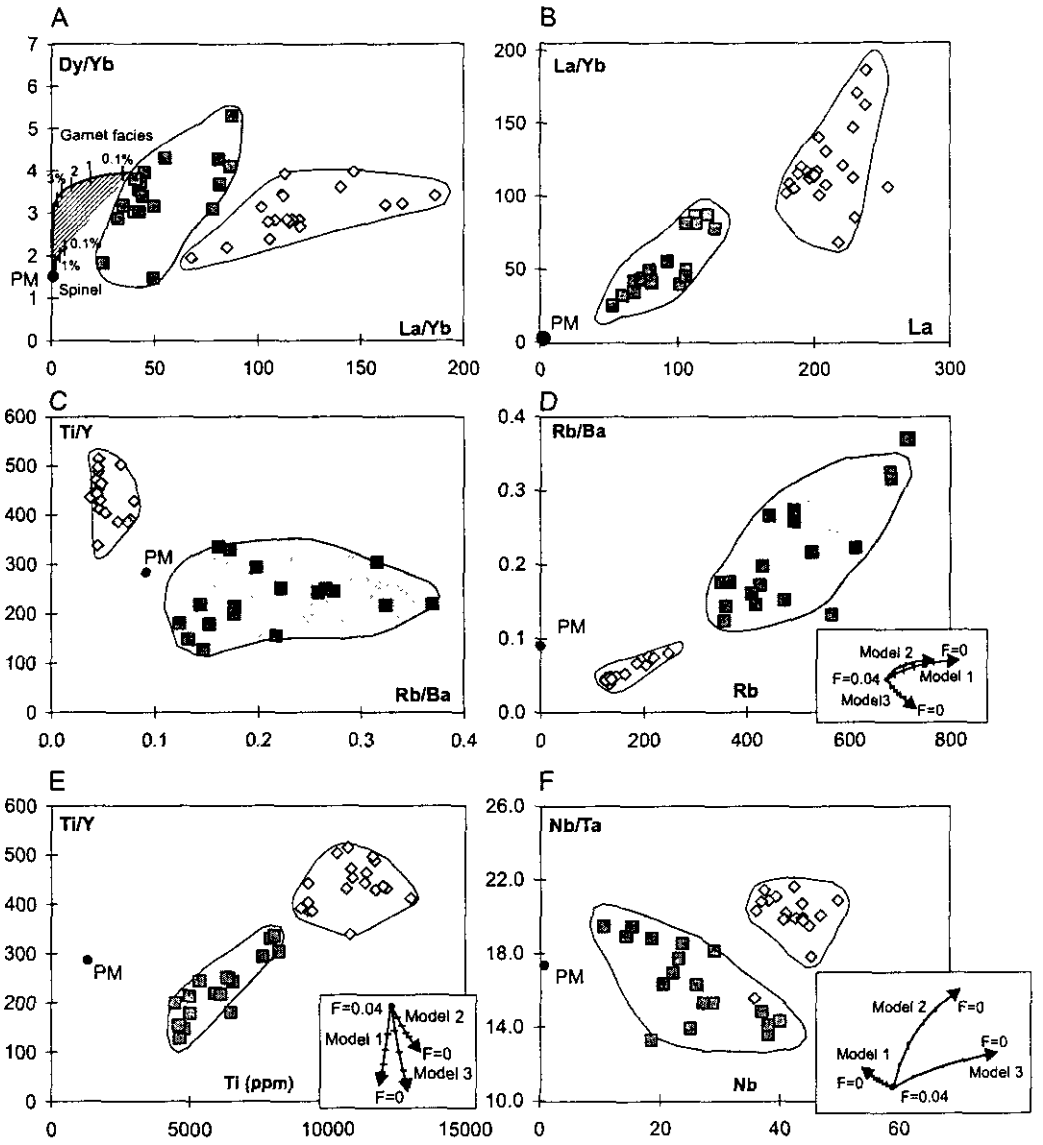

Figure 5.12 (caption on previous page).
All elemental concentrations and ratios are given in ppm

Rb/Ba relative to the southern group, which define a horizontal field. The steep array of the northern magmas to high Ti/Y and low Rb/Ba could be interpreted as metasomatism of their source by small degree melts derived from the asthenosphere, whereas the horizontal array extending to higher values of Rb/Ba formed by the southern samples might reflect metasomatism by a sedimentary component, introduced during a past subduction event (e.g. Rogers, 1992). However, partial melting in the presence of residual phases such as rutile, ilmenite, phlogopite and amphibole can fractionate both Rb/Ba and Ti/Y. This is investigated in Figure 5.12, D and E. Both northern and southern groups show a positive correlation between Rb/Ba and Rb (D), which is interpreted in terms of Rb/Ba fractionation during melting. Fractional melting vectors for melting metasomatised peridotites are shown for comparison. The influence of residual phases is investigated using three different metasomatic mineral assemblages: a complex metasomatic amphibole+rutile+phlogopite assemblage (model 1); residual amphibole with a small phlogopite component (model 2) and residual phlogopite only (model 3). In both groups, the positive slope of Rb/Ba against Rb implies that Rb is enriched compared to Ba at the lowest degrees of melting, i.e. bulk $D_{Rb} < D_{Ba}$ for the southern magmas. This indicates the presence of residual pargasitic amphibole, which has a stronger affinity for Ba relative to Rb (Adam et al., 1993; Dalpe and Baker, 1994). Comparison with the melting vectors (model 1 and model 2) confirms this. The presence of riebeckite inclusions within high Mg# phlogopites (interpreted as mantle xenocrysts) in the southern samples (section 5.2) is consistent with the presence of a MARID-type assemblage within the source region (Kramers, 1983). The shallower slope of the northern samples suggests less of a contrast in the partitioning of Ba and Rb during melting. This reflects either a lower modal abundance of amphibole relative to phlogopite in the northern source relative to the southern source, or a lower overall abundance of hydrous potassic phases in the northern source region. In Figure 5.12 E, Ti/Y is positively correlated

with Ti in the southern magmas implying that melting exerts a strong control on magma HFSE compositions. There are two possible interpretations: either $D_{Ti} < D_{Yb}$, or else $D_{Ti} \sim 1$ in the source and that Ti/Y is increasing with degree of melting. Partial melting vectors for the same metasomatised peridotite assemblages indicate that Ti/Y and Ti increase with the degree of melting for source regions where residual amphibole, phlogopite ± rutile are present. In an anhydrous peridotite source without residual phases, the converse is true, and Ti is enriched in the smallest melt fractions. The corresponding increase in Ti and Ti/Y with melt fraction predominantly reflects the high D's for Ti in the metasomatic mineral phases (D_{Ti} for phlogopite = 0.9 (Schmidt et al., 1999); for pargasitic amphibole = 0.7 (Dalpe and Baker, 1994); for rutile ~20, calculated using the approach of Ryerson and Watson (1987)). Therefore the positive slope of the southern group is consistent with melting in the presence of residual amphibole and rutile. However, the full range in Ti and Ti/Yb in the southern magmas cannot be explained by melting of a compositionally homogenous source. No clear correlation is observed for the northern lavas on the Ti vs. Ti/Yb diagram. This may be a consequence of source heterogeneity or more complex melting processes than investigated here. The influence of melting processes on the HFSE compositions of the southern group is further emphasised in Figure 5.12, F. Southern magmas are characterised by lower Nb/Ta (13.3-19.4, average 16.5) than the northern group (15.5-21.6, average 20.0). The negative correlation between Nb/Ta and Nb in the southern lavas is suprising, as $D_{Nb\ min/melt} < D_{Ta\ min/melt}$ for the majority of metasomatic mantle phases (e.g. Green and Pearson, 1986; Dalpe and Baker, 1994; Jenner et al., 1994; Foley et al., 1996; Foley, 2000), and a positive relationship would therefore be expected on this element-ratio diagram (Minster and Allègre, 1978). There are two interpretations of the negative correlation - either bulk $D_{Nb} > D_{Ta}$ in the southern source, or else both Nb and Ta are behaving compatibly. The latter interpretation is consistent with flat arrays of Nb against MgO (Figure 5.6 C) and

La (not shown). Compatible behaviour of Nb and Ta implies the presence of Fe-Ti oxides such as rutile in the southern magma source, as these have D_{Nb} of 26 to 100 and D_{Ta} of 44 to 100 (Green and Pearson, 1986; Jenner et al., 1994; Foley, 2000). The influence of rutile on the Nb/Ta and Nb concentrations of small degree melts is illustrated by partial melting vectors – the negative slope of the southern magmas can only be approximated by invoking residual rutile (Model 1) in their source region. Rutile is present in mantle xenoliths, notably the well-studied MARID (Mica-Amphibole-Rutile-Ilmentite-Diopside) suite (Sweeney et al., 1993) and kinked crystals of rutile in the Xungba ultrapotasssics of SW Tibet have been tentatively interpreted as mantle xenocrysts (Miller et al., 1999). The northern lavas do not show a strong correlation between Nb/Ta and Nb, precluding a significant role for residual Fe-Ti oxides in their source region. Residual rutile in the source region of the southern shoshonites will buffer Ti, Nb and Ta, which is consistent with the flat arrays formed by the southern shoshonites on the plots of TiO_2 against MgO (Figure 5.5 D) and Nb against MgO (Figure 5.6 C), and with the lower $Ti_{(6)}$ contents of the southern shoshonites relative to the northern samples (Figure 5.11 A).

5.4.3 Isotopic constraints on source region and residual mineralogy

On the basis of major and trace element data, it appears reasonable to suggest that the northern and southern shoshonite series were derived from distinct SCLM source regions containing different metasomatic mineral assemblages. Constraining the relative proportions of these phases and the exact nature of the melting processes is limited by a lack of direct information regarding the composition of the source region. This problem is

addressed further in Section 5.5, where an inverse approach to modelling trace element data is used. In this section, isotopic evidence for two distinct source regions is discussed, and used to further constrain the residual mineralogy of these source regions, building on the trace element modelling in section 5.4.2.

The high incompatible element concentrations of the primitive magmas, and minimal correlations between $^{87}Sr/^{86}Sr_{(i)}$ and $\varepsilon Nd_{(i)}$ with SiO_2 (Figure 5.9, B and C) indicates that the isotope signatures of these samples are insensitive to assimilation processes and must therefore reflect the source region. $^{87}Sr/^{86}Sr_{(i)}$ signatures (0.7123-0.739) of the southern shoshonites are generally more radiogenic than known proxies for the time integrated $^{87}Sr/^{86}Sr$ composition of the Lhasa Terrane crust, upper crustal sediments (0.7071-0.7076) and the Nyainqentanghla granites (0.7092-0.7160; Harris et al, 1988), consistent with this hypothesis. Southern samples show a wide range in $^{87}Sr/^{86}Sr_{(i)}$ at more restricted $\varepsilon Nd_{(i)}$, while the northern lavas form a vertical trend on the $^{87}Sr/^{86}Sr_{(i)}$ - $\varepsilon Nd_{(i)}$ diagram (Figure 5.9 A), a consequence of their relatively invariant $^{87}Sr/^{86}Sr_{(i)}$ compositions. Given the lack of trace element evidence for mixing relationships between the two groups, the isotopic signatures of the northern and southern shoshonites may be interpreted in terms of contrasting time-integrated source histories. The range in $^{87}Sr/^{86}Sr_{(i)}$ shown by the southern magmas indicates variation in the Rb/Sr composition of the source, whereas the vertical array of the northern group implies a source characterised by variable Sm/Nd. Such isotopic heterogeneities may be interpreted in terms of the variable proportions of peridotite host and metasomatic vein material involved in partial melting processes (Foley, 1992). Similar conclusions were reached by Schaefer et al. (2000) on the basis of Re-Os systematics for these rocks.

Interpreting the Pb isotope systematics of ultrapotassic magma suites derived from the SCLM is complex, due to the multi-stage histories often inferred for SCLM source regions, the unknown ages and compositions of potential metasomatic agents. Northern and southern suites have extremely radiogenic $^{207}Pb/^{204}Pb_{(i)}$ and $^{208}Pb/^{204}Pb_{(i)}$ and moderate $^{206}Pb/^{204}Pb_{(i)}$ (Figure 5.10 A, B). As pointed out by Nelson et al. (1985), these Pb signatures cannot be produced by the closed system decay of U, as this would result in highly radiogenic $^{206}Pb/^{204}Pb$. This alone suggests a multi-stage evolution for the source regions of both northern and southern magmas, and the model ages presented in section 5.3.3.2 must be regarded as a broad indication of source or component antiquity, as opposed to absolute age constraints. If derivation from a depleted mantle reservoir is assumed for illustrative purposes, the high $^{207}Pb/^{204}Pb_{(i)}$ and relatively low $^{206}Pb/^{204}Pb_{(i)}$ shown by both groups suggests an early increase in U/Pb, followed by a later decrease. Such changes in U/Pb can result from fractionation during partial melting and/or from the introduction of metasomatic components with different U/Pb compositions to that of the SCLM. High U/Pb compositions in the southern samples (0.2 to 1.3, average 30.8 corresponding to $^{238}U/^{204}Pb$ of ~ 13 to 90, average 47) must reflect either considerable fractionation of U/Pb during melting, or recent metasomatism and an increase in U/Pb, with minimal time for ^{206}Pb ingrowth. Alternatively, the range in $^{207}Pb/^{204}Pb_{(i)}$ and $^{208}Pb/^{204}Pb_{(i)}$ seen for the southern samples may reflect some degree of mixing between fusable and non-fusable SCLM components, as the sample with the most radiogenic Pb compositions contains > 40% modal phlogopite, whose high Mg#'s, Cr and F abundances imply a xenocrystic SCLM origin. The northern shoshonites have more restricted range in U/Pb (0.09 to 0.145) and do not show the trend to higher values of $^{206}Pb/^{204}Pb_{(i)}$ seen in the southern group.

Pb isotopes do not show mixing arrays with respect to Sr and Nd isotopes and are not correlated with trace element ratios such as Ce/Pb. $^{207}Pb/^{206}Pb$ model ages calculated for individual samples in both groups are consistently older than their respective Nd model ages, suggesting decoupling of the two isotopic systems during the evolution of the SCLM source regions. However, the slope defined by the southern array on the $^{207}Pb/^{204}Pb$-$^{206}Pb/^{204}Pb$ diagram (Figure 5.10 A) gives an age of 2.3 Ga, falling within the brackets of individual sample Nd model ages. If this array truly defines an isochron as opposed to a binary mixing trend, then the younger age may reflect a later resetting (effectively a clockwise rotation of the array on the $^{207}Pb/^{204}Pb$-$^{206}Pb/^{204}Pb$ diagram) of U-Pb systematics. No such event is evident from the Pb isotopic compositions of the northern magmas, again indicating contrasts in source evolution.

Sr model ages (depleted mantle) based on measured Rb/Sr are variable: ranging from 0.8 to 2.4 Ga and 0.3 to 1.5 Ga for the northern and southern shoshonites, respectively. This can be interpreted in terms of variable Rb/Sr in the source region and/or fractionation of Rb/Sr during melting. As shown in Figure 5.13 A, the southern magmas display consistently younger Sr model ages compared to the northern samples. In contrast, their Nd model ages (1.5 to 3.0 Ga) are variable and generally older than those of the northern group (1.0 to 1.3 Ga). The relative differences between Sr and Nd model ages indicate that the two isotope systems have been decoupled from each other at some point prior to the emplacement of the magmas. Rb/Sr is easily fractionated during melting, particularly in potassic rocks derived from LILE enriched source regions containing phases such as amphiboles, micas, oxides and apatite. If it is assumed that the two isotopic systems were in equilibrium at least shortly before melt generation, and that the Nd model ages are roughly equivalent to the source value at the time of melting, then Rb/Sr fractionation during melting can be constrained.

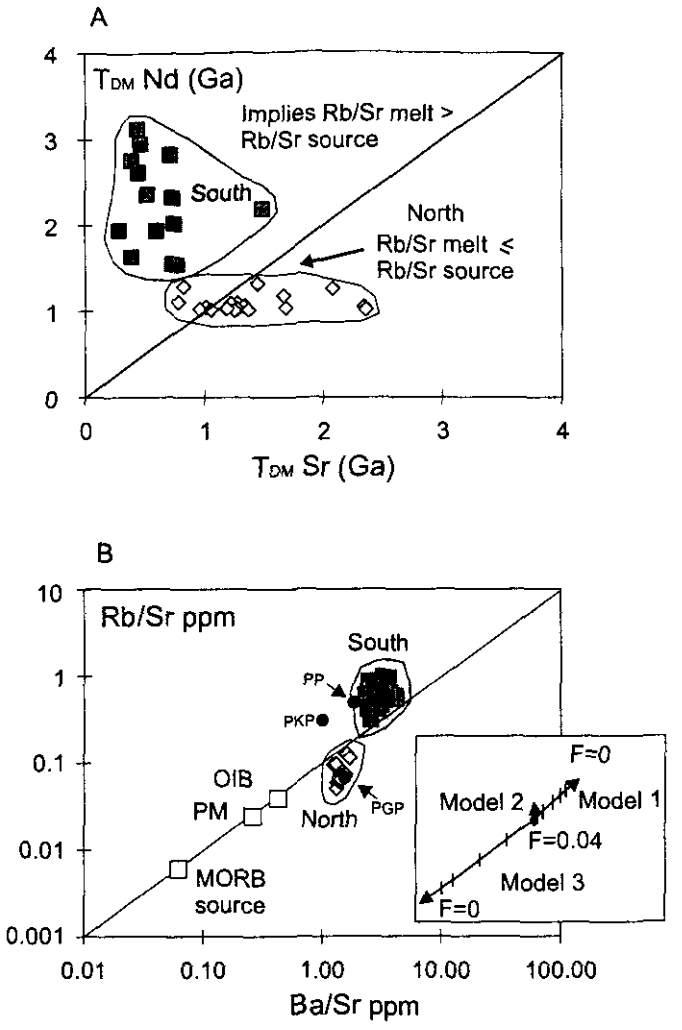

Figure 5.13 Nd_{DM} model ages - Sr_{DM} model ages; Rb/Sr - Ba/Sr for the northern and southern shoshonites

A) Nd model ages (time since separation of the source from the depleted mantle reservoir) vs. Sr model ages (depleted mantle), calculated with whole rock Sm/Nd and Rb/Sr. No fractionation of Sm/Nd during melting is assumed; note that correcting for a 30% decrease of Sm/Nd during melting would result in a corresponding increase in the Nd model age calculated. B) Rb/Sr vs Ba/Sr, data for MORB source from (Stolper, 1994), OIB and PM (Sun and McDonough, 1989). Whole rock metasomatised mantle xenolith compositions: PP, phlogopite peridotite; PKP, phlogopite-K-richterite-peridotite; PGP, phlogopite garnet peridotite (Erlank et al., 1982). Modal mineralogies and melt modes for melting vectors as in Figure 5.12.

No fractionation of Sm/Nd during melting was assumed, but as Sm/Nd can be reduced by as much as 30% during melting the estimates of Rb/Sr fractionation must be regarded as minima. For the southern group $[Rb/Sr]_{melt}/[Rb/Sr]_{source}$ is 2 to 8, for the north it is 0.5 to 1.8 (~1 for most samples). The fractionation of Rb/Sr and Ba/Sr is investigated further in Figure 5.13 B, where it can be seen that the southern samples are elevated above the Bulk Earth Rb/Ba of ~ 0.1 to higher values, in contrast to the northern group, which is displaced slightly below this value. Average whole-rock compositions for phlogopite peridotite, phlogopite-K-richterite peridotite and phlogopite-garnet peridotite xenoliths (Erlank et al., 1982) are shown for reference. Comparison with the melting vectors in Figure 5.13 B shows that the displacement of the northern lava to lower Rb/Sr is consistent with variable amounts of phlogopite and amphibole in the source region (note that model 2, residual amphibole and minor phlogopite does not significantly fractionate these ratios).

There are two possible interpretations of the high $[Rb/Sr]_{melt}/[Rb/Sr]_{source}$ of the southern samples: disequilibrium melting of phlogopite, which, due to its high D_{Rb} relative to D_{Sr}, produces a melt with high Rb/Sr, or the presence of a residual phase in the source for which $D_{Sr} >> D_{Rb}$. Experimental studies suggest that melting of phlogopite, or phlogopite-clinopyroxenite will produce highly potassic (K_2O > 12 wt%) silica undersaturated melts (Lloyd et al., 1985; Luth, 1997), which is inconsistent with the major element characteristics of the southern magmas. Pure metasomatic vein melting is precluded by the presence of low CaO, Fo_{93} olivine xenocrysts in the southern lavas (Miller et al., 1999), which indicate involvement of a peridotite component in the melts. Therefore, the second interpretation is preferred. In section 5.4.2, residual pargasitic amphibole and rutile were invoked to explain variations in Rb/Ba, Ti/Y and Nb/Ta seen in the southern lavas. Whereas residual phlogopite will strongly reduce the Rb/Sr of a melt relative to its source, pargasitic

amphibole has D_{Sr}/D_{Rb} ~1, and will have little effect on $[Rb/Sr]_{melt}/[Rb/Sr]_{source}$. Melt model vectors (Figure 5.13 B) demonstrate that the increase in Rb/Sr and Ba/Sr in the southern melts can be explained by residual rutile, for which D_{Sr}/D_{Rb} ~70 (Jenner et al., 1994; Foley, 2000) in addition to amphibole in the source. This is consistent with rutile xenocrysts in lava flows from southwest Tibet (Miller et al., 1999) and high Mg# phlogopite megacrysts with abundant amphibole inclusions in the glimmerite dykes.

In summary, major, trace element and isotope data indicate that the northern and southern shonshonites originated by melting two compositionally and mineralogically distinct SCLM source regions. Constraining the exact nature of the melting regime, and – critically - the past thermal structure of the Tibetan SCLM, is difficult as there are few direct constraints on source composition. Despite the wide spatial distribution of samples and the inferred heterogeneity in source region compositions, the trace element variations within, as opposed to between, these suites appear to be dominated by melting processes and the influence of the residual mineralogy. Trace element variations within the groups may therefore be interpreted in terms of the degree and nature of the melting processes and residual source mineralogy, and will be largely independent of source composition. This is the rationale adopted in the next section, which concerns inverse modelling of trace element variations with a view to constraining melting regimes and the composition of the north and south Tibetan SCLM.

5.5 Discussion 2: Constraints on degree of melting and source region mineralogy

5.5.1 Inverse modelling

The partitioning of trace elements between mineral phases and melt is commonly expressed in terms of mass balance (Shaw, 1970). This assumption underpins inverse trace element modelling, which utilises the variation of trace element concentrations within cogenetic magmas derived from a source by varying degrees of melting to calculate the initial concentrations of trace elements in their source, the range in degree of melting and the source mineralogy. Methods of inverting trace element data have been extensively discussed (Minster and Allègre, 1978; Albarède, 1983; Hofmann and Feigenson, 1983; McKenzie and O'Nions, 1991); here a modified version of the approach adopted by Class and Goldstein (1997) is employed, the main features of which are discussed in the next section.

First, it is important to address the implicit assumptions in such modelling and the degree to which the northern and southern shoshonites can be treated as two separate but cogenetic magma suites. Both groups show variable Sr, Nd and Pb isotopic signatures, raising the possibility that trace element variations within these suites may reflect pure binary mixing of melts derived from different sources under different melting regimes, as opposed to different degrees of partial melting of moderately heterogeneous source regions. However, binary

mixing is inconsistent with trace element data, as demonstrated for Ce and Cr in Figure 5.7. Moreover, fractionation-corrected incompatible element ratios are not correlated with isotopic signatures, suggesting that source region heterogeneity does not exert a strong control on the variation of incompatible trace elements *relative to each other* in the sample suites. As pointed out by Minster and Allègre (1978), cogenetic lava suites show strong positive correlations on incompatible element ratio-element plots, reflecting slightly different degrees of equilibrium melting. This trait is seen in both Tibetan sample groups (Figure 5.12, B and D), implying that despite the heterogeneity inferred in their source regions, their trace element variations are dominantly controlled by melting processes and that, for practical purposes, they may be treated as broadly time-averaged cogenetic suites. Therefore, the distribution of trace elements within these magma suites may be interpreted in terms of the nature of melting processes and source mineralogy, and will be largely independent of the composition of their source regions.

5.5.1.1 Model outline and assumptions

The enrichment of incompatible elements in fractional melts that are derived from a relatively uniform source will be a function of the mineralogy and degree of melting of that source. Although the absolute degree of melting is not known, the relative degree of melting may be described by the concentration of a highly incompatible index element, whose abundance will be inversely proportional to the degree of melting. The variation of the elements of interest relative to this index element will be a function of their bulk D's relative to the index element and the range in degree of melting (F). This will generally take the form of a linear relationship between an incompatible element (j) and the index element, providing that the proportions of minerals entering the melt phase do not change dramatically over the range of melting. For the small degrees of melting (typically, F<0.04) invoked to explain the petrogenesis of potassic lavas, this assumption is reasonable. Elements that are compatible or buffered with respect to the source region will show a horizontal, or even a negative correlation with the index element. The enrichment of elements relative to a highly incompatible index element can be used in conjunction with the traditional sequence of elements in mantle normalised multi-element diagrams to evaluate the relative D values of the elements of interest, and allow the identification of residual phases. Therefore, these relationships provide a means of modelling the petrogenesis of a suite of rocks in terms of melt fraction and source mineralogy, independently of source composition. This approach is described in detail by Class and Goldstein (1997), after Minster and Allègre (1978) and only a summary of the salient points and the approach used towards the Tibetan magma suites are presented here.

The sample sets used in this study correspond to the groups defined in section 5.4.1, which have MgO > 3wt%. As detailed earlier, trace element abundances were extrapolated back to 6wt% MgO to correct for fractionation, crustal assimilation and cumulate accumulation. As melting trends with MgO are nearly vertical for small degrees of melting (Figure 5.7 B and C, $F < 0.04$) these regressions do not overprint trace element variations produced by the melting regime. This approach contrasts with that taken by Hofmann and Feigenson (1983) and Class and Goldstein (1997), who both utilise the stepwise addition of mineral phases until the composition of the sample approaches that of a primary magma. This is avoided here, as it involves *a priori* assumptions regarding the nature of the fractionating assemblages - poorly constrained in potassic systems. Furthermore, regression analysis allows identification of outliers and samples showing alteration effects.

La provides the best available index for degree of melting in both northern and southern suites. It is measured on all samples, behaves incompatibly in both suites (unequivocally demonstrated in Figure 5.13 A and B), and is not easily modified by secondary alteration processes. For the two suites, low (FL) and high (FH) degrees of melting are "fixed" at set concentrations of La. For south Tibet, La concentrations of 60 (C_{LaFH}) and 120 ppm (C_{LaFL}) were set for high and low degrees of melting, respectively. For northern Tibet, $C_{LaFH} = 180$ ppm, $C_{LaFL} = 250$ ppm. Concentrations of other elements at these values were calculated based on least-squares regression against the index element La (Figure 5.14). More compatible elements have shallower slopes against La, and are characterised by greater abundances at the higher degrees of melting represented by C_{LaFH}, compared to lower abundances at lower degrees of melting, i.e. C_{LaFL}. The converse is true for incompatible elements. This is clearly seen in Figure 5.14 (A, B) where Ce shows a steep positive

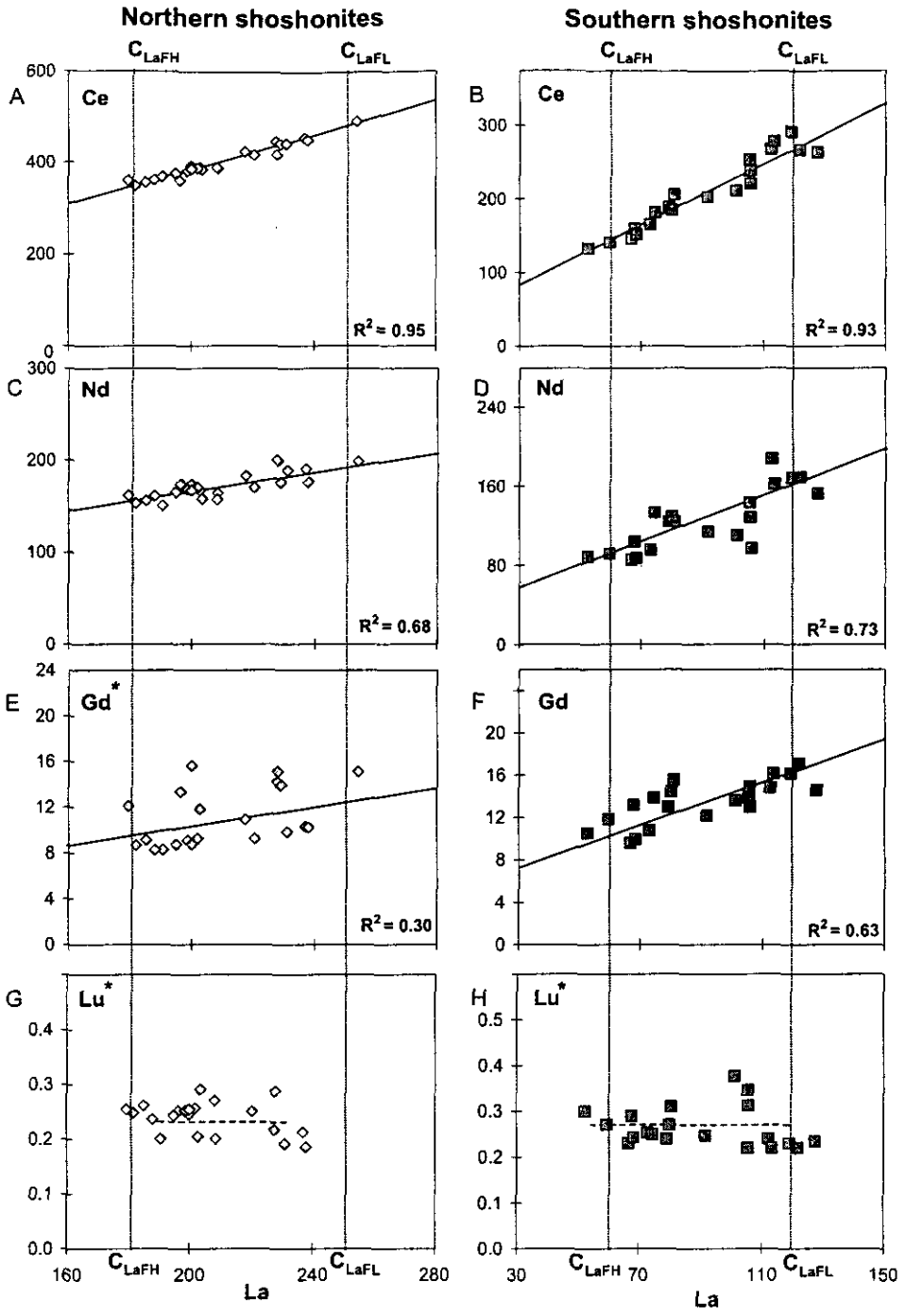

Figure 5.14 REE variations against La in the northern and southern shoshonites. All axes are ppm.

REE variations in the northern (A, C, E, G) and southern (B, D, F, H) shoshonite series used to calculate the enrichment ratios discussed in the text. REE abundances have been normalised to MgO = 6 wt%, except where asterisked. In these latter cases, the elements of interest either showed a flat array with MgO, or no correlation at all. In the southern group, Tm, Yb and Lu were not corrected for these reasons. Similarly in the northern series, elements Gd to Lu are not fractionation corrected.

relationship with La and the slopes of the arrays become progressively shallower from Nd to Lu (Figure 5.14 C to G). Lu shows little correlation with La in either group, reflecting more compatibile behaviour. The increase in compatibility from Ce to Lu is systematic in both groups, supporting the "cogenetic" treatment of the samples. Ce is tightly correlated with La in both groups ($R^2 = 0.95$ for the north, and = 0.93 for the south) as would be expected for elements of similar compatibility, and extrapolation of both trends gives intercepts of ~ 0. This is consistent with melting trends where two elements have extremely similar D values and further emphasises that pure binary mixing, which would require two components with Ce/La =1, is unlikely. The behaviour of an element (j) relative to La may be effectively summarised by calculating an "enrichment ratio" (E) (Class and Goldstein, 1997), i.e. $E= C_{jFL}/C_{jFH}$, where the concentrations of element (j) at the index values of La are termed C_{jFH} and C_{jFL}. This ratio is a function (see below) of the D value for that element: high enrichment ratios correspond to low D values and vice versa. Differences in E values therefore correspond to differences in bulk D values between two different elements i.e. for element j and k, if $E_j < E_k$, then $D_j > D_k$

This is expressed below, using bulk fractional melting as an example:

Equation 5-1

$$E = \frac{C_{jFL}}{C_{jFH}} = \frac{FH}{FL} \times \frac{\left\{1-(1-FH)^{1/D}\right\}}{\left\{1-(1-FL)^{1/D}\right\}}$$

Where: E is the enrichment ratio discussed above; D the bulk distribution coefficient for the element of interest (j); FH and FL are the high and low melt fractions corresponding to the set low and high concentrations of the index element La, C_{LaFH} and C_{LaFL} respectively. C_{jFL} and C_{jFH} are the concentrations of the element of interest at FL and FH, determined by least-squares regression of the data array against La. This expression may be adjusted to account for non-modality, but is only applicable where there is little change in the modes of mineral phases entering the melt between FL and FH. As pointed out earlier, potassic magmas generally reflect very small degrees of melting with limited potential for extensive changes in the crystallising assemblage (all phases are essentially residual) so this assumption seems reasonable. As $D \Rightarrow 0$, $E \Rightarrow FH/FL$, the enrichment ratio calculated for an extremely incompatible element, e.g. Ce, will therefore approximate the range in degrees of melting. This can be used to calculate FH for a given FL, which is required to convert the relative C_{melt}/C_{source} values calculated in partial melting models into enrichment ratios. Similarly, as $D \Rightarrow \infty$, E will approach a constant, depending on the values of FL and FH. Therefore E, as defined here, will never fall below 1, although the more compatible elements may show flat or negative trends against La (Figure 5.14 G and H). Using this approach, the resolution of relative D values is therefore limited to the moderately incompatible elements.

5.5.1.2 Residual mineralogy and degree of melting

The residual mineralogy of the northern and southern Tibetan magma sources can be evaluated using multi element diagrams, in which the sequence of elements, from left to right, reflects increasing element compatibility in an anhydrous spinel or garnet peridotite source (i.e. ol + opx + cpx + sp ± grt). Enrichment ratios calculated, using appropriate

partition coefficients, for melts derived from anhydrous peridotite sources will form smooth patterns, the slope of which conveys information regarding FL/FH. Negative anomalies indicate the presence of a residual phase or phases other than the "normal" anhydrous mantle assemblages.

The enrichment ratio patterns of the northern and southern suites are not smooth, but show negative anomalies for Rb, Ba, Nb, Ta, K, Sr and Ti; in addition the southern group gives a small negative Eu anomaly (Figure 5.15 A). In both groups it is apparent that Th and U are behaving more compatibly than Ce. The southern trace is steeper than the northern trace between Ce and Y, showing both higher values and greater variation in enrichment ratios. Both traces have similar slopes between Y and Lu, although the northern trace is offset to negative values. The negative anomalies shown by north and south traces (Figure 5.15 A) indicate that residual phases in addition to the conventional anhydrous peridotite assemblages are present in the source regions of both groups, in agreement with the trace element and isotopic arguments presented earlier. Differences in the patterns (e.g. K is completely buffered with E=1 in the north, but to a lesser degree in the south) indicate contrasts in the phase assemblages of the two source regions. Higher E values for the south suggests a greater range in the degree of melting (i.e. larger FL/FH), although it should be borne in mind that this may also be accounted for in part by a greater degree of compositional variation in their source (c.f. Figure 5.12). However, the slopes are not sensitive to source heterogeneity, and the steeper slope and greater enrichment in the highly incompatible elements of the southern group relative to the northern group can be interpreted as reflecting a genuine difference in melting regime.

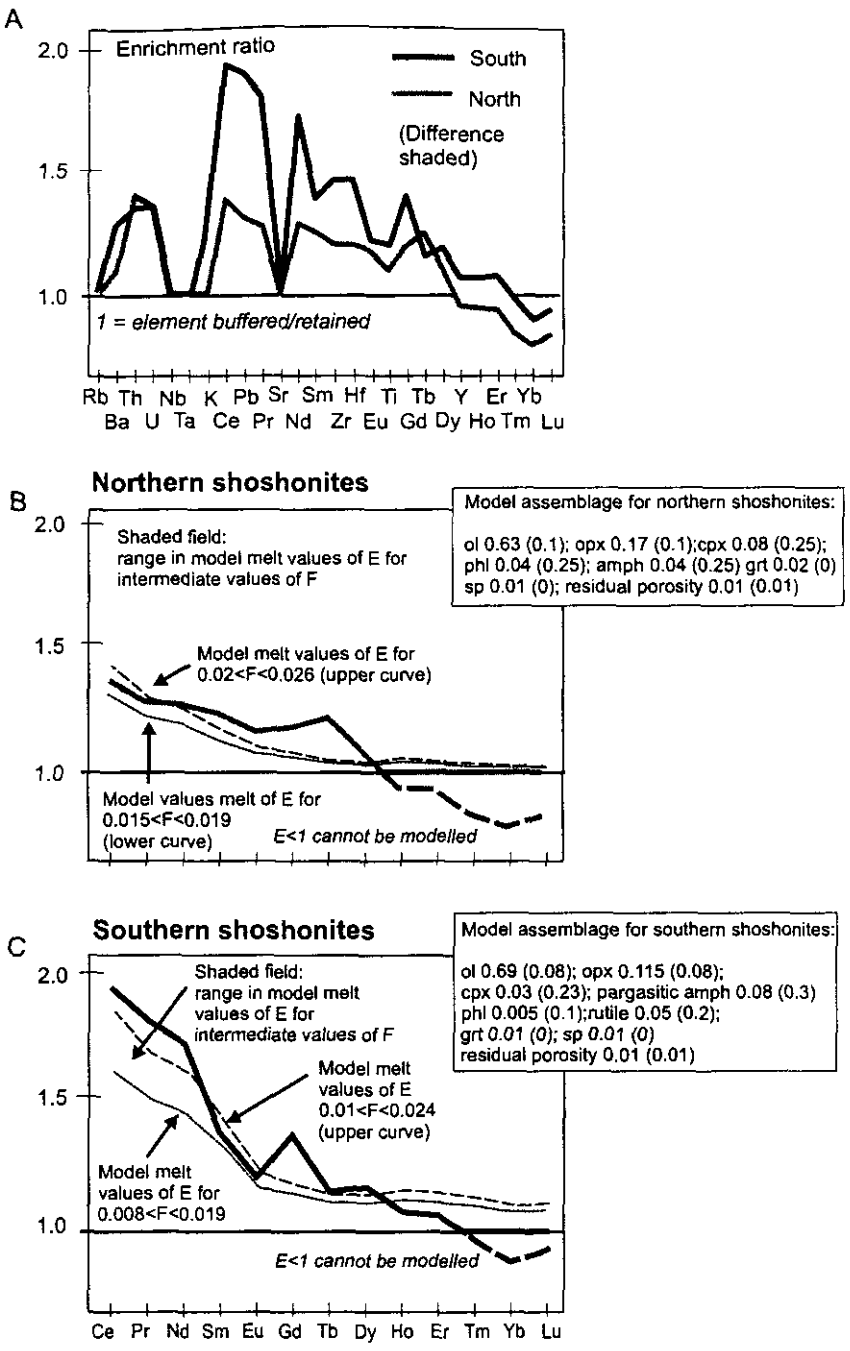

Figure 5.15 Enrichment ratio patterns calculated for the northern and southern shoshonites

Constraints on degree of melting and magma source mineralogy. A) Enrichment ratio pattern plotted on a multi element diagram. Higher enrichment ratios indicate greater incompatibility, values that approach or equal 1 indicate buffering or compatibility. Values <1 also indicate compatibility but cannot be used for modelling and are shown for illustrative purposes only. B) REE trace for northern shoshonites (pale grey line); the dashed continuation of this line shows negative HREE values that cannot be modelled. The dashed and dotted lines correspond to the two melt models which best fitted the data (the shaded region - field of likely enrichment ratios generated from intermediate models). Note that the peak at Tb likely reflects interpolation of D values. FL/FH=1.7, based on Ce (discussed in text). C) REE trace for southern shoshonites (dark grey line); dashed continuation, negative HREE values that cannot be modelled. The optimal melt models and range of intermediate solutions are displayed as for B; FL/FH=2.4. The D values used are presented in Appendix E

The traces formed by the two magma groups may be used to quantify residual mineralogy and degree of melting. The degree of melting is modelled in terms of the minimum melt fraction FL; FH/FL is calculated from the ratio of the maximum and minimum concentrations of the most incompatible element, excluding the index element. Ce was used to calculate FL/FH for both the northern and southern suites, giving FL/FH values of 1.7 (north) and 2.4 (south). Maximum melt fractions (FH) were calculated as a function of FL and FL/FH. As in section 5.4, a non-modal fractional melting model is used, in which a trapped melt component remains present (Pearce and Parkinson, 1993). Trapped melt is treated as a phase with a partition coefficient of 1, increasing the bulk D's for all elements, having the greatest effect on the most incompatible elements. The enrichment ratios of the REE alone (Figure 5.15 B, C) were used to quantify the degree of melting and the garnet/clinopyroxene ratio of the source region. This approach is insensitive to the exact modal proportions of olivine, orthopyroxene and spinel in the source region. Elements such as Nb, Ta, Rb, Sr and K have values of E equal to or approaching 1, consistent with the arguments for residual amphibole, phlogopite and rutile presented in section 5.4. These buffered/compatible elements cannot be modelled using Equation 5.1., so the relative abundances of phlogopite, pargasitic amphibole and rutile are determined by incorporating the constaints from section 5.4 into the REE model, and optimising this to match the observed traces in Figure 5.15, B and C.

Anomalies can be expressed in terms of the difference between a reference element and the element of interest, an approach analogous to the more conventional calculation of trace element abundance ratios. To compare anomalies between the northern and southern series,

these differences were then scaled to the enrichment ratio obtained for the reference element in the southern group. For example the K anomaly in the northern group is expressed as the difference between enrichment ratios calculated for Ce and K, i.e. $(E_{Ce}-E_K)$ x $(E_{Ce\text{-}south}/E_{Ce\text{-}north})$. Where the element of interest is buffered (i.e. E=1) then this is a minimum estimate. Scaled anomalies for K (0.5), Nb ($E_{Ce}-E_{Nb}$; 0.5), Sr ($E_{Pr}-E_{Sr}$; 0.4), Ti ($E_{Gd}-E_{Ti}$; 0.1) for the northern group are lower than those obtained for the southern group (K 0.8; Nb 0.9; Sr 0.8; Ti 0.2). This reflects the lower degrees of melting inferred for the southern group based on the REE enrichment ratios – all phases are highly residual. The larger negative Nb, Ta and Ti anomalies of the southern group relative to the northern group are consistent with the hypothesis that residual titanites are present in the source of the southern magmas, but are absent from the northern source. However, the significant negative Nb, Ta and Ti anomalies evident for the northern group implies some control by residual phases. Although partitioning data for amphibole and mica (Adam et al., 1993; Dalpe and Baker, 1994; LaTourette et al., 1995; Foley et al., 1996; Schmidt et al., 1999) suggests low D_{Nb} and D_{Ta}, high concentrations of Nb and Ta have been observed in amphibole and phlogopite within metasomatic veins (Ionov and Hofmann, 1995). On this basis, Ionov and Hofmann (1995) suggested that these phases could be important reservoirs for Nb and Ta within the SCLM, and that the presently available partition coefficients could be underestimates. Therefore, the presence of phlogopite and amphibole in the northern source region may be sufficient to explain the slight negative Nb and Ta anomalies observed. The presence of negative Eu anomalies ($E_{Sm}-E_{Eu}$ 0.2) in the southern series is surprising, as the relatively mafic nature of the magmas suggests they did not originate from a source region containing residual plagioclase. Moreover, the oxygen fugacities inferred for the mantle source (Section 4.2.1) preclude the formation of Eu^{2+}. The presence of these negative Eu anomalies is difficult to

explain, but may reflect the initial fractionation/assimilation correction used, which is based only on trace element variations with MgO.

5.5.2 Source compositions and evolution

Constraints on melt fraction and modal mineralogy can be used in combination with the composition of the northern and southern magmas to estimate the source composition and the time-averaged compositions of the metasomatic components. Primitive mantle normalised trace-element compositions for the source and metasomatic agent are shown in Figure 5.16, the shaded areas represent metasomatic addition to the source regions (assuming an orginal composition similar to primitive mantle). The compositions calculated for the northern and southern SCLM source regions (in the following discussion, referred to as N-SCLM and S-SCLM, respectively) reflect the ranges in the composition of the northern and southern shoshonites, and the mass balance nature of the calculation.

Comparison of the source compositions presented on primitive mantle normalised multi-element diagrams (Figure 5.16, A and B) indicates that both are considerably enriched in the LILE and LREE-MREE relative to primitive mantle (Sun and McDonough, 1989). Both sources show similar depletion in the HREE (e.g. Yb south, 0.2 to 0.3 ppm; north 0.4 to 0.5 ppm). Mass balance calculations based on non-modal partial melting of a fertile garnet-bearing PM source (modal mineralogy; melt modes in brackets: ol 0.65 (0.13); opx 0.12 (0.15); cpx 0.14 (0.15); grt 0.08 (0.25); sp 0.01 (0.12)) indicate that the low HREE concentrations can only result from melt extraction prior to metasomatism and re-enrichment: 10 to 12% melt extraction is required for the N-SCLM, 25 to 30% for the

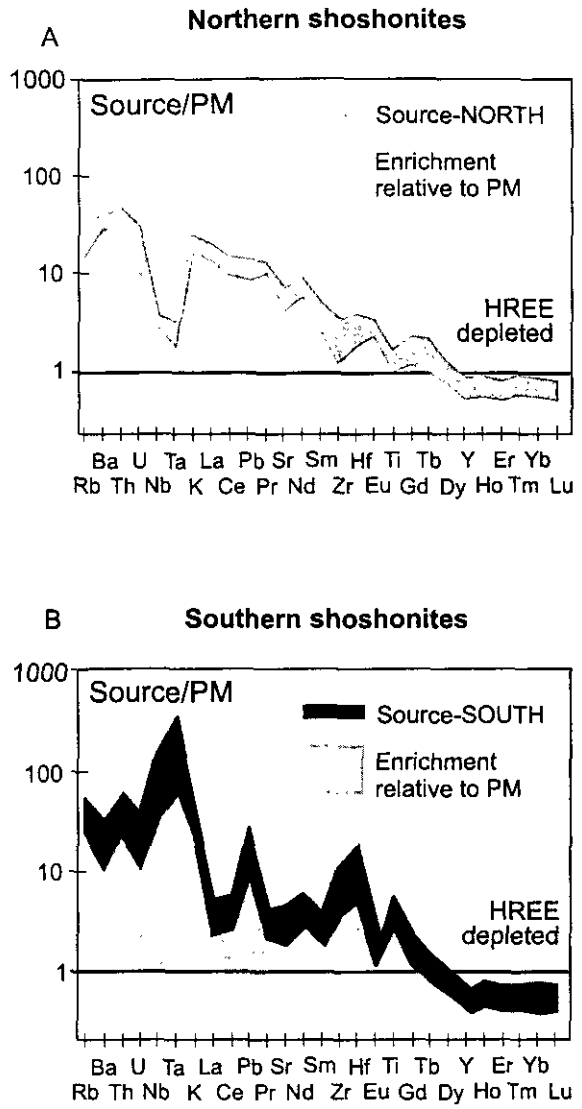

Figure 5.16 Calculated source compositions for the northern and southern shoshonites, normalised to primitive mantle

Calculation of the northern (A) and southern (B) sources is based on the degrees of melting and residual mineralogy modelled in the previous section, and the fractionation corrected compositions of the least evolved magmas. D values used in the calculation are the same used for both forward (section 5.4) and inverse (section 5.5.1) modelling. As the calculated compositions are normalised to primitive mantle, any deviation from unity reflects either source enrichment or depletion.

S-SCLM. These finding are consistent with the low $Fe_{(6)}$ and $Ca_{(6)}$ of the southern group relative to the northern samples and the presence of low-Ca (< 0.01 wt%), Fo_{93} olivines in the southern shoshonites, interpreted as mantle xenocrysts (Miller et al., 1999). The refractory nature and large degrees of melt extraction inferred in the history of the S-SCLM are consistent with current models of SCLM formation by melt extraction from the convecting mantle and segregation of the buoyant residua (Jordan, 1978; Pollack, 1986). Interestingly, the primitive (Fo_{93}) compositions of the olivine xenocrysts identified by Miller et al. (1999) are comparable to those of komatiitic olivines (Nisbet et al., 1993), indicating that the true timing of S-SCLM stabilisation may be Archean, as suggested by Pearson et al. (1995) for the Kaapvaal Craton. A Nd depleted mantle model age of ~3.3 Ga for one of the olivine xenocrysts entrained in the southern shoshonites (Miller et al., 1999) may be in accord with an Archean component. Although there are no constraints on the timing of stabilisation of the N-SCLM, the lower degrees of melt extraction required to explain the HREE concentrations of the source indicate lower ambient temperatures for the convecting mantle at the time of stabilisation. Given models for the secular cooling of the Earth (Davies, 1995), this implies a younger, probably Proterozoic, stabilisation age for the N-SCLM. Stabilisation of the both lithosphere terranes by the early Proterozoic is consistent with the ages of detrital zircon populations from major rivers draining northeastern regions of the plateau, which indicate two major periods of crustal growth 2.3 and 1.9 Ma (Bodet and Schärer, 2000).

The calculated compositions of the southern and northern shoshonite source regions show enrichment in the more incompatible elements and are clearly distinct from primitive mantle. Furthermore, they suggest strikingly different time-averaged patterns of enrichment. Pb and Nd depleted mantle model ages for the northern shoshonites (Nd, 1.0-1.3 Ga; Pb 2.8

to 3.3 Ga) are consistently younger than those of the southern shoshonites (Nd 1.5 to 3.0 Ga; Pb 3.3 to 4.1). This difference in model ages is likely to result from the metasomatism of these source regions at different times, with metasomatic components of different ages and isotopic compositions. The N-SCLM shows the classical "subduction signature": negative Nb-Ta, Ti, Zr and Sr anomalies in addition to LREE/HREE enrichment (La/Yb_N 20.8, average composition calculated, number of sample composition used =23), Rb/Ba_N (av. 0.63, n= 18), moderately high Nb/Ta (av. 20.5, n=17) and high Th/U (av. 6.8, n= 16). In contrast, the S-SCLM is characterised by a marked increase in the HFSE relative to the LILE and REE, with large positive Nb, Ta and Ti anomalies and smaller positive Pb, Zr and Hf anomalies. The southern source also shows greater enrichment of Rb relative to Ba (Rb/Ba_N 2.2, n=20), and of the LREE compared to the HREE (av. La/Yb_N 7.7, n=20), high Th/U (av. 6.8, n=20) and subchondritic Nb/Ta (av. 8.8, n=20).

5.5.2.1 Nb-Ta fractionation and HFSE enrichment in the SCLM source regions

The contrasting incompatible element signatures of the southern and northern SCLM source regions are likely to reflect differences in the composition and origin of the metasomatic components introduced into these source regions. Models in which the SCLM is progressively enriched by small degree asthenospheric melts (McKenzie, 1989) predict systematic enrichment of trace elements according to their relative incompatibility in an anhydrous peridotite, and do not explain the negative and positive anomalies shown here for the N- and S-SCLM sources. The most distinctive trace element features of the two source regions are their strikingly different HFSE signatures and Nb/Ta values. In this section,

these will be used to place broad constraints on the metasomatic processes that affected the N- and S-SCLM sources, and the tectonic regimes under which these events occurred.

The origin of HFSE depletions relative to the REE and LILE in island-arc volcanics and potassic magmas in subduction settings has attracted considerable attention in recent years. Most explanations invoke processes such as the addition of bulk sediment or sediment-derived components to the mantle wedge, previous depletion due to melt extraction from the peridotite mantle wedge and the selective retention of HFSE in the mantle wedge or subducted slab by accessory phases. Due to their high D values for the HFSE, Ti bearing phases, particularly rutile, have been assigned a major role in the generation of HFSE anomalies (e.g. Foley and Wheller, 1990; Green, 1995). However, despite negative Nb, Ta and Ti anomalies, the northern Tibetan source remains enriched in these elements - average calculated concentrations for Nb, Ta and Ti are 2.2, 2.1 and 1.3 times primitive mantle, respectively. The enrichment of HFSE in the N-SCLM suggests that the origin of the negative HFSE anomalies and the moderately high Nb/Ta signatures must relate to metasomatism, as opposed to previous depletion events. Mechanisms for HFSE transport and addition to the SCLM are a subject of debate; they include release of aqueous fluids following slab dehydration (Brenan et al., 1994); metasomatism by carbonatite melts (Yaxley et al., 1991) and hybridisation of the mantle wedge by silicic melts derived from either altered oceanic crust, pelagic or terrigenous sediments. The moderately high Nb/Ta (20.2) of the N-SCLM compared to the chondritic value of 17.5 (Jochum et al., 1986; Jochum et al., 1989) suggests either fractionation of Nb/Ta during metasomatism and preferential enrichment in Nb, or addition of a metasomatic component characterised by high Nb/Ta. Experimental studies (see Green, 1995, for a compilation of available partitioning data) suggest that Nb/Ta and LILE/HFSE may be significantly increased in

carbonatite melts that have equilibrated with pargasitic amphibole. However, carbonatite melts typically have CaO/Al_2O_3 greater than 2 (Yaxley et al., 1991), inconsistent with the major element signatures of the northern lavas ($CaO_{(6)}/Al_2O_{3(6)}$, 0.2 to 1.0). Turner et al. (1996) suggested, on the basis of negative Nb, Ta and Ti anomalies in the northern lavas, that ancient subduction processes were responsible for the metasomatism of the Tibetan SCLM. The addition of fluids derived from dehydration of the downgoing slab to the mantle wedge have been invoked to explain the LILE compositions of arc volcanics, but recent experimental studies (Brenan et al., 1994) indicate that the concentrations of Nb and Ta in aqueous fluid in equilibrium with rutile are negligible, ruling this out as a mechanism for Nb and Ta enrichment. However, Ta and Nb partition more readily into silicate melts and as $D_{Nb} < D_{Ta\ min/melt}$ for pargasitic amphibole, rutile and ilmentite (Green and Pearson, 1986; Green, 1995), silicic melts of either altered oceanic crust or sedimentary material will be characterised by moderately high Nb/Ta. The addition of such components to the N-SCLM is therefore a plausible mechanism for both HFSE enrichment and increasing Nb/Ta of the source. Residual Ti bearing phases or residual amphibole in the slab allow for HFSE depleted signatures in the N-SCLM, even though the absolute abundances of these elements in the N-SCLM are increased with respect to primitive mantle as a consequence of metasomatism. If this model is correct, the sediment component must have had an isotopic composition considerably different to that of globally subducted average sediment (Plank and Langmuir, 1998) - no clear mixing trends with GLOSS and other end-members e.g. MORB are apparent in Figure 5.9 A, and the vertical trends to radiogenic $^{207}Pb/^{204}Pb_{(i)}$ and $^{208}Pb/^{204}Pb_{(i)}$ (Figure 5.10 A, B) are not explained.

The unusual trace element pattern of the S-SCLM, which shows strong enrichment in the HFSE relative to the LREE, is strikingly similar to hornblendite (amphibole-phlogopite-

ilmenite-rutile) and garnet-amphibole-pyroxenite metasomatic veins (McPherson et al., 1996), which also have pronounced positive Nb, Ta and Ti anomalies. The similarity of the S-SCLM composition to the bulk composition of these metasomatic veins provides evidence for a vein component in the petrogenesis of the southern magmas, although the silica-saturated, low $CaO_{(6)}$ compositions of the magmas precludes an origin purely by pyroxenite vein melting. Furthermore, high Cr and Ni concentrations in the southern magmas (Cr, 143 to 649 ppm; Ni 72 to 467 pmm) and olivine xenocrysts imply a significant contribution from the host peridotite. The large positive Nb-Ta anomalies relative to the LILE and REE in the S-SCLM suggests that either metasomatism involved the preferential addition of Nb and Ta to the source region, or that the processes which resulted in HFSE enrichment were decoupled from the REE and LILE addition, in terms of mechanism and/or time. The presence of a positive Pb anomaly, indicative of altered oceanic crust (Hart, 1984), and the absence of any correlation between Nb/Ta and La/Yb, Nb/La or the LILE in the southern shonshonites supports the latter hypothesis. Nonetheless, a mechanism for the transfer of substantial Nb and Ta (and to a lesser extent Zr, Hf and Ti) to the SCLM source region is required. Such a process must also explain the subchondritic Nb/Ta (average 8.8, range 7.2 to 10.3) of the S-SCLM, as the high Nb and Ta concentrations in the source region preclude an origin by a previous melt extraction event. Nb/Ta may be fractionated in aqueous fluids in equilibrium with residual rutile where $D_{Ta\ rutile/fluid} < D_{Nb\ rutile/fluid}$ (Brenan et al., 1994), however, as discussed above, the absolute concentrations of Ta in the fluid are likely to be insignificant, and certainly cannot account for the extreme enrichment observed here. Carbonatite metasomatism is also unlikely, as the $CaO_{(6)}/Al_2O_{3\,(6)}$ of the southern magmas is low (0.2 to 0.7). Therefore, it seems most probable that the metasomatic agent(s) must be silicate melts of some description. Ocean Island Basalts (OIB) are characterised by positive Nb and Ta anomalies (Sun and McDonough, 1989) and percolation of the S-SCLM by small

degree OIB melts in a manner similar to that envisaged by McKenzie (1989) could explain the enrichment pattern of the S-SCLM. However, metasomatism by an OIB component is inconsistent with the radiogenic $^{207}Pb/^{204}Pb_{(i)}$ and $^{208}Pb/^{204}Pb_{(i)}$ of the southern shoshonites. Furthermore, OIB's are characterised by Nb/Ta of ~ 17.7 (Sun and McDonough, 1989), too high to explain the subchondritic Nb/Ta of the S-SCLM. Kepezhinkas et al. (1996) suggested that metasomatism of mantle peridotite by slab melts (adakites) could produce a source with high Nb and Sr concentrations. This mechanism is thought unlikely as adakite metasomatism will result in a source with high Na_2O/K_2O (3 to 6.5; Kepezhinkas et al., 1996), inconsistent with the potassic nature of the southern magmas (Na_2O/K_2O of 0.1 to 0.5). Furthermore, melts of eclogitised oceanic crust will have Nb/Ta similar to, or greater than, MORB and OIB. Enrichment by either bulk addition of sediment, or melts derived from post Archean crust (Nb/Ta ~ 11; Taylor and McLennan, 1985), proposed to explain the trace element signature of the N-SCLM, will produce Nb/Ta signatures too high to explain the Nb/Ta of the S-SCLM. However, Archaean crust has considerably lower Nb/Ta signatures (~6; Wedepohl, 1991) and metasomatism by either bulk addition of Archean sediment, or by Archean sediment melts, can explain the low Nb/Ta of the S-SCLM.

5.6 Discussion 3: The post-collisional evolution of the Tibetan lithosphere

In this section, the petrogenesis of the northern and southern shoshonites and the southern dacites is discussed with a view to constraining the thermal state of the SCLM at the time of their emplacement. Building on the arguments presented in Chapter 4, these finding are then evaluated in terms of their geodynamic significance.

5.6.1 Depths of melting for the shoshonite series: constraints from residual source mineralogy

In section 5.5.1, it was argued that residual pargasitic amphibole in the source region was required to explain the petrogenesis of both lava suites. Pargasitic amphibole is not stable above pressures of 2.7 GPa at 1050-1100°C in the lithospheric mantle (Mengel and Green, 1989; Wallace and Green, 1991; Konzett et al., 1997; Niida and Green, 1999) although flourine rich endmembers ($F^-/F^-+OH^- > 0.43$) may be stable up to 3.5 GPa and 1300°C (Foley, 1991). The presence of amphibole and garnet in the source of both groups of magmas constrains the pressures of melt generation to be between the garnet-spinel transition (Wallace and Green, 1991; Robinson and Wood, 1998; Klemme and O'Neill, 2000) and the limits of pargasite amphibole stability (Figure 5.17). The lower pressures inferred by Hirschmann and Stolper (1996) for the garnet spinel transition in pyroxenite are not adopted here, given the low amounts of clinopyroxene inferred in both source regions

(5.4.1.1) and the arguments against pure vein melting discussed in section 5.5.2. If the higher clinopyroxene D_{HREE} values of Blundy et al. (1998) are incorporated into the melting models (section 5.5.1), then there is no requirement for garnet in the S-SCLM, and < 1% garnet is needed in the N-SCLM. Irrespective of this, the data indicate that melting took place in the spinel-garnet transition zone i.e. ≥ 1.8 GPa, possibly at slightly higher pressures for the northern group (Figure 5.17). The small degrees of melting inferred for both groups suggest that melting occurred just above the solidus and do not support a long melting column. Therefore the lower pressure stability limit for pargasite amphibole, 2.7 to 2.8 GPa is preferred here and provides a maximum constraint on the depth of melting (~ 80 km). The inferred depths of melting (~ 65 to 80 km) are somewhat deeper than the depths of ~58 km inferred by McKenzie (pers comm.) based on inverse modelling of the same datasets. This discrepancy may arise from the fact that the parameterisations used by McKenzie and O'Nions (1991) and Tainton and McKenzie (1994) are based on the REE, and do not implicitly involve the LILE, critical for determining the presence of residual phase assemblages such as amphibole, which impose their own depth constraints.

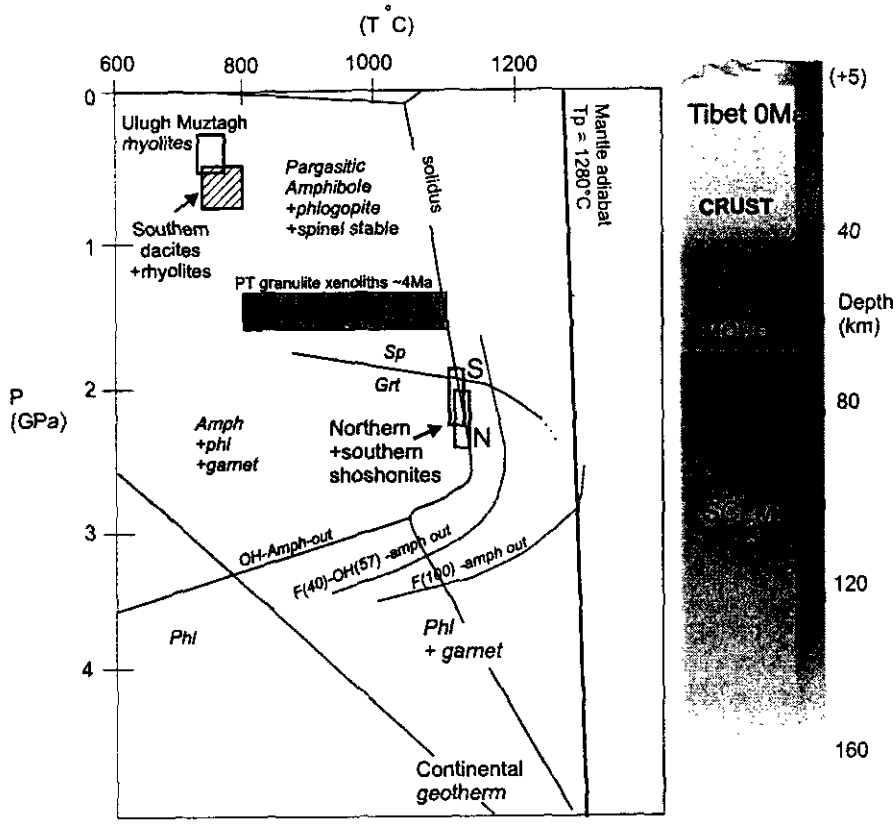

Figure 5.17 Pressure temperature diagram and schematic crustal section for the post-collision Tibetan lithosphere

Based on seismic data from McNamura et al. (1997). Stability fields of amphibole, phlogopite (Mengel and Green, 1989; Wallace and Green, 1991; Konzett et al., 1997; Niida and Green, 1999) and garnet (Wallace and Green, 1991; Robinson and Wood, 1998; Klemme and O'Neill, 2000) are shown. Also shown is a typical continental geotherm for comparison (calculated for a surface temperature of 0°C, a lithospheric thickness of 180 km, and a mantle heat flux of 24 Wm^{-2}), and the PT conditions recorded by anhydrous granulite xenocrysts entrained in 4 Ma Dogai Coring lavas. PT constraints for the shoshonites, southern Tibetan rhyolites/dacites, and the Ulugh Muztagh rhyolites are shown.

5.6.2 Petrogenesis of the southern Tibetan dacites and rhyolites

The Daggyai Tso (discussed briefly in Chapter 4), Namling and Manasarowar (Miller et al., 1999) series consist of high-K calc-alkaline dacites and rhyolites, with lower incompatible trace element concentrations than either the southern or northern shoshonite series (Figure 5.7 A, B.). The absence of significant Eu anomalies (Figure 5.8 B) indicates that feldspar was not present in their source region, and low HREE concentrations suggest garnet in the melting residue. Their Sr and Nd isotopic compositions are distinct from the southern shoshonite series (Figure 5.9 A) and appear similar to those of the northern groups. However, the data do not support mixing with the northern magmas or a relationship via fractional crystallisation-assimilation processes. The constraints on intensive parameters discussed in Section 5.2.1 can be used to place broad constraints on the origin of the the southern dacites and rhyolites. Estimated magma temperatures, based on zircon and monazite saturation (Watson and Harrison, 1983; Montel, 1993) and Fe-Ti oxide thermometry (Ghiorso and Sack, 1991) are 720 to 800°C and 830 to 900°C, respectively (section 5.2.1). Pressures of 0.55 to 0.82 GPa obtained using the Al-hornblende calibration of Johnson and Rutherford (1989) and Schmidt (1992) suggest that amphibole crystallised within the melt at depths of 15 to 23 km (assuming a lithostatic gradient of 27 GPa km^{-1}). This probably reflects the depths of magma storage within the crust. These observations imply a dominant contribution from the upper crust, although a minor mantle component cannot be ruled out (e.g. Patiño Douce, 1999). Interestingly, zircon and monazite saturation temperatures calculated for the Ulugh Muztagh rhyolites (using data from McKenna and Walker, 1990) give similar temperatures of 720 to 760°C, although the shallow depths of

melting (<15km) suggested by these authors are less well constrained. These temperatures indicate the presence of elevated crustal geotherms in both northern and southern Tibet (Figure 5.17), and probably relate to the advection of heat from mafic shoshonitic magmas.

5.6.3 Tectonic Implications

In Chapter 4, a link between east-west extension and Miocene potassic magmatism in southern Tibet was inferred from north-south trending dykes, including the Pabbai Zong glimmerites and dykes from the Daggyai Tso graben. On the basis of these observations, it was argued that the Miocene uplift of the plateau could not be related solely to plate boundary forces or to continental subduction, and that removal or erosion of part of the south Tibetan SCLM was required. This is consistent with the refractory compositions inferred for both the remaining N-SCLM and the S-SCLM – depleted SCLM is typically more buoyant than more fertile compositions (Jordan, 1978), and therefore will be harder to destabilise during convergence. Mesozoic removal or erosion of the lower (more fertile?) SCLM beneath Tibet and its replacement by asthenosphere could have been accomplished in a number of ways, as discussed in Chapter 2. Models include wholesale delamination of the SCLM (Bird, 1979), destabilisation and convective thinning following distributed shortening (Houseman et al., 1981), more episodic convective thinning involving dripping (Rayleigh-Taylor) instabilities at the mechanical boundary layer (Conrad and Molnar, 1999). Thinning of the SCLM may also be accomplished by subduction- related processes; these include thermal erosion of the SCLM above the subduction zone by asthenosphere upwelling through "slab windows" (Hole et al., 1991) or similarly, upwelling following slab breakoff (Davies and von Blanckenburg, 1995; Von Blanckenburg and Davies, 1995; Davies and von

Blanckenburg, 1997). Delamination (Bird, 1979) and the formation of "slab windows" (Hole et al., 1991) are both considered unlikely in the case of Tibet, due to the absence of large volumes of asthenosphere-derived magmatism on the plateau and evidence for remaining SCLM to depths of at least 90 km (section 5.6.1). The relative importance of the remaining mechanisms remains a subject of debate, and the true situation is clearly more complex. This point is emphasised by recent analogue modelling (Pysklywec et al., 2000) which demonstrates that the SCLM can exhibit a range of deformation modes during convergence, including Rayleigh-Taylor type instabilities, ablative SCLM consumption and slab breakoff, and transitional modes between these.

Further understanding of the behaviour of the SCLM during convergence and refining existing geodynamic models has so far been limited by the lack of direct knowledge regarding the thermal evolution of the continental lithosphere following orogenesis. The pressures and temperatures required for the genesis of the shoshonitic and dacitic-rhyolitic melts (sections 5.6.1 and 5.6.2) place constraints on the thermal structure of the northern and southern Tibetan lithosphere. Time-averaged geotherms calculated by simple linear extrapolation from the pressures and temperatures of shoshonite genesis to those inferred for the dacites and rhyolites (Figure 5.17) are ~ 7 to 12°Ckm^{-1} (south) and ~ 4 to 6°Ckm^{-1} (north). The shallow geotherm implied for northern Tibet is broadly consistent with thermobarometric constraints on lower crustal xenoliths within Dogai Coring volcanics (Hacker et al., 2000), which indicate that temperatures of 800 to 1000°C were attained at depths of ~ 55 km in the lower crust (Figure 5.17). Although the geotherms calculated are highly approximate, they unequivocally imply a thermally elevated Tibetan lithosphere during the Neogene. Seismic and magnetic data indicate that the same thermal structure prevails today in northern Tibet, with the speed of mantle P waves implying Moho

temperatures of 840 to 1170°C (McNamura et al., 1997) and magnetic satellite data indicating temperatures of >550°C across the plateau of depths at ~15 km (Alsdorf and Nelson, 1999). The thermal structures inferred for the northern and southern Tibetan lithosphere are remarkably similar and indicate that an elevated thermal gradient was widespread across the plateau for a considerable period of time, although the chronology of shoshonitic magmatism across the plateau (Figure 5.1) argues against a synchronous event.

Although a hot Tibetan SCLM during the Neogene is consistent with the convective removal of much of the SCLM following distributed lithosphere shortening (Houseman et al., 1981), it does not unambiguously support this model. There are many reasons to question this model – *synchronous* removal of lower SCLM is inconsistent with the diachronous patterns of volcanism (Figure 5.1), extension (Bi et al., 1999; Yin et al., 1999b) and unroofing (Mock et al., 1999; Zheng et al., 2000) across Tibet. Furthermore, convective removal does not explain why the warm area of upper mantle inferred by McNamura et al. (1997) on the basis of slow S-wave propagation does not correspond to the region of Recent volcanism (Figure 5.1). Several studies have suggested that convective thinning should be an event with a timescale no greater than ~5 Ma (e.g. Lenardic and Kaula, 1995). However, mafic potassic magmatism has been ongoing in northern and southern Tibet for > 18 Ma (> 36 Ma including the Qiangringnoinza samples) and 12 Ma, respectively. One means of reconciling prolonged phases of SCLM derived magmatism with the short timescales inferred for convective thinning by Lenardic and Kaula (1995) is to invoke more episodic instabilities, with variable lengthscales and amplitudes (e.g.Conrad and Molnar, 1999). Such episodic SCLM thinning could explain the diachronous pattern of magmatism and uplift in northern Tibet in terms of heterogeneous shortening and delayed instabilities. This is supported by seismic evidence for destruction and recycling of Asian lithosphere beneath northern Tibet.

However, the relationship of SCLM thinning in the north to underthrusting of Indian lithosphere in the south appears more complex (Kosarev et al., 1999).

The arcuate pattern of magmatism in southern Tibet, which mirrors the trace of the Indus-Tsangpo Suture Zone (ITSZ), implies some link between elevated thermal structures in the southern Tibetan lithosphere during the Miocene and the original geometry of the subduction zone. Miller et al. (1999) suggested that the volcanics exposed at Maquiang in southern Tibet, which have OIB-like Sr and Nd isotope signatures, were derived from the asthenosphere, lending support to near-complete removal of SCLM in the Maquiang region. However, there are too few samples to be conclusive. Interestingly, the oldest mafic magmatism is found in the southwest, and emplacment ages become progressively younger to the east (Figure 5.1), although the correlation is weak. This may reflect the original collision geometry, as the timing of continental collision decreases from 60 to 65 Ma in the west (Klootwijk et al., 1992) to between 48 and 50 Ma further east (Patriat and Achache, 1984; Klootwijk et al., 1992). Such a relationship implies a role for lithosphere thinning coupled to slab breakoff, or a similar process, in the evolution of southern Tibet. High P-wave velocity zones ~350 to 800 km below India, Pakistan and Nepal have been interpreted as slab remnants overriden by the Indian plate (Van der Voo et al., 1999); an alternative interpretation would be that they represent sinking fragments of removed Tibetan SCLM. Kosarev et al. (1999) suggested, from seismic evidence, that the destruction of the underthrusting Indian slab beneath Tibet is an ongoing process, and presently coupled to the destruction of northern Tibetan SCLM. As discussed by Chemenda et al. (2000), some role for the removal of the dense oceanic slab is implied by the change in the angle of underthrusting Indian lithosphere from near vertical at ~ 60 Ma (O'Brien et al., 1999; de Sigoyer et al., 2000) to its present shallow angle. If this is the case, the timing of mafic

magmatism indicates that "breakoff" and local thinning of the overlying SCLM occurred by 25 Ma, resulting in uplift and extension of southern Tibet by 18.3 ±1.6 Ma. In this context, the cessation of mafic magmatism at 13.3 ± 0.8 Ma may reflect the switch from subduction to underthrusting, which would shield the remaining SCLM against further removal. However, there are strong arguments for the presence of young (< 1 Ma) basaltic (Hoke et al., 2000) and silicic (Nelson et al., 1996) melts within the southern Tibetan crust, and the transition from volcanism to plutonism may be explained by the extension enhanced mid-crustal crystallisation of melts (Gans and Bohrson, 1998). As pointed out in Chapter 4, the youngest mafic and silicic post collisional volcanics (13.3 ± 0.8 and 10.5 ± 0.4 Ma, respectively) in southern Tibet do not significantly post-date upper crustal extension in southern Tibet and northern Nepal, constrained to be from 8 to 14 Ma (Coleman and Hodges, 1995; Harrison et al., 1995). This lends support to the model of Gans and Bohrson (1998). The present-day mid-crustal plutonism inferred by Nelson et al. (1996) may reflect a continuation of the processes which produced the Miocene shoshonites, or alternatively may be caused by a separate mechanism (e.g. Harrison et al., 1998). Given the evidence for the ongoing destruction of the Indian lithospheric mantle and thinning of Asian lithospheric mantle (Kosarev et al., 1999) the first hypothesis is preferred.

This discussion indicates that while elements of episodic convective removal envisaged by Conrad and Molnar (1999) and slab detachment (Chemenda et al., 2000) can be applied to north and south Tibet, respectively, their mechanisms and interaction with each other are considerably more complex than accounted for in any of the present models. Recent numerical modelling by Pysklywec et al. (2000) suggests a meld of both models - consistent with the patterns of surface volcanism on the plateau, evidence for diachronous uplift (Copeland et al., 1987; Copeland and Harrison, 1990; Mock et al., 1999; Zheng et al., 2000)

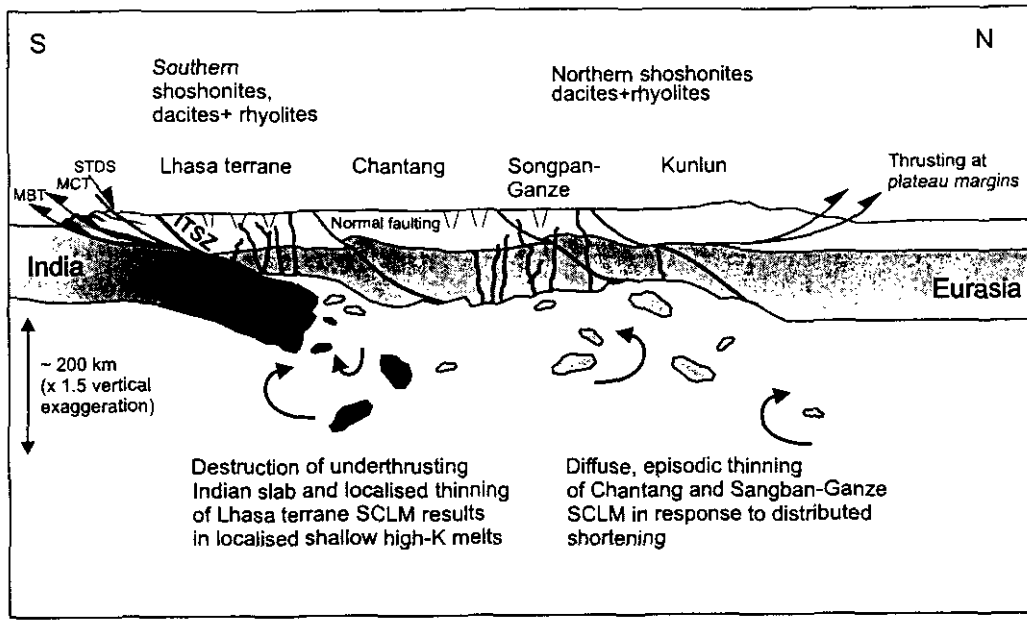

Figure 5.18 Illustration of the combined slab breakoff and episodic convective removal model

Based on the spatial distribution of the northern and southern shoshonites, in particular the absence of magmatism in the northern Lhasa and southern Changtang terranes, although it must be borne in mind that this may simply reflect a sampling bias. Incorporates the data and models of McNamura et al. (1997); Rodgers and Schwartz (1997); Kosarev et al. (1999); Van der Voo et al. (1999); Pysklywec et al.(2000).

and seismic constraints (Kosarev et al., 1999). This scenario is illustrated in Figure 5.18. While it is difficult to constrain the absolute timing of SCLM thinning resulting from either slab breakoff or convective processes, it is clear that it must predate the oldest shoshonitic magmatism, constrained to be 25.4 ± 0.2Ma in southern Tibet (Miller et al., 1999) and 18.5 ± 0.8 Ma in the north (Turner et al., 1996). If the 36 Ma Quangringnoinza lavas in north-central Tibet (Hacker, pers comm.) and the belt of 30.0 ± 1.1 to 36.7 ± 0.3 Ma volcanics in eastern Tibet (Chung et al., 1998) are also derived by shallow small degree melting of the SCLM, then an earlier episode of SCLM thinning is implied. Alternatively, they may represent an unrelated event – clearly, hydrated SCLM provides a potential source for alkaline magmas which can be tapped as a consequence of various geodynamic processes at various times.

5.6.3.1 ^{40}Ar-^{39}Ar constraints: a role for recent metasomatism?

In further evaluating the relative significance of slab breakoff and distributed shortening in triggering SCLM thinning beneath southern Tibet, unambiguous age constraints on the timing of events affecting the southern Tibetan SCLM between collision and shoshonite genesis are required. Despite their fundamental importance, these events have proved elusive to date. In the model of slab breakoff, the detachment of the oceanic part of the subducting slab is triggered by tensional forces produced by the resistance of the more buoyant continental crust to subduction and the opposing pull of the dense slab. Therefore, models invoking some component of SCLM thinning following slab break-off predict that subduction-realted metasomatism of Tibetan SCLM must occur prior to breakoff; i.e. either

it should be synchronous with, or post-date collision slightly. In contrast, convective removal makes no specific predictions regarding metasomatism.

While obtaining absolute age constraints on metasomatism is difficult, recent research (Kelley and Wartho, 2000) demonstrates that mantle phlogopites can retain Ar while remaining substantially above the conventional closure temperatures (~400°C, dependent on grain size, (Dodson, 1973)) and therefore xenocrystic phlogopites have the potential to provide age constraints on metasomatic processes. Following this approach, magnesian (Mg#'s of 91 to 94) phlogopite megacrysts from the glimmerite dyke T2A were analysed by ^{40}Ar-^{39}Ar techniques outlined in Chapter 3. These megacrysts are interpreted as mantle xenocrysts, based on petrographic observations, high Mg#'s and concentrations of compatible elements such as Cr (section 5.2). Preliminary results from IR laser spot traverses are shown in Figure 5.20; the traverses were performed on the same crystal and are orthogonal to each other. In common with other xenocrystic phlogopites (Kelley and Wartho, 2000), they show Ar diffusive loss profiles with ages decreasing towards the eruption age at the grain margins. This is typical of partial resetting, as opposed to incorporation of excess ^{40}Ar, which would produce a U-shaped profile (Pickles et al., 1997). In both profiles (Figure 5.19 A and B), the core ages of 55.2 ± 1.1 Ma (A) and 69.4 ± 0.4 Ma (B) are striking, and suggest that the Ar loss at the crystal margins is not a late stage alteration feature but reflects diffusive loss, recording the incorporation of the crystal in a melt and its subsequent transport from the mantle source to the surface. This is supported by the positive slope of the individual core analyses on the inverse isochron diagram (Figure 5.19 C), which is indicative of diffusive loss (see Chapter 3). These results can be used to place a preliminary age constraint of 62 ± 1.7 Ma (average of the two core ages) for the most recent – or conceivably all of- the metasomatism of the southern Tibetan SCLM.

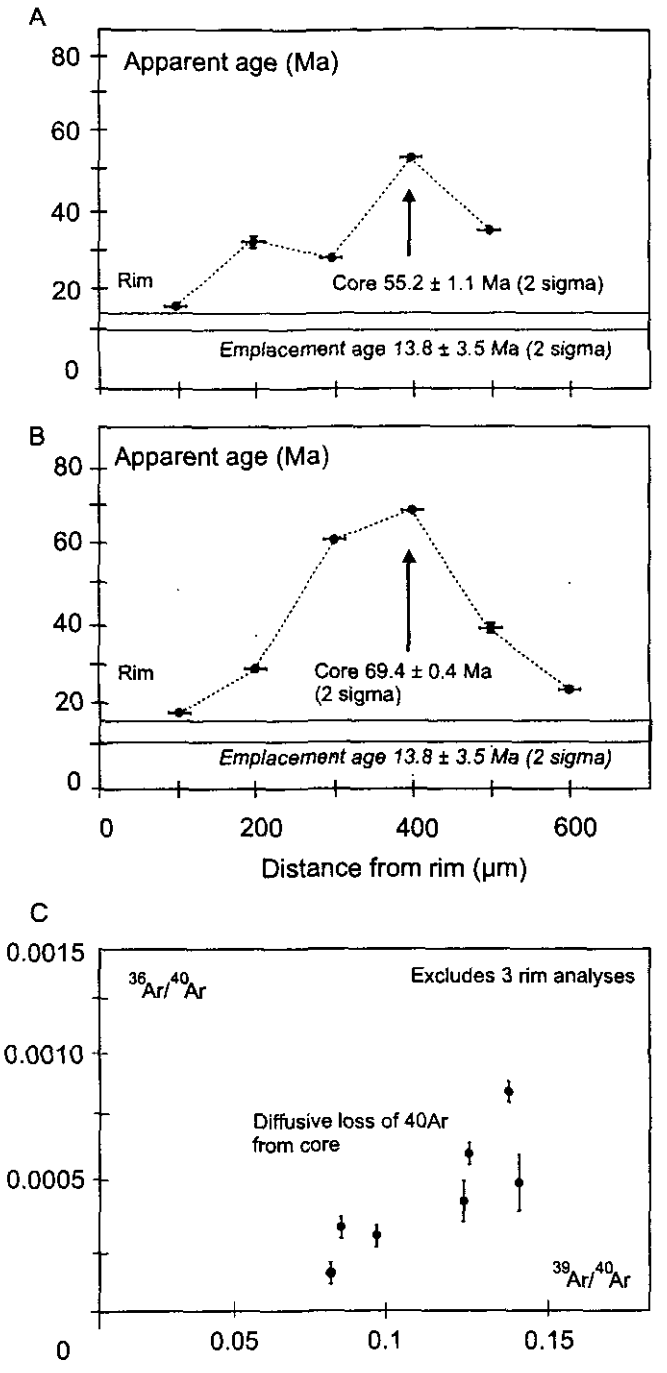

Figure 5.19 Apparent ^{40}Ar-^{39}Ar age profiles in xenocrystic phlogopites

A) and B) Plots of apparent ^{40}Ar-^{39}Ar age vs. distance from the rim of the xenocrystic phlogopite grain from sample T2A. Note that although the two traverses are orthogonal, they do not intersect precisely in the centre of the crystal. The individual ages were obtained using single IR laser spots, which have a diameter of ~ 20μm. Error bars are shown for both ages (1 sigma) and position (set at 20μm). At the crystal rims the ages obtained approach the emplacement age, calculated from individual crystal fusions with the IR laser (presented in Chapter 4). C) Inverse isochron diagram, rim analyses are omitted. Error bars are 1 sigma. The positive slope is interpreted in terms of coupled diffusive loss of ^{40}Ar and gain of atmospheric ^{36}Ar.

If these ages are correct, the timing of metasomatism of the southern Tibetan lithosphere is synchronous with the onset of continental collision, constrained by APWP to be between 60 and 65 Ma (Klootwijk et al., 1992). As significant thickening of the southern Tibetan lithosphere is unlikely to have occurred prior to continent-continent collision, this metasomatic event cannot reflect the convective removal of Lhasa terrane SCLM. The most reasonable explanation for this early Tertiary age is that it reflects crystallisation of phlogopite following the introduction of LILE and K enriched melts/fluids from the subducting slab (Maury et al., 1992). The ^{40}Ar-^{39}Ar constraints on metasomatism emphasise that the model ages recorded by Sr, Nd, Pb and Os isotopes (Schaefer et al., 2000) in the southern shoshonites cannot be interpreted in terms of absolute timing of SCLM stabilisation - these model ages probably reflect the age(s) of the metasomatic component(s). Metasomatism related to early continental collision is a strong argument for the role of slab detachment in the genesis of the southern Tibetan shoshonites, however, independent constraints on both the timing of this event, and the origins of the metasomatic components involved, are required. These are discussed further in Chapter 6.

5.7 Summary

While constraining the petrogenesis of potassic magmas is often difficult, and subject to many assumptions, it has been demonstrated here that a combination of forward and inverse approaches towards trace element modelling can provide insights into the conditions of melting and the composition of SCLM source regions. The contrasting geochemistry of the northern and southern Tibetan volcanics can be explained in terms of derivation from two distinct SCLM source regions beneath the Tibetan plateau. Both the northern and southern

Tibetan SCLM source regions record early depletion by melt extraction, followed by metasomatic re-enrichment. The two source regions have contrasting metasomatic signatures, although the timing of metasomatic events is not well constrained by whole rock Sr, Nd or Pb model ages. The petrogenesis of both the northern and southern magmas can be explained by small degree melting of a peridotite source in the presence of residual pargasitic amphibole, garnet and phlogopite – and additionally rutile, in the case of southern Tibet. The presence of residual pargasitic amphibole and garnet constrains melting to be at depths between 65 to 85 km, just below the MOHO in both cases. This implies elevated temperatures within the northern and southern SCLM during the Miocene, supporting geodynamic models which invoke a major component of SCLM thinning or erosion. However, the diachroneity of magmatism and extension across the plateau imply that SCLM thinning is a more spatially and temporally complex processes than predicted by models of convective removal (Houseman et al., 1981) or of slab breakoff (Davies and von Blanckenburg, 1995; Chemenda et al., 2000). A combination of both models is suggested here, with SCLM thinning linked to subduction and detachment of the oceanic slab in southern Tibet, while more episodic convective removal of thickened lithosphere occurs beneath northern Tibet. This can explain the relatively narrow band of potassic magmatism north of the ITSZ in the south and the more widespread and diffuse distribution of potassic magmatism in central and northern Tibet. Preliminary ^{40}Ar-^{39}Ar data suggests that the southern SCLM was metasomatised as recently as 62 ± 1.7 Ma, synchronous with the onset of continental collision (Klootwjick et al., 1992).

6 Conclusions and Future Research

A major objective of this thesis has been to investigate the postcollisional thermal and tectonic evolution of the Himalayan-Tibetan orogen. The last three chapters have focussed on individual aspects of this problem, and their results are summarised and integrated together here, allowing an overview of post-collisional events within the Himalaya and Tibet. The implications of these results for models of continental orogenesis are then discussed.

6.1 Conclusions

In southern Tibet and the Himalaya, a number of major deformation and magmatic events were initiated during the early Miocene, indicative of a major change in the dynamics of the orogen at this time. ^{40}Ar-^{39}Ar ages for the HHCS and the TSS in the proximity of the Malari normal fault (the STDS in the Garhwal Himalaya), indicate that these units cooled through muscovite closure temperatures between 12.6 ± 0.7 Ma to 16.0 ± 0.3 Ma, and 24.3 ± 1.6 to 41.5 ± 1.9 Ma respectively (note that a detrital component, dated at 598 ± 82 Ma, was preserved in one sample). The older Ar-Ar ages of the TSS indicate that this unit experienced a different thermal history to the HHCS and that the HHCS and TSS were juxtaposed by the Malari Fault following cooling of the TSS through muscovite closure temperatures. This places a maximum age constraint of 24.3 ± 1.6 Ma on the timing of normal movement on the Malari Fault. A deformation age of 17.3 ± 0.4 Ma from the

fault zone provides a minimum age constraint. One-dimensional thermal modelling demonstrates that the synchronous cooling of the HHCS is consistent with normal movement on the STDS between 17.3 ± 0.4 and 24.3 ± 1.6 Ma. The hornblende ^{40}Ar-^{39}Ar age of 19.8 ± 2.6 Ma obtained by (Metcalfe, 1993) in the footwall of the MCT is within error of these constraints for extension on the Malari Fault, implying that movement on the STDS and MCT in Garhwal was relatively synchronous. This onset of north-south extension in the Garhwal region between 17.3 ± 0.4 and 24.3 ± 1.6 Ma is in accord with data from other sections in the central and western Himalaya (Figure 2.2) (Coleman and Hodges, 1998; Vance et al., 1998; Harrison et al., 1999). This suggests that the initiation of extension was widespread for over 800 km along strike in the orogen the early Miocene.

Preservation of detrital ages in muscovites from the TSS indicates that the peak prograde temperatures experienced by the TSS approached muscovite closure temperatures (~ 400°C). Therefore, the timing of prograde metamorphism in the TSS is constrained from the ^{40}Ar-^{39}Ar data to be at least 41.5 ± 1.9 Ma, similar to prograde metamorphism in the HHCS of this region (Prince, 1999). The Tertiary ^{40}Ar-^{39}Ar ages of the TSS reflect cooling either due to thermal relaxation or due to thrusting on the Malari Fault. South-vergent shear fabrics in the TSS are in accord with the latter hypothesis. One-dimensional thermal modelling using the ^{40}Ar-^{39}Ar ages obtained for the TSS in conjunction with Sm-Nd garnet ages (Prince, 1999) and U-Th-Pb monazite inclusion ages (Foster et al., 2000) from the HHCS indicates that prograde metamorphism of the HHCS resulted from burial to depths of 17.9 to 28.7 km, while the TSS (two samples) were buried 16.4 to 28.5 km. This is consistent with burial of the HHCS by the TSS, following southward thrusting on Malari Fault, whereas the TSS must have been buried by south-directed thrusting on faults to the north. Early reverse activity on the Malari Fault is supported by shear criteria and probably

occurred between 41.5 ± 1.9 to 24.3 ± 1.6 Ma, consistent with the progressive transferral of deformation to the south over a period of ~ 55 Ma, from the ITSZ to the Main Boundary Thrust and ultimately the Main Frontal Thrust. A switch from a compressive to an extensional styles of deformation in the Malari region between 24.3 ± 1.6 and 17.3 ± 0.4 Ma, and in other sections of the western and central Himalaya in the Early Miocene indicates a major change in the stress balance of the orogen at this time.

The emplacement of north-south trending shoshonitic (Pabbai Zong group) and calc-alkaline (Daggyai Tso group) dykes in southern Tibet is constrained by ^{40}Ar-^{39}Ar dating to be from 18.3 ± 2.7 Ma to 13.3 ± 0.8 Ma and at 17.3 ± 1.9 Ma, respectively. The north-south orientation of the dykes (Figure 4.1) indicates that they were emplaced in a dominantly east-west extensional strain field, similar to the present-day tectonic regime indicated by both field observations (Armijo et al., 1986) and earthquake fault plane solutions (Molnar and Tapponnier, 1978). Therefore the earliest phase of dyke emplacement constrains the initiation of east-west extension in southern Tibet to be at least 18.3 ± 2.7 Ma. The Pabbai Zong shoshonite dykes have enriched isotopic and trace element signatures (Figure 4.3), similar to early Miocene lava flows in southern Tibet, attributed to small-degree melting of enriched regions within the SCLM (Miller et al., 1999). This comparison suggests that regional east-west extension and mantle derived magmatism in southern Tibet were linked, an observation not predicted by rigid plate models. Moreover, the magnitude of extension in south Tibet (< 1 %), constrained by the distribution of north-south dykes and and normal faults (Armijo et al., 1986), is insufficient to cause melting decompression melting of normal potential temperature mantle (McKenzie and Bickle, 1988). A possible explanation for SCLM melting and associated extension is the thinning of lower SCLM following either

orogenic thickening (Houseman et al., 1981; Turner et al., 1992) or slab breakoff (Davies and von Blanckenburg, 1995). In these models, extension reflects the dissipation of potential energy following isostatic uplift of the region, a consequence of the removal of dense SCLM and replacement with more buoyant asthenosphere. The earliest phase of volcanism may constrain SCLM thinning to be at 24.2 ± 0.2 Ma in southern Tibet (Miller et al., 1999), while dyke emplacement ~ 8 Ma later suggests a delay between SCLM thinning and the onset of observable surface extension. This is consistent with the short timescales of melt migration (Spera, 1987; Asmerom et al., 2000) relative to those of isostatic and thermal re-equilibration of the lithosphere.

Direct relationships between extension and uplift are supported by $\delta^{18}O$ data for sediments in the Thakkola graben of Nepal which show that significant elevation was attained prior to extension (Garzione et al., 2000). In this context, the onset of extension, constrained by the oldest dykes to be 18.3 ± 2.7 Ma, places a minimum constraint on the time at which southern Tibet achieved excess potential energy and high elevation. If the emplacement of northwest-southeast trending shoshonitic dykes in the northern Karakoram at 22 ± 1.0 to 24.0 ± 1.0 Ma (Rex et al., 1988; Pognante, 1990) is related to the same processes, then high elevation may have been attained even earlier. Indeed, excess potential energy relating to plateau uplift may have been achieved before 24.5 ± 0.2 Ma in S. Tibet, when the earliest dated mafic lavas were emplaced (Miller et al., 1999). This is consistent with the exhumation of the Gangdese Batholith between 17 and 20 Ma (Copeland et al., 1987) and molasse deposition, indicative of enhanced denudation, from 19 to 20 Ma (Harrison et al., 1993).

The uplift of the southern margin of the Tibetan plateau, inferred to be between 18.3 ± 2.7 and 24.2 ± 0.2 Ma, overlaps with movement on the STDS and the MCT in the central and western Himalaya (this study; see Hodges, 2000 for a review). This relationship is consistent with the southward extrusion of a crustal wedge from the orogenic region by synchronous normal and reverse faulting in response to an increased potential energy contrast at the southern margin of the plateau (Platt and England, 1994; Grujic et al., 1996; Hodges, 2000). If uplift of the southern margin of the plateau intensified the Asian monsoon as suggested by Kutzbach et al. (1989), this would enhance silicate weathering, increasing seawater $^{87}Sr/^{86}Sr$ (Palmer and Elderfield, 1985). Normal movement on the STDS and exhumation of high grade rocks in the Himalaya would be expected to produce a similar result.

The relatively high Mg#'s of mafic shoshonites from northern and southern regions (Figure 5.1) of the plateau indicate derivation from a mantle source. High K_2O contents and flat K_2O–SiO_2 trends (Figure 5.4) for both northern and southern suites implies phlogopite or K-amphibole saturation (Mengel and Green, 1989) and therefore the presence of these phases within the source region. This alone indicates an origin by the melting of enriched regions within the SCLM. Shoshonites from both northern and southern regions of the plateau have distinctive trace element signatures, with steep LREE/HREE, negative Nb, Ta and Ti anomalies and positive Pb anomalies (Figure 5.8). The main geochemical characteristics of the northern and southern shoshonites are summarised and compared in Table 6.1. Incompatible element and LREE concentrations in the northern and southern shoshonites are elevated relative to average continental crust (Taylor and McLennan, 1985) and primitive mantle (Sun and McDonough, 1989). The northern and southern shoshonites have enriched Sr, Nd and Pb isotopic signatures that cannot be explained by mixing asthenospheric and

crustal endmembers, in accord with a SCLM origin (Figure 5.9, Figure 5.10). Nd model ages for the southern and northern groups are 1.5 to 3.0 Ga and 1.0 to 1.3 Ga, respectively. $^{207}Pb/^{206}Pb$ model ages (Silver et al., 1988) range from 2.8 to 3.3 Ga (north), and 3.3 to 4.1 Ga (south). The isotope data suggest that the northern and southern shoshonites were derived from different source regions. This is consistent with the higher $Si_{(6)}$, lower $Fe_{(6)}$, $Ti_{(6)}$ and $Ca_{(6)}$ of the southern group relative to the northern group (Figure 5.11) which suggests that their source region had experienced a greater degree of depletion.

The nature of the melting regimes, and the mineralogy and composition of the mantle source regions were constrained using forward and inverse methods of trace element modelling. Calculated source compositions are enriched in incompatible elements relative to primitive mantle. The SCLM source of the northern Tibetan shoshonites shows a "subduction signature": negative HFSE anomalies (relative to the LILE and REE), LILE and LREE/HREE enrichment (Figure 5.16 A). In contrast, the source of the southern Tibetan magmas is characterised by higher concentrations of the HFSE relative to the LILE and REE (Figure 5.16 B). Both source compositions can be explained in terms of metasomatism by subducted sediment components. The southern source has a subchondritic Nb/Ta signature (Nb/Ta ~ 8.8), in contrast to the northern source (Nb/Ta ~ 20.5). The lower Nb/Ta of the southern source can be explained by metasomatism by an Archean sediment component; the corollary of this is that the Archean Pb and Nd model ages of the southern shoshonites undoubtedly reflect the antiquity of the metasomatic component(s) and therefore do not convey information about the age of the SCLM. ^{40}Ar-^{39}Ar dating of xenocrystic phlogopites suggests an age of 62 ± 1.7 Ma for the most recent – or conceivably all of- the metasomatism of the southern Tibetan SCLM. This age overlaps with APWP estimates for the onset of collision, between 60 and 65 Ma (Klootwijk et al., 1992), implying a

Table 6.1 Summary geochemistry of the northern and southern shoshonites

		North	South
isotope model ages (Ga)	Sr_{DM}	0.8 - 2.4	0.3 - 1.5
	Nd_{DM}	1.0 - 1.3	1.5 - 3.0
	$Pb_{DM-NHRL}$	2.8 - 3.3	3.3 - 4.1
major elements	$Si_{(6)}$	36.9 - 54.2	54.1 - 62.6
	$Ca_{(6)}$	3.0 - 11.6	2.1 - 7.6
	$Fe_{(6)}$	7.4 - 11.0	4.6 - 7.2
trace elements and REE	La/Yb	68.0 - 186.1	25.0 - 86.8
	Dy/Yb	1.9 - 4.0	1.5 - 5.3
	Ti/Y	338.0 - 514.1	128.3 - 336.1
	Rb/Ba	0.04 - 0.08	0.12 - 0.37
calculated source/ primitive mantle	LILE (Rb)	15.7 - 33.4	22.8 - 49.8
	HFSE (Nb)	2.7 - 3.8	38.3 - 143
	LREE (La)	14.2 - 20.1	2.3 - 5.4
	HREE (Yb)	0.6 - 1.4	0.4 - 0.7
	Nb/Ta	15.9 - 22.1	7.0 - 10.3
residual mineralogy used to calculate melting and source composition (modal abundance)	ol	0.63	0.69
	opx	0.17	0.115
	cpx	0.08	0.03
	phl	0.04	0.005
	amph	0.04	0.08
	rutile	0	0.05
	grt	0.02	0.01
	spinel	0.01	0.01

relationship between metasomatism and continent-continent collision. Both source regions are depleted in the HREE with respect to primitive mantle (Figure 5.16); mass balance calculations show this is consistent with melt extraction prior to metasomatism, in accord with the major element data. The relatively large amounts of melt extraction (25 to 30 %) inferred for the southern SCLM, suggest stabilisation during the early Proterozoic or even the Archaean, although they are not as great as the amounts of melting inferred in the stabilisation of cratonic regions, generally considered to be 30 to 40 %. The lower degrees of melt extraction (10 to 12 %) required to explain the genesis of the northern source suggest later SCLM stabilisation in a cooling Earth (Davies, 1995). Stabilisation of the southern and northern SCLM by the early Proterozoic is consistent with the ages of detrital zircon populations from major rivers draining northeastern regions of the plateau, which indicate major periods of crustal growth at 2.3 and 1.9 Ma (Bodet and Schärer, 2000).

Irrespective of the absolute timing of lithosphere stabilisation, the marked differences inferred for the source regions of the southern and northern shoshonites (the southern SCLM and northern SCLM, respectively) can be related to their derivation from the tectonically juxtaposed lithospheric terranes which comprise the plateau (Figure 5.1) (Dewey et al., 1988). It is suggested that the southern SCLM corresponds to the Lhasa Terrane, whereas the northern SCLM corresponds to the Changtang, Songpan-Ganze and Kunlun terranes.

Forward and inverse trace element modelling indicates that residual pargasitic amphibole, phlogopite and garnet are present in both southern and northern source regions, additionally, rutile is present in the southern source. The small amounts of garnet inferred in both sources (1 to 2 %) and the presence of pargasitic amphibole suggest that melting occurred at pressures between 1.8 and 2.7 GPa, probably just below the Moho (65 to 85 km). These

shallow depths of melting are consistent with the conductive heating of thinned or thermally eroded SCLM. Shallow SCLM melting is not predicted by rigid plate models, such as the eastward extrusion of lithospheric blocks (Tapponnier et al., 1982), or intracontinental subduction (Willett and Beaumont, 1994); in the latter case, continental subduction would predict melting at the base of the SCLM (> 170 km from seismic tomography, Kosarev et al., 1999).

While the shallow depths of melting inferred for the northern and southern shoshonites are consistent with convective removal of thickened SCLM (Houseman et al., 1981), the diachroneity of magmatism and extension across the plateau is more difficult to explain. Three broad pulses of magmatism in northern, southern and eastern regions of the plateau are discernable (Figure 6.1); magmatism is oldest in the eastern regions and youngest in the north, with considerable overlap in the timing of shoshonite magmatism in the northern and southern regions. In southern Tibet, potassic magmatism defines an arcuate band north of the ITSZ, mirroring the geometry of the suture zone, and emplacement ages of the shoshonites young towards the east, perhaps reflecting the west to east collision diachroneity (Klootwijk et al., 1985; Rowley, 1996). A link between Miocene potassic magmatism in southern Tibet and collision in the early Tertiary is suggested by the "metasomatic" ^{40}Ar-^{39}Ar age of 62 ± 1.7 Ma, and geochemical evidence for a subducted sediment component in the southern Tibetan SCLM. These observations are consistent with SCLM thinning following breakoff of the subducting slab after a diachronous collision and partial subduction of Indian lithosphere (Davies and von Blanckenburg, 1995; Chemenda et al., 2000). However the slab breakoff model cannot explain the more diffuse distribution of potassic magmatism in central and northern Tibet. While the diachroneity of magmatism in northern Tibet is not consistent with rapid, widespread convective removal (Houseman et

al., 1981), it may be attributed to more episodic convective thinning processes (Conrad and Molnar, 1999). Models of episodic convective thinning are based on the original continuum model (Houseman et al., 1981; England and McKenzie, 1982), but allow for the diachronous patterns of magmatism and extension in northern Tibet. Hence, a combination of both models is suggested here, with SCLM thinning linked to slab breakoff in southern Tibet, while more episodic convective removal of thickened lithosphere occurs beneath northern Tibet (Figure 5.18). Asthenospheric upwelling following slab breakoff could conceivably enhance the generation of convective instabilities at the base of the northern Tibetan SCLM. Such a scenario is consistent with the generally older ages of the southern shoshonites relative to the northern magmas and the younger ages for extension in northern Tibet (Bi et al., 1999)(Figure 6.1) but cannot be easily tested from the available data. Clearly, both slab breakoff and convective removal represent end-member descriptions of lithosphere behaviour during orogenesis, and the true situation is undoubtedly more complex.

Shoshonitic lavas from eastern Tibet form a broadly linear belt (Figure 5.1) that extends into Yunnan in the far south, where they are associated with the Red River Fault Zone and intrusions of similar age (Zhang and Schärer, 1999). These lavas predate both the northern and southern shoshonites (Figure 6.1) and probably represent small-degree melting of the SCLM in this region. The 36 Ma Quangringnoinza group (Hacker et al., 2000) probably forms the western end of this belt of lavas. Although they appear spatially associated with the Red River Fault Zone in the southeast, it is unlikely that their genesis can be related to transcurrant movement on this fault, as magmatism spans a period of over 7 Ma, a timespan greater than predicted by shear heating models (Kameyama et al., 1999). If the RRFZ is a lithosphere-scale fault, as has been suggested for the Altyn Tagh fault (Wittlinger et al., 1998), then it may have facilitated the transport of the southernmost magmas to the surface.

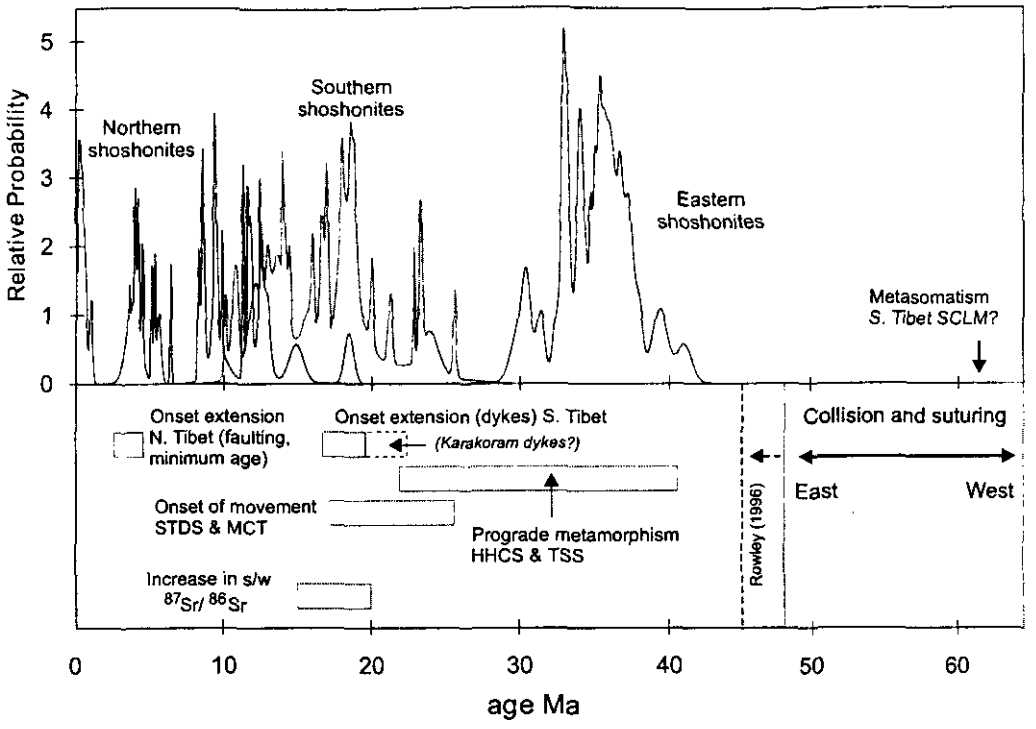

Figure 6.1 Age ranges of major Himalayan and Tibetan magmatic and deformation events

Cumulative probability of the timing of shoshonite magmatism in northern, southern and eastern Tibet. Cumulative probabilities were calculated using the Isoplot program (Ludwig, 1999); the calculation involves summing the individual ages and their associated errors within each group and then normalising to the number of samples in the group (so that the area under the probability curve is equal for each group, allowing their probabilities to be directly compared with each other). It is assumed that the errors on individual ages (2 sigma) have a Gaussian distribution around the quoted age. Data from Wanming (1991); Turner et al. (1996); Chung et al. (1998); Miller et al. (1999); Hacker et al.(2000); Hacker(pers. comm). Also shown are geochronological constraints for the timing of continent-continent collision (Rowley, 1996); prograde metamorphism of the TSS and HHCS (Prince, 1999; Vance and Harris, 1999; Foster et al., 2000); the onset of movement on the MCT and STDS (sources in Chapter 2); east-west extension in southern Tibet (this study) and in northern Tibet (Yin et al., 1999b; Hacker et al., 2000); the increase in seawater $^{87}Sr/^{86}Sr$ (Richter et al., 1992).

However, this mechanism cannot explain the linear pattern of magmatism further north, which is not associated with major faults active in the Tertiary. Chung et al. (1998) attributed the genesis of the eastern Tibetan shoshonites to the convective removal of lower SCLM. However, suturing was only complete by 48 to 50 Ma (Patriat and Achache, 1984), and subsidence records indicate that thrusting and the development of fore-deep basins was initiated no earlier than 47 Ma and probably after 45 Ma (Rowley, 1998). Given that deformation of the Asian plate is unlikely to precede thrusting and fore-deep basin formation, the deformation of the eastern Asia lithosphere can only have predated potassic magmatism in Yunnan by ~6 Ma. The short interval between deformation of the Asian lithosphere and the onset of potassic magmatism in eastern Tibet is difficult to reconcile with convective removal models, as lithospheric thickening sufficient to trigger convective instabilities is unlikely within such a short timescale. The broadly linear distribution of the Eocene shoshonites is reminiscent of that defined by the southern shoshonites, and could conceivably reflect an early episode of slab breakoff. Indeed, Chemenda et al. (2000) proposed that at least two such breakoff events followed collision, the first being the detachment of Neo-Tehys oceanic lithosphere at ~ 40 Ma, followed by the breakoff of Indian SCLM, which is partially subducted (O'Brien et al., 1999) as the Indian plate continues to move northwards. However, it should be emphasised that hydrous, metasomatised regions within the SCLM may be melted as a consequence of many processes, and cannot automatically be used to verify a single geodynamic model. In order to determine the tectonic significance of the eastern lavas it would be necessary to determine i) the stress regime in which they were emplaced and ii) whether proxies for elevation increase e.g. enhanced erosion rates, molasse deposition are associated with this magmatism.

From the above discussion, it is clear that the post-collision evolution of the Himalayan-Tibetan orogen cannot be explained purely in terms of rigid plate models such as the eastward extrusion of the plateau along strike-slip faults (Tapponnier et al., 1982). Rigid plate models do not predict extensive thermal perturbation of the SCLM during orogensis, and so cannot account for the distribution of shoshonitc magmatism across the plateau, or the association between this magmatism and extension, and the apparent synchroneity of magmatism and extension in southern Tibet with movement on the STDS and MCT in the Himalaya (Figure 6.1). However, viscous sheet models (England and McKenzie, 1982) do not take pre-existing lithospheric structures, or the collision geometry into account and thus cannot account for the narrow belt of extension and magmatism in southern Tibet.

If the shoshonitic magmatism in eastern Tibet is related to geodynamic processes such as slab breakoff, then the evolution of the Himalayan-Tibetan orogen may follow a semi-cyclic pathway, in which the underthrusting of Indian lithosphere is accommodated by repeated phases of slab breakoff, shortening of Asian lithosphere and episodic convective thinning (c.f. Figure 6.1). These events may be intermittent, governed by the build up of stress in the orogen and the need to accommodate the ongoing convergence. Such an evolutionary pattern has probably continued into the present day, given evidence for i), widespread crustal melting across the Tibetan plateau (Alsdorf and Nelson, 1999), ii) a hotter Moho in north central Tibet (McNamura et al., 1997), iii) active volcanism in the Ashikule region of northwest Tibet (Liu and Maimaiti, 1989), iv) active normal faulting in Tibet (Molnar and Tapponnier, 1978), v) ongoing south-directed thrusting in the Himalaya (Wesnousky et al., 1999), and vi), for the ongoing destruction and recycling of both Indian and Asian SCLM into the convecting asthenosphere (Kosarev et al., 1999.). The region of poor Sn wave

propagation in north central Tibet (McNamura et al., 1997) is likely to be a site of "active" convective thinning, although no surface volcanism is apparent at present.

Clearly, these data indicate that the Himalayan mountain belt and the Tibetan plateau cannot be considered as separate systems - the Himalayan belt may have evolved in a considerably different way in the absence of the development of the Tibetan plateau. There is evidence for isolated slab breakoff and for convective thinning in the geological record, the best examples probably being the Alps, where post-collisional magmatism appears associated with the Insubric Line (Venturelli et al., 1984b; Von Blanckenburg and Davies, 1995), and the Basin and Range, respectively. In the Basin and Range, SCLM derived magmatism (Hawkesworth et al., 1995) is associated with extension, which reaches ~ 100 % ($\beta = 2$) (Wernike, 1981). In contrast, there are few known analogues in the geological record for a system as complex and closely coupled as the Himalayan-Tibetan orogen, and it may therefore be best treated as a special case rather than as an archetype. Nonetheless, the complexity of this system and its relative youth provide a unique opportunity to explore the inter-relationships between thermal and mechanical processes in a collisional setting, and how these processes influence the behaviour and stability of both crust and mantle.

6.2 Further Work

While a diachronous collision between India and Eurasia - younging from 60 to 65 Ma west to 48 to 50 Ma in the east - is generally accepted (Patriat and Achache, 1984; Klootwijk et al., 1992), the extent to which the original collision geometry influences the evolution of the orogen remains a subject of debate. Geochronological studies imply that prograde

metamorphism of the HHCS was older in the western Himalaya (Prince, 1999; Vance and Harris, 1999; Foster et al., 2000) and that movement on the STDS initiated much later in the east (Edwards and Harrison, 1997; Wu et al., 1998) than in the west (Dezes et al., 1999). Guillot et al. (1999) suggested that the decrease in prograde (HHCS) and cooling ages eastward and the higher prograde pressures in the western sections could be explained by a diachronous collision, the counterclockwise rotation of India with respect to Eurasia, and by a shallower angle of subduction in the east. In order to test the model proposed by Guillot et al. (1999) the diachroneity of prograde metamorphism and movement on the MCT and STDS in central and eastern regions of the Himalaya must be addressed. This can be achieved by integrated geochronologic and thermobarometric studies on specific sections, with a view to obtaining comparable data to that already in existence for the Malari and Zanskar sections. Of particular interest is the timing of prograde metamorphism in the TSS, as the data for the Malari section indicate that this unit was probably buried by south-directed thrusting on the suture zone itself, whereas the HHCS were buried by the TSS, thrust southwards on the STDS prior to reactivation.

The extent to which the oblique convergence of the Indian plate influenced the development of the Tibetan plateau is unclear. It is possible that shoshonitic dykes exposed in the northern Karakoram reflect the same geodynamic process that produced the shoshonite dykes exposed in southern Tibet. If this is the case, then the older ages of the Karakoram dykes (22 ± 1 to 24 ± 1 Ma; (Rex et al., 1988)), which are to the far west of the southern Tibetan dykes (13.3 ± 0.5 to 18.3 ± 1.6 Ma), suggest that onset of east-west extension may have been earlier in the west. This has implications for the timing and diachroneity of uplift in southern Tibet and for geodynamic models such as slab breakoff. A progressive trend in the timing of magmatism along the strike of the suture would suggest that the failure of the

slab was gradual, and progressed laterally from west to east, perhaps better described in terms of "slab tearing" as opposed to "slab breakoff". Further geochemical and geochronological studies of potassic magmatism in this area are required to confirm this. In order to evaluate potential relationships between post-collisional magmatism in southern and northern Tibet, and the inferred transition between regions affected by slab breakoff and convective thinning, detailed geological studies and extensive sampling within the northern Lhasa terrane and the southern Changtang terrane are also required. However, the accessibility of such areas is presently limited by both political and geographical factors.

A critical distinction between models of slab breakoff and convective removal is that slab breakoff could be associated with metasomatism of southern Tibetan SCLM synchronous with or following collision in the early Tertiary, prior to the actual detachment event, whereas convective removal predicts metasomatism any time before collision. Therefore, the key issues in testing these models are i) when was the most recent metasomatism of the southern Tibetan SCLM and ii) what are the origins of the metasomatic components – are they related to subduction or to asthenospheric processes? Preliminary ^{40}Ar-^{39}Ar dating of a mantle phlogopite, entrained within a shoshonitic dyke, implies a relationship between metasomatism and continent-continent collision in the earliest Tertiary, but this requires confirmation. One means of assessing both the use of the ^{40}Ar-^{39}Ar technique in dating mantle events and the different geodynamic models for the uplift of southern Tibet is to determine the timing and nature of the metasomatism of the south Tibetan SCLM using U-Pb and Lu-Hf isotopes on zircons within the same xenocrystic mantle phlogopites, which crystallised in the SCLM during an earlier metasomatic event. Zircon is not normally present in anhydrous peridotite and probably crystallised within the mantle during modal metasomatism (e.g. Odling, 1995). Mantle zircons have the potential to record age

information due to the closed system behaviour of Pb at temperatures up to 900°C (Lee et al., 1997), and therefore U-Pb analyses of these zircons can constrain the timing of metasomatism within the S. Tibetan SCLM. Discordance, perhaps due to inheritance of older components, may provide information about older metasomatic events and the evolution of the mantle source. Lu-Hf analyses on the same zircons will constrain the Lu/Hf and initial $^{177}Hf/^{176}Hf$ compositions of the melt from which the zircons crystallised and therefore the isotopic composition(s) of metasomatic agents. This information can be linked with tectonic processes, as the $^{177}Hf/^{176}Hf$ compositions of melts or fluids derived from asthenosphere-derived and subducted sediment components are distinctive (Patchett and Tatsumoto, 1980; Patchett, 1984).

A further means of investigating SCLM thinning due to either distributed shortening of the lithosphere or due to asthenosphere upwelling following slab breakoff would be to utilise the extreme sensitivity shown by helium isotope variations ($^3He/^4He$) to the presence of small amounts of volatiles derived from the convecting asthenosphere. The convecting mantle is the principal source of ^3He, and is sampled by mid ocean ridge basalts, which have $^3He/^4He$ (R/R_A; normalised to atmospheric helium) of ~ 8 (Farley and Neroda, 1998). In contrast, crustal and SCLM reservoirs have low $^3He/^4He$ signatures (< 1, normalised to air), due to ^4He ingrowth from the decay of principally U, Th and K, which are abundant in these reservoirs. On the basis of the helium isotope compositions of hydrothermal springs in southern Tibet, (Hoke et al., 2000) identified "mantle" and "crustal" helium domains in northern and southern parts of the Lhasa terrane, respectively. Hoke et al. (2000) proposed that the boundary between the "crustal" domain with the "mantle" domain to the north coincided with the junction between the Indian and Asian plates, in the region where seismic studies (Kosarev et al., 1999) indicate that the underthrusting Indian lithosphere steepens to

subduct below the plateau. Their findings broadly support ongoing thinning of the lithosphere beneath the plateau, however, their study does not constrain the mechanisms responsible. Clearly more extensive sampling, extending into northern and eastern Tibet, would be desirable. While hydrothermal He isotope studies indicate that mantle He signatures can be resolved, even in regions of thickened crust and enriched SCLM where there are considerable concentrations of U, Th and K, they do not shed light on the early evolution of the plateau in the Miocene. This issue could be further addressed by undertaking He isotope analyses on mineral separates (olivine, pyroxenes, garnet) from well-characterised volcanic rocks from both northern and southern regions of the plateau. A combined study involving the U-Pb dating and Hf isotopes on xenocrystic zircons and He isotopes on associated magnesian pyroxenes in the southern Tibetan dykes could be extremely powerful; a pilot study is presently underway.

References

Abdrakhmatov, K.Y., Aldazhanov, S.A., Hager, B.H., Hamburgers, M.W., Herring, T.A., Kalabaev, K.B., Makarov, V.I., Molnar, P., Panasyuk, S.V., Prilepin, M.T., Reilinger, R.E., Sadybakasov, I.S., Souter, B.J., Trapeznikov, Y.A., Tsurkov, V.Y., and Zubovich, A.V., 1996, Relatively recent construction of the Tien Shan inferred from measurements of present day crustal deformation rates: Nature, v. 384, p. 450 - 453.

Adam, J., Green, T.H., and Sie, S.H., 1993, Proton microprobe determined partitioning of Rb, Sr, Ba, Y, Zr, Nb and Ta between experimentally produced amphiboles and silicate melts with variable F content: Chemical Geology, v. 109, p. 29-49.

Ahmad, T., Harris, N., Bickle, M., Chapman, H., Bunbury, J., and Prince, C., 2000, Isotopic constraints on the structural relationships between the Lesser Himalaya Series and the High Himalayan Crystalline Series, Garhwal Himalaya: Geological Society of America Bulletin, v. 112, p. 467-477.

Albarède, F., 1983, Inversion of batch melting equations and the trace element pattern of the mantle: Journal of Geophysical Research, v. 88, p. 10573-10583.

Allmendinger, R.W., Jordan, T.E., Kay, S.M., and Isacks, B.L., 1997, The evolution of the Altiplano-Puna plateau of the Central Andes: Annual Reviews of Earth and Planetary Sciences, v. 25, p. 139-174.

Alsdorf, D., and Nelson, D., 1999, Tibetan satellite magnetic low: evidence for widespread melt in the Tibetan crust?: Geology, v. 27, p. 943-946.

Armijo, R., Tapponier, P., Mercier, J.L., and Tong-Lin, H., 1986, Quartenary extension in Southern Tibet: field observations and tectonic implications: Journal of Geophysical Research, v. 91, p. 13803-13872.

Arnaud, N.O., 1992, Apport de la thermochronologie $^{40}Ar/^{39}Ar$ sure feldspath potassique connassance de la tectonique cénozoique d'Asie [PhD thesis], Université de Clermont-Ferrand.

Arnaud, N.O., and Kelley, S.P., 1995, Evidence for excess argon during high-pressure metamorphism in the Dora Maira Massif (western Alps, Italy), using an ultra-violet laser ablation microprobe ^{40}Ar-^{39}Ar technique: Contributions to Mineralogy and Petrology, v. 121, p. 1-11.

Arnaud, N.O., Vidal, P., Tapponier, P., Matte, P., and Deng, W.M., 1992, The high K_2O volcanism of northwestern Tibet: Geochemistry and tectonic implications: Earth and Planetary Science Letters, v. 111, p. 351 - 367.

Asmerom, Y., Cheng, H., Thomas, R., Hirschmann, M., and Edwards, L., 2000, Melting of the Earth's lithospheric mantle inferred from protactinium-thorium-uranium isotopic data: Nature, v. 406, p. 293-295.

Ayers, J.C., and Miller, C.F., 1998, How do monazite and zircon grow, and what do monazite and zircon U-Pb age dates mean? Insights obtained from experiments, Geological Society of America, 1998 annual meeting, Volume Abstracts with Programs - Geological Society of America, v. 30,: Toronto, Ontario, Canada: Oct. 26-29, 1998, Geological Society of America (GSA), Boulder, CO, United States, p. 214.

Bi, S., Blisniuk, P.M., Hacker, B.R., Glodny, J., Ryerson, R.J., and Ratchbacher, L., 1999, Timing of late Neogene extension in Central Tibet, American Geophysical Union 1999 Fall meeting: San Francisco, American Geophysical Union, p. F1015.

Bilham, R., Larson, K., Freymueller, J., Jouanne, F., LeFort, P., Leturmy, P., Mugnier, J.L., Gamond, J.F., Glot, J.P., Martinod, J., Chaudury, N.L., Chitrakar, G.R., Gautam, U.P., Koirala, B.P., Pandey, M.R., Ranabhat, R., Sapkota, S.N., Shrestha, P.L., Thakuri, M.C., Timilsina, U.R., Tiwari, D.R., Vidal, G., Vigny, C., Galy, A., and de Voogd, B., 1997, GPS measurements of present-day convergence across the Nepal Himalaya: Nature, v. 386, p. 61-64.

Bird, P., 1979, Continental delamination and the Colorado Plateau: Journal of Geophysical Research, v. 84, p. 7561-7571.

Blundy, J.D., Robinson, J.A.C., and Wood, B.J., 1998, Heavy REE are compatible in clinopyroxene on the spinel lherzolite solidus: Earth and Planetary Science Letters, v. 160, p. 493-504.

Bodet, F., and Schärer, U., 2000, Evolution of the SE-Asian continent from U-Pb and Hf isotope in single grains of zircon and baddeleyite from large rivers: Geochimica et Cosmochimica Acta, v. 64, p. 2067-2091.

Braathen, A., Nordgulen, O., Osmundsen, P.-T., Andersen, T.B., Solli, A., and Roberts, D., 2000, Devonian, orogen parallel, opposed extension in the Central Norwegian Caledonies: Geology, v. 28, p. 615-618.

Brenan, J.M., Shaw, H.F., Phinney, D.L., and Ryerson, F.J., 1994, Rutile-aqueous fluid partitioning of Nb, Ta, Hf, Zr , U and Th: Implications for high field strength depletions in island-arc basalts: Earth and Planetary Science Letters, v. 128, p. 327-339.

Brown, L.D., Zhao, W., Nelson, K.D., Hauck, M., Alsdorf, D., Cogan, M., Clark, M., Liu, X., and Che, J., 1996, Bright spots, structure and magmatism in Southern Tibet from INDEPTH seismic reflection profiling: Science, v. 274, p. 1688-1690.

Burbank, D.W., Leland, J., Fielding, E., Anderson, R.S., Brozovic, N., Reid, M.R., and Duncan, C., 1996, Bedrock incision, rock uplift and threshold hillslopes in the northwestern Himalayas: Nature, v. 379, p. 505-510.

Burchfiel, B.C., Chen, Z., Hodges, K.V., Yuping, L., L.H., R., Deng, C., and Xu, J., 1992, The Southern Tibet Detachment System, Himalayan Orogen: Extension contemporaneous with and parallel to shortening in a collisional mountain belt: Geological Society of America Special Publication, v. 269.

Burg, J.P., Brunel, M., Gapais, D., Chen, G.M., and Liu, G.H., 1984, Deformation of leucogranites of the crystalline Main Central Sheet in southern Tibet (China): Journal of Structural Geology, v. 6, p. 535-542.

Burg, J.-P., Proust, F., Tapponnier, P., and Ming, C.G., 1983, Deformation phases and tectonic evolution of the Lhasa Block (southern Tibet, China): Eclogae Geologicae Helvetiae, v. 76, p. 643-665.

Catlos, E.J., Harrison, T.M., Searle, M.P., and Hubbard, M.S., 1999, Evidence for Late Miocene reactivation of the Main Central Thrust: From Garhwal to the Nepali Himalaya: Terra Nostra, v. 2, p. 20-22.

Chemenda, A.I., Burg, J.-P., and Mattauer, M., 2000, Evolutionary model of the Himalaya-Tibet system: geopoem based on new modelling, geological and geophysical data: Earth and Planetary Science Letters, v. 174, p. 397-409.

Chung, S.-L., Lo, C.-H., Lee, T.-Y., Zhang, Y., Xie, Y., Li, X., Wang, K.-L., and Wang, P.-L., 1998, Diachronous uplift of the Tibetan plateau starting from 40 My ago: Nature, v. 394, p. 769-773.

Class, C., and Goldstein, S.L., 1997, Plume-lithosphere interactions in the ocean basins: constraints from the source mineralogy: Earth and Planetary Science Letters, v. 150, p. 245-260.

Cliff, R.A., 1985, Isotopic dating in metamorphic belts: Journal of the Geological Society of London, v. 142, p. 97-110.

Coleman, M., and Hodges, K., 1995, Evidence for Tibetan plateau uplift before 14 My ago from a new minimum age for east - west extension: Nature, v. 374, p. 49-52.

Coleman, M.E., 1998, U-Pb constraints on Oligocene-Miocene deformation and anatexis within the Central Himalaya, Marsyandi Valey, Nepal: American Journal of Science, v. 298, p. 553-571.

Coleman, M.E., and Hodges, K.V., 1998, Contrasting Oligocene and Miocene thermal histories from the hanging wall and footwall of the Southern Tibetan detachment in the central Himalaya from $^{40}Ar/^{39}Ar$ thermochronology, Marsyandi Valley, central Nepal: Tectonics, v. 17, p. 726-740.

Conrad, C.P., and Molnar, P., 1999, Convective instability of a boundary layer with temperature- and strain- dependent viscosity in terms of "available buoyancy": *Geophysical Journal International*, v. 131, p. 51-68.

Copeland, P., Parrish, R.R., and Harrison, T.M., 1988, Identification of inherited radiogenic Pb in monazite and implications for U-Pb systematics: Nature, v. 333, p. 760-763.

Copeland, P., and Harrison, T.M., 1990, Episodic rapid uplift in the Himalaya revealed by $^{40}Ar/^{39}Ar$ analysis of detrital K-feldspar and muscovite, Bengal Fan: Geology, v. 18, p. 354-357.

Copeland, P., Harrison, T.M., Kidd, W.S.F., Ronghua, X., and Yuquan, Z., 1987, Rapid early Miocene acceleration of uplift in the Gangdese belt, Xizang (southern Tibet), and its bearing on accommodation mechanisms of the India-Asia collision: Earth and Planetary Science Letters, v. 86, p. 240-252.

Coulon, C., Maluski, H., Bollinger, C., and Wang, S., 1986, Mesozoic and Cenozoic volcanic rocks from central and southern Tibet: $^{39}Ar/^{40}Ar$ dating, petrological characteristics and geoodynamical significance: Earth and Planetary Science Letters, v. 79, p. 281-302.

Coward, M.P., and Butler, R.W.H., 1985, Thrust tectonics and the deep structure of the Pakistan Himalaya: Geology, v. 13, p. 417-420.

Coward, M.P., Kidd, W.S.F., Pan, Y., Shackelton, R.M., and Zhang, H., 1988, The structure of the 1985 Tibet Geotraverse, Lhasa to Golmud: Philosophical Transactions of the Royal Society of London, v. A327, p. 307-336.

Dahl, P.S., 1996, The crystal-chemical basis for Ar retention in micas: inferences from interlayer partitioning and implications for geochronology`: Contributions to Mineralogy and Petrology, v. 123, p. 22-39.

Dalpe, C., and Baker, D.R., 1994, Partition coefficients for rare-earth elements between calcic amphibole and Ti-rich basanite glass at 1.5 GPa, 1100°C: Mineralogical Magazine, v. 58A, p. 207-208.

Dalrymple, G.B., Alexander, E.C., Lanphere, M.A., and Kraker, G.P., 1981, Irradiation of samples for $^{40}Ar/^{39}Ar$ dating using the Geological Survey TRIGA reactor: US Geological Survey Prof. Paper, v. 1176

Davies, G.F., 1995, Punctuated tectonic evolution of the Earth: Earth and Planetary Science Letters, v. 136, p. 363-379.

Davies, J.H., and von Blanckenburg, F., 1995, Slab breakoff: a model of lithosphere detachment and its test in the magmatism and deformation of collisional orogens: Earth and Planetary Science Letters, v. 129, p. 85-102.

Davies, J.H., and von Blanckenburg, F., 1997, Thermal controls on slab breakoff and the rise of high-pressure rocks during continental collisions, *in* Hacker, B.R., and Liou, J.G., eds., When continents collide: Geodynamics and Geochemistry of Ultrahigh Pressure rocks, Volume 1, Kluwer Academic Publishers, p. 97-115.

de Sigoyer, J., Chavagnac, V., Blichert-Toft, J., Villa, I.M., Luais, B., Guillot, S., Cosca, M., and Mascle, G., 2000, Dating the Indian continental subduction and collisional thickening in the northwest Himalaya: Multichronology of Tso Morari eclogites: Geology, v. 28, p. 487-490.

Debon, F., Zimmermann, J.-L., Nancy, L., Guogul, J., Chengwei, and Ronghua, X., 1985, Time relationships between magmatism, tectonics and metamorphism in three plutonic belts in Southern Tibet: new K-Ar data: Geologische Rundschau, v. 74, p. 229-236.

DePaolo, D.J., 1981, Trace element and isotopic effects of combined wallrock assimilation and fractional crystallisation: Earth and Planetary Science Letters, v. 53, p. 189-202.

Dewey, J.F., 1988, Extensional collapse of orogens: Tectonics, v. 6, p. 1123-1139.

Dewey, J.F., and Bird, J.M., 1970, Mountain belts and the new global tectonics: Journal of Geophysical Research, v. 75, p. 2625-2647.

Dewey, J.F., Shackelton, R.M., Chengfa, C., and Yiyin, S., 1988, The tectonic evolution of the Tibetan Plateau: Philosophical Transactions of the Royal Society of London, v. A 327, p. 379-413.

Dezes, P.J., Vannay, J.-C., Steck, A., Bussy, F., and Cosca, M., 1999, Synorogenic extension: Quantitatitve constraints on the age and displacement of the Zanskar shear zone (northwest Himalaya): Geological Society of America Bulletin, v. 111, p. 34-374.

Dodson, M.H., 1973, Closure temperature in cooling geochronological and petrological systems: Contributions to Mineralogy and Petrology, v. 40, p. 259-274.

Dunlap, W.J., 1997, Neocrystallization or cooling? $^{40}Ar/^{39}Ar$ ages of white micas from low-grade mylonites: Chemical Geology, v. 143, p. 181-203.

Dunlap, W.J., Teyssier, C., McDougall, I., and Baldwin, S., 1991, Ages of deformation from K/Ar and $^{40}Ar/^{39}Ar$ dating of white micas: Geology, v. 19, p. 1213-1216.

Edwards, M.A., and Harrison, T.M., 1997, When did the roof collapse? Late Miocene north - south extension in the high Himalaya revealed by Th - Pb monazite dating of the Khula Kangri granite: Geology, v. 25, p. 543-546.

Edwards, M.A., Kidd, W.S.F., Li, J., Yue, Y., and Clark, M., 1996, Multi-stage development of the southern Tibet detachment system near Khula Kangri. New data from Gonto La: Tectonophysics, v. 260, p. 1-19.

England, P., and Houseman, G., 1986, Finite strain calculations of continental deformation 2. Comparison with the India-Asia collision zone: Journal of Geophysical Research, v. 91, p. 3664-3676.

England, P., and Houseman, G., 1989, Extension during continental convergence, with application to the Tibetan plateau: Journal of Geophysical Research, v. 94, p. 17561-17579.

England, P., and McKenzie, D., 1982, A thin viscous sheet model for continental deformation: Geophysical Journal of the Royal Astronomical Society, v. 70, p. 295-321.

England, P., and Molnar, P., 1993, Cause and effect among thrust and normal faulting, anatectic melting and exhumation in the Himalaya, *in* Treloar, P.J., and Searle, M.P., eds., Himalayan Tectonics, Volume 74: Geological Society Special Publication: London, Geological Society of London, p. 401-411.

England, P.C., and Thompson, A.B., 1984, Pressure-Temperature-Time paths of regional metamorphism 1. Heat transfer during the evolution of regions of thickened continental crust: Journal of Petrology, v. 25, p. 894-928.

Erlank, A., Allsopp, H.L., Hawkesworth, C.J., and Menzies, M.A., 1982, Chemical and isotopic characterisation of upper mantle metasomatism in peridotite nodules from the Bultfontein kimberlite: Terra Cognita, v. 2, p. 261-263.

Falloon, T.J., and Green, D.H., 1988, Anhydrous Partial melting of peridotite from 8 to 35 kb and the petrogenesis of MORB: Journal of Petrology, v. 29 - Special Lithosphere Issue, p. 379-414.

Farley, K.A., and Neroda, E., 1998, Noble gases in the earth's mantle: Annual Reviews of Earth and Planetary Sciences, v. 26, p. 189-218.

Fielding, E., Isaacks, B., Barazangi, M., and Duncan, C., 1994, How flat is Tibet?: Geology, v. 22, p. 163-167.

Foley, S., 1991, High-pressure stability of the fluor- and hydroxy-endmembers of pargasite and K-richterite: Geochimica et Cosmochimica Acta, v. 55, p. 2689-2694.

Foley, S.F., 1992, Vein-plus-wall-rock melting mechanisms in the lithosphere and the origins of potassic alkaline magmas: Lithos, v. 28, p. 435-453.

Foley, S.F., Barth, M.G., Jenner, G.A., 2000, Rutile/melt partition coefficients for trace elements and an assessment of the influence of rutile on the trace element characteristics of subduction zone magmas: Geochimica et Cosmochimica Acta, v. 64, p. 933-938.

Foley, S.F., Jackson, S.E., Fryer, B.J., Greenough, J.D., and Jenner, G.A., 1996, Trace element partition coefficients for clinopyroxene and phlogopite in an alkaline lamprophyre from Newfoundland by LAM-ICP-MS: Geochimica et Cosmochimica Acta, v. 60, p. 629-638.

Foley, S.F., and Wheller, G.E., 1990, Parallels in the origin of the geochemical signatures of island arc volcanics and continental potassic igneous rocks: The role of residual titanites: Chemical Geology, v. 85, p. 1-18.

Fossen, H., and Dunlap, W.J., 1998, Timing and kinematics of Caledonian thrusting and extensional collapse, southern Norway: evidence from $^{40}Ar/^{39}Ar$ thermochronology: Journal of Structural Geology, v. 20, p. 765-781.

Foster, G., Kinney, P., Vance, D., Prince, P., and Harris, N., 2000, The significance of monazite U-Th-Pb age data in metamorphic assemblages: a combined study of monazite and garnet chronometry: Earth and Planetary Science Letters, v. 181, p. 327-340.

Gaetani, M., and Garzanti, E., 1991, Multicyclic History of the Northern India Continental-Margin (Northwestern Himalaya): AAPG Bulletin of the American Association of Petroleum Geologists, v. 75, p. 1427-1446.

Galer, S.J.G., and Abouchami, W., 1998, Practical application of lead triple spiking for correction of instrumental mass discrimination: Mineralogical Magazine, v. 62A, p. 491-492.

Gans, P.B., and Bohrson, W.A., 1998, Suppression of volcanism during extension in the Basin and Range Province, United States: Science, v. 279, p. 66-68.

Gansser, A., 1964, Geology of the Himalayas: London, Interscience publishers, 289 p.

Gapais, D., 1989, Shear structures within deformed granites: mechanical and thermal indicators: Geology, v. 17, p. 1144-1147.

Garzione, C.N., Dettman, D.L., Quade, J., DeCelles, P.G., and Butler, R.F., 2000, High times on the Tibetan Plateau: Palaeoelevation of the Thakkola Graben, Nepal: Geology, v. 28, p. 339-342.

Ghiorso, M.S., and Sack, R.O., 1991, Fe-Ti oxide geothermometry: thermodynamic formulation and the estimation of intensive variables in silicic magmas: Contributions to Mineralogy and Petrology, v. 108, p. 485-510.

Gibson, S.A., Thompson, R.N., Leonardos, G.H., Dickin, A.P., and Mitchell, J.G., 1995, The late Cretaceous impact of the Trinidade mantle plume: evidence from large-volume, mafic, potassic magmatism in SE Brazil: Journal of Petrology, v. 36, p. 189-229.

Green, T.H., 1995, Significance of Nb/Ta as an indicator of geochemical processes in the crust-mantle system: Chemical Geology, v. 120, p. 347-359.

Green, T.H., and Pearson, N.J., 1986, An experimental study of Nb and Ta partitioning between Ti-rich minerals and silicate liquids at high pressure and temperature: Geochimica et Cosmochimica Acta, v. 51, p. 55-62.

Grove, M., and Harrison, T.M., 1996, $^{40}Ar^{*}$ diffusion in Fe-rich biotite: American Mineralogist, v. 81, p. 940-951.

Grujic, D., Casey, M., Davidson, C., Hollister, L.H., Kundig, R., Pavlis, T., and Schmid, S., 1996, Ductile extrusion of the Higher Himalayan Crystalline in Bhutan: evidence from quartz microfabrics: Tectonophysics, v. 260, p. 21-43.

Guillot, S., Cosca, M., Allemand, P., and Le Fort, P., 1999, Contrasting metamorphic and geochronologic evolution along the Himalayan belt, *in* A. Maacfarlane, R. B. Sorkhabi, and Quade, J., eds., Mountain Roots to mountain tops, Volume 328: Special Paper, Geological Society of America, p. 117-128.

Guillot, S., Hodges, K., Le Fort, P., and Pêcher, A., 1994, New evidence on the age of the Manasalu leucogranite: Evidence for episodic tectonic denudation in the central Himalayas: Geology, v. 22, p. 559-562.

Hacker, B.R., Gnos, E., Ratschbacher, L., Grove, M., McWilliams, M., and Wan, J., 2000, Hot and dry xenoliths from the bottom of Tibet: Science, v. 287, p. 2463-2466.

Halliday, A.N., Lee, D.-C., Tommasini, S., Davies, G.R., Paslick, C.R., Fitton, J.G., and James, D.E., 1995, Incompatible trace elements in OIB and MORB and source enrichment in the sub-oceanic mantle: Earth and Planetary Science Letters, v. 133, p. 379-395.

Hames, W.E., and Bowring, S.A., 1994, An empirical evaluation of the argon diffusion geometry in muscovite: Earth and Planetary Science Letters, v. 124, p. 161-167.

Harris, N., and Massey, J., 1994, Decompression and anatexis of Himalayan metapelites: Tectonics, v. 13, p. 1537-1546.

Harris, N.B.W., Ronghua, X., Lewis, C.L., Hawkesworth, C.J., and Yuquan., Z., 1988, Isotope geochemistry of the 1985 Tibet Geotraverse, Lhasa to Golmud: Philosophical Transactions of the Royal Society of London, v. A327, p. 263-285.

Harrison, T.M., 1981, Diffusion of ^{40}Ar in hornblende: Contributions to Mineralogy and Petrology, v. 78, p. 324-331.

Harrison, T.M., Copeland, P., Hall, S.A., Quade, J., Burner, S., Ojha, T.P., and Kidd, W.S.F., 1993, Isotopic preservation of Himalayan/ Tibetan uplift, denudation and climatic histories of two molasse deposits: The Journal of Geology, v. 101, p. 157-175.

Harrison, T.M., Copeland, P., Kidd, W.S.F., and Lovera, O.M., 1995, Activation of the Nyainqentanghla shear zone: Implications for the uplift of the southern Tibetan Plateau: Tectonics, v. 14, p. 658-676.

Harrison, T.M., Grove, M., Lovera, O.M., and Catlos, E.J., 1998, A model for the origin of Himalayan anatexis and inverted metamorphism: Journal of Geophysical Research, v. 103, p. 27017-27032.

Harrison, T.M., Grove, M., McKeegan, K.D., Coath, C.D., Lovera, O.M., and Le Fort, P., 1999, Origin and episodic emplacement of the Manaslu Intrusive Complex, Central Himalaya: Journal of Petrology, v. 40, p. 3-19.

Harrison, T.M., Lovera, O.M., and Grove, M., 1997a, New insights into the origin of two contrasting Himalayan granite belts: Geology, v. 25, p. 899-902.

Harrison, T.M., Ryerson, F.J., Le Fort, P., Yin, A., Lovera, O.M., and Catlos, E.J., 1997b, A late Miocene-Pliocene origin for the central Himalayan inverted metamorphism: Earth and Planetary Science Letters, v. 146, p. E1-E7.

Hart, S.R., 1984, A large-scale isotope anomaly in the Southern Hemisphere mantle: Nature, v. 309, p. 753-757.

Hauk, M.L., Nelson, K.D., Brown, L.D., Zhao, W., Ross, A.R., 1998, Crustal structure of the Himalayan orogen at 90° East longitude from Project INDEPTH deep reflection profiles: Tectonics, v. 17, p. 481-500.

Hawkesworth, C., Turner, S., Gallagher, K., Hunter, A., Bradshaw, T., and Rogers, N., 1995, Calc-alkaline magmatism, lithospheric thinning and extension in the Basin and Range: Journal of Geophysical Research, v. 100, p. 10271-10286.

Heaman, L., and Parrish, R.R., 1991, U-Pb geochronology of accessory minerals, *in* Heaman, L., and Ludden, J.N., eds., Short Course Handbook on Applications of Radiogenic Isotope Systems to Problems in Geology: Toronto, Mineralogical Association of Canada, p. 59-100.

Herren, E., 1987, Zanskar shear zone: northeast-southwest extension within the Higher Himalayas (Ladakh, India): Geology, v. 15, p. 409-413.

Hirn, A., Jiang, M., Sapin, M., Diaz, J., Nercessian, A., Lu, Q.T., Lepine, J.C., Shi, D.N., Sachpazi, M., Pandey, M.R., Ma, K., and Gallart, J., 1995, Seismic anisotropy as an indicator of mantle flow beneath the Himalayas and Tibet: Nature, v. 375, p. 571-574.

Hirose, K., 1997, Melting experiments on lherzolite KLB-1 under hydrous conditions and generation of high-magnesian andesitic melts: Geology, v. 25, p. 42-44.

Hirose, K., and Kawamoto, T., 1995, Hydrous partial melting of lherzolite at 1 GPa: the effect of H_2O on the genesis of basaltic magmas: Earth and Planetary Science Letters, v. 133, p. 463-473.

Hirose, K., and Kushiro, I., 1993, Partial melting of dry peridotites at high pressures: determination of compositions using aggregates of diamond: Earth and Planetary Science Letters, v. 114, p. 477-489.

Hirschmann, M.M., and Stolper, E.M., 1996, A possible role for garnet pyroxenite in the origin of the "garnet signature" in MORB: Contributions to Mineralogy and Petrology, v. 124, p. 185-208.

Hodges, K.V., 2000, Tectonics of the Himalaya and southern Tibet from two perspectives: Geological Society of America Bulletin, v. 112, p. 324-350.

Hodges, K.V., Hames, W.E., Olszewski, W., Burchfiel, B.C., Royden, L.H., and Chen, Z., 1994, Thermobarometric and 40Ar/39Ar geochronologic constraints on Eohimalayan metamorphism in the Dinggyê area, southern Tibet: Contributions to Mineralogy and Petrology, v. 117, p. 151-163.

Hodges, K.V., and Hurtado, J.M., Jr., 1998, Dynamics of the southern margin of the Tibetan Plateau, Geological Society of America, 1998 annual meeting, Volume 30: Toronto, ON, Canada, Abstracts with Programs - Geological Society of America, p. 270.

Klein, E.M., and Langmuir, C.M., 1987, Global correlations of ocean ridge basalt chemistry with axial depth and crustal thickness: Journal of Geophysical Research, v. B8, p. 8089-8115.

Klemme, S., and O'Neill, H.S., 2000, The near-solidus transition from garnet lherzolite to spinel lherzolite: Contributions to Mineralogy and Petrology, v. 138, p. 237-248.

Klootwijk, C.T., Conaghan, P.J., and Powell, C.M., 1985, The Himalayan Arc: large-scale continental subduction, oroclinal bending and back-arc spreading: Earth and Planetary Science Letters, v. 75, p. 167-183.

Klootwijk, C.T., Gee, J.S., Peirce, J.W., Smith, G.M., and McFadden, G.L., 1992, An early India-Asia contact - paleomagnetic constraints from the Ninetyeast Ridge, ODP Leg 121: Geology, v. 20, p. 395-398.

Kong, X., Yin, A., and Harrison, T.M., 1997, Evaluating the roles of preexisting weaknesses and topographic distributions in the Indo-Asia collision by use of a thin-shelled numerical model: Geology, v. 25, p. 527-530.

Konzett, J., Sweeney, R.J., Thompson, A.B., and Ulmer, P., 1997, Potassium amphibole stability in the upper mantle: an experimental study in a peralkaline KNCMASH system to 8.5 GPa: Journal of Petrology, v. 38, p. 537-568.

Kosarev, G., Kind, R., Sobolev, S.V., Yuan, X., Hanka, W., and Oreshin, S., 1999, Seismic evidence for a detached Indian lithospheric mantle beneath Tibet: Science, v. 283, p. 1306-1309.

Kramers, J., 1983, Trace element and isotope studies on veined, metasomatic and "MARID" xenoliths from Bultfontein, South Africa: Earth and Planetary Science Letters, v. 65, p. 90-106.

Kutzbach, J.E., Guetter, P.J., Ruddiman, W.F., and Prell, W.L., 1989, Sensitivity of climate to late Cenozoic uplift in southern Asia and the American West; numerical experiments: Journal of Geophysical Research, v. 94, p. 18393-18407.

LaTourette, T., Hervig, R.L., and Holloway, J.R., 1995, Trace element partitioning between amphibole, phlogopite and basanite melt: Earth and Planetary Science Letters, v. 135, p. 13-30.

Le Breton, N., and Thompson, A.B., 1988, Fluid-absent (dehydration) melting of biotite in metapelites in the early stages of crustal anatexis: Contributions to Mineralogy and Petrology, v. 99, p. 226-237.

Le Fort, P., 1975, Himalayas: the collision range. Present knowledge of the continental arc: American Journal of Science, v. 275-A, p. 1-44.

Le Maitre, R.W., Bateman, P., Dudek, A., Keller, J., Lameyre Le Bas, M.J., Sabine, P.A., Schmid, R., Sorensen, H., Streikeisen, A., Woolley, A.R., and Zanettin, 1989, A classification of igneous rocks and a glossary of terms: Oxford, Blackwell.

Lee, J.K.W., 1995, Multipath diffusion in geochronology: Contributions to Mineralogy and Petrology, v. 120, p. 60-82.

Lee, J.K.W., Williams, I.S., and Ellis, D.J., 1997, Pb, U and Th diffusion in natural zircon: Nature, v. 390, p. 159-162.

Leeder, M.R., Smith, A.B., and Yin, J., 1988, Sedimentology, palaeoecology and palaeoenvironmental evolution of the 1985 Lhasa to Golmud Geotraverse: Philosophical Transactions of the Royal Society of London, v. A327, p. 107-142.

Leloup, P.H., Lacassin, R., Tapponier, P., Scharer, U., Dalai, Z., Xiaohan, L., Liangshang, Z., Shaocheng, J., and Trinh, P.T., 1995, The Ailao Shan-Red River shear zone (Yunnan, China), Tertiary transform boundary of Indochina: Tectonophysics, v. 251, p. 3-84.

Leloup, P.H., Ricard, Y., Battaglia, J., and Lacassin, R., 1999, Shear heating in continental strike-slip shear zones: model and field examples: Geophysical Journal Inrternational, v. 136, p. 19-40.

Lenardic, A., and Kaula, W.M., 1995, More thoughts on convergent crustal plateau formation and mantle dynamics with regard to Tibet: Journal of Geophysical Research, v. B8, p. 15193-15203.

Lin, J., and Watts, D.R., 1988, Paleomagnetic constraints on Himalayan-Tibetan tectonic evolution: Philosophical Transactions of the Royal Society, London, v. A326, p. 177-188.

Lindsley, D.H., 1983, Pyroxene thermometry: American Mineralogist, v. 68, p. 477-493.

Lindsley, D.H., and Andersen, D.J., 1983, A Two-Pyroxene thermometer: Journal of Geophysical Research, v. 88, p. A887- A906.

Liu, J., and Maimaiti, Y., 1989, Distribution and ages of Ashikule volcanoes on the West Kunlun mountains, west China: Bulletin of Glacier Research, v. 7, p. 193-196.

Lloyd, F.E., Arima, M., and Edgar, A.D., 1985, Partial melting of a phlogopite-clinopyroxenite nodule from south-west Uganda: an experimental study bearing on the origin of highly potassic continental rift volcanics: Contributions to Mineralogy and Petrology, v. 91, p. 321-329.

Ludwig, K.R., 1999, Isoplot/Ex: A geochronological toolkit for Microsoft Excel: Berkeley, Berkeley Geochronology Center.

Luth, R.W., 1997, Experimental study of the system phlogopite-diopside from 3.5 to 17 GPa: American Mineralogist, v. 82, p. 1198-1209.

Maluski, H., Matts, P., Brunel, M., and Xiao, X., 1988, Argon39-argon40 dating of metamorphic and plutonic events in the north and High Himalaya belts (southern Tibet- China): Tectonics, v. 7, p. 299-325.

Maury, R.C., Dufant, M.J., and Joron, J.-L., 1992, Metasomatism of the sub-arc mantle inferred from trace elements in Phlippine xenoliths: Nature, v. 360, p. 661-663.

McCaffrey, R., and Nabelek, J., 1998, Role of Oblique convergence in the active deformation of the Himalayas and southern Tibet plateau: Geology, v. 26, p. 691-694.

McCulloch, M.T., and Black, L.P., 1984, Sm-Nd isotope systematics of Enderby Land granulites and evidence of redistribution of Sm and Nd during metamorphism: Earth and Planetary Science Letters, v. 71, p. 46-58.

McDougall, I., and Harrison, T.M., 1999, Geochronology and thermochronology by the $^{40}Ar/^{39}Ar$ method: New York, Oxford University Press, 263 p.

McFarlane, A.M., 1995, An evaluation of the inverted metamorphic gradient at Langtang National Park, Central Nepal Himalaya: Journal of Metamorphic Geology, v. 13, p. 595-612.

McIntyre, G.A., Brooks, C., Compton, W., and Turek, A., 1966, The statistical assessment of Rb/Sr isochrons: Journal of Geophysical Research, v. 71, p. 5459-5468.

McKenna, L.W., and Walker, J.D., 1990, Geochemistry of Crustally Derived Igneous Rocks from the Ulugh Muztagh area, Northern Tibet, and their implications for the formation of the Tibetan plateau: Journal of Geophysical Research, v. 95, p. 21,483 - 21,502.

McKenzie, D., 1989, Some remarks on the movement of small melt fractions in the mantle: Earth and Planetary Science Letters, v. 95, p. 53-72.

McKenzie, D., and O'Nions, R.K., 1991, Partial Melt distributions from Inversion of Rare Earth Element Concentrations: Journal of Petrology, v. 35, p. 1021-1091.

McKenzie, D.P., and Bickle, M.J., 1988, The volume and composition of melts generated by extension of the lithosphere: Journal of Petrology, v. 29, p. 625-679.

McNamura, D.E., Walter, W.R., Owens, T.J., and Ammon, C.J., 1997, Upper mantle velocity structure beneath the Tibetan plateau from Pn travel time tomography: Journal of Geophysical Research, v. 102, p. 493-505.

McPherson, E., Thirlwall, M.F., Parkinson, I.J., Menzies, M.A., Bodinier, J.L., Woodland, A., and Bussod, G., 1996, Geochemistry of metasomatism adjacent to amphibole-bearing veins in the Lherz peridotite massif: Chemical Geology, v. 134, p. 135-157.

Mengel, K., and Green, D.H., 1989, Stability of amphibole and phlogopite in metasomatised peridotite under water-saturated and water-undersaturated conditions: *Geol. Soc. Aus.* Special Publication, v. 14, p. 571-581.

Menzies, M., Rogers, N., Tindle, A., and Hawkesworth, C., 1987, Metasomatic and enrichment processes in lithospheric peridotites, an effect of asthenosphere-lithosphere interaction, *in* Menzies, M.A., and Hawkesworth, C.J., eds., Mantle Metasomatism: London, Academic Press.

Mercier, J., Armijo, R., Tapponier, P., Carey-Gailhardiz, E., and Lin, H.T., 1987, Change from late Tertiary compression to Quartenary extension in southern Tibet during the India-Asia collision: Tectonics, v. 6, p. 275-304.

Merrihue, C., and Turner, G., 1966, Potassium -argon dating by activation with fast neutrons: Journal of Geophysical Research, v. 71, p. 2852-2857.

Metcalfe, R.P., 1993, Pressure, temperature and time constraints on metamorphism across the Main Central Thrust in the Garwhal Himalaya.: Geological Society Special Publications, v. 74 Himalayan Tectonics, p. 485-509.

Meyer, B., Tapponier, P., Bourjot, L., Metiver, F., Gaudemer, Y., Peltzer, G., Shunmin, G., and Zhitai., C., 1998, Crustal thickening in Gansu-Quighai, lithospheric mantle subduction, and oblique, strike-slip controlled growth of the Tibet plateau: Geophysical Journal International, v. 13, p. 1-47.

Michard, A., Gurriet, P., Soudant, M., and Albarède, F., 1985, Nd isotopes in Frence Phanerozoic shales: external vs internal aspects of crustal evolution: Geochimica et Cosmochimica Acta, v. 49, p. 601-610.

Miller, C., Schuster, R., Klotzli, U., Frank, W., and Grasemann, B., 2000, Late Cretaceous-Tertiary magmatic and tectonic events in the Transhimalaya Batholith (Kailas area, SW Tibet): Schweiz. Mineral. Petrogr. Mitt., v. 80, p. 1-20.

Miller, C., Schuster, R., Klotzli, U., Mair, V., Frank, W., and Purtscheller, F., 1999, Post-collisional potassic and ultrapotassic magmatism in SW Tibet: Geochemical, Sr-Nd-Pb-O isotopic constraints for mantle source characteristics and petrogenesis: Journal of Petrology, v. 40, p. 1399-1424.

Minster, J.F., and Allègre, C.J., 1978, Systematic use of trace elements in igneous processes. Part III: Inverse problem of batch partial melting in volcanic suites: Contributions to Mineralogy and Petrology, v. 68, p. 37-52.

Mitchell, J.G., 1968, The argon-40/argon-39 method for potassium-argon age determination: Geochimica et Cosmochimica Acta, v. 32, p. 781-790.

Mock, C., Arnaud, N.O., and Cantagrel, J.-M., 1999, An early unroofing in northwestern Tibet? Constraints from ^{40}Ar-^{39}Ar thermochronology on granitoids from the eastern Kunlun range (Qianghai, NW China): Earth and Planetary Science Letters, v. 171, p. 107-122.

Molnar, P., England, P., and Martinod, J., 1993, Mantle Dynamics, uplift of the Tibetan plateau, and the Indian Monsoon: Reviews of Geophysics, v. 31, p. 357-396.

Molnar, P., and Lyon-Caen, H., 1989, Fault plane solutions of earthquakes and tectonics of the northern and eastern parts of the Tibetan Plateau: Geophysical Journal Interational, v. 99, p. 123-153.

Molnar, P., and Tapponnier, P., 1978, Active tectonics of Tibet: Journal of Geophysical Research, A, Space Physics,, v. 83, p. 5361-5375.

Montel, J.-M., 1993, A model for monazite/melt equilibrium and application to the generation of granitic magmas: Chemical Geology, v. 110, p. 127-146.

Murphy, M.A., and Harrison, T.M., 1999, Relationship between leucogranites and the Qomolangma detachment in the Rongbuk Valley, south Tibet: Geology, v. 27, p. 831-834.

Murphy, M.A., Yin, A., Harrison, T.M., Durr, S.B., Chen, Z., Ryerson, F.J., Kidd, W.S.F., Wang, X., and Zhou, X., 1997, Did the Indo - Asian collision alone create the Tibetan plateau?: Geology, v. 25, p. 719-722.

Murphy, M.A., Yin, A., Kapp, P., Harrison, T.M., Lin, D., and Jinghui, G., 2000, Southward propagation of the Karakorum fault system, southwest Tibet: Timing and magnitude of slip: Geology, v. 28, p. 451-454.

Nakamura, N., 1974, Determination of REE, Ba, Fe, Mg, Na and K in carbonaceous and ordinary chondrites: Geochimica et Cosmochimica Acta, v. 38, p. 757-775.

Nelson, D.R., McCulloch, M., and Sun, S.S., 1985, The origins of ultrapotassic rocks as inferred from Sr, Nd and Pb isotopes: Geochimica et Cosmochimica Acta, v. 50, p. 231-245.

Nelson, K.D., Zhao, W., Brown, L.D., Kuo, J., Che, J., Liu, X., Klemperer, S.L., Makovsky, Y., Meisser, R., Mechie, J., Kind, R., Wenzel, F., Ni, J., Nabelek, J., Leshou, C., Tan, H., Wei, W., Jones, A.G., Booker, J., Unsworth, M., Hauck, M., Alsdorf, D., Ross, A., Cogan, M., Wu, C., Sandvoi, E., and Edwards, M., 1996, Partially Molten middle crust beneath Southern Tibet: Synthesis of Project INDEPTH results: Science, v. 274, p. 1684-1688.

Niida, K., and Green, D.H., 1999, Stability and chemical composition of pargasitic amphibole in MORB pyrolite under upper mantle conditions: Contributions to Mineralogy and Petrology, v. 135, p. 18-40.

Nisbet, E.G., Cheadle, M., Arndt, N.T., and Bickle, M.J., 1993, Constraining the potential temperature of the Archaean mantle: a review of the evidence from komatiites: Lithos, v. 30, p. 291-307.

Norin, E., 1946, Geological explorations in western Tibet: Report of the Scientific expedition to the northwestern provinces of China under the leadership of Dr. Sven Hedin, Tryckeri Aktiebolaget, Thule, Stockholm.

O'Brien, P., Zotov, N., Law, R., Khan, M.A., and Jan, M.Q., 1999, Coesite in eclogite from the Upper Kaghan Valley, Pakistan: a first record and implications, *in* Sobel, E., Appel, E., Strecker, M., Ratchbacher, L., and Blisniuk, P., eds., 14th Himalayan-Karakorum-Tibet Workshop: Kloster Ettal, Germany, p. 109-110.

Odling, N.W.A., 1995, An experimental replication of upper-mantle metasomatism: Nature, v. 373, p. 58-60.

Oliver, G.J.H., Johnson, M.R.W., and Fallick, A.E., 1995, Age of metamorphism in the Lesser Himalaya and the main central thrust zone, Garhwl India: results of illite crystallinity, 40Ar-39Ar fusion and K-Ar studies: Geological Magazine, v. 132, p. 139-149.

Onsott, T.C., Phillips, D., and Pringle-Goodell, L., 1991, Laser microprobe measurement of chlorine and argon zonation in biotite: Chemical Geology, v. 90, p. 145-168.

Owens, T.J., Zandt, G, 1997, Implications of crustal property variation for models of Tibetan plateau evolution: Nature, v. 387, p. 37-43.

Palmer, M.R., and Elderfield, H., 1985, Sr isotope composition of sea water over the past 75 Myr: Nature, v. 314, p. 526-528.

Pan, Y., and Kidd, W.S.F., 1992, Nyainqentanghla shear zone: A late Miocene extensional detachment in the southern Tibetan Plateau: Geology, v. 20, p. 775-778.

Parrish, R.R., and Hodges, K.V., 1996, Isotopic constraints on the age and provenance of the Lesser and Greater Himalayan sequences, Nepalese Himalaya: Geological Society of America Bulletin, v. 108, p. 904-911.

Parsons, B., and McKenzie, D.P., 1978, Mantle convection and the thermal structure of the plates: Journal of Geophysics Research, v. 82, p. 803-27.

Patchett, P.J., White, W.M., Feldmann, H., Kielinczuk, S., Hofmann, A.W., 1984, Hafnium/rare earth element fractionation in the sedimentary system and crustal recycling into the Earth's mantle: Earth and Planetary Science Letters, v. 69, p. 365-378.

Patchett, P.J., and Tatsumoto, M., 1980, Hafnium isotope variations in oceanic basalts: Geophysical Research Letters, v. 7, p. 1077-1080.

Patel, R.C., Singh, S., Asokan, A., Manickavasagam, R.M., and Jain, A.K., 1993, Extensional tectonics in the Himalayan orogen, Zanskar, NW India: Geological Society Special Publication, v. 74, p. 445-459.

Patiño Douce, A.E., 1999, What do experiments tell us about the relative contributions of crust and mantle to the origin of ganitic magmas?, *in* Castro, A., Fernandez, C. and Vigneresse, J.L., ed., Understanding granites: Integrating new and classical techniques, Volume 158: London, Geological Society Special Publications, p. 55-75.

Patiño Douce, A.E., and Harris, N., 1998, Experimental constraints on Himalayan Anatexis: Journal of Petrology, v. 39, p. 689-710.

Patriat, P., and Achache, J., 1984, India-Eurasia collision chronology has implications for crustal shortening and driving mechanism of plates: Science, v. 211, p. 615-621.

Pearce, J.A., and Houjun, M., 1988, Volcanic rocks of the 1985 Tibet Geotraverse: Lhasa to Golmud: A327.

Pearce, J.A., and Parkinson, I.J., 1993, Trace element models for mantle melting: application to volcanic arc petrogenesis: Geological Society Special Publication, v. 76 Magmatic Processes and Plate Tectonics, p. 373-403.

Pearson, D.G., Carlson, R.W., Shirey, S.B., Boyd, F.R., and Nixon, P.H., 1995, Stabilisation of archaean lithospheric mantle: A Re-Os isotope study of peridotite xenoliths from the Kaapvaal craton: Earth and Planetary Science Letters, v. 134, p. 341-357.

Pêcher, A., 1991, The contact between the higher Himalaya crystallines and the Tibetan sedimentary series: Miocene large-scale dextral shearing.: Tectonics, v. 10, p. 587-598.

Pickles, C.S., Kelley, S.P., Reddy, S.M., and Wheeler, J., 1997, Determination of high-spatial resolution argon isotope variations in metamorphic biotites: Geochimica et Cosmochimica Acta, v. 61, p. 3809-3833.

Plank, T., and Langmuir, C.H., 1998, The chemical composition of subducting sediment and its consequences for the crust and mantle: Chemical Geology, v. 145, p. 325-394.

Platt, J.P., and England, P.C., 1994, Convective removal of lithosphere beneath mountain belts: thermal and mechanical consequences: American Journal of Science, v. 294, p. 301-336.

Pognante, U., 1990, Shoshonistic and ultrapotassic post-collisional dykes from northern Karakorum (Sinkiang, China): Lithos, v. 26, p. 305-316.

Pollack, H.S., 1986, Cratonization and thermal evolution of the mantle: Earth and Planetary Science Letters, v. 80, p. 175-182.

Potts, P.J., Webb, P.C., and Watson, J.S., 1984, Energy dispersive X-ray flourescence of silicate rocks for major and trace elements: X-ray spectrometry, v. 13, p. 2-15.

Pouchou, J.L., and Pichoir, F., 1985, "PAP" procedure for improved quantitative analysis: Microbeam Analysis, v. 20, p. 104-105.

Prince, C., Harris, N., and Vance, D., 2000, Fluid enhanced melting during prograde metamorphism: Journal of the Geological Society of London. *in press*

Prince, C.I., 1999, The timing of prograde metamorphism in the Garhwal Himalaya, India [PhD thesis]: Milton Keynes, The Open University.

Prince, P.I., Kosler, J., Vance,D., Günther, D., 2000, Comparison of laser ablation ICP-MS and isotope dilution REE analyses - implications for Sm-Nd garnet geochronology: Chemical Geology, v. 168, p. 255-274.

Purdy, J.W., and Jager, E., 1976, K-Ar ages on rock-forming minerals from the Central Alps: Mem. Inst. Geol. Mineral Univ. Padova, v. 30, p. 3-31.

Pryer, L.L., 1993, Microstructures in feldspars froma major crustal thrust zone: the Grenville Front, Ontario, Canada: Journal of Structural Geology, v. 15, p. 221-36.

Pysklywec, R.N., Beaumont, C., and Fullsack, P., 2000, Modelling the behaviour of the continental mantle lithosphere during plate convergence: Geology, v. 28, p. 655-658.

Quidelleur, X., Grove, M., Lovera, O.M., Harrison, T.M., and Yin, A., 1997, Thermal evolution and slip history of the Renbu Zedong Thrust, southeastern Tibet: Journal of Geophysical Research, v. 102, p. 2659-2679.

Ramsey, M.H., Potts, P.J., Webb, P.C., Watkins, P., Watson, J.S., and Coles, B.J., 1995, An objective assessment of analytical method precision: comparison of ICP-AES and XRF for the analysis of silicate rocks: Chemical Geology, v. 124, p. 1-19.

Ratschbacher, L., Frisch, W., Liu, G., and Chen, C., 1994, Distributed deformation in the southern and western Tibet during and after the India-Asia collision: Journal of Geophysical Research, v. 99, p. 19917-19945.

Raymo, M.E., and Rudiman, W.F., 1992, Tectonic forcing of late Cenozoic climate: Nature, v. 359, p. 117-122.

Reddy, S.M., and Potts, G.J., 1999, Constraining absolute deformation ages: the relationship between deformation mechanisms and isotope systematics: Journal of Structural Geology, v. 21, p. 1255-1265.

Reed, S.J.B., 1995, Electron probe microanalysis, *in* Potts, P.J., Bowles, J.F.W., Reed, S.J.B., and Cave, M.R., eds., Microprobe techniques in the Earth Sciences: London, Chapman and Hall, p. 49-89.

Rex, A.J., Searle, M.P., Tirrul, R., Crawford, M.B., D.J., P., Rex, D.J., and Barnicoat, A., 1988, The geochemical and tectonic evolution of the central Karakorum, North Pakistan: Philosophical Transactions of the Royal Society of London, v. A 326, p. 229-255.

Richard, P., Shimizu, N., Allègre, C.J., 1976, $^{143}Nd/^{144}Nd$, a natural tracer: an application to oceanic basalts: Earth and Planetary Science Letters, v. 31, p. 269-278.

Richter, F.M., Rowley, D.M., and DePaolo, D.J., 1992, Sr isotope composition of seawater: the role of tectonics: Earth and Planetary Science Letters, v. 109, p. 11-23.

Robinson, J.A.C., and Wood, B.J., 1998, The depth of the spinel to garnet transition at the peridotite solidus: Earth and Planetary Science Letters, v. 164, p. 277-284.

Roddick, J.C., 1978, The application of isochron diagrams in ^{40}Ar-^{39}Ar dating: a discussion: Earth and Planetary Science Letters, v. 41, p. 233-244.

and Searle, M.P., eds., Himalayan Tectonics, Volume 74: Geological Society Special Publication: London, Geological Society of London, p. 429-444.

Searle, M.P., Noble, S.R., Hurford, A.J., and Rex, C.J., 1999b, Age of crustal melting, emplacement and exhumation history of the Shivling leucogranite, Garhwal Himalaya: Geological Magazine, v. 136, p. 513-525.

Searle, M.P., Weinburg, R.F., and Dunlap, W.J., 1998, Transpressional tectonics along the Karakorum fault zone, northern Ladakh: constraints on Tibetan extrusion, Continental Transpressional and Transtensional Tectonics, Volume 135: London, Geological Society of London Special Publication, p. 307-326.

Searle, M.P., Windley, B.F., Coward, M.P., Cooper, D.J.W., Rex, A.J., Rex, D., Tingdon, L., Xuchang, X., Thakur, V.C., and Kumar, S., 1987, The closing of Tethys and the tectonics of the Himalaya: *Geological Societry of America Bulletin*, v. 98, p. 678-701.

Shackleton, R.M., 1981, Structure of Southern Tibet: report from a traverse from Lhasa to Khatmandu organised by Academica Sinica: Journal of Structural Geology, v. 3, p. 97-105.

Shah, S.K., and Sinha, A.K., 1974, Stratigraphy and tectonics of the "Tethyan " zone in a part of western Kumaun Himalaya: Himalayan Geology, v. 4, p. 1-27.

Shaw, D.M., 1970, Trace element fractionation during anatexis: Geochimica and Cosmochimica Acta, v. 84, p. 237-243.

Silver, P.G., Carlson, R.W., and Olson, P., 1988, Deep slabs, geochemical heterogeneity, and the large-scale structure of mantle convection: Annual Reviews of Earth and Planetary Sciences, v. 16, p. 477-541.

Smith, A.B., and Xu, J., 1988, Paleontology of the 1985 Tibet Geotraverse, Lhasa to Golmud: *Philosophical Transactions of the Royal Society of London*, v. A327, p. 53-105.

Smith, H.A., and Barreiro, B., 1990, Monazite U-Pb dating of staurolite-grade metamorphism in pelitic schists: Contributions to Mineralogy and Petrology, v. 105, p. 602-615.

Sorkhabi, R.B., Stump, E., Foland, K., and Arvind, K.J., 1996, Fission-track and $^{40}Ar/^{39}Ar$ evidence for episodic denudation of the Gangotri granitoids in the Garhwal Himalaya, India: Tectonophysics, v. 260, p. 187-199.

Spear, F.S., and Parrish, R.R., 1996, Petrology and Cooling Rates of the Valhalla Complex, British- Columbia, Canada: Journal of Petrology, v. 37, p. 733-765.

Spera, F.J., 1987, Dynamics of translithospheric migration of metasomatic fluid and alkaline magma, *in* Menzies, M.A., Hawkesworth, C.J., ed., Mantle Metasomatism: Academic Press Geology Series: London, Academic Press Inc., p. 1-18.

Srivastava, P., and Mitra, G., 1994, Thrust geometries and deep structure of the outer and lesser Himalaya, Kumaon and Garhwal (India): Implications for evolution of the Himalayan fold-and-thrust belt: *Tectonics*, v. 13, p. 89-109.

Steck, A., Spring, L., Vannay, J.-C., Masson, H., Bucher, H., Stutz, E., Marchant, R., and Tieche, J.-C., 1993, The tectonic evolution of the Northwestern Himalaya in eastern Ladakh and Lahul, India: Geological Society Special Publications, v. 74 Himalayan Tectonics, p. 265-276.

Steiger, R.H., and Jäger, E., 1977, Subcomission of geochronology: Convention on the use of decay constants in geo- and cosmochronology: Earth and Planetary Science Letters, v. 36, p. 359-262.

Stern, C.R., Klingfield, R., Schelling, D., N.S., V., Futa, K., Peterman, Z.E., and Amini, H., 1989, The Bhagirathi leucogranite of the High Himalaya (Garhwal, India): age,

petrogenesis and tectonic implications: Geological Society of America, Special Paper, v. 232.

Stolper, E., Newman, S., 1994, The role of water in the petrogenesis of Mariana trough magmas: Earth and Planetary Science Letters, v. 121, p. 293-325.

Sun, S., and McDonough, W.F., 1989, Chemical and isotopic systematics of oceanic basalts: implications for mantle composition and processes: Geological Society Special Publication, v. 42 (Magmatism in the Ocean Basins), p. 313-345.

Sweeney, R.J., Thompson, A.B., and Ulmer, P., 1993, Phase relations of a natural MARID composition and implications for MARID genesis, lithospheric melting and mantle metasomatism: Contributions to Mineralogy and Petrology, v. 115, p. 225-241.

Tainton, K.M., and McKenzie, D., 1994, The generation of kimberlites, Lamproites, and their source rocks: Journal of Petrology, v. 35, p. 787-817.

Tapponier, and Molnar, 1976, Slip-line field theory and large-scale continental tectonics: Nature, v. 264, p. 32-39.

Tapponnier, P., Meyer, B., Avouac, J.P., Peltzer, G., Gaudemer, Y., Shunmin, G., Hongfa, X., Kelun, Y., Zhitai, C., Shuahua, C., and Huagang, D., 1990, Active thrusting and folding in the Qilian Shan, and decoupling between upper crust and mantle in northeastern Tibet: Earth and Planetary Science Letters, v. 97, p. 382-403.

Tapponnier, P., Peltzer, G., Le Dain, A.Y., Armijo, R., and Cobbold, P., 1982, Propagating extrusion tectonics in Asia: new insights from simple experiments with plasticine: Geology, v. 10, p. 611-616.

Taylor, S.R., and McLennan, S.M., 1985, The Continental Crust: its Composition and Evolution, Blackwell Scientific Publications.

Tindle, A.G., and Webb, P.C., 1990, Estimation of lithium contents in trioctahedral micas using microprobe data; application to micas from granitic rocks: European Journal of Mineralogy, v. 2, p. 595-610.

Tullis, J., and Yund, R.A., 1987, Transition from cataclastic flow to dislocation creep of feldspar: mechanisms and microstructures: Geology, v. 15, p. 606-609.

Turner, G., 1971, Agon-40-argon-39 dating: the optimisation of irradiation parameters: Earth and Planetary Science Letters, v. 10, p. 227-234.

Turner, G., and Cadogan, P.H., 1974, Possible effects of ^{39}Ar recoil in $^{40}Ar/^{39}Ar$ dating: Proceedings of the 5th Lunar Science Conference, p. 1601-1615.

Turner, S., Arnaud, N., Liu, J., Rogers, N., Hawkesworth, C., Harris, N., Kelley, S., Van Calsteren, P., and Wanming, D., 1996, Post-Collision, Shoshonitic Volcanism on the Tibetan plateau: Implications for Convective Thinning of the Lithosphere and the source of Ocean Island Basalts: Journal of Petrology, v. 27, p. 45-71.

Turner, S., and Hawkesworth, C., 1995, The nature of the sub-continental mantle: constraints from the major-element composition of continental flood basalts: Chemical Geology, v. 120, p. 295-314.

Turner, S., Hawkesworth, C., Liu, J., Rogers, N., Kelley, S., and Van Calsteren, P., 1993, Timing of Tibetan uplift constrained by analysis of volcanic rocks: Nature, v. 364, p. 50-53.

Turner, S., Platt, J.P., George, R.M.M., Kelley, S.P., Pearson, D.G., and Nowell, G.M., 1998, Magmatism associated with orogenic collapse of the Betic-Alboran Domain, SE Spain: Journal of Petrology, v. 40, p. 1011-1036.

Turner, S., Sandiford, M., and Foden, J., 1992, Some geodynamic and compositional constraints on "postorogenic" magmatism: Geology, v. 20, p. 931-934.

Valdiya, K.S., 1980, The two intracrustal boundary thrusts of the Himalaya: Tectonophysics, v. 66, p. 323-348.

Valdiya, K.S., 1988, Tectonics and evolution of the central sector of the Himalaya: Philosophical Transactions of the Royal Society of London, v. A 326, p. 151-175.

Van der Voo, R., Spakman, W., and Bijwaard, H., 1999, Tethyan subducted slabs under India: Earth and Planetary Science Letters, v. 171, p. 7-20.

Vance, D., and O'Nions, R.K., 1990, Isotopic chronometry of zoned garnets: growth kinetics and metamorphic histories: Earth and Planetary Science Letters, v. 97, p. 227-240.

Vance, D., Ayres, M., Kelley, S., and Harris, N., 1998, The thermal response of a metamorphic belt to extension: contraints form laser Ar data on metamorphic micas: Earth and Planetary Science Letters, v. 162, p. 153-164.

Vance, D., and Harris, N., 1999, Timing of prograde metamorphism in the Zanskar Himalaya: Geology, v. 27, p. 395-398.

Vance, D., and Mahar, E., 1998, Pressure-temperature paths from P-T pseudosections and zoned garnets: potential, limitations and examples from the Zanskar Himalaya, NW India: Contributions to Mineralogy and Petrology, v. 132, p. 225-245.

Vannay, J.C., and Hodges, K.V., 1996, Tectonomorphic evolution of the Himalayan metamorphic core between the Annapurna and Dhaulagiri, central Nepal: Journal of Metamorphic Geology, v. 14, p. 635-656.

Venturelli, G., Capedri, S., Di Battistini, G., Crawford, A., Kogarko, L.N., and Celestini, S., 1984a, The ultrapotassic rocks from southeastern Spain: Lithos, v. 17, p. 37-54.

Venturelli, G., Thorpe, R.S., Dal Piaz, G.P., Del Moro, A., and Pots, P.J., 1984b, Petrogenesis of calc-alkaline, shoshonitic and associated ultrapotassic Oligocene volcanic rocks from the Northwestern Alps: Contributions to Mineralogy and Petrology, v. 86, p. 209-220.

Villa, I.M., Huneke, J.C., and Wasserburg, G.J., 1983, ^{39}Ar recoil losses and and presolar ages in Allende inclusions: Earth and Planetary Science Letters, v. 63, p. 1-12.

Vine, F.J., 1966, Spreading of the ocean floor: new evidence: Science, v. 154, p. 1405-1415.

Vine, F.J., and Matthews, D.H., 1963, Magnetic anomalies over oceanic ridges: Nature, v. 199, p. 947-949.

Virdi, N.S., 1986, Lithostratigraphy and Stucture of the Central Crystallines in the Alaknanda and Dhauliganga valleys of Garhwal, Uttar Predesh: Current trends in Geology, v. 9, p. 155-166.

Von Blanckenburg, F., and Davies, H.J., 1995, Slab breakoff: A model for syncollisional magmatism and tectonics in the Alps: Tectonics, v. 14, p. 120-131.

Wallace, M.E., and Green, D.T., 1991, The effect of bulk rock composition on the stability of amphibole in the upper mantle: Implications for solidus peridotites and mantle metasomatism: Mineralogy and Petrology, v. 44, p. 1-19.

Wanming, D., 1991, Cenozoic volcanism and intraplate subduction at the northern margin of the Tibetan Plateau: Chinese Journal of Geochemistry, v. 10, p. 140-152.

Wanming, D., 1997, Cenozoic volcanism and liihosphere tectonic evolution in the northern Tibetan plateau, China, *in* Zhaonai, L., ed., 30th International Geological Conference, Volume 15, p. 3-12.

Watson, E.B., and Harrison, T.M., 1983, Zircon saturation revisited; temperature and composition effects in a variety of crustal magma types: Earth and Planetary Science Letters, v. 64, p. 295-304.

Watson, J., 1996, Fast and simple method of powder pellet preparation for x-ray flourescence analysis: X-ray Spectrometry, v. 25, p. 173-174

Wedepohl, K.H., 1991, Chemical characteristics and genesis of the quartz-feldspathic rocks in the Archaean crust of Greenland: Contributions to Mineralogy and Petrology, v. 107, p. 163-179.

Wernike, B., 1981, Low angle faults in the Basin and Range Province: nappe tectonics in an extending orogen: Nature, v. 291, p. 645-646.

Wesnousky, S.G., Kumar, S., Mohindra, R., and Thakur, V.C., 1999, Uplift and convergence along the Himlayan Frontal Thrust of India: Tectonics, v. 18, p. 967-976.

Willett, S.D., 1999, Rheological dependence of extension in wedge models of convergent orogens: Tectonophysics, v. 305, p. 419-435.

Willett, S.D., and Beaumont, C., 1994, Subduction of Asian lithospheric mantle beneath Tibet inferred from models of continental collision: Nature, v. 369, p. 642-645.

Williams, M.L., Jercinovic, M.J., and Terry, M.P., 1999, Age mapping and dating of monazite on the electron microprobe: deconvoluting multistage tectonic histories: Geology, v. 27, p. 1023-1026.

Wittlinger, G., Tapponier, P., Poupinet, G., Mei, J., Danian, S., Herquel, G., and Masson, F., 1998, Tomographic evidence for localised lithospheric shear along the Altyn Tagh fault: Science, v. 282, p. 74-76.

Wu, C., Nelson, K.D., Wortman, G., Samson, S.D., Yue, Y., Li, J., Kidd, W.S.F., and Edwards, M.A., 1998, Yandong cross structure and South Tibetan Detachment in the east central Himalaya (89°-90°E): Tectonics, v. 17, p. 28-45.

Yaxley, G.M., Crawford, A.J., and Green , D.H., 1991, Evidence for carbonatite metasomatism in spinel peridotite xenoliths from western Victoria, Australia: Earth and Planetary Science Letters, v. 107, p. 305-317.

Yin, A., and Harrison, T.M., 2000, Geologic evolution of the Himalayan-Tibetan orogen: Annual Reviews of Earth and Planetary Sciences, v. 28, p. 211-280.

Yin, A., Harrison, T.M., Murphy, M.A., Grove, M., Nie, S., Ryerson, E.J., Feng, W.X., and Le., C.Z., 1999a, Tertiary deformation history of southeastern and southwestern Tibet during the Indo-Asia collision: Geological Society of America Bulletin, v. 111, p. 1644-1664.

Yin, A., Harrison, T.M., Ryerson, F.J., Kidd, W.S.F., and Copeland, P., 1994, Tertiary structural evolution of the Gangdese thrust system, Southern Tibet: Journal of Geophysical Research, v. 99, p. 18175-18201.

Yin, A., Kapp, P.A., Murphy, M.A., Manning, C.E., Harrison, T.M., Grove, M., Lin, D., Xi-Guang, D., and Cun-Ming., W., 1999b, Significant Late Neogene east-west extension in northern Tibet: Geology, v. 27, p. 787-790.

Yin, J., 1997, Stratigraphic geology of Gondwanan facies of Qinghai-Xiang (Tibet) Plateau and adjacent areas: Beijing, Geologic Publishing House, 206 p.

Yin, J., Xu, J., Liu, C., and Li, H., 1988, The Tibetan Plateau: regional stratigraphic context and previous work: Philosophic Transactions of the Royal Society of London, v. A327, p. 5-52.

York, D., 1969, Least-squares fitting of a straight line with correlated errors: Earth and Planetary Science Letters, v. 5, p. 320-324.

Zhang, K.J., Zhang, Y.J., and Xia, B.D., 1998, Did the Indo-Asian collision alone create the Tibetan plateau? Comment: Geology, v. October, p. 958-959.

Zhang, L.-S., and Schärer, U., 1999, Age and origin of magmatism along the Cenozoic Red River shear belt, China: Contributions to Mineralogy and Petrology, v. 134, p. 67-85.

Zhao, W., Nelson, K.D., and Team, P.I., 1993, Deep seismic reflection evidence for continental underthrusting beneath southern Tibet: Nature, v. 366, p. 557-559.

Zheng, H., Powell, C.M., An, Z., Zhou, J., and Dong, G., 2000, Pliocene uplift of the northern Tibetan Plateau: Geology, v. 28, p. 715-718.

A Sample locations and descriptions

This appendix lists the location and description of samples used in this study, although a number of samples from northern Tibet were only available as powders and so are not described in detail.

A.1 Malari Region, Garhwal Himalaya

A.1.1 High Himalayan Crystalline Series

Sample: HW24B
Latitude/Longitude: 30°41.20', 79°51.80'
Location description: 1km north Bhap Kund, about 3.5 km south of the Malari Fault
Rock type: gneiss
Field description: Gneiss alternated with calc-silicate layers and intruded by at least two generations of leucogranite veins, 1 pre- and 1 post- main fabric forming phase
Mineral assemblage: *Mu + bi + fsp + qz*
Petrographic description: Fabric predominantly defined by micas, quartz shows undulose extinction with sutured boundaries. Feldspars are seritised, and show evidence for grain boundary migration

Sample: HW61A
Latitude/Longitude: 30°40.80', 79°50.80'
Location description: Bhap Kund
Rock type: Augen gneiss
Field description: Strongly segregated, Migmatic gneiss, intruded by leucocratic veins and pegmatites
Mineral assemblage: *sill + mu + bi + fsp + qz*
Petrographic description: Complicated multi-stage deformation and fabric development. *Micas define fabric; evidence for 2 generations of muscovites. In some cases, sillimanite is* overgrown by muscovite. Fibrolite shows evidence of shearing. Feldspar seritised, quartz shows undulose extinction

Sample: HW65
Latitude/Longitude: 30°40.80', 79°52.90'

Location description: S of Malari
Rock type: schist
Field description: HW65 is intruded by a leucogranite - shearing at margins of intrusion appears to be normal top-to-the-north, but granite post-dates the main fabric forming phase.
Mineral assemblage: Gt, chl, fsp, qz, mu, bi
Petrographic description: This sample is highly sheared, with bent white micas, undulose extinction and crenular margins in quartz, and pull apart garnet fabrics with retrograde chlorite. The retrograde chlorite associated with the pull-apart cracks is relatively coarse, implying a high temperature for deformation. Garnets are large, cracked with abundant inclusions.

Sample: HW80
Latitude/Longitude: 30°28.50', 79°44.90'
Location description:
Rock type: Augen gneiss
Field description: Augen gneiss with well developed top-to-the-south fabric. Contains leucocratic boudins (scale of 50 cm) which show top-to-the-south shear
Mineral assemblage: Bi + fsp + qz + grt
Petrographic description: Micas define main foliation and wrap around garnets, which are well-preserved, with a euhedral habit.

Sample: HW98
Latitude/Longitude: 30°33.00', 79°33.50'
Location description: Just west of Josimath, on road to Helang
Rock type: gneiss
Field description: Gneiss with well developed top-to-the-south fabric. Some leucocratic segregation. Large kyanites are parallel to foliation
Mineral assemblage: Bi + fsp + qz + grt ± ky
Petrographic description: Micas show sweeping extinction and curved cleavage. Micas form fish around euhedral garnets and kspars. The sample is fresh, with few signs of alteration.

Sample: G53-1
Latitude/Longitude: 30°32.43', 79°44.85'
Location description: north of Suraithota. Collected by C. Prince in 1996.
Rock type: schist
Field description: Well developed top-to-the-south fabric, defined by feldspars and biotite
Mineral assemblage: Bi + fsp + qz + mu
Petrographic description: Fabric defined by micas, which form fish around kspars, defining a top-to-the-south shear fabric.

A.1.2 High Himalayan Leucogranites

Sample: HW28A

Latitude/Longitude: 30°41.51', 79°52.25'
Location description: 2.5 km south of Malari fault
Rock type: granite
Field description: Leucogranite cross-cut by fibrolitic sillimanite. Sillimanite cross cuts both the leucogranite and the metamorphic fabric. The leucogranite intrudes approx parallel to foliation and is moderately deformed. Cut by minor N-S trending faults
Mineral assemblage: Qz+ plag+ksp+mu
Petrographic description: Coarse crystalline rock (grain size > 3mm) Moderately deformed: micas show textures intermediate between cleavage bending and semi-brittle kinking. No coherent fabric defined

Sample:HW40A
Latitude/Longitude: 30°41.51', 79°52.25'
Location description: just S of Malari village
Rock type: granite
Field description: Highly sheared granite. Intruded by leucogranite dykes that are relatively undeformed
Mineral assemblage: Qz+ plag+ksp+mu
Petrographic description: Highly deformed with the development of ribbon textures, kinked muscovites and sericitised feldspars. Micas showing bending and slip parallel to 001 planes and feldspars showing micro-faulting textures. In places, the muscovites show evidence of new crystal growth and sub-grain development.

Sample: HW61B
Latitude/Longitude:30°40.80', 79°50.80'
Location description: Bhap Kund
Rock type: pegmatite
Field description: pegmatite vein intruding HW61A; there is no sharp intrusive contact with the gneiss, but a zone where the crystal size is smaller at the rims of the veins. The veins appear to post-date the main fabric forming phase of the gneiss.
Mineral assemblage: sill + mu + bi + fsp + qz
Petrographic description: Undeformed with large platy muscovites and sericitised feldspars.

Sample: HW61C
Latitude/Longitude:30°40.80', 79°50.80'
Location description: Bhap Kund
Rock type: pegmatite
Field description: blocky pegmatite vein intruding HW61A
Mineral assemblage: sill + mu + bi + fsp + qz
Petrographic description: Undeformed with very large platy muscovites (0.5 to 5 mm) and sericitised feldspars.

Sample: HW66
Latitude/Longitude: 30°40.70', 79°40.10'
Location description: 2.5 km south of Malari fault
Rock type: sheared leucogranite

Field description: The entire rock is cross-cut by veins, indicating further fluid infiltration and alteration. Brittle faulted, fault orientations are ~ 330, parallel to the strike of the Malari fault
Mineral assemblage: Graph, chl, mu, rutile, sericite, bi, cc
Petrographic description: The entire sample shows evidence of pervasive deformaion. Matric chlorite and sericite are deformed. Muscovites are kinked and show cleavage-parallel slip. Chlorite grows after biotite.

A.1.3 Tibetan Sedimentary Series

Sample: HW39
Latitude/Longitude: 30°42.45', 79°30.10'
Location description: within minor fault zone east of Malari fault
Rock type: psammite
Field description: Uniformly textured psammite, some relict bedding preserved
Mineral assemblage: Fsp + mus + calcite + Fe-Ti oxides + tourmaline
Petrographic description: Layered sample, layerrs are mica-rich, or consist of feldspar in a mica/calcite/clay groundmass. Mica-rich layers define the fabric of the rock.. Feldspars show a slight preferred orientation. Large micas do not appear to show evidence of ductile deformation and appear altered.

Sample: HW44
Latitude/Longitude: 30°39.45', 79°38.00'
Location description: blocky outcrops, exposed in valley SE of Malari village
Rock type: psammite
Field description: Recrystallised psammite with no relict bedding apparent
Mineral assemblage: Qz + fsp + cc + mu + Fe-Ti oxides + detrital pyrite
Petrographic description: Oxide and carbonate veins. Veins cross cut the metamorphic fabric. Rare mica ribbons wrap around quartz and feldspar grains. Groundmass micas are small and show a preferred orientation.

Sample: GA 173
Latitude/Longitude: 30°41.45', 79°37.50'
Location description: exposed in valley SE of Malari village
Rock type: granite
Field description: Isolated outcrop
Mineral assemblage: Chl + mu + qz
Petrographic description: The entire sample appears to have been affected by shearing, with the development of weak C-S fabrics and undulose extinction in quartz. Micas from small "fish", show sweeping extinction, and have curved cleavage planes. There is no evidence for muscovite recrystallisation and the main means of deformation appears to have been by cleavage-parallel slip. The metamorphic grade of this sample is likely to be lower greenschist and below the biotite-in isograd, as the chlorite appears to be primary, as opposed to growing after biotite.

A.2 South Tibet

A.2.1 Shoshonites

Sample: JPT7
Latitude/Longitude:29°19.63', 86°57.75'
Location description: *Pabbai Zong, cuts deformed shales*
Rock type: shoshonite-ultrapotassic
Field description: glimmerite dyke
Mineral assemblage: phl + cpx + kfsp + ox
Petrographic description: The sample contains > 40 modal % phlogopite, with subordinate clinopyroxene and K-feldspar. The matrix is microcrystalline, consisting of phlogopite, Kfeldspar, and accessory oxides. They sample is highly altered, with late calcite formation

Sample: T2A
Latitude/Longitude:29°19.56', 86°57.38'
Location description: Pabbai Zong, cuts deformed shales
Rock type: shoshonite-ultrapotassic
Field description: 5m thick glimmerite dyke
Mineral assemblage: phl + cpx + kfsp + ox + ap +zr
Petrographic description: The sample contains > 40 modal % phlogopite, with subordinate clinopyroxene and K-feldspar, in a crystalline matrix, consisting of phlogopite, Kfeldspar, and accessory oxides. Phlogopites contain inclusions of zircon, F-apatite, zircon and rare amphibole.

Sample: T3B
Latitude/Longitude:29°19.53', 87°0.40'
Location description: Pabbai Zong, cuts deformed shales
Rock type: shoshonite-ultrapotassic
Field description: 5m wide glimmerite dyke, narrows and bifurcates at tip
Mineral assemblage: phl + cpx + kfsp + grt + ox +ap + zr
Petrographic description: The sample contains > 40 modal % phlogopite, with subordinate clinopyroxene and K-feldspar, in a crystalline matrix, consisting of phlogopite, Kfeldspar, and accessory oxides. Garnet is a common phenocryst phase, and has a euhedral habit. Phlogopites contain inclusions of zircon, F-apatite, zircon and Fe-Ti oxides.

Sample: T3F
Latitude/Longitude:29°19.53', 87°0.40'
Location description: Pabbai Zong, cuts deformed shales
Rock type: shoshonite

Field description: volcanic xenolith within T3B
Mineral assemblage: bi + cpx + kfsp + ox
Petrographic description: Phenocrysts of clinopyroxene and K-feldspar in a matrix of microcrystalline feldspar and biotite. The sample is altered, with evidence of fluid infiltration.

Sample: T4A
Latitude/Longitude:29°19.23', 87°0.58'
Location description: Pabbai Zong, cuts deformed shales
Rock type: shoshonite-ultrapotassic
Field description: 2 m wide glimmerite dyke
Mineral assemblage: phl + kfsp + ox +ap + zr
Petrographic description: > 40 modal % phlogopite, with subordinate K-feldspar. The matrix consists of phlogopite, Kfeldspar, and accessory oxides.

Sample: T5A
Latitude/Longitude:29°19.46', 87°01.21'
Location description: Pabbai Zong, cuts deformed shales
Rock type: shoshonite-ultrapotassic
Field description: 0.5 m wide fine-textured glimmerite dyke, weathering pale red-brown
Mineral assemblage: phl + kfsp + qz + ox +ap + zr
Petrographic description: ~ 30 modal % phlogopite, with subordinate quartz and K-feldspar. The matrix consists of phlogopite, Kfeldspar, and accessory oxides.

Sample: T5B
Latitude/Longitude:29°19.46', 87°01.21'
Location description: Pabbai Zong, cuts deformed shales
Rock type: shoshonite-ultrapotassic
Field description: 0.5 m wide fine-textured glimmerite dyke, with late clay minerals; *subparallel to T5A (T5A and T5B may represent bifurcations of a larger dyke at depth; this* could not be constrained from the available field evidence)
Mineral assemblage: phl + kfsp + qz + ox +ap + zr
Petrographic description: 30 modal % phlogopite, with subordinate quartz and K-feldspar, in a matrix of quartz, Kfeldspar, and accessory oxides. Altered.

Sample: T6
Latitude/Longitude:29°19.05', 87°01.21'
Location description: Pabbai Zong, cuts deformed shales
Rock type: shoshonite-ultrapotassic
Field description: 2 m wide coarse crystalline glimmerite dyke, associated with gypsum deposits. Highly altered
Mineral assemblage: no sample taken
Petrographic description: no sample taken

Sample: JPT23
Latitude/Longitude:32°02.55, 81°52.64'
Location description: road from Gerze to Shiquanhe
Rock type: basaltic andesite
Field description: agglomerate from Recent? cinder cone

Mineral assemblage: phl + cpx + qz + fsp (cc + dol)
Petrographic description: The sample contains angular fragments of a mafic lava, which contains aggregates of phlogopite, orthopyroxene and clinopyroxene. The matrix is fine grained, consisting of phlogopite, feldspar, quartz and accessaory oxides, and is intruded by calcite-dolomite veins

Sample: JPT24A
Latitude/Longitude:32°03.67', 81°48.11'
Location description: Shiquanhe, collected by J. Platt
Rock type: basaltic andesite
Field description: mafic lava flow, one of 3 (JPT24B and JPT24C). The flows sampled probably derive from the same parent lava
Mineral assemblage: phl + cpx + opx + kfsp + ox
Petrographic description: The sample contains contains megacrysts of phlogopite, orthopyroxene and clinopyroxene, phlogopites are surrounded by heavy oxide rims. The matrix is microcrystalline, consisting of phlogopite, feldspar, fresh glass and accessory oxides.

Sample: JPT24B
Latitude/Longitude:32°03.67', 81°48.11'
Location description: Shiquanhe (as for JPT24A)
Rock type: basaltic andesite
Field description: mafic lava (as for JPT24A)
Mineral assemblage: phl + cpx + opx + kfsp + ox
Petrographic description: The sample contains contains aggregates of phlogopite, orthopyroxene and clinopyroxene. The matrix is microcrystalline, consisting of phlogopite, feldspar, fresh glass and accessory oxides. There are some vesicles, filled with late zeolites.

Sample: JPT24C
Latitude/Longitude:32°03.67', 81°48.11'
Location description: Shiquanhe (as for JPT24A)
Rock type: basaltic andesite
Field description: mafic lava (as for JPT24A)
Mineral assemblage: phl + cpx + opx + ol + kfsp + ox
Petrographic description: This flow contains a large number of phlogopite-clinopyroxene-orthopyroxene aggregates, which are rimmed by a second growth of clinopyroxenes. Phlogopte megacrysts are kinked and rimmed by microcrystalline clinopyroxene. Olivine is rare, where present is it highly resorbed and sepentinised. The matrix is microcrystalline, consisting of phlogopite, feldspar, fresh glass and accessaory oxides.

A.2.2 Dacites and Rhyolites

Sample: JPT3
Latitude/Longitude:29°41.08', 89°34.78'

Location description: Namling Basin
Rock type: dacite
Field description: reddish weathering silicic volcanic rock
Mineral assemblage: bi + qz +plag + ox
Petrographic description: Phenocrysts of biotite, quartz and plagioclase in a microcrystaline matrix. Contains rounded crustal xenoliths.

Sample: JPT4
Latitude/Longitude:29°41.15', 89°35.32'
Location description: Namling Basin
Rock type: dacite
Field description: silicic pyroclastic flow rock
Mineral assemblage: bi + qz +plag + ox
Petrographic description: Phenocrysts of biotite, quartz and plagioclase in a microcrystaline matrix. Altered

Sample: JPT5.2
Latitude/Longitude:29°41.90', 89°34.21'
Location description: Namling Basin
Rock type: dacite
Field description: intermediate volcanic
Mineral assemblage: bi + qz +plag + ox
Petrographic description: Phenocrysts of biotite, quartz and plagioclase in a microcrystaline matrix.

Sample: JPT8
Latitude/Longitude:29°41.90', 89°34.21'
Location description: Namling Basin
Rock type: dacite
Field description: intermediate volcanic
Mineral assemblage: bi + qz +plag + ox
Petrographic description: Phenocrysts of biotite, quartz and plagioclase in a microcrystaline matrix. Contains abundant rounded feldspar xenoliths of probable crustal origin.

Sample: JPT14.1
Latitude/Longitude:29°50.15', 85°46.04'
Location description: Daggyai Tso
Rock type: dacite
Field description: reddish weathering quartz porphyry
Mineral assemblage: bi + qz +ksp + ox
Petrographic description: Phenocrysts of biotite, quartz and alkaline feldspar in a microcrystaline matrix.

Sample: JPT14.2
Latitude/Longitude:29°50.15', 85°46.04'
Location description: Daggyai Tso
Rock type: dacite
Field description: coarse crystalline dyke intruding JPT14.1
Mineral assemblage: hbl+ qz +ksp + ox

Petrographic description: Phenocrysts of hornblende, quartz and alkaline feldspar in a microcrystaline matrix. Preferred orientations of amphiboles define an approximate flow direction of 000°

Sample: T11B
Latitude/Longitude:29°50.15', 85°46.04'
Location description: Daggyai Tso
Rock type: *dacite*
Field description: fine crystalline dyke intruding JPT14.1
Mineral assemblage: hbl+ qz +ksp + ox
Petrographic description: Phenocrysts of hornblende, quartz and alkaline feldspar in a glassy matrix. Preferred orientations of amphiboles define an approximate flow direction of 000°

A.2.3 Dyke orientations

Table A.1 Orientations of shoshonitic and dacitic dykes

sample	*locality*	*trend*
T2A	Pabbai Zong	022°
T3B	Pabbai Zong	159°
T4A	Pabbai Zong	008°
T5A	Pabbai Zong	157°
T6	Pabbai Zong	180°
T11B	Daggyai Tso	000°
JPT14.2	Daggyai Tso	025°

A.3 North Tibet

The majority of samples were only available as powders, however petrographic and field descriptions for the different series are available in the literature: Dogai Coring, K9007-

K9021 and Kunlun, K9001, K9002, K9024-K9038, (Turner et al., 1996); Tienchuhai, K89G185-K89G200 (Arnaud et al., 1992); Heishebei, KP12.6-K 47.5P, Qiangshuigou Bb119-Bb135, Bq137, Yongbocuo Bq142-Bq141, (Wanming, 1991); Asikule K702 and K703 (Liu and Maimaiti, 1989). Samples 1105 and 912 were collected from the Ashikule region by E. Norin on an early expedition to western Tibet in 1946 and were obtained from J. Pearce. A description of the general area can be found in (Norin, 1946). Field descriptions for the Quangringnoinza group, 11H7/1-11H7/7 and Dogai Coring samples 12K1, 12K3, 12H91-12H94, 12H101-12H104, 12615A-C, 15G15A3 were provided by E. Gnos. Thin sections of selected samples from this collection were available. Petrographic descriptions and field observations (Gnos, pers comm.) are detailed below:

Sample: 11H7/1, 11H7/2, 11H7/3, 11H7/4, 11H7/5, 11H7/6, 11H7/7
Latitude/Longitude:34°19.43', 88°59.61'
Location description: Quangringnoinza mountains
Rock type: dacitic to rhyolitic (11H7/7 only)
Field description: boulders of fresh subvolcanic rocks originating from the Quangringnoinza mountains – the field party was not permitted to enter the Quangringnoinza region itself; the mountains are snow covered and inaccessible.
Mineral assemblage: n/a
Petrographic description: n/a

Sample: 12K1
Latitude/Longitude:34°22.00', 89°09.00'
Location description: Dogai Coring
Rock type: basaltic andesite
Field description: intermediate lava flow, contains small vugs filled with zeolites
Mineral assemblage: n/a
Petrographic description: n/a

Sample: 12K3
Latitude/Longitude:34°22.00', 89°09.00'
Location description: Dogai Coring
Rock type: andesite
Field description: intermediate lava flow
Mineral assemblage: n/a
Petrographic description: n/a

Sample: 12G15A, 12G15B, 12G15C

Latitude/Longitude:34°21.28', 89°02.61'
Location description: Dogai Coring
Rock type: andesite
Field description: intermediate lava flows
Mineral assemblage: n/a
Petrographic description: n/a

Sample: 12H9-1
Latitude/Longitude:34°24.00', 89°14.00'
Location description: SE of Dogai Coring lake
Rock type: dacite
Field description: intermediate lava flow
Mineral assemblage: kfsp + qz + bi + Fe-Ti ox
Petrographic description: phenocrysts of potassium feldspar, biotite and quartz in a microcrystalline groundmass consisting of feldspar, mica and opaque phases. Biotites show resorbed margins and anomalous extinction colours

Sample: 12H9-2
Latitude/Longitude:34°24.00', 89°14.00'
Location description: SE of Dogai Coring lake
Rock type: dacite
Field description: intermediate lava flow
Mineral assemblage: kfsp + qz + bi + Fe-Ti ox
Petrographic description: potassium feldspar, biotite and quartz phenocrysts in a groundmass consisting of feldspar mico-laths, mica and opaque phases and relatively fresh glass. Biotites show resorbed margins and anomalous extinction colours

Sample: 12H9-4
Latitude/Longitude:34°24.00', 89°14.00'
Location description: SE of Dogai Coring lake
Rock type: dacite
Field description: intermediate lava flow
Mineral assemblage: n/a
Petrographic description: n/a

Sample: 12H10-1
Latitude/Longitude:34°24.00', 89°14.00'
Location description: SE of Dogai Coring lake
Rock type: dacite
Field description: intermediate lava flow
Mineral assemblage: kfsp + qz + bi + Fe-Ti ox
Petrographic description: phenocrysts of potassium feldspar, biotite and quartz in a groundmass consisting of feldspar mico-laths, mica and opaque phases. Biotites show resorbed margins and anomalous extinction colours. Small (< 3mm) crustal xenoliths are present; these are rounded and have thick reaction rims.

Sample: 12H10-2
Latitude/Longitude:34°24.00', 89°14.00'
Location description: SE of Dogai Coring lake

Rock type: dacite
Field description: intermediate lava flow
Mineral assemblage: n/a
Petrographic description: n/a

Sample: 12H10-3
Latitude/Longitude:34°24.00', 89°14.00'
Location description: SE of Dogai Coring lake
Rock type: dacite
Field description: intermediate lava flow
Mineral assemblage: kfsp + qz + bi + Fe-Ti ox
Petrographic description: phenocrysts of potassium feldspar, biotite and quartz in a groundmass consisting of feldspar mico-laths, mica and opaque phases. Biotites show resorbed margins and anomalous reddish extinction colours. The sample is quite vesicular.

Sample: 12H10-4
Latitude/Longitude:34°24.00', 89°14.00'
Location description: SE of Dogai Coring lake
Rock type: dacite
Field description: intermediate lava flow
Mineral assemblage: kfsp + qz + bi + Fe-Ti ox
Petrographic description: potassium feldspar, biotite and quartz phenocrysts in a microcrystalline matrix of feldspar mico-laths, mica and opaque phases. Micas show embayed, resorbed margins and have anomalous birefringence colours.

Sample: 12H10-4
Latitude/Longitude:34°24.00', 89°14.00'
Location description: SE of Dogai Coring lake
Rock type: dacite
Field description: intermediate lava flow
Mineral assemblage: kfsp + qz + bi + Fe-Ti ox
Petrographic description: phenocrysts of potassium feldspar, biotite and quartz in a microcrystalline matrix of feldspar mico-laths, mica and opaque phases. Biotites show resorbed margins and anomalous birefringence colours.

Sample: 12G15A-2
Latitude/Longitude:34°24.00', 89°14.00'
Location description: SE of Dogai Coring lake
Rock type: dacite
Field description: intermediate lava flow
Mineral assemblage: kfsp + cpx + qz + Fe-Ti ox
Petrographic description: phenocrysts of potassium feldspar, clinopyroxene and quartz in a microcrystalline matrix of feldspar mico-laths, glass and opaque phases. Pyroxenes are small (< 100 μm), resorbed and are serpentinised.

Sample: 12G15A-3
Latitude/Longitude:34°24.00', 89°14.00'
Location description: SE of Dogai Coring lake
Rock type: dacite

Field description: intermediate lava flow
Mineral assemblage: kfsp + qz + bi + Fe-Ti ox
Petrographic description: potassium feldspar, biotite and quartz phenocrysts in a microcrystalline matrix of feldspar mico-laths, mica and opaque phases. Biotites have resorbed margins with thick oxide rims and anomalous birefringence colours.

B ^{40}Ar-^{39}Ar Data Tables

B.1 List of Tables

Appropriate J values and mineral abbreviations are detailed in the table captions. Note that all values are blank-corrected and quoted at the 1σ level (in the main text of this thesis, ages are quoted at the 2σ level).

B.1.1 Malari Region, Garhwal Himalaya

B.1.2 Tibetan Volcanics

Table B.1 ^{40}Ar-^{39}Ar ages for the High Himalayan Crystalline Series

sample	unit	mineral	crystal size (μ)	$^{40}Ar/^{39}Ar$	±	$^{38}Ar/^{39}Ar$	±	$^{37}Ar/^{39}Ar$	±	$^{36}Ar/^{39}Ar$	±	$^{39}Ar^{(1)}$	±	$^{40}Ar^{*}/^{39}Ar$	±	age (Ma)	±
HW24-B	HHCS	mu	250	0.78727	0.00072	0.01307	0.00013	0.00013	0.00011	0.00086	0.00013	1.63384	0.00122	0.53260	0.03502	11.69	0.77
HW24-B	HHCS	mu	250	0.93878	0.00328	0.01315	0.00015	0	0	0.00137	0.00032	0.65959	0.00164	0.53423	0.08471	11.72	1.85
HW24-B	HHCS	mu	250	0.94407	0.00246	0.01244	0.00014	0	0	0.00205	0.00050	0.42094	0.00088	0.33965	0.13592	7.46	2.98
HW24-B	HHCS	mu	250	0.98668	0.00375	0.01353	0.00012	0	0	0.00106	0.00010	2.12650	0.00777	0.67443	0.06742	14.78	1.47
HW24-B	HHCS	mu	250	1.02998	0.00147	0.01375	0.00029	0	0	0.00166	0.00021	1.02397	0.00105	0.53910	0.13992	11.83	3.06
HW24-B	HHCS	mu	250	0.92953	0.00407	0.01317	0.00014	0.00057	0.00019	0.00079	0.00021	1.00590	0.00433	0.69511	0.07809	15.23	1.71
HW24-B	HHCS	mu	250	0.89046	0.00664	0.01276	0.00010	0.00005	0.00006	0.00071	0.00007	2.90540	0.02155	0.68114	0.02648	14.93	0.58
HW24-B	HHCS	mu	250	0.87663	0.00283	0.01248	0.00009	0	0	0.00025	0.00019	1.09192	0.00299	0.80275	0.11991	17.58	2.62
HW24-B	HHCS	mu	250	1.05415	0.00277	0.01282	0.00008	0	0	0.00036	0.00033	0.63445	0.00090	0.94656	0.20635	20.71	4.49
HW24-B	HHCS	mu	250	0.77063	0.00184	0.01243	0.00014	0	0	0.00043	0.00013	1.59836	0.00336	0.64251	0.06648	14.09	1.45
HW24-B	HHCS	mu	250	0.79429	0.00136	0.01269	0.00057	0.00184	0.00324	0.00037	0.00047	0.44977	0.00067	0.68391	0.28141	14.99	6.14
HW24-B	HHCS	mu	250	0.72896	0.00375	0.01104	0.00024	0	0	0	0	0.39664	0.00186	0.93234	0.14432	20.41	3.14
HW24-B	HHCS	mu	250	0.85414	0.00464	0.01212	0.00013	0	0	0	0	1.14065	0.00613	0.89221	0.09323	19.53	2.03
HW24-B	HHCS	mu	250	0.76815	0.00295	0.01211	0.00006	0	0	0	0	1.40740	0.00467	0.79901	0.04353	17.50	0.95
HW66	HHCS	mu	250	0.87348	0.00237	0.01283	0.00007	0	0	0.00044	0.00012	1.69936	0.00231	0.74202	0.01058	16.26	0.24
HW66	HHCS	mu	250	0.82578	0.00623	0.01168	0.00014	0	0	0.00058	0.00018	1.15024	0.00328	0.65314	0.01642	14.32	0.37
HW66	HHCS	mu	250	0.81177	0.00476	0.01272	0.00016	0	0	0.00023	0.00017	1.25423	0.00466	0.74250	0.07012	16.27	1.53
HW66	HHCS	mu	250	0.75036	0.00230	0.01252	0.00015	0	0	0.00063	0.00021	0.99579	0.00118	0.56341	0.08816	12.36	1.93
HW66	HHCS	mu	250	0.79381	0.00250	0.01260	0.00017	0	0	0.00064	0.00023	0.91508	0.00071	0.60394	0.09593	13.24	2.10
HW66	HHCS	mu	250	1.36468	0.00216	0.01255	0.00007	0	0	0.00102	0.00003	6.32652	0.00756	1.06356	0.02467	23.26	0.55
HW66	HHCS	mu	250	0.88344	0.00083	0.01205	0.00005	0	0	0.00043	0.00004	5.30014	0.00462	0.75582	0.02937	16.56	0.65
HW66	HHCS	mu	250	0.85655	0.00257	0.01237	0.00015	0	0	0.00025	0.00036	0.58281	0.00097	0.78202	0.26959	17.13	5.88
HW80	HHCS	bi	1000	1.86394	0.00135	0.01259	0.00008	0	0	0.00116	0.00018	1.13872	0.00064	1.52062	0.05369	33.16	1.17
HW80	HHCS	bi	1000	1.61828	0.00287	0.01332	0.00014	0	0	0.00063	0.00031	0.66712	0.00060	1.43224	0.05890	31.25	1.28
HW80	HHCS	bi	1000	2.52668	0.00446	0.01264	0.00013	0	0	0.00435	0.00028	0.74366	0.00101	1.24163	0.05018	27.12	1.10
HW80	HHCS	bi	1000	3.59913	0.00178	0.01313	0.00009	0	0	0.00741	0.00013	1.65423	0.00042	1.40838	0.02710	30.74	0.61
HW80	HHCS	bi	1000	1.59538	0.00498	0.01262	0.00011	0.00022	0.00078	0.00132	0.00015	1.43593	0.00441	1.20644	0.02621	26.36	0.58
HW80	HHCS	bi	1000	1.64164	0.00417	0.01262	0.00026	0	0	0.00186	0.00041	0.50685	0.00057	1.09069	0.02766	23.85	0.61
HW80	HHCS	bi	1000	1.46529	0.00439	0.01235	0.00027	0	0	0.00039	0.00043	0.49024	0.00070	1.35136	0.02863	29.50	0.64
HW80	HHCS	bi	1000	2.07666	0.00610	0.01208	0.00040	0	0	0.00215	0.00055	0.38037	0.00060	1.44040	0.03691	31.43	0.81
HW80	HHCS	bi	1000	2.14067	0.00640	0.01279	0.00007	0	0	0.00335	0.00017	1.25405	0.00361	1.15099	0.13896	25.16	3.02
HW80	HHCS	bi	1000	1.72760	0.00182	0.01180	0.00010	0	0	0.00132	0.00015	1.42753	0.00059	1.33637	0.12204	29.18	2.65
HW80	HHCS	bi	1000	1.51404	0.00147	0.01286	0.00024	0	0	0.00093	0.00024	0.87601	0.00063	1.23777	0.06532	27.04	1.42
HW80	HHCS	bi	1000	1.48466	0.00502	0.01223	0.00012	0	0	0	0	0.54400	0.00181	1.58733	0.10531	34.60	2.28

errors on individual fusions are 1 σ, calculated using equation 3.2

(1) cm^3 X 10^{-10} *Samples were irradiated at the McMaster Reactor, Canada, J = 0.01220 ± 0.00006* *mu, muscovite; bi, biotite; gms, groundmass*

Table B.1 ^{40}Ar-^{39}Ar ages for the High Himalayan Crystalline Series

sample	unit	mineral	crystal size (μ)	$^{40}Ar/^{39}Ar$	±	$^{38}Ar/^{39}Ar$	±	$^{37}Ar/^{39}Ar$	±	$^{36}Ar/^{39}Ar$	±	$^{39}Ar^{(1)}$	±	$^{40}Ar^{*}/^{39}Ar$	±	age (Ma)	±
HW98	HHCS	gms	<20	3.25624	0.00623	0.01333	0.00009	0	0	0.00364	0.00039	0.54257	0.00097	2.18113	0.09442	47.38	2.04
HW98	HHCS	gms	<20	2.62650	0.00410	0.01408	0.00016	0	0	0.00288	0.00072	0.29120	0.00021	1.77409	0.17577	38.63	3.79
HW98	HHCS	gms	<20	2.21914	0.00208	0.01269	0.00018	0	0	0.00107	0.00011	1.90568	0.00093	1.90328	0.13416	41.41	2.89
HW98	HHCS	gms	<20	2.21270	0.00176	0.01229	0.00030	0.001158836	0.000632987	0.00138	0.00014	1.53903	0.00038	1.80546	0.16552	39.31	3.57
HW98	HHCS	gms	<20	2.12677	0.00342	0.01246	0.00010	0	0	0.00094	0.00016	1.31641	0.00206	1.84864	0.02556	40.24	0.58
HW98	HHCS	gms	<20	1.03073	0.00064	0.01225	0.00011	0	0	0.00053	0.00011	1.85376	0.00034	0.87340	0.01804	19.12	0.40
HW98	HHCS	gms	<20	1.74835	0.00363	0.01227	0.00011	0	0	0.00047	0.00018	1.15838	0.00236	1.60907	0.19318	35.07	4.17
HW98	HHCS	gms	<20	2.19932	0.00111	0.01252	0.00011	0	0	0.00111	0.00004	5.95412	0.00207	*1.66998*	*0.03759*	*40.70*	*0.83*
HW98	HHCS	gms	<20	5.45634	0.01717	0.01160	0.00029	0	0	0.00268	0.00047	0.44587	0.00139	4.66303	0.13786	99.82	2.91
HW98	HHCS	gms	<20	2.66314	0.01456	0.01243	0.00008	0	0	0.00097	0.00011	1.88724	0.00777	2.37707	0.03326	51.58	0.75
HW98	HHCS	mu	400-1250	2.25588	0.00892	0.01066	0.00138	0.004930381	0.007877571	0	0	0.18517	0.00063	2.59100	0.67366	56.15	14.4
HW98	HHCS	mu	400-1250	2.07007	0.00558	0.01270	0.00019	0	0	0.00101	0.00015	1.41662	0.00374	1.77220	0.08818	38.59	1.91
HW98	HHCS	mu	400-1250	2.35673	0.01481	0.01059	0.00025	0	0	0.00178	0.00111	0.18858	0.00055	1.83023	0.98730	39.84	21.26
HW98	HHCS	mu	400-1250	2.45818	0.00703	0.01312	0.00020	0.000354374	0.000744041	0.00156	0.00019	1.07845	0.00302	1.99786	0.12879	43.45	2.78
HW98	HHCS	mu	400-1250	2.63496	0.02561	0.01321	0.00034	0	0	0.00268	0.00022	0.94055	0.00416	1.84323	0.14950	40.12	3.22
HW98	HHCS	mu	400-1250	2.18968	0.00699	0.01183	0.00026	0	0	0.00103	0.00026	0.79274	0.00235	1.88459	0.07243	41.01	1.57
HW98	HHCS	mu	400-1250	2.30448	0.01130	0.01265	0.00022	0	0	0.00158	0.00018	1.17927	0.00538	1.83615	0.04941	39.97	1.08
HW98	HHCS	bi	250-1000	2.31491	0.00413	0.01177	0.00011	0	0	0.00110	0.00026	0.80053	0.00092	1.98934	0.23310	43.26	5.01
HW98	HHCS	bi	250-1000	2.22877	0.00505	0.01180	0.00019	0	0	*0.00121*	*0.00022*	*0.97537*	*0.00197*	*1.87249*	*0.10268*	*40.75*	*2.22*
HW98	HHCS	bi	250-1000	2.09000	0.00595	0.01187	0.00029	0.001123121	0.000632394	0.00146	0.00032	0.66165	0.00147	1.65858	0.15132	36.14	3.27
HW98	HHCS	bi	250-1000	2.10434	0.00447	0.01229	0.00008	0	0	0.00172	0.00035	0.59895	0.00101	1.59667	0.12133	34.80	2.62
HW98	HHCS	bi	250-1000	3.05578	0.00546	0.01281	0.00011	0	0	0.00323	0.00027	0.78601	0.00118	2.10050	0.08837	45.65	1.91
G53-1	HHCS	mu		0.82369	0.00051	0.01281	0.00005	0.000239837	0.000162786	0.00045	0.00006	3.36400	0.00147	0.69087	0.00524	15.14	0.14
G53-1	HHCS	mu		*0.91492*	*0.00058*	*0.01211*	*0.00005*	*0.000576917*	*0.000201079*	*0.00032*	*0.00008*	*2.72337*	*0.00151*	*0.81922*	*0.00647*	*17.94*	*0.17*
G53-1	HHCS	mu		0.56073	0.00037	0.01243	0.00002	0	0	0.00003	0.00011	1.93710	0.00097	0.55112	0.03155	12.09	0.69
G53-1	HHCS	mu		0.62254	0.00037	0.01299	0.00013	0.00023	0.00021	0.00022	0.00009	2.34884	0.00097	0.55649	0.02602	12.21	0.57
G53-1	HHCS	mu		0.62144	0.00170	0.01179	0.00008	0.00154	0.00098	0.00129	0.00039	0.53899	0.00055	0.24150	0.11340	5.31	2.49
G53-1	HHCS	mu		0.70129	0.00135	0.01242	0.00020	0.00007	0.00073	0.00070	0.00014	1.53449	0.00160	0.49504	0.08493	10.86	1.86
G53-1	HHCS	mu		*0.68140*	*0.00097*	*0.01253*	*0.00007*	*0*	*0*	*0.00053*	*0.00005*	*4.33553*	*0.00458*	*0.52538*	*0.03021*	*11.53*	*0.66*
G53-1	HHCS	mu		0.62377	0.00060	0.01246	0.00005	0	0	0.00064	0.00006	3.26984	0.00256	0.43589	0.04004	9.57	0.88
G53-1	HHCS	mu		0.75893	0.00200	0.01223	0.00006	0	0	0.00046	0.00014	1.46220	0.00298	0.62312	0.07688	13.66	1.68
G53-1	HHCS	mu		0.74068	0.00288	0.01261	0.00016	0	0	0.00031	0.00018	1.15896	0.00386	0.64965	0.08107	14.24	1.77
G53-1	HHCS	mu		0.77216	0.00506	0.01305	0.00016	0.002048443	0.002121126	0.00199	0.00041	0.51824	0.00294	0.18543	0.18122	4.08	3.98
G53-1	HHCS	mu		0.77254	0.00473	0.01250	0.00030	0	0	0.00119	0.00017	1.24837	0.00710	0.41960	0.04019	9.21	0.88
G53-1	HHCS	mu		0.82673	0.00129	0.01279	0.00077	0.003119071	0.000710517	0.00058	0.00058	0.36078	0.00021	0.65473	0.04867	14.35	1.06
G53-1	HHCS	mu		0.96954	0.00114	0.01210	0.00010	0	0	0	0	1.16914	0.00105	1.02792	0.03866	22.48	0.85
G53-1	HHCS	mu		0.65897	0.00466	0.01153	0.00031	0	0	0	0	0.43001	0.00122	0.90429	0.11645	19.79	2.54
G53-1	HHCS	mu		0.50484	0.00136	0.01193	0.00027	0	0	0	0	0.48590	0.00055	0.61978	0.26941	13.59	5.89
G53-1	HHCS	mu		0.56952	0.00454	0.01246	0.00074	0	0	0	0	0.49449	0.00160	0.75776	0.10129	16.60	2.21
G53-1	HHCS	mu		0.53500	0.00321	0.01069	0.00030	0	0	0	0	0.46377	0.00273	0.68219	0.04035	14.95	0.88
G53-1	HHCS	mu		0.82339	0.00209	0.01136	0.00062	0	0	0	0	0.51950	0.00070	1.06229	0.03386	23.23	0.74
G53-1	HHCS	mu		*0.67787*	*0.00112*	*0.01180*	*0.00033*	*0*	*0*	*0*	*0*	*1.25306*	*0.00152*	*0.73235*	*0.03607*	*16.05*	*0.79*
G53-1	HHCS	mu		0.62525	0.00607	0.01258	0.00241	0	0	0	0	0.16888	0.00038	0.80897	0.26758	17.72	5.83

errors on individual fusions are 1 σ, calculated using equation 3.2

(1) cm³ X 10⁻¹⁰ *Samples were irradiated at the McMaster Reactor, Canada, J = 0.01220 ± 0.00006* *mu, muscovite; bi, biotite; gms, groundmass*

Table B.2 ^{40}Ar-^{39}Ar ages for the High Himalayan Leucogranites

sample	unit	mineral	crystal size (μ)	$^{40}Ar/^{39}Ar$	±	$^{38}Ar/^{39}Ar$	±	$^{37}Ar/^{39}Ar$	±	$^{36}Ar/^{39}Ar$	±	$^{39}Ar^{(1)}$	±	$^{40}Ar^{*}/^{39}Ar$	±	age (Ma)	±
HW24-A	HHL	mu	800	0 78375	0.00144	0.01225	0.00004	0	0	0.00027	0.00010	2.20762	0.00160	0 70504	0 01265	15.45	0 29
HW24-A	HHL	mu	800	0.72927	0.00049	0.01238	0.00002	0	0	0.00022	0.00002	8.65978	0 00470	0.66549	0.01655	14.59	0 37
HW24-A	HHL	mu	800	0.82746	0 00188	0.01220	0.00006	0	0	0.00079	0.00006	3 41117	0.00596	0.59279	0 04203	13 00	0.92
HW24-A	HHL	mu	800	0.81518	0.00191	0.01224	0.00005	0	0	0.00036	0.00007	3 16956	0.00680	0.70945	0 03161	15 55	0.69
HW24-A	HHL	mu	800	0.76528	0.00168	0.01252	0.00003	0	0	0.00045	0.00002	9.05816	0.01747	0 63237	0.01139	13.87	0 26
HW24-A	HHL	mu	800	0.80722	0.00182	0.01252	0.00008	0	0	0 00035	0.00007	2.98567	0.00575	0.70330	0.03355	15.41	0.74
HW24-A	HHL	mu	800	0 86594	0.00153	0.01200	0.00004	0	0	0 00043	0.00005	4.19475	0.00496	0.73872	0 04155	16.19	0 91
HW24-A	HHL	mu	800	0.73366	0.00046	0.01244	0.00003	0	0	0.00017	0.00002	9.76329	0.00374	0.68408	0 01785	14 99	0 40
HW24-A	HHL	mu	800	0 72470	0.00062	0.01243	0.00003	0.00002	0.00017	0.00018	0.00003	7.52317	0.00584	0 67026	0.02310	14 69	0 51
HW24-A	HHL	mu	800	0.72603	0.00122	0.01215	0.00002	0	0	0.00016	0.00002	8 80755	0.01176	0.67741	0.02332	14 85	0.51
HW24-A	HHL	mu	800	0.71071	0.00101	0.01225	0 00002	0	0	0.00025	0.00005	4 54166	0.00395	0.63556	0.04518	13 93	0.99
HW24-A	HHL	mu	800	0.79679	0.00166	0.01068	0.00029	0	0	0 00000	0	0.38395	0.00059	1.65340	0.24460	36.03	5.28
HW24-A	HHL	mu	800	0.81070	0.00147	0.01170	0.00010	0	0	0.00000	0	1.19433	0 00101	0.82629	0 07864	18.10	1.72
HW24-A	HHL	mu	800	1.00949	0.00147	0.01187	0 00012	0	0	0.00000	0	1.24002	0 00067	1.08956	0.14049	23.82	3.05
HW24-A	HHL	mu	800	0.71747	0 00257	0.01198	0.00014	0	0	0.00000	0	1.31157	0.00281	1 05812	0 13285	23 14	2 89
HW24-A	HHL	mu	800	0.77099	0.00370	0.01157	0.00008	0	0	0.00000	0	0.78313	0.00064	0.85023	0.02272	18.62	0 50
HW28-A	HHL	mu	400	0.74009	0.00630	0 01091	0.00089	0	0	0.00000	0	0.17120	0.00034	2.08123	0 69254	45.24	14.87
HW28-A	HHL	mu	400	0.69246	0.00517	0.01231	0.00020	0	0	0.00000	0	0.95741	0.00664	0.89339	0.12400	19.56	2.70
HW28-A	HHL	mu	400	0.82531	0.00066	0.01250	0.00005	0	0	0.00021	0.00003	7.22444	0.00441	0.76346	0 02260	16.73	0 50
HW28-A	HHL	mu	400	0.76849	0.00063	0.01198	0.00007	0	0	0.00030	0.00006	3.76142	0.00252	0.67940	0 04302	14 89	0.94
HW28-A	HHL	mu	400	0.76350	0.00404	0.01189	0.00015	0	0	0.00007	0.00007	2.83326	0 01462	0.74159	0 03122	16.25	0 69
HW28-A	HHL	mu	400	1.11942	0.00177	0.01244	0.00002	0	0	0.00056	0.00001	18.09690	0 02738	0.95346	0.00544	20.86	0 16
HW40-A	HHL	mu	250	1.00471	0.00171	0.01271	0.00005	0	0	0.00088	0.00011	1.93510	0.00239	0.74496	0.08044	16.32	1.76
HW40-A	HHL	mu	250	0.95703	0.00131	0.01200	0.00004	0.00017	0.00006	0.00060	0.00006	3.39483	0.00437	0.77972	0.04586	17 08	1.00
HW40-A	HHL	mu	250	0.89191	0.00131	0 01223	0.00003	0	0	0.00031	0.00005	4.12656	0.00475	0 80018	0.00971	17 53	0.23
HW40-A	HHL	mu	250	0.92805	0.00107	0.01261	0.00007	0	0	0.00049	0.00005	4.10074	0.00218	0.78429	0.00974	17.18	0 23
HW40-A	HHL	mu	250	0.85918	0.00188	0 01202	0.00004	0	0	0.00011	0.00009	2 22687	0.00113	0.82574	0 02848	18 08	0.63
HW40-A	HHL	mu	250	0.86053	0.00126	0.01253	0.00005	0	0	0.00029	0.00027	0.79137	0.00047	0.77428	0 07231	16 96	1.58
HW40-A	HHL	mu	250	0.96998	0.00533	0.01340	0.00019	0.00047	0 00502	0.00000	0.00000	0.22425	0.00076	1 21903	0.25520	26 63	5 54
HW40-A	HHL	mu	250	1.86543	0.00053	0.01295	0.00001	0	0	0.00293	0.00001	26.74827	0.00735	0.99870	0 00239	21 85	0.12
HW40-A	HHL	mu	250	1.86840	0.00280	0.01260	0.00004	0	0	0.00059	0 00008	2.54644	0.00202	1.69294	0 02639	36.88	0.60
HW40-A	HHL	mu	250	1.54322	0.00148	0.01246	0.00005	0	0	0.00036	0.00009	2.35851	0.00160	1.43797	0 02687	31.38	0.60

errors on individual fusions are 1 σ, calculated using equation 3.2

(1) cm^3 X 10 $^{-10}$ *Samples were irradiated at the McMaster Reactor, Canada, J = 0.01220 ± 0.00006* *mu, muscovite; bi, biotite; gms, groundmass*

Table B.2 ^{40}Ar-^{39}Ar ages for the High Himalayan Leucogranites

sample	unit	mineral	crystal size (μ)	$^{40}Ar/^{39}Ar$	±	$^{38}Ar/^{39}Ar$	±	$^{37}Ar/^{39}Ar$	±	$^{38}Ar/^{39}Ar$	±	^{39}Ar[1]	±	$^{40}Ar^*/^{39}Ar$	±	age (Ma)	±
HW61-B	HHL	mu	800	1.05419	0.00122	0.01210	0.00009	0	0	0.00063	0.00020	1.03937	0.00059	0.86911	0.11407	19.03	2.49
HW61-B	HHL	mu	800	0.69726	0.00373	0.01435	0.00038	0	0	0.00008	0.00085	0.24822	0.00047	0.67226	0.48543	14.74	10.60
HW61-B	HHL	mu	800	1.56936	0.00287	0.01278	0.00008	0	0	0.00226	0.00023	0.91879	0.00044	0.90072	0.02451	19.72	0.54
HW61-B	HHL	mu	800	0.82520	0.00128	0.01191	0.00014	0	0	0.00026	0.00010	2.04486	0.00256	0.74933	0.08217	16.42	1.79
HW61-B	HHL	mu	800	0.76116	0.00134	0.01239	0.00006	0	0	0.00030	0.00003	6.45555	0.00823	0.67369	0.02606	14.77	0.57
HW61-B	HHL	mu	800	0.74188	0.00099	0.01258	0.00011	0.00002	0.00036	0.00001	0.00011	1.93467	0.00164	0.73867	0.02337	16.19	0.52
HW61-B	HHL	mu	800	0.84203	0.00219	0.01280	0.00036	0	0	0.00029	0.00025	0.85529	0.00101	0.75497	0.07402	16.54	1.62
HW61-B	HHL	mu	800	0.80053	0.00303	0.01233	0.00009	0	0	0.00041	0.00005	4.01674	0.01121	0.68003	0.01600	14.91	0.36
HW61-B	HHL	mu	800	0.72633	0.00116	0.01229	0.00004	0	0	0.00018	0.00003	6.76582	0.01042	0.67313	0.03675	14.76	0.81
HW61-B	HHL	mu	800	0.69999	0.00225	0.01213	0.00005	0	0	0.00021	0.00003	7.30339	0.02323	0.63881	0.03409	14.01	0.75
HW61-B	HHL	mu	800	0.72972	0.00262	0.01349	0.00023	0	0	0.00000	0	0.33565	0.00061	1.04401	0.09249	22.83	2.01
HW61-B	HHL	mu	800	0.71559	0.00099	0.01152	0.00031	0	0	0.00000	0	0.87570	0.00080	0.76520	0.05160	16.76	1.13
HW61-C	HHL	mu	1200	2.06703	0.00348	0.01302	0.00023	0	0	0.00271	0.00026	0.80445	0.00076	1.26478	0.09762	27.63	2.12
HW61-C	HHL	mu	1200	0.87079	0.00136	0.01301	0.00011	0	0	0.00060	0.00011	1.89987	0.00114	0.69441	0.03976	15.22	0.87
HW61-C	HHL	mu	1200	0.79163	0.00730	0.01144	0.00045	0	0	0.00000	0	0.09383	0.00021	1.78362	1.00081	38.84	21.56
HW61-C	HHL	mu	1200	0.79819	0.01048	0.00722	0.00064	0	0	0.00000	0	0.06537	0.00021	4.50047	1.43666	96.43	29.98
HW61-C	HHL	mu	1200	0.94197	0.00486	0.01060	0.00025	0.00051	0.00685	0.00000	0	0.16604	0.00046	1.80157	0.56561	39.22	12.18
HW61-C	HHL	mu	1200	0.80064	0.00270	0.01254	0.00017	0	0	0.00000	0	0.76323	0.00143	1.03642	0.12307	22.67	2.68
HW61-C	HHL	mu	1200	0.79894	0.00491	0.01377	0.00038	0.00191	0.00060	0.00000	0	0.15582	0.00035	1.95388	0.36722	42.50	7.90
HW61-C	HHL	mu	1200	0.87098	0.01023	0.00550	0.00076	0.00272	0.00120	0.00135	0.00269	0.07806	0.00019	0.47351	0.73298	10.39	16.04
HW61-C	HHL	mu	1200	0.87845	0.01788	0.01209	0.00156	0.01125	0.00530	0.00243	0.00348	0.06038	0.00014	0.15902	0.42413	3.50	9.32
HW61-C	HHL	mu	1200	1.23004	0.00520	0.01221	0.00047	0.00064	0.00160	0.00115	0.00105	0.20036	0.00018	0.88935	0.06945	19.47	1.52
HW61-C	HHL	mu	1200	0.78197	0.00323	0.01133	0.00026	0	0	0.00000	0	1.24086	0.00361	0.84698	0.15539	18.55	3.39
HW61-C	HHL	mu	1200	0.75230	0.00063	0.01224	0.00004	0.00012	0.00002	0.00010	0.00002	9.87721	0.00777	0.72277	0.01953	15.84	0.43
HW61-C	HHL	mu	1200	0.73348	0.00079	0.01197	0.00014	0.00018	0.00010	0.00036	0.00009	2.38752	0.00151	0.62691	0.08074	13.75	1.76
HW61-C	HHL	mu	1200	0.75276	0.00253	0.01093	0.00015	0	0	0.00000	0	1.45378	0.00420	1.32901	0.05629	29.02	1.23
HW61-C	HHL	mu	1200	0.77990	0.00346	0.01203	0.00011	0	0	0.00000	0	5.98757	0.02071	0.86592	0.01412	18.96	0.32
HW61-C	HHL	mu	1200	0.78383	0.00249	0.01171	0.00009	0	0	0.00000	0	2.78937	0.00722	0.85725	0.02938	18.77	0.65
HW61-C	HHL	mu	1200	0.77764	0.00042	0.01216	0.00011	0	0	0.00000	0	2.27687	0.00089	0.89484	0.03585	19.59	0.79
HW61-C	HHL	mu	1200	0.90317	0.00311	0.01211	0.00009	0	0	0.00038	0.00008	2.62032	0.00764	0.79186	0.03128	17.35	0.69
HW61-C	HHL	mu	1200	0.75739	0.00558	0.01187	0.00013	0	0	0.00005	0.00006	3.26565	0.01386	0.74219	0.02377	16.26	0.52
HW61-C	HHL	mu	1200	1.03368	0.00767	0.01319	0.00009	0.00023	0.00037	0.00072	0.00006	3.73194	0.02276	0.82084	0.02129	17.98	0.47
HW65	HHL	bi	250	9.22714	0.01118	0.01388	0.00016	0	0	0.00900	0.00033	0.64171	0.00049	6.56784	0.24273	139.06	4.99
HW65	HHL	bi	250	1.65991	0.00189	0.01263	0.00008	0	0	0.00104	0.00011	1.88145	0.00098	1.35317	0.08274	29.54	1.80
HW65	HHL	bi	250	5.52977	0.00973	0.01406	0.00038	0	0	0.00578	0.00105	0.19999	0.00030	3.82317	0.78563	82.24	16.53
HW65	HHL	bi	250	3.24200	0.00361	0.01361	0.00020	0	0	0.00174	0.00030	0.71101	0.00065	2.72707	0.21891	59.05	4.67
HW65	HHL	bi	250	3.89804	0.01051	0.01257	0.00013	0	0	0.00347	0.00016	1.29653	0.00286	2.87379	0.08869	62.17	1.91
HW65	HHL	bi	250	2.55380	0.00295	0.01210	0.00010	0.00067	0.00017	0.00267	0.00024	0.88724	0.00059	1.76347	0.06454	38.40	1.40
HW65	HHL	bi	250	3.04156	0.00560	0.01253	0.00008	0	0	0.00218	0.00013	1.66482	0.00252	2.39672	0.03470	52.00	0.78
HW65	HHL	bi	250	2.20717	0.00415	0.01411	0.00040	0.00330	0.00056	0.00532	0.00050	0.41842	0.00034	0.63512	0.26862	13.93	5.87
HW65	HHL	bi	250	1.98485	0.00814	0.01327	0.00027	0	0	0.00482	0.00074	0.28295	0.00094	0.55933	0.55527	12.27	12.14
HW65	HHL	bi	250	2.92902	0.01442	0.01440	0.00027	0	0	0.00000	0	0.28764	0.00069	3.51151	0.54128	75.68	11.43
HW65	HHL	mu	250	0.91171	0.00164	0.01193	0.00036	0	0	0.00060	0.00005	4.21603	0.00701	0.73361	0.02936	16.07	0.65
HW65	HHL	mu	250	0.84626	0.00047	0.01223	0.00006	0.00026	0.00007	0.00044	0.00005	4.23170	0.00118	0.71575	0.02848	15.69	0.63
HW65	HHL	mu	250	0.76964	0.00150	0.01238	0.00007	0	0	0.00006	0.00004	4.87771	0.00550	0.75056	0.06003	16.44	1.31
HW65	HHL	mu	250	0.87454	0.00496	0.01267	0.00009	0.00009	0.00021	0.00052	0.00003	7.82112	0.03982	0.71982	0.03757	15.77	0.82
HW65	HHL	mu	250	0.84506	0.00543	0.01267	0.00013	0	0	0.00024	0.00009	2.24437	0.01142	0.77317	0.07759	16.94	1.69
HW65	HHL	mu	250	0.77952	0.00205	0.01205	0.00011	0	0	0.00005	0.00012	1.69461	0.00147	0.76488	0.10282	16.76	2.24
HW65	HHL	mu	250	0.74789	0.00432	0.01236	0.00016	0	0	0.00016	0.00014	1.46251	0.00794	0.70121	0.11495	15.37	2.51
HW65	HHL	mu	250	0.95359	0.00216	0.01222	0.00021	0	0	0.00000	0	1.37169	0.00051	0.99431	0.21341	21.75	4.64
HW65	HHL	mu	250	0.96452	0.00562	0.01334	0.00084	0.00050	0.00209	0.00289	0.00083	0.25427	0.00063	0.11035	0.66076	2.43	14.52

errors on individual fusions are 1 σ, calculated using equation 3.2

[1] cm^3 X 10^{-10} *Samples were irradiated at the McMaster Reactor, Canada, J = 0.01220 ± 0.00006* *mu, muscovite; bi, biotite; gms, groundmass*

Table B.3 ^{40}Ar-^{39}Ar ages for the Tibetan Sedimentary Series

sample	unit	mineral	crystal size (μ)	$^{40}Ar/^{39}Ar$	±	$^{38}Ar/^{39}Ar$	±	$^{37}Ar/^{39}Ar$	±	$^{36}Ar/^{38}Ar$	±	$^{39}Ar^{(1)}$	±	$^{40}Ar^{*}/^{39}Ar$	±	age (Ma)	±
HW39	TSS	mu -sep	250	0	0	0	0	0	0	0	0	0	0	0	0	0	0
HW39	TSS	mu	250	0	0	0	0	9.29692	20.17428	0	0	0	0	0	0	0	0
HW39	TSS	mu	250	29.55074	0 06816	0.01181	0.00024	0	0	0	0	0.89030	0.00177	29.63438	0 08927	556 77	2 76
HW39	TSS	mu	250	25 54166	0.03011	0.01209	0.00045	0	0	0	0	0.50768	0.00057	25.68834	0 10524	491 83	2.76
HW39	TSS	mu	250	21 54734	0.02055	0.01130	0.00035	0	0	0	0	0.61182	0.00049	21 60820	0.08614	422.12	2.38
HW39	TSS	mu	250	28 01909	0.03493	0.01255	0.00014	0.00004	0.00027	0.00061	0.00013	1.64219	0.00156	27.83771	0.04671	527 49	2.38
HW39	TSS	mu	250	40 92807	0.05097	0.01291	0.00024	0.00037	0.00119	0.00192	0.00026	0.79808	0.00098	40.36045	0.06543	722.33	3.06
HW39	TSS	mu	250	38.51821	0.07619	0.01275	0.00038	0 00276	0.00201	0.00096	0.00046	0.46114	0.00074	38.23561	0.10489	690.72	3.23
HW39	TSS	mu	250	35.33235	0.06983	0.01152	0.00020	0	0	0.00207	0.00045	0.46589	0.00038	34.71965	0.07917	637.16	2.91
HW39	TSS	mu	250	26.31173	0.17225	0.01266	0.00019	0.00066	0.00084	0.00153	0.00038	0.54916	0.00357	25.85974	0.17233	494.70	3.56
HW39	TSS	mu	250	24.29254	0.16138	0.01331	0.00028	0	0	0.00052	0.00048	0.44177	0.00214	24.13803	0.17774	465.66	3 63
HW39	TSS	mu	250	50.79973	0.43605	0.01254	0.00076	0	0	0.00051	0.00170	0.12327	0.00068	50.64871	0.51299	868.02	7.76
HW44	TSS	mu - slab	20	2.61614	0.00259	0.01217	0 00019	0	0	0.00016	0.00005	4.46631	0.00349	2.56751	0.03770	55.64	0 85
HW44	TSS	mu	20	2.85860	0.00245	0.01202	0.00008	0	0	0.00028	0.00006	3.37789	0.00235	2.77593	0.02790	60 09	0 66
HW44	TSS	mu	20	2.99539	0.00394	0.01253	0.00011	0.00007	0.00004	0.00028	0.00007	2.95569	0 00332	2.91351	0 03201	63.01	0 75
HW44	TSS	mu	20	2.22236	0.01225	0.01215	0.00016	0	0	0.00044	0.00013	1.56354	0.00861	2.09139	0 06116	45.45	1 33
HW44	TSS	mu	20	2.96816	0.01852	0.01208	0.00021	0.00003	0.00046	0 00393	0.00011	1.96302	0.01063	1.80800	0.02665	39 36	0 61
HW44	TSS	mu	20	11.31437	0.01415	0.01273	0.00012	0 00106	0.00013	0.00242	0.00017	1.25774	0.00089	10.59896	0.04213	219.39	1 31
HW44	TSS	mu	20	2.43865	0.00275	0.01267	0.00008	0.00225	0.00012	0.00197	0.00014	1.46329	0.00143	1 85766	0.03096	40 43	0 69
HW44	TSS	mu	20	262.77747	763.090	3.95725	11.69313	0	0	0	0	0	0	7556.41	21972.61	8180.91	5190
HW44	TSS	mu	20	2.66420	0.01055	0.01125	0.00050	0	0	0	0	0.26712	0.00105	3.66315	0.62913	78.88	13.26
HW44	TSS	gms - slab	<20	156.79546	2.73365	0	0	0	0	0.07234	0.03447	0.00610	0 00011	135.41995	25.87952	1759 65	214.84
HW44	TSS	gms	<20	1007.6742	4.29107	0.08466	0.00439	0	0	0.09717	0.00532	0 03955	0.00014	978.96186	5 75966	4619.54	12.77
HW44	TSS	gms	<20	175.34953	2.55972	0.05976	0.04161	0	0	0.07146	0.06497	0.00323	0.00005	154 23361	25.34926	1909.39	193 70
HW44	TSS	gms	<20	1471.3152	18.00770	0.15091	0.02951	0	0	0.26796	0.05478	0.00384	0 00005	1392.13317	27.24213	5212.92	34.38
HW44	TSS	gms	<20	122.64333	1.65265	0	0	0	0	0.00664	0.02215	0.00948	0.00013	120.67977	8.76110	1532.97	78.17
GA-173	TSS	mu - sep	250	1.18886	0.00170	0.01151	0.00012	0.00074	0.00055	0.00013	0.00019	1.09485	0.00089	1.14918	0.01279	25.12	0.30
GA-173	TSS	mu	250	1.27366	0.00342	0.01208	0.00014	0.00014	0.00050	0.00019	0.00018	1.19265	0.00143	1 21643	0.01212	26 58	0 29
GA-173	TSS	mu	250	2 00905	0.00669	0.01059	0.00176	0.00243	0.00124	0	0	0.13981	0.00023	2.23099	0.23913	48.45	5.13
GA-173	TSS	mu	250	1.14810	0.00239	0.01209	0.00013	0	0	0.00035	0.00011	1.83793	0 00177	1.04343	0.01833	22 82	0.41
GA-173	TSS	mu	250	1.16768	0.00217	0.01296	0.00012	0.00066	0.00010	0	0	0.74364	0 00023	1.17602	0 01878	25.70	0.43
GA-173	TSS	mu	250	1.57225	0.00449	0.01335	0.00017	0.00134	0.00052	0.00008	0.000781854	0.26859	0 00015	1.54915	0 05186	33.78	1.13

errors on individual fusions are 1 σ, calculated using equation 3.2

(1) cm^3 X 10^{-10} Samples were irradiated at the McMaster Reactor, Canada, J = 0.01220 ± 0.00006

mu, muscovite; bi, biotite; gms, groundmass

Table B.4 ^{40}Ar-^{39}Ar ages for the Southern Tibetan Dykes

sample	subgroup	mineral	crystal size (μ)	$^{40}Ar/^{39}Ar$	±	$^{38}Ar/^{39}Ar$	±	$^{37}Ar/^{39}Ar$	±	$^{36}Ar/^{39}Ar$	±	^{39}Ar (1)	±	$^{40}Ar^*/^{39}Ar$	±	Age (Ma)	±
T2A/98	Pabbai Zong	phl	250	13.53673	0.023203	0.035094	0.00029	0.032442	0.001828	0.033314	0.000843	0.048929	3.61E-05	*3.6925488*	*0.2499043*	*21.62758*	*1.455*
T2A/98	Pabbai Zong	phl	250	15.916627	0.026159	0.042003	0.000392	0.043488	0.002342	0.037534	0.001131	0.0365	0.00005	4.8253735	0.3341767	28.21099	1.939
T2A/98	Pabbai Zong	phl	250	16.75082	0.030188	0.041192	0.000767	0.060085	0.003224	0.039278	0.00141	0.029279	0.00005	5.1443087	0.4163337	30.06016	2.413
T2A/98	Pabbai Zong	phl	250	15.948343	0.03717	0.040512	0.000571	0.059983	0.002161	0.037112	0.001044	0.03961	8.54E-05	4.9818209	0.3081021	29.1183	1.786
T2A/98	Pabbai Zong	phl	250	20.434404	0.128157	0.044059	0.001516	0.078686	0.02379	0.046836	0.004924	0.021458	0.000132	6.5944944	1.4533189	38.44443	8.383
T2A/98	Pabbai Zong	phl	250	14.36585	0.018978	0.038329	0.000418	0.042787	0.003258	0.03233	0.000675	0.156663	0.000201	4.8121998	0.1990953	28.13457	1.155
T2A/98	Pabbai Zong	phl	250	14.087894	0.007965	0.040664	0.000129	0.044207	0.000304	0.031755	0.000175	0.162495	8.73E-05	4.7043679	0.0515568	27.50891	0.299
T2A/98	Pabbai Zong	phl	250	12.280719	0.008843	0.038673	7.55E-05	0.043193	0.000529	0.028037	0.00018	0.15765	0.000106	3.9958503	0.053179	23.39257	0.31
T2A/98	Pabbai Zong	phl	250	13.776357	0.015033	0.038766	0.000363	0.04493	0.000818	0.031349	0.000243	0.074483	6.18E-05	4.5126368	0.0722813	26.39592	0.42
T2A/98	Pabbai Zong	phl	250	14.885667	0.009397	0.041532	0.000233	0.044418	0.000523	0.035269	0.000182	0.137938	7.16E-05	4.4635373	0.0538731	26.11079	0.313
T2A/98	Pabbai Zong	phl	250	13.736486	0.030461	0.041076	0.000348	0.05181	0.001916	0.031176	0.000488	0.095425	0.000211	4.5238648	0.1431312	26.46112	0.831
T2A/98	Pabbai Zong	phl	250	18.23253	0.063703	0.042374	0.000379	0.057064	0.002045	0.045381	0.000559	*0.091778*	*0.00032*	*4.8223509*	*0.1594693*	*28.19346*	*0.925*
T2A/98	Pabbai Zong	phl	250	14.037784	0.015319	0.039739	0.000243	0.050535	0.001637	0.031239	0.000348	0.104036	9.22E-05	4.8065963	0.1028885	28.10206	0.597
T2A/98	Pabbai Zong	phl	250	12.984394	0.024452	0.043199	0.000416	0.05075	0.0028	0.029267	0.000331	0.061161	0.000112	4.336009	0.0971323	25.37	0.564
T2A/98	Pabbai Zong	phl	250	14.258199	0.016998	0.042511	0.000118	0.050941	0.001502	0.031641	0.000447	0.103504	0.000113	4.9081845	0.1318961	28.69131	0.765
T2A/98	Pabbai Zong	phl	250	15.070168	0.05033	0.046142	0.000938	0.050669	0.013079	0.025265	0.00408	0.012072	3.91E-05	7.6043946	1.205715	44.26025	6.932
T3B/98	Pabbai Zong	bi*	250	6.2075	0.0107	0.0288	0.0011	0.0000	0.0000	0.0001	0.0004	0.0403	0.0001	6.1708	0.1328	36.00	0.77
T3B/98	Pabbai Zong	bi*	250	9.9306	0.0514	0.0379	0.0005	0.0005	0.0002	0.0132	0.0001	0.1889	0.0009	6.0286	0.0540	35.18	0.31
T3B/98	Pabbai Zong	bi*	250	29.3064	0.2964	0.0864	0.0062	0.0000	0.0000	0.0912	0.0026	0.0075	0.0001	2.3563	0.7157	13.83	4.19
T3B/98	Pabbai Zong	bi*	250	18.8520	0.0608	0.0822	0.0026	0.0188	0.0025	0.0595	0.0014	0.0177	0.0001	1.2672	0.4168	7.45	2.45
T3B/98	Pabbai Zong	bi*	250	11.6333	0.0410	0.0774	0.0002	0.0065	0.0007	0.0314	0.0010	0.0460	0.0001	2.3466	0.2986	13.77	1.75
T3B/98	Pabbai Zong	bi*	250	7.5601	0.0376	0.0351	0.0002	0.0020	0.0002	0.0073	0.0004	0.1218	0.0006	5.4138	0.1341	31.62	0.78
T3B/98	Pabbai Zong	bi*	250	10.5192	0.0216	0.0492	0.0011	0.0160	0.0032	0.0273	0.0004	0.0453	0.0001	2.4580	0.1191	14.43	0.70
T3B/98	Pabbai Zong	bi*	250	3.8282	0.0025	0.0543	0.0003	0.0217	0.0007	0.0050	0.0001	0.2052	0.0001	2.3522	0.0260	13.81	0.15
T3B/98	Pabbai Zong	bi*	250	5.6291	0.0082	0.0617	0.0003	0.0157	0.0003	0.0109	0.0002	0.2136	0.0002	2.3981	0.0468	14.08	0.27
T3B/98	Pabbai Zong	bi*	250	9.9886	0.0361	0.0468	0.0010	0.0037	0.0026	0.0274	0.0007	0.0261	0.0001	1.8941	0.2044	11.13	1.20
T3B/98	Pabbai Zong	bi*	250	13.8969	0.0191	0.0609	0.0002	0.0191	0.0018	0.0401	0.0003	0.0658	0.0001	2.0475	0.1008	12.02	0.59
T5A/98	Pabbai Zong	phl	250	0.8650	0.0016	0.0137	0.0001	0.0073	0.0002	0.0000	0.0001	1.7019	0.0029	0.8561	0.0375	16.93	0.74
T5A/98	Pabbai Zong	phl	250	1.0694	0.0022	0.0140	0.0001	0.0150	0.0001	0.0011	0.0001	2.4058	0.0015	0.7474	0.0270	14.79	0.54
T5A/98	Pabbai Zong	phl	250	0.7809	0.0018	0.0137	0.0000	0.0072	0.0001	0.0003	0.0001	2.9041	0.0005	0.7004	0.0222	13.86	0.44
T5A/98	Pabbai Zong	phl	250	1.1314	0.0009	0.0137	0.0001	0.0015	0.0002	0.0015	0.0001	1.7887	0.0011	0.7017	0.0356	13.88	0.71
T5A/98	Pabbai Zong	phl	250	1.2330	0.0028	0.0140	0.0000	0.0090	0.0001	0.0019	0.0000	8.5638	0.0181	0.6764	0.0077	13.39	0.16
T5A/98	Pabbai Zong	phl	250	1.0175	0.0025	0.0130	0.0002	0.0013	0.0007	0.0013	0.0005	0.4341	0.0004	0.6423	0.1481	12.71	2.92
T5A/98	Pabbai Zong	phl	250	0.8505	0.0009	0.0136	0.0000	0.0058	0.0001	0.0007	0.0001	2.7673	0.0010	0.6379	0.0230	12.63	0.46
T5A/98	Pabbai Zong	phl	250	0.9022	0.0009	0.0131	0.0001	0.0341	0.0002	0.0006	0.0002	1.3023	0.0009	0.7273	0.0491	14.39	0.97
T5A/98	Pabbai Zong	phl	250	0.9248	0.0009	0.0139	0.0000	0.0105	0.0002	0.0012	0.0001	1.9553	0.0006	0.5801	0.0329	11.49	0.65
T5A/98	Pabbai Zong	phl	250	0.8751	0.0028	0.0133	0.0001	0.0006	0.0002	0.0006	0.0002	1.3404	0.0027	0.6875	0.0478	13.60	0.94

phl, phlogopite; hbl, hornblende; WR, whole-rock

(1) $cm^3 \times 10^{-10}$ *errors on individual fusions are 1 σ, calculated using equation 3.2*

Samples were irradiated at the McMaster Reactor, Canada, in three separate irradiations. J values for the irradiations, calculated from repeat analyses of biotite standard GA1550 are 0.00327± 0.00001 (T3B, T2A); 0.01101± 0.00006 (T5A, T11B/98) and 0.01220 ± 0.00006 (JPT 7, JPT 14.2).

** biotites from a volcanic xenolith entrained in the dyke were analysed to avoid problems of alteration within the sample*

Table B.4 ^{40}Ar-^{39}Ar ages for the Southern Tibetan Dykes

sample	subgroup	mineral	crystal size (μ)	$^{40}Ar/^{39}Ar$	±	$^{38}Ar/^{39}Ar$	±	$^{37}Ar/^{39}Ar$	±	$^{36}Ar/^{39}Ar$	±	^{39}Ar (1)	±	$^{40}Ar^*/^{39}Ar$	±	Age (Ma)	±
JPT 7	Pabbai Zong	phl	250	1.1347	0.0020	0.0130	0.0001	0.0438	0.0249	0.0006	0.0001	0.8234	0.0005	0.9622	0.0184	20.54	0.40
JPT 7	Pabbai Zong	phl	250	1.4238	0.0029	0.0133	0.0001	0.0441	0.0177	0.0009	0.0000	1.1552	0.0018	1.1457	0.0133	24.43	0.31
JPT 7	Pabbai Zong	phl	250	2.2396	0.0019	0.0136	0.0001	-0.0239	-0.0324	0.0028	0.0001	0.5713	0.0003	1.4154	0.0264	30.13	0.58
JPT 7	Pabbai Zong	phl	250	1.6687	0.0034	0.0134	0.0000	0.0086	0.0088	0.0013	0.0000	2.0938	0.0034	1.2855	0.0125	27.39	0.30
JPT 7	Pabbai Zong	phl	250	2.1709	0.0021	0.0145	0.0001	0.0104	0.0347	0.0021	0.0001	0.5343	0.0003	1.5633	0.0298	33.25	0.65
JPT 7	Pabbai Zong	phl	250	1.3804	0.0037	0.0128	0.0003	-0.0116	-0.0807	0.0009	0.0002	0.2298	0.0001	1.1095	0.0657	23.66	1.40
JPT 7	Pabbai Zong	phl	250	2.3245	0.0018	0.0133	0.0001	0.0160	0.0267	0.0022	0.0001	0.6943	0.0004	1.6788	0.0273	35.69	0.60
JPT 7	Pabbai Zong	phl	250	2.5661	0.0064	0.0155	0.0004	0.1875	0.1049	0.0000	-0.0003	0.1954	0.0002	2.5802	0.0817	54.56	1.72
T11B/98	Daggyai Tso	WR		1.0189	0.0039	0.0154	0.0002	0.0736	0.0010	0.0001	0.0005	0.1419	0.0001	0.9955	0.1336	19.67	2.63
T11B/98	Daggyai Tso	WR		0.8536	0.0029	0.0142	0.0002	0.0730	0.0008	0.0000	0.0004	0.1815	0.0001	0.8515	0.1044	16.84	2.06
T11B/98	Daggyai Tso	WR		1.7361	0.0081	0.0156	0.0003	0.0915	0.0006	0.0013	0.0003	0.1226	0.0004	1.3667	0.0963	26.94	1.89
T11B/98	Daggyai Tso	WR		0.8194	0.0083	0.0147	0.0004	0.0692	0.0020	0.0000	0.0000	0.0708	0.0001	0.8194	0.2677	16.20	5.27
T11B/98	Daggyai Tso	WR		0.8661	0.0055	0.0152	0.0002	0.0571	0.0005	0.0000	0.0000	0.0667	0.0000	0.8661	0.1710	17.12	3.37
T11B/98	Daggyai Tso	WR		1.2771	0.0042	0.0138	0.0002	0.0675	0.0011	0.0000	0.0000	0.1375	0.0001	1.2771	0.1379	25.19	2.70
JPT 14.2	Daggyai Tso	hbl	250	1.7797	0.0079	0.0140	0.0001	1.1423	0.8745	0.0022	0.0000	1.5565	0.0049	1.1263	0.0129	24.02	0.29
JPT 14.2	Daggyai Tso	hbl	250	1.1885	0.0034	0.0135	0.0001	1.7676	2.0197	0.0001	0.0001	0.6747	0.0003	1.1670	0.0238	24.88	0.52
JPT 14.2	Daggyai Tso	hbl	250	1.0386	0.0044	0.0138	0.0001	1.9698	1.2628	0.0000	0.0000	1.0833	0.0035	1.0370	0.0146	22.13	0.33
JPT 14.2	Daggyai Tso	hbl	250	0.9053	0.0052	0.0134	0.0002	2.2100	3.1450	0.0000	0.0001	0.4340	0.0001	0.9053	0.0351	19.33	0.75
JPT 14.2	Daggyai Tso	hbl	250	1.1467	0.0061	0.0135	0.0001	2.4758	1.7440	0.0000	0.0001	0.7840	0.0019	1.1363	0.0202	24.23	0.44
JPT 14.2	Daggyai Tso	hbl	250	1.4217	0.0043	0.0136	0.0000	1.5092	0.4253	0.0007	0.0000	3.2142	0.0071	1.2033	0.0071	25.65	0.19
JPT 14.2	Daggyai Tso	hbl	250	1.3794	0.0032	0.0140	0.0001	1.9206	0.9794	0.0005	0.0000	1.4014	0.0021	1.2405	0.0118	26.44	0.28
JPT 14.2	Daggyai Tso	hbl	250	1.3230	0.0021	0.0136	0.0001	1.2194	1.1968	0.0005	0.0000	1.1442	0.0005	1.1819	0.0141	25.20	0.32
JPT 14.2	Daggyai Tso	hbl	250	1.3995	0.0028	0.0140	0.0001	3.2484	1.6530	0.0005	0.0001	0.8298	0.0003	1.2410	0.0184	26.45	0.41

phl, phlogopite; hbl, hornblende; WR, whole-rock

(1) $cm^3 \times 10^{-10}$ *errors on individual fusions are 1 σ, calculated using equation 3.2*

Samples were irradiated at the McMaster Reactor, Canada, in three separate irradiations. J values for the irradiations, calculated from repeat analyses of biotite standard GA1550 are 0.00327± 0.00001 (T3B); 0.01101± 0.00006 (T2A, T5A, T11B/98) and 0.01220 ± 0.00006 (JPT 7, JPT 14.2).

Table B.5 ^{40}Ar-^{39}Ar ages for the Southern Tibetan shoshonites

sample	subgroup	mineral	crystal size (μ)	$^{40}Ar/^{39}Ar$	±	$^{38}Ar/^{39}Ar$	±	$^{37}Ar/^{39}Ar$	±	$^{36}Ar/^{39}Ar$	±	^{39}Ar (1)	±	$^{40}Ar^{*}/^{39}Ar$	±	Age (Ma)	±
JPT24C	Shiquanhe	phl	250	1.3355	0.0040	0.0128	0.0001	0.7060	0.0017	0.0007	0.0001	0.7065	0.0008	1.1288	0.0214	24.68	0.48
JPT24C	*Shiquanhe*	*phl*	*250*	*1.3067*	*0.0112*	*0.0124*	*0.0002*	*0.2241*	*0.0011*	*0.0005*	*0.0002*	*0.2229*	*0.0002*	*1.1496*	*0.0637*	*25.13*	*1.39*
JPT24C	Shiquanhe	phl	250	1.3956	0.0100	0.0121	0.0002	0.2388	0.0012	0.0010	0.0002	0.2497	0.0002	1.1044	0.0568	24.15	1.24
JPT24C	Shiquanhe	phl	250	1.3064	0.0050	0.0132	0.0001	0.4885	0.0007	0.0004	0.0001	0.5000	0.0003	1.1888	0.0284	25.98	0.63
JPT24C	Shiquanhe	phl	250	1.2433	0.0047	0.0131	0.0001	0.2111	0.0008	0.0005	0.0001	0.5526	0.0005	1.1088	0.0273	24.24	0.61
JPT24C	Shiquanhe	phl	250	1.2014	0.0028	0.0124	0.0001	0.1315	0.0007	0.0001	0.0001	1.0380	0.0012	1.1584	0.0286	25.32	0.63
JPT24C	Shiquanhe	phl	250	1.2448	0.0074	0.0127	0.0001	0.2428	0.0014	0.0004	0.0003	0.3589	0.0004	1.1184	0.0827	24.45	1.80
JPT24C	Shiquanhe	phl	250	1.2899	0.0043	0.0129	0.0001	0.3623	0.0013	0.0006	0.0001	0.6783	0.0004	1.1056	0.0438	24.17	0.96
JPT24C	Shiquanhe	phl	250	1.5881	0.0065	0.0125	0.0002	0.3377	0.0012	0.0017	0.0003	0.3877	0.0003	1.0909	0.0777	23.85	1.69
JPT24c	Shiquanhe	phl	250	1.2576	0.0020	0.0127	0.0000	0.0909	0.0003	0.0004	0.0000	0.9216	0.0012	1.1394	0.0074	24.90	0.20
JPT24c	Shiquanhe	phl	250	1.2367	0.0010	0.0129	0.0001	0.1851	0.0004	0.0004	0.0000	1.7142	0.0006	1.1231	0.0040	24.55	0.15
JPT24C	*Shiquanhe*	*phl*	*250*	*1.2033*	*0.0027*	*0.0122*	*0.0001*	*0.2114*	*0.0005*	*0.0004*	*0.0001*	*1.9114*	*0.0020*	*1.0746*	*0.0157*	*23.50*	*0.36*
JPT24B	Shiquanhe	phl	250	1.6119	0.0185	0.0129	0.0004	0.6003	0.0054	0.0021	0.0007	0.1381	0.0002	1.0029	0.2149	21.94	4.67
JPT24B	Shiquanhe	phl	250	1.2253	0.0117	0.0139	0.0002	0.1284	0.0020	0.0004	0.0005	0.2200	0.0005	1.1064	0.1349	24.19	2.93
JPT24B	*Shiquanhe*	*phl*	*250*	*1.3563*	*0.0048*	*0.0130*	*0.0001*	*0.2555*	*0.0010*	*0.0009*	*0.0002*	*0.5446*	*0.0006*	*1.0957*	*0.0545*	*23.96*	*1.19*
JPT24B	Shiquanhe	phl	250	1.2596	0.0074	0.0126	0.0002	0.1501	0.0013	0.0003	0.0003	0.3543	0.0003	1.1578	0.0850	25.30	1.85
JPT24B	Shiquanhe	phl	250	1.3026	0.0093	0.0134	0.0002	0.3469	0.0020	0.0009	0.0004	0.2784	0.0002	1.0466	0.1066	22.89	2.32
JPT24B	Shiquanhe	phl	250	1.4935	0.0028	0.0129	0.0001	0.5822	0.0019	0.0010	0.0001	1.0589	0.0011	1.1840	0.0191	25.87	0.43
JPT24B	Shiquanhe	phl	250	1.5188	0.0042	0.0132	0.0001	0.2377	0.0011	0.0014	0.0001	0.6658	0.0006	1.0947	0.0287	23.94	0.63
JPT24B	Shiquanhe	phl	250	1.1978	0.0092	0.0116	0.0005	0.0552	0.0036	0.0005	0.0003	0.1914	0.0004	1.0383	0.0956	22.71	2.08
JPT24B	Shiquanhe	phl	250	1.2570	0.0099	0.0130	0.0004	0.1538	0.0037	0.0009	0.0003	0.1935	0.0007	0.9845	0.0947	21.54	2.06
jpt23	Shiquanhe	phl	250	1.3697	0.0008	0.0129	0.0000	0.0056	0.0087	0.0002	0.0000	2.3469	0.0006	1.3047	0.0065	27.79	0.19
jpt23	Shiquanhe	phl	250	1.5929	0.0023	0.0128	0.0001	0.0178	0.0222	0.0005	0.0001	0.9252	0.0009	1.4345	0.0173	30.54	0.40
jpt23	Shiquanhe	phl	250	1.6671	0.0016	0.0128	0.0001	0.0222	0.0155	0.0003	0.0000	1.3243	0.0008	1.5750	0.0115	33.50	0.29
jpt23	Shiquanhe	phl	250	1.0743	0.0017	0.0126	0.0001	0.0165	0.0177	0.0003	0.0000	1.1542	0.0013	0.9962	0.0132	21.26	0.30
jpt23	*Shiquanhe*	*phl*	*250*	*1.1264*	*0.0021*	*0.0124*	*0.0001*	*0.0314*	*0.0175*	*0.0002*	*0.0000*	*1.1670*	*0.0013*	*1.0655*	*0.0131*	*22.73*	*0.30*
jpt23	Shiquanhe	phl	250	1.3963	0.0019	0.0129	0.0001	0.0397	0.0317	0.0004	0.0001	0.6444	0.0003	1.2847	0.0235	27.37	0.51
jpt23	Shiquanhe	phl	250	1.6055	0.0031	0.0131	0.0001	0.0227	0.0101	0.0001	0.0000	2.0162	0.0023	1.5618	0.0081	33.22	0.24

phl, phlogopite

errors on individual fusions are 1 σ, calculated using equation 3.2

(1) cm^3 X 10 $^{-10}$

Samples were irradiated at the McMaster Reactor, Canada. J values for the irradiation, calculated from repeat analyses of biotite standard was 0.01220 ± 0.00006 (JPT24A, JPT24B, JPT23).

Table B.6 ^{40}Ar-^{39}Ar ages for the Southern Tibetan dacites and rhyolites

sample	subgroup	mineral	ystal size (μ	$^{40}Ar/^{39}Ar$	±	$^{38}Ar/^{39}Ar$	±	$^{37}Ar/^{39}Ar$	±	$^{36}Ar/^{39}Ar$	±	^{39}Ar (1)	±	$^{40}Ar^*/^{39}Ar$	±	Age (Ma)	±
JPT3	Namling	bi	250	0.9559	0.0015	0.0140	0.0001	0.0400	0.0001	0.0011	0.0000	3.6976	0.0036	0.6383	0.0046	14.00	0.12
JPT3	Namling	bi	250	0.7623	0.0006	0.0134	0.0000	0.0428	0.0001	0.0004	0.0000	6.5223	0.0027	0.6473	0.0026	14.19	0.09
JPT3	Namling	bi	250	0.8042	0.0113	0.0130	0.0002	0.1875	0.0011	0.0008	0.0002	0.2230	0.0003	0.5650	0.0623	12.39	1.36
JPT3	*Namling*	*bi*	*250*	*0.7927*	*0.0058*	*0.0148*	*0.0001*	*0.0291*	*0.0005*	*0.0004*	*0.0001*	*0.4525*	*0.0003*	*0.6700*	*0.0334*	*14.69*	*0.73*
JPT3	Namling	bi	250	0.8862	0.0032	0.0136	0.0001	0.0731	0.0003	0.0007	0.0000	1.3431	0.0015	0.6714	0.0115	14.72	0.26
JPT3	Namling	bi	250	1.0094	0.0038	0.0136	0.0001	0.0347	0.0002	0.0012	0.0000	1.3436	0.0031	0.6489	0.0109	14.23	0.25
JPT3	Namling	bi	250	0.9199	0.0038	0.0140	0.0001	0.0981	0.0003	0.0008	0.0001	0.7225	0.0005	0.6814	0.0209	14.94	0.46
JPT3	Namling	bi	250	0.9974	0.0031	0.0143	0.0001	0.0462	0.0003	0.0012	0.0001	0.8956	0.0008	0.6573	0.0169	14.41	0.38
JPT5.2	Namling	bi	250	0.7779	0.0029	0.0128	0.0003	0.0365	0.0649	0.0005	0.0002	0.2853	0.0002	0.6356	0.0529	13.59	1.13
JPT5.2	Namling	bi	250	0.6349	0.0010	0.0139	0.0001	0.0228	0.0115	0.0001	0.0000	1.6069	0.0020	0.6072	0.0094	12.99	0.21
JPT5.2	Namling	bi	250	0.6150	0.0009	0.0134	0.0001	0.0216	0.0161	0.0001	0.0000	1.1527	0.0006	0.5782	0.0131	12.37	0.29
JPT5.2	Namling	bi	250	0.6339	0.0009	0.0142	0.0001	0.0500	0.0177	0.0002	0.0000	1.0497	0.0007	0.5673	0.0144	12.14	0.31
JPT5.2	Namling	bi	250	0.6132	0.0011	0.0133	0.0001	0.0391	0.0229	0.0003	0.0001	0.8122	0.0004	0.5179	0.0186	11.09	0.40
JPT5.2	Namling	bi	250	0.6456	0.0019	0.0133	0.0002	0.0662	0.0405	0.0007	0.0001	0.4600	0.0003	0.4321	0.0328	9.25	0.70
JPT5.2	Namling	bi	250	0.6142	0.0005	0.0137	0.0001	0.0239	0.0114	0.0002	0.0000	1.6473	0.0002	0.5586	0.0092	11.95	0.20
JPT5.2	Namling	bi	250	0.6217	0.0008	0.0135	0.0001	0.0303	0.0145	0.0002	0.0000	1.2779	0.0006	0.5708	0.0125	12.21	0.27
JPT8	Namling	bi	250	2.4233	0.0098	0.0150	0.0001	0.0207	0.0092	0.0011	0.0000	1.6984	0.0052	2.1012	0.0143	44.56	0.37
JPT8	Namling	bi	250	1.7029	0.0035	0.0141	0.0001	0.0273	0.0307	0.0008	0.0001	0.5071	0.0007	1.4661	0.0341	31.20	0.74
JPT8	Namling	bi	250	1.6284	0.0038	0.0147	0.0001	0.0273	0.0399	0.0008	0.0001	0.3956	0.0004	1.4064	0.0383	29.94	0.82
JPT8	Namling	bi	250	0.8779	0.0040	0.0138	0.0001	0.0386	0.0142	0.0004	0.0000	1.1040	0.0041	0.7577	0.0141	16.19	0.31
JPT8	Namling	bi	250	0.7522	0.0022	0.0142	0.0001	0.0359	0.0275	0.0001	0.0001	0.5742	0.0004	0.7086	0.0278	15.15	0.60
JPT8	Namling	bi	250	4.7008	0.0110	0.0163	0.0001	0.0604	0.0104	0.0040	0.0001	1.5154	0.0024	3.5139	0.0289	73.91	0.70
JPT8	Namling	bi	250	0.7253	0.0034	0.0135	0.0001	0.0621	0.0411	0.0004	0.0001	0.3816	0.0002	0.5984	0.0396	12.80	0.85
JPT8	Namling	bi	250	1.7289	0.0032	0.0143	0.0001	0.0679	0.0381	0.0011	0.0001	0.4118	0.0001	1.3967	0.0367	29.74	0.79
JPT8	Namling	bi	250	3.2009	0.0118	0.0161	0.0004	0.3355	0.1280	0.0033	0.0004	0.1237	0.0002	2.2226	0.1223	47.10	2.57
JPT8	Namling	bi	250	2.6262	0.0120	0.0151	0.0001	0.0513	0.0066	0.0020	0.0000	2.3612	0.0081	2.0481	0.0176	43.44	0.43
JPT14.1	Daggyai Tso	bi	250	0.9196	0.0027	0.0136	0.0001	0.0515	0.0010	0.0006	0.0001	0.6870	0.0008	0.7360	0.0267	16.13	0.59
JPT14.1	Daggyai Tso	bi	250	1.2844	0.0035	0.0142	0.0001	0.0167	0.0012	0.0020	0.0001	0.5676	0.0004	0.6995	0.0323	15.33	0.71
JPT14.1	Daggyai Tso	bi	250	0.8346	0.0038	0.0138	0.0001	0.0113	0.0007	0.0003	0.0001	1.0196	0.0032	0.7584	0.0189	16.62	0.42
JPT14.1	Daggyai Tso	bi	250	0.8782	0.0032	0.0137	0.0001	0.0226	0.0010	0.0002	0.0001	0.7080	0.0007	0.8106	0.0259	17.75	0.57
JPT14.1	Daggyai Tso	bi	250	0.9900	0.0016	0.0137	0.0001	0.0300	0.0005	0.0008	0.0000	1.5422	0.0006	0.7459	0.0124	16.34	0.28
JPT14.1	Daggyai Tso	bi	250	0.9190	0.0021	0.0138	0.0001	0.0129	0.0007	0.0006	0.0001	1.0708	0.0011	0.7334	0.0171	16.07	0.38

bi, biotite

errors on individual fusions are 1 σ, calculated using equation 3.2

(1) cm^3 X 10 $^{-10}$

Samples were irradiated at the McMaster Reactor, Canada. J values for the irradiation, calculated from repeat analyses of biotite standard GA1550 0.01220 ± 0.00006 (JPT3, JPT5.2, JPT8, JPT14.1).

Table B.7 ^{40}Ar-^{39}Ar ages for a phlogopite xenocryst, sample T2A

sample	subgroup	mineral	dist from starting rim (μ)	$^{40}Ar/^{39}Ar$	±	$^{38}Ar/^{39}Ar$	±	$^{37}Ar/^{39}Ar$	±	$^{36}Ar/^{39}Ar$	±	^{39}Ar (1)	±	$^{40}Ar^{*}/^{39}Ar$	±	Age (Ma)	±
PROFILE A																	
T2A	100	phl	100	0.0999	0.0002	0.0039	0.0000	0.0040	0.0002	0.0023	0.0000	0.0373	0.0001	3.0767	0.0897	18.04	0.52
T2A	200	phl	200	0.1429	0.0005	0.0035	0.0000	0.0009	0.0007	0.0006	0.0001	0.0424	0.0002	5.8481	0.2544	34.13	1.47
T2A	300	phl	300	0.1394	0.0001	0.0036	0.0000	0.0013	0.0001	0.0010	0.0000	0.2746	0.0002	5.1458	0.0379	30.07	0.22
T2A	400	phl	400 (core)	0.0951	0.0001	0.0023	0.0000	0.0000	0.0000	0.0003	0.0000	0.1266	0.0002	9.5124	0.0970	55.20	0.55
T2A	500	phl	500	0.1258	0.0001	0.0032	0.0000	0.0008	0.0000	0.0007	0.0000	0.5864	0.0001	6.3358	0.0228	36.95	0.13
PROFILE B																	
T2A	100	phl	100	0.1057	0.0001	0.0036	0.0001	0.0027	0.0005	0.0022	0.0000	0.0867	0.0001	3.2916	0.0487	19.29	0.28
T2A	200	phl	200	0.0960	0.0001	0.0033	0.0000	0.0022	0.0002	0.0017	0.0000	0.1529	0.0001	5.1752	0.0443	30.24	0.26
T2A	300	phl	300	0.0832	0.0001	0.0021	0.0000	0.0006	0.0003	0.0004	0.0000	0.1849	0.0001	10.7358	0.0517	62.17	0.30
T2A	400	phl	400 (core)	0.0792	0.0000	0.0019	0.0000	0.0003	0.0002	0.0002	0.0000	0.2660	0.0001	12.0202	0.0309	69.47	0.18
T2A	500	phl	500	0.1244	0.0003	0.0030	0.0000	0.0002	0.0000	0.0005	0.0001	0.1540	0.0004	6.9067	0.2127	40.24	1.23
T2A	600	phl	600	0.0766	0.0000	0.0029	0.0000	0.0026	0.0000	0.0023	0.0000	0.3415	0.0002	4.2685	0.1013	24.98	0.59

phl, phlogopite

(1) cm^3 X 10^{-10} *errors on individual fusions are 1 σ, calculated using equation 3.2*

Irradiated at the McMaster Reactor, Canada, J = 0.00327, calculated from repeat analyses of biotite standard GA1550

Table B.8 ^{40}Ar-^{39}Ar ages for the Northern Tibetan dacites and rhyolites

sample	subgroup	mineral	crystal size (μ)	$^{40}Ar/^{39}Ar$	±	$^{38}Ar/^{39}Ar$	±	$^{37}Ar/^{39}Ar$	±	$^{36}Ar/^{39}Ar$	±	^{39}Ar (1)	±	$^{40}Ar^*/^{39}Ar$	±	Age (Ma)	±
Bb124	Quianshuigou	phl	100	0.7202	0.0034	0.0169	0.0007	0.0519	0.0071	0.0009	0.0019	0.0486	0.0001	0.4527	0.5494	8.97	10.86
Bb124	Quianshuigou	phl	100	0.7411	0.0010	0.0141	0.0001	0.0548	0.0010	0.0005	0.0003	0.3413	0.0002	0.6078	0.0797	12.03	1.57
Bb124	Quianshuigou	phl	100	0.7086	0.0008	0.0150	0.0001	0.0619	0.0009	0.0001	0.0002	0.3744	0.0001	0.6659	0.0713	13.18	1.41
Bb124	Quianshuigou	phl	100	0.8262	0.0054	0.0142	0.0002	0.0604	0.0015	0.0005	0.0004	0.2352	0.0015	0.6829	0.1136	13.51	2.24
Bb124	Quianshuigou	phl	100	1.1803	0.0012	0.0136	0.0002	0.0565	0.0015	0.0021	0.0004	0.2287	0.0001	0.5679	0.1189	11.25	2.35
Bb124	Quianshuigou	phl	100	0.7402	0.0008	0.0142	0.0003	0.0580	0.0024	0.0013	0.0007	0.1426	0.0001	0.3590	0.1962	7.12	3.88
Bb124	Quianshuigou	phl	100	0.8752	0.0008	0.0150	0.0002	0.0631	0.0017	0.0006	0.0005	0.1968	0.0001	0.6890	0.1356	13.63	2.67
Norin 1105	Ashikule	phl	80	3.1157	0.0054	0.0180	0.0001	0.0008	0.0004	0.0018	0.0002	0.3905	0.0005	2.5698	0.0505	50.34	1.01
Norin 1105	Ashikule	phl	80	0.7468	0.0042	0.0136	0.0000	0.0353	0.0002	0.0015	0.0000	1.4407	0.0011	0.3035	0.0138	6.02	0.27
Norin 1105	Ashikule	phl	80	0.5660	0.0050	0.0134	0.0001	0.0363	0.0006	0.0006	0.0002	0.2730	0.0002	0.3915	0.0721	7.76	1.43
Norin 1105	Ashikule	phl	80	0.4886	0.0005	0.0142	0.0000	0.0322	0.0001	0.0008	0.0000	1.4660	0.0005	0.2525	0.0129	5.01	0.26
Norin 1105	Ashikule	phl	80	1.1523	0.0024	0.0154	0.0001	0.0268	0.0006	0.0000	0.0000	0.2436	0.0001	1.1523	0.0778	22.74	1.53
Norin 1105	Ashikule	phl	80	5.0522	0.0089	0.0130	0.0000	0.0031	0.0001	0.0022	0.0001	1.2015	0.0017	4.4026	0.0178	85.40	0.54
Norin 1105	Ashikule	phl	80	41.6887	2.7637	0.0650	0.0226	1.1665	0.1348	0.1192	0.0511	0.0013	0.0001	6.4616	14.9574	123.99	277.37
Norin 1105	Ashikule	phl	80	4.5516	0.0061	0.0141	0.0002	0.0050	0.0008	0.0023	0.0004	0.1714	0.0002	3.8599	0.1107	75.09	2.14
Norin 912	Ashikule	WR	50	6.8671	0.0185	0.0201	0.0001	0.0000	0.0000	0.0158	0.0004	0.1132	0.0003	2.1849	0.1045	42.89	2.04
Norin 912	Ashikule	WR	50	123.11	2.6291	0.0402	0.0198	0.0000	0.0000	0.3333	0.0636	0.0013	0.0000	24.6111	18.7715	432.59	293.37
Norin 912	Ashikule	WR	50	104.56	0.9212	0.1004	0.0112	0.0000	0.0000	0.3175	0.0365	0.0023	0.0000	10.7419	10.7928	201.66	191.71
Norin 912	Ashikule	WR	50	1.5058	0.0040	0.0149	0.0001	0.0377	0.0009	0.0035	0.0004	0.2245	0.0002	0.4857	0.1088	9.62	2.15
Norin 912	Ashikule	WR	50	2.3376	0.0026	0.0164	0.0001	0.0157	0.0006	0.0021	0.0003	0.2823	0.0001	1.7253	0.0865	33.95	1.69
Norin 912	Ashikule	WR	50	0.2172	0.0007	0.0140	0.0001	0.0307	0.0003	0.0003	0.0002	0.5317	0.0001	0.1366	0.0456	2.71	0.90
Norin 912	Ashikule	WR	50	3.3950	0.0013	0.0185	0.0000	0.0027	0.0002	0.0036	0.0001	0.8469	0.0002	2.3430	0.0288	45.95	0.60
Norin 912	Ashikule	WR	50	3.6141	0.0026	0.0188	0.0001	0.0041	0.0003	0.0044	0.0001	0.6197	0 0002	2.3242	0.0403	45.59	0.81
Norin 912	Ashikule	WR	50	2.9942	0.0082	0.0176	0.0001	0.0068	0.0006	0.0023	0.0003	0.2909	0.0007	2.3187	0.0842	45.48	1.65
Norin 912	Ashikule	WR	50	2.5349	0.0395	0.0164	0.0002	0.0031	0.0002	0.0006	0.0005	0.2340	0.0002	2.3622	0.1403	46.32	2.73

phl, phlogopite; bi, biotite; WR, whole-rock

(1) $cm^3 \times 10^{-10}$ *errors on individual fusions are 1 σ, calculated using equation 3.2*

Samples were irradiated at the McMaster Reactor, Canada. J values for the irradiation, calculated from repeat analyses of biotite standard GA1550 was 0.01101± 0.00006 (Bb124, Norin 1105, Norin 912)

C Geochemical Data

The following tables list the whole-rock, major, trace and rare earth element data as well as Sr, Nd and Pb whole rock isotope data, and electron microbe data. Major elements are given as oxide wt %, trace element and REE data are given in ppm ($\mu g\ g^{-1}$). Major element and Cr compositions were determined by XRF at the OU, trace element compositions were determined by ICP-MS at Durham University. Major element compositions are shown with and without anhydrous normalisation. Electron microprobe analyses were carried out at the OU. Isotope analyses were carried out by TIMS (OU, University of Cambridge) and IC-MC-MS (OU). Analytical details are give in Appendix D. The data are subdivided according to sample area (defined in Chapter 5). Total iron content is expressed as Fe_2O_3 throughout.

C.1 List of Tables

C.1.1 Whole-rock geochemistry; northern and southern Tibet samples

C.1.2 Electron Microprobe Data

Table C-5 clinopyroxenes

Table C-6 orthopyroxenes

Table C-7 amphiboles

Table C-8 Fe-Ti oxides

Table C-9 phlogopites

C.2 Notes to Tables

C.2.1 Key to Whole-Rock Geochemistry Tables

a) XRF, ICP-MS analyses courtesy of J. Pearce

b) XRF courtesy of E. Gnos

c) new ICP-MS analyses. XRF data (major elements + Cr), Sr, Nd and Pb isotope data taken from (Turner et al., 1996).

d) as for c) ; new Pb isotope analyses

e) as for c); new Sr isotope analyses

f) as for c); new Sr, Nd and Pb isotope analayses

CU = Sr isotope analyses carried out at the University of Cambrigde

* = sample used in inverse trace element modelling

Table C.1 XRF, ICP-MS, Sr, Nd and Pb isotope data for southern Tibetan samples

series	shoshonite	shoshonite	shoshonite	shoshonite	shoshonite	dacite	shoshonite	shoshonite	shoshonite	shoshonite	shoshonite	shoshonite
subgroup	Shiquanhe	Shiquanhe	Shiquanhe	Shiquanhe	Shiquanhe	Shiquanhe	Pabbai Zong	Pabbai Zong	Pabbai Zong	Pabbai Zong	Pabbai Zong	Pabbai Zong
sample	JPT24A*	JPT24B*	JPT24C*	20E39A	K89G162	JPT22	T2A*	T3B*	T3F*	T4A*	T5A*	T5B*
notes					c							
age	23.6	23.6	23.6	18	18	21.2	13.8	13.8	13.8	n.d.	13.3	18.3
XRF												
MgO	2.7	5.2	5.8	1.8	2.3	1.5	11.4	5.2	2.6	6.9	4.3	3.7
SiO_2	64	56	56	62	64	67	51	56	61	52	57	66
TiO_2	0.8	1.1	1.0	0.9	0.8	0.6	1.0	1.0	0.7	1.0	0.7	0.7
Al_2O_3	14.1	12.4	12.4	14.9	14.3	15.0	11.0	14.4	15.4	13.7	11.2	12.2
Fe_2O_3	3.8	5.4	5.6	7.3	3.4	2.9	6.4	6.7	4.4	6.0	4.2	4.2
MnO	0.1	0.1	0.1	0.1	0.1	0.1	0.1	0.1	0.1	0.1	0.1	0.1
CaO	4.2	7.4	7.3	3.0	2.9	2.6	5.4	3.7	2.4	5.8	7.1	1.8
Na_2O	2.7	2.2	2.2	4.1	3.0	2.9	1.1	2.1	2.3	2.1	2.0	1.5
K_2O	4.7	5.7	5.7	3.4	7.2	4.2	7.7	6.0	7.6	6.5	5.0	5.0
P_2O_5	0.3	0.7	0.7	0.3	n.d.	0.2	1.3	0.8	0.6	1.0	0.6	0.7
LOI	2.5	3.1	2.8	2.4	2.1	2.3	2.5	3.3	2.0	4.1	7.4	3.6
Total	99.4	98.9	99.3	99.8	99.8	99.5	99.1	99.4	99.1	99.0	99.6	99.3
(anhydrous)												
MgO	2.8	5.3	5.9	1.8	2.3	1.5	11.5	5.3	2.6	6.9	4.4	3.8
SiO_2	64	56	56	62	64	68	52	56	62	52	57	66
TiO_2	0.8	1.1	1.1	0.9	0.8	0.6	1.0	1.1	0.7	1.0	0.7	0.7
Al_2O_3	14.2	12.5	12.5	14.9	14.3	15.1	11.1	14.5	15.5	13.9	11.2	12.3
Fe_2O_3	3.8	5.5	5.6	7.4	3.4	2.9	6.5	6.8	4.4	6.1	4.2	4.2
MnO	0.1	0.1	0.1	0.1	0.1	0.1	0.1	0.1	0.1	0.1	0.1	0.1
CaO	4.2	7.5	7.4	3.0	2.9	2.6	5.4	3.8	2.4	5.8	7.1	1.8
Na_2O	2.7	2.2	2.2	4.1	3.0	2.9	1.2	2.2	2.3	2.2	2.0	1.5
K_2O	4.7	5.7	5.7	3.4	7.2	4.2	7.8	6.0	7.7	6.6	5.1	5.0
P_2O_5	0.3	0.7	0.7	0.3	0.0	0.2	1.3	0.8	0.6	1.0	0.6	0.7
Mg#	0.6	0.7	0.7	0.3	0.6	0.5	0.8	0.6	0.5	0.7	0.7	0.6
ICP-MS												
Rb	360	462	438	67	541	327	643	326	425	398	284	276
Sr	372	733	724	660	575	221	921	1115	882	694	767	470
Y	22	27	25	26	18	20	36	36	32	27	22	23
Zr	263	401	377	182	154	207	323	368	197	482	253	269
Nb	18	29	27	12	33	14	19	20	11	24	14	15
Cs	30	51	49	2	40	21	13	3	4	4	3	4
Ba	1002	1726	1640	948	1322	711	4221	2696	3439	2735	1593	1535
Hf	7.5	10.7	10.2	4.7	6.0	6.1	8.4	9.6	5.0	12.5	6.9	7.2
Ta	1.4	1.9	1.8	0.8	2.0	1.2	1.0	1.2	0.6	1.3	0.8	0.8
Pb	43.7	47.3	44.5	21.0	113.8	43.6	10.3	52.7	77.8	59.6	47.0	49.0
Th	54.0	86.2	81.6	19.1	135.9	40.4	118.0	68.3	84.0	146.7	79.3	84.1
U	11.3	18.2	17.2	1.6	11.0	8.3	13.6	10.4	9.1	21.2	13.8	14.1
La	68.3	62.5	58.6	49.3	110.2	73.5	145.8	96.0	80.8	134.2	56.4	56.8
Ce	147.1	146.8	138.5	97.6	232.7	152.2	314.8	198.9	179.7	279.7	123.5	127.0
Pr	18.7	21.2	20.1	12.1	29.7	18.1	40.7	25.1	22.5	40.5	16.1	16.5
Nd	73.4	94.8	90.2	48.5	117.5	65.6	167.1	101.5	85.5	164.9	67.0	67.7
Sm	13.2	20.3	19.2	8.6	18.5	10.3	30.1	18.2	16.9	27.2	11.9	12.1
Eu	1.9	3.2	3.1	2.2	3.0	1.3	5.3	3.5	3.3	4.6	2.2	2.2
Gd	8.1	12.2	11.7	6.7	10.4	6.4	19.9	12.7	10.6	15.8	7.9	8.0
Tb	0.9	1.3	1.2	0.9	1.0	0.8	2.0	1.5	1.3	1.5	0.9	0.9
Dy	4.2	5.6	5.2	4.8	4.1	3.7	8.2	7.1	6.2	5.9	4.2	4.3
Ho	0.7	0.9	0.8	0.9	0.6	0.7	1.2	1.2	1.1	0.9	0.7	0.8
Er	1.8	2.2	2.1	2.3	1.4	1.7	2.7	3.0	2.7	2.1	1.8	2.0
Tm	0.3	0.3	0.3	0.3	0.2	0.3	0.3	0.4	0.4	0.3	0.3	0.3
Yb	1.7	2.0	1.9	2.1	1.1	1.6	2.1	2.5	2.4	1.6	1.6	1.7
Lu	0.2	0.3	0.3	0.3	0.1	0.2	0.3	0.4	0.3	0.2	0.2	0.3
Ga	24	19	18	16	20	27	16	18	18	20	13	14
V	77	118	112	65	63	61	106	125	78	115	78	71
Sc	10	14	14	25	6	8	14	16	13	15	10	11
Co	16	30	28	32	10	9	36	25	13	26	19	15
Ni	72	196	180	51	40	10	467	106	42	150	114	109
Cu	19	39	41	26	23	10	73	63	n.d.	62	31	35
Zn	72	77	71	75	60	73	76	72	n.d.	69	41	41
Cr (XRF)	143	351	354	129	59	36	849	186	67	275	219	241
$^{87}Sr/^{86}Sr_i$	0.714315	0.714651	0.714459	0.711549	0.714855	0.733819	0.739376	0.712191	0.714613	0.711592	0.715947	0.720272
$^{143}Nd/^{144}I$	0.511938	0.511894	0.511748	0.512406	0.511983	0.511993	0.511690	0.511877	0.511838	0.511968	0.512172	n.d.
$E\,Nd_{(t)}$	-13.07	-13.91	-16.78	-4.07	-12.33	-12.06	-18.14	-14.50	-15.27	-12.60	-8.77	n.d.
$^{206}Pb/^{204}I$	18.652	n.d.	n.d.	n.d.	18.740	n.d.	19.147	n.d.	n.d.	18.524	n.d.	n.d.
$^{207}Pb/^{204}I$	15.750	n.d.	n.d.	n.d.	15.792	n.d.	15.840	n.d.	n.d.	15.759	n.d.	n.d.
$^{208}Pb/^{204}I$	39.349	n.d.	n.d.	n.d.	39.802	n.d.	41.283	n.d.	n.d.	39.424	n.d.	n.d.

Table C.1 XRF, ICP-MS, Sr, Nd and Pb isotope data for southern Tibetan samples

series	shoshonite	dacite	dacite	dacite	dacite	dacite	dacite	dacite	dacite	rhyolite	rhyolite
subgroup	Pabbai Zong	Daggyai Tso	Daggyai Tso	Daggyai Tso	Daggyai Tso	Daggyai Tso	Namling	Namling	Namling	Namling	Namling
sample	JPT7*	JPT14.1	JPT14.2	T11A/99 av	T11B/98	T11C/98	JPT3	JPT4	JPT5.2	JPT8	95RAS11 3
notes											
age	18.3	19.3	19.3	19.3	17.3	19 3	14.1	10-14	11 6	13 8	10-14
XRF											
MgO	4.3	3.0	2.2	2.7	2.2	2.1	1 2	0.7	1.3	0.5	0.8
SiO_2	57	63	62	64	63	62	62	68	62	73	71
TiO_2	0.7	0.7	0 8	0.7	0.7	0.8	0.7	0.4	0.6	0.3	0.3
Al_2O_3	11 2	16.5	17.3	16.1	16.5	17.4	15.1	15.7	15.0	14 6	12.4
Fe_2O_3	4.4	4.2	4.1	4 1	4.0	3.9	4.7	1 9	2.9	2.0	1.5
MnO	0.1	0.1	0.1	0.1	0.1	0.1	0.2	0.0	0.0	0.0	0.0
CaO	7.1	4.8	5.0	4.6	4.7	4.8	4.5	2.8	4.4	0.4	3.9
Na_2O	1.8	4.1	4.4	4.1	4.4	4.4	3.1	3.3	0.8	0 8	1.1
K_2O	5.0	2.9	2 7	3.3	2.8	2 8	4.5	4.0	4.3	5.0	2.3
P_2O_5	0.7	0.2	0.3	0.2	0 3	0.2	0.3	0.1	0.2	0.2	0.1
LOI	6.6	0.6	1.0	0.4	2.3	0 9	3.2	2.5	8.1	3.1	5.0
Total	99 1	100.0	99.2	100.6	100.4	99.6	99.7	99.7	99.5	99.5	98.0
(anhydrous)											
MgO	4.3	3.0	2.2	2.7	2.2	2.1	1.2	0.7	1.3	0.5	0.8
SiO_2	58	63	62	64	62	63	63	69	62	73	72
TiO_2	0.7	0.7	0.8	0.7	0.7	0.8	0.7	0.4	0.6	0.3	0.3
Al_2O_3	*11.4*	*16.5*	*17.5*	*16.0*	*16.4*	*17.4*	*15.2*	*15.8*	*15.1*	*14.6*	*12.7*
Fe_2O_3	4.5	4.2	4.1	4.1	3.9	3.9	4.7	1.9	2.9	2.0	1.5
MnO	0.1	0.1	0.1	0.1	0.1	0.1	0.2	0.0	0.0	0.0	0.0
CaO	7.1	4.8	5.0	4.5	4.6	4.8	4.5	2.8	4.4	0.4	4.0
Na_2O	1.8	4.1	4.4	4.1	4.3	4.4	3.1	3.3	0.8	0.8	1.1
K_2O	5.1	2.9	2.7	3.3	2.8	2.8	4.5	4.0	4.4	5.0	2.3
P_2O_5	0.7	0.2	0.3	0.2	0.2	0.2	0.3	0.1	0.2	0.2	0.1
Mg#	0.7	0.6	0.5	0.6	0.5	0.5	0.3	0.4	0.5	0.3	0.5
ICP-MS											
Rb	*258*	*91*	*65*	*148*	*100*	*77*	*116*	*147*	*206*	*315*	*71*
Sr	716	949	880	894	996	1015	803	651	472	158	3352
Y	21	11	9	11	9	10	11	5	7	4	7
Zr	239	109	126	105	139	140	122	27	79	47	51
Nb	14	9	6	9	8	6	8	5	6	14	6
Cs	3	2	2	4	6	2	20	12	28	11	16
Ba	1878	846	708	743	740	751	914	760	1060	963	877
Hf	6.4	3.1	3.4	2.9	3.6	3.7	3.5	1.2	2.5	2.1	1.9
Ta	0.7	0.6	0.4	0.6	0.4	0.4	0.7	0.4	0.5	1.2	0.5
Pb	50.6	28.4	24.3	29.9	25.8	26.2	33.0	36.5	44.2	60.5	41.2
Th	*75.0*	*16.0*	*8.9*	*15.3*	*9.4*	*9.5*	*19.3*	*16.4*	*23.9*	*56.2*	*17.8*
U	13.2	2.7	1.9	3.1	2.0	2.1	3.7	3.7	2.2	8.1	4.7
La	54.3	34.1	25.9	33.8	28.5	28.5	30.9	22.8	33.3	22.3	26.8
Ce	116.3	65.3	51.5	63.5	56.2	55.7	63.5	41.7	66.0	88.9	51.3
Pr	15.4	7.9	6.3	7.4	6.8	6.8	7.8	4.8	8.0	3.5	5.6
Nd	64.1	30.1	24.3	28.5	26.3	26 6	31.1	17.0	30.0	11.4	19.4
Sm	11.3	4.9	4.0	4.5	4.3	4.4	5.3	2.6	4.7	1.6	2.9
Eu	2.0	1 2	1.1	1.1	1.1	1.1	1.2	0.6	1.0	0.4	0.5
Gd	7.4	3.6	3.0	3.4	3.1	3.2	3.7	1.8	3.1	1.1	2.0
Tb	0.9	0.4	0.3	0.4	0.4	0.4	0.4	0.2	0.3	0 1	0.2
Dy	*4.1*	*2.1*	*1.7*	*1.9*	*1.7*	*1 8*	*2.1*	*0.9*	*1.5*	*0.7*	*1.2*
Ho	0.7	0.4	0.3	0.3	0.3	0.3	0.4	0.2	0.2	0.1	0.2
Er	1.8	1.0	0.7	0.9	0.7	0.8	0.9	0.4	0.6	0.4	0.6
Tm	0.2	0.1	0.1	0.1	0.1	0.1	0.1	0.1	0.1	0.1	0 1
Yb	1.6	0.8	0.6	0.8	0.6	0.6	0.8	0.4	0.5	0.6	0.6
Lu	0.2	0.1	0.1	0.1	0.1	0.1	0.1	0.1	0.1	0.1	0.1
Ga	13	21	19	20	21	21	18	16	19	19	11
V	73	77	72	73	77	78	74	31	61	26	16
Sc	10	8	5	7	6	6	6	2	5	3	2
Co	20	14	12	13	12	12	11	4	9	4	3
Ni	112	51	*22*	*47*	*20*	*21*	*15*	*5*	30	*10*	*4*
Cu	31	16	17	12	17	20	31	11	23	8	9
Zn	40	65	65	59	64	64	49	33	46	40	33
Cr (XRF)	270	69	30	69	31	34	41	13	50	17	10
$^{87}Sr/^{86}Sr_i$	n.d.	0.707119	0.706918	0.707132	0.706856	0.706867	0.706594	0.706794	0.706753	0.709956	n.d.
$^{143}Nd/^{144}i$	n.d.	0.512009	0.512308	0.512407	0.512058	0.512146	0.512348	0.512353	0.512300	0.511732	n.d.
E $Nd_{(t)}$	n.d.	-11.79	-5 96	-4.02	-10.88	-9.11	-5.31	-5.57	-6.30	-17.32	n.d.
$^{206}Pb/^{204}i$	n.d.	18.577	n.d.	n.d.	18.613	n.d.	n.d.	n.d.	n.d	n.d.	n.d.
$^{207}Pb/^{204}i$	n.d.	15 690	n.d.	n.d.	15.685	n.d.	n.d.	n.d.	n.d.	n.d.	n.d.
$^{208}Pb/^{204}i$	n.d.	39.123	n.d.	n.d.	39.141	n d.	n d.	n.d.	n.d.	n.d.	n.d.

Table C-2 XRF, ICP-MS, Sr, Nd and Pb isotope data for northern Tibetan samples

series	shoshonite	shoshonite	shoshonite	shoshonite	shoshonite	shoshonite	shoshonite	shoshonite	shoshonite	shoshonite	shoshonite
subgroup	Ashikule	Ashikule	Ashikule	Ashikule	Tienchuhai	Tienchuhai	Tienchuhai	Heshibei	Heshibei	Heshibei	Heshibei
sample	912*	1105	K702*	K703*	K89G185*	K89G186*	K89G200*	KP 24-1*	KP.12.6	KP.13.1a	KP13-3A
notes	a	a	c	c	c	c	c	a	a	a	a
age	2.7	5.0	<1	<1	5.6	6.4	3.6	2.2	1-3	1-3	1-3
XRF											
MgO	4.3	1.8	4.1	3.9	5.6	4.0	4.4	3.9	2.0	7.0	5.2
SiO_2	58	60	50	56	50	51	57	57	61	46	45
TiO_2	1.8	0.7	1.8	2.0	1.8	1.9	1.4	1.9	2.0	2.1	4.0
Al_2O_3	14.3	14.5	13.1	14.7	13.7	14.6	13.8	14.5	13.7	16.1	16.9
Fe_2O_3	*7.2*	*5.7*	*6.8*	*7.7*	*9.1*	*9.6*	*7.3*	*8.0*	*7.1*	*10.8*	
MnO	0.1	0.1	0.2	0.1	0.1	0.1	0.1	0.1	0.1	0.2	2.5
CaO	5.6	5.2	10.3	6.3	7.2	7.6	6.4	5.6	5.6	8.5	5.5
Na_2O	2.6	3.1	2.8	2.8	3.8	4.6	4.0	2.9	3.0	5.1	5.6
K_2O	5.0	4.1	3.6	4.1	4.7	4.8	5.4	4.3	3.9	1.0	9.9
P_2O_5	1.1	0.6	1.6	1.1	n.d.	n.d.	n.d.	1.1	0.9	0.8	0.8
LOI	n.d.	n.d.	2.4	1.1	4.2	2.1	0.3	0.4	0.8	3.3	0.9
Total	95.8	93.8	97.1	99.4	99.9	100.7	99.8	99.2	100.0	93.4	95.8
(anhydrous)											
MgO	4.4	1.9	4.2	4.0	5.6	4.0	4.4	3.9	2.0	7.0	5.5
SiO_2	61	64	52	56	50	51	57	57	61	45	46
TiO_2	1.8	0.7	1.9	2.0	1.8	1.8	1.4	1.9	2.0	2.1	4.2
Al_2O_3	14.9	15.4	13.5	14.8	13.7	14.5	13.8	14.6	13.7	16.1	17.6
Fe_2O_3	7.5	6.1	7.0	7.8	9.1	9.5	7.3	8.1	7.2	10.7	0.0
MnO	0.1	0.1	0.2	0.1	0.1	0.1	0.1	0.1	0.1	0.2	2.6
CaO	5.8	5.5	10.7	6.4	7.2	7.5	6.4	5.6	5.6	8.5	5.7
Na_2O	2.7	3.3	2.9	2.8	3.8	4.6	4.0	2.9	3.0	5.1	5.9
K_2O	5.3	4.4	3.7	4.1	4.7	4.7	5.4	4.3	3.9	1.0	10.4
P_2O_5	1.1	0.7	1.6	1.1	0.0	0.0	0.0	1.1	0.9	0.8	0.9
LOI	0.0	0.0	2.4	1.1	4.2	2.1	0.3	0.4	0.8	3.3	0.9
Mg#	0.5	0.4	0.5	0.5	0.5	0.5	0.5	0.5	0.4	0.6	1.0
ICP-MS											
Rb	236	124	114	126	132	122	208	136	182	8	n.d.
Sr	1387	296	1217	1177	2120	1968	1682	*1158*	*813*	*1095*	n.d.
Y	27	25	28	32	32	28	24	n.d.	30	28	n.d.
Zr	600	72	432	532	452	452	328	488	573	267	n.d.
Nb	45	14	44	50	42	39	36	n.d.	64	77	n.d.
Cs	7	3	3	3	2	3	7	n.d.	4	1	n.d.
Ba	2429	599	2134	2132	2854	2697	2287	n.d.	1650	884	n.d.
Hf	14.2	2.4	9.6	11.5	9.6	9.4	8.1	n.d.	12.3	5.2	n.d.
Ta	2.5	1.3	2.1	2.4	2.0	1.9	1.8	n.d.	3.2	4.2	n.d.
Pb	30.0	22.8	34.4	40.4	34.0	31.5	38.4	n.d.	34.4	6.3	n.d.
Th	30.5	18.0	27.0	31.9	29.4	27.5	46.3	n.d.	37.7	8.1	n.d.
U	5.6	4.4	4.3	4.8	4.2	4.4	9.7	n.d.	7.5	2.2	n.d.
La	141.2	36.1	153.0	177.6	190.2	178.6	162.9	202.0	173.0	62.8	n.d.
Ce	*285.7*	*69.1*	*275.0*	*318.3*	*373.4*	*349.0*	*310.4*	*388.0*	*337.0*	*112.0*	*n.d.*
Pr	33.3	7.8	35.4	40.9	43.6	40.4	34.8	40.2	38.7	12.3	n.d.
Nd	123.3	29.3	129.9	148.5	163.8	150.2	126.7	146.0	139.7	44.9	n.d.
Sm	18.1	5.5	18.8	21.3	23.3	21.4	18.0	21.2	19.9	7.7	n.d.
Eu	3.9	1.1	3.9	4.5	5.1	4.7	3.9	4.1	3.6	2.4	n.d.
Gd	12.1	5.0	13.3	15.1	15.6	14.2	11.8	15.1	13.8	6.9	n.d.
Tb	1.3	0.7	1.4	1.6	1.6	1.5	1.2	2.1	1.5	0.9	0.6
Dy	5.6	4.2	6.0	6.9	6.9	6.2	5.2	5.7	6.4	5.0	n.d.
Ho	0.9	0.8	1.0	1.1	1.1	0.9	0.8	n.d.	1.0	0.9	n.d.
Er	2.2	2.3	2.3	2.6	2.5	2.2	1.9	n.d.	2.3	2.4	n.d.
Tm	0.3	0.4	0.3	0.4	0.3	0.3	0.2	n.d.	0.3	0.4	n.d.
Yb	1.8	2.4	1.8	2.0	1.8	1.6	1.4	2.4	1.9	2.1	n.d.
Lu	0.3	0.4	0.3	0.3	0.2	0.2	0.2	0.9	0.3	0.3	n.d.
Ga	22	17	20	22	22	20	21	*n.d.*	25	21	*n.d.*
V	106	95	99	107	135	128	105	61	71	195	n.d.
Sc	11	14	10	11	10	10	9	n.d.	7	18	n.d.
Co	15	15	20	19	31	32	21	n.d.	13	41	n.d.
Ni	30	31	51	43	69	69	69	55	11	126	n.d.
Cu	23	25	34	26	32	29	18	n.d.	21	27	n.d.
Zn	104	56	113	126	120	111	114	n.d.	145	99	n.d.
Cr (XRF)	83	184	57	87	88	122	83	89	26	241	n.d.
$^{87}Sr/^{86}Sr_{(i)}$	0.708354	0.710287	0.710204	0.708777	0.708086	0.708064	0.708944	0.710359	n.d.	n.d.	n.d.
$^{143}Nd/^{144}Nd_{(i)}$	0.512151	0.511888	0.512157	0.512110	0.512291	0.512330	0.512272	0.512226	n.d.	n.d.	n.d.
$\varepsilon Nd_{(i)}$	-9.44	-14.60	-9.35	-10.28	-6.63	-5.84	-7.05	-7.99	n.d.	n.d.	n.d.
$^{206}Pb/^{204}Pb_{(i)}$	n.d.	n.d.	18.758	18.783	n.d.	n.d	n.d.	n.d.	n.d.	n.d.	n.d.
$^{207}Pb/^{204}Pb_{(i)}$	n.d.	n.d.	15.638	15.655	n.d.	n.d.	n.d.	n.d.	n.d.	n.d.	n.d.
$^{208}Pb/^{204}Pb_{(i)}$	n.d.	n.d.	38.959	39.023	n.d.	n.d.	n.d.	n.d.	n.d.	n.d.	n.d.

Table C-2 XRF, ICP-MS, Sr, Nd and Pb isotope data for northern Tibetan samples

series	shoshonite	shoshonite	shoshonite	shoshonite	shoshonite	shoshonite	shoshonite	shoshonite	shoshonite	shoshonite	shoshonite
subgroup	*Heshibei*	*Heshibei*	*Heshibei*	*Heshibei*	*Heshibei*	*Qiangshuigou*	*Qiangshuigou*	*Qiangshuigou*	*Qiangshuigou*	*Qiangshuigou*	*Qiangshuigou*
sample	KP23-2*	KP35-10*	KP39-3	KP47-2*	KP47-5*	8b 124*	Bb119	Bb121*	Bb122	Bb135	Bq137*
notes	a, c	a, c	a, c	a, c	a, c	b, c	b	b, c	b	b	b
age	1-3	1-3	1-3	1-3	1-3	12.7	12-14	14	12-14	12-14	12-14
XRF											
MgO	4.2	2.5	7.9	4.0	4.2	2.8	1.4	2.8	1.8	1.6	3.8
SiO_2	53	55	48	51	53	58	62	61	63	63	63
TiO_2	2.3	1.9	1.9	1.6	1.6	1.3	1.6	1.5	1.5	1.5	1.5
Al_2O_3	15.8	15.6	12.3	14.0	13.9	14.2	14.4	15.2	14.4	14.8	15.2
Fe_2O_3	9.4	6.4	9.1	7.3	8.7	5.7	7.3	7.2	5.7	5.3	5.6
MnO	0.1	0.1	0.1	0.1	0.1	0.1	0.1	0.1	0.1	0.0	0.1
CaO	6.0	4.9	7.9	9.5	7.2	7.3	3.4	4.9	5.2	3.4	1.8
Na_2O	3.4	3.2	3.0	4.4	3.4	3.2	4.1	3.4	3.1	3.9	3.6
K_2O	4.1	3.9	5.2	4.1	4.2	3.7	3.7	3.9	4.1	4.2	4.3
P_2O_5	1.2	0.9	1.3	1.0	0.9	0.7	1.3	0.7	0.1	1.2	0.7
LOI	1.0	2.7	3.2	2.2	2.6	1.9	0.5	1.0	n.d.	1.1	0.3
Total	100.8	96.9	99.7	99.0	99.8	98.3	98.5	98.6	97.6	98.2	96.3
(anhydrous)											
MgO	4.2	2.6	7.9	4.0	4.2	2.9	1.4	2.8	1.8	1.7	3.9
SiO_2	53	57	48	51	53	59	63	62	65	64	66
TiO_2	2.3	1.9	1.9	1.6	1.6	1.3	1.6	1.5	1.5	1.5	1.5
Al_2O_3	15.6	16.1	12.4	14.2	13.9	14.4	14.6	15.4	14.8	15.1	15.8
Fe_2O_3	9.3	6.7	9.2	7.4	8.7	5.8	7.4	7.3	5.9	5.4	5.9
MnO	0.1	0.1	0.1	0.1	0.1	0.1	0.1	0.1	0.1	0.0	0.1
CaO	6.0	5.1	7.9	9.6	7.2	7.4	3.4	5.0	5.3	3.4	1.9
Na_2O	3.4	3.3	3.0	4.5	3.4	3.2	4.1	3.5	3.1	4.0	3.7
K_2O	4.0	4.0	5.2	4.1	4.2	3.7	3.8	3.9	4.2	4.3	4.4
P_2O_5	1.2	0.9	1.3	1.0	0.9	0.7	1.3	0.7	0.1	1.2	0.7
LOI	1.0	2.7	3.2	2.2	2.6	1.9	0.5	1.0	0.0	1.1	0.3
Mg#	0.5	0.4	0.6	0.5	0.5	0.5	0.3	0.4	0.4	0.4	0.6
ICP-MS											
Rb	n.d.	107	166	103	144	145	176	122	162	183	173
Sr	1279	968	1841	1621	1562	1135	921	1065	933	861	906
Y	*n.d.*	*n.d.*	*n.d.*	*n.d.*	*n.d.*	*23*	*22*	*21*	*20*	*20*	*21*
Zr	n.d.	414	516	348	399	525	566	500	597	536	485
Nb	n.d.	n.d.	n.d.	n.d.	n.d.	38	38	37	36	38	37
Cs	n.d.	n.d.	n.d.	n.d.	n.d.	2	4	2	3	4	4
Ba	105	n.d.	n.d.	n.d.	n.d.	1844	2002	1789	1968	1970	1924
Hf	*n.d.*	*n.d.*	*12.2*	*8.6*	*9.4*	*11.1*	*12.3*	*10.6*	*12.5*	*11.8*	*10.9*
Ta	n.d.	n.d.	1.8	2.3	1.5	1.8	1.8	1.8	1.7	1.8	1.7
Pb	n.d.	n.d.	n.d.	n.d.	n.d.	35.0	36.0	31.6	42.2	42.4	40.5
Th	n.d.	n.d.	16.0	9.0	18.0	38.5	49.0	37.3	49.2	52.6	48.7
U	n.d.	n.d.	n.d.	n.d.	n.d.	6.3	6.3	5.1	7.5	7.8	6.1
La	184.0	134.0	110.5	154.0	165.0	160.0	204.8	152.4	184.2	191.2	186.1
Ce	352.0	260.0	229.0	287.5	304.0	302.7	377.4	286.9	341.7	353.3	347.5
Pr	36.2	26.3	n.d.	n.d.	n.d.	32.7	39.3	31.4	36.1	37.0	36.8
Nd	130.0	98.4	101.0	108.0	113.5	112.7	134.8	109.3	121.3	123.3	123.7
Sm	19.6	14.6	17.1	17.3	19.4	14.9	16.9	14.7	15.5	15.7	15.8
Eu	4.2	3.3	4.1	3.7	4.4	3.1	3.1	3.1	3.0	3.0	3.1
Gd	13.9	10.9	n.d.	n.d.	n.d.	10.3	11.3	9.8	10.0	10.4	10.2
Tb	2.0	1.5	1.4	1.4	1.5	1.1	1.2	1.1	1.0	1.1	1.1
Dy	5.9	6.2	n.d.	n.d.	n.d.	4.7	4.8	4.4	4.3	4.4	4.4
Ho	n.d.	n.d.	n.d.	n.d.	n.d.	0.8	0.8	0.7	0.7	0.7	0.7
Er	2.4	n.d.	n.d.	n.d.	n.d.	1.8	1.7	1.7	1.6	1.6	1.6
Tm	*n.d.*	*n.d.*	*n.d.*	*n.d.*	*n.d.*	*0.2*	*0.2*	*0.2*	*0.2*	*0.2*	*0.2*
Yb	2.7	3.2	1.8	2.0	1.9	1.5	1.2	1.4	1.3	1.3	1.3
Lu	0.8	0.6	0.3	0.3	0.3	0.2	0.2	0.2	0.2	0.2	0.2
Ga	n.d.	n.d.	n.d.	n.d.	n.d.	22	23	22	22	23	23
V	85	99	222	162	169	82	74	80	74	67	72
Sc	*n.d.*	*n.d.*	*20*	*19*	*16*	*8*	*7*	*8*	*7*	*6*	*6*
Co	n.d.	n.d.	n.d.	n.d.	n.d.	14	8	13	9	7	9
Ni	37	37	100	60	87	33	7	31	9	8	8
Cu	n.d.	n.d.	n.d.	n.d.	n.d.	21	21	20	22	15	12
Zn	n.d.	n.d.	n.d.	n.d.	n.d.	145	104	177	127	111	107
Cr (XRF)	38	76	258	125	79	73	29	73	28	24	25
$^{87}Sr/^{86}Sr_{(i)}$	n.d.	0.708513	n.d.	n.d.	n.d.	0.708849	n.d.	0.708719	n.d.	n.d.	0.708737
$^{143}Nd/^{144}Nd_{(i)}$	n.d.	0.512334	n.d.	n.d.	n.d.	0.512250	n.d.	0.512283	n.d.	n.d.	0.512204
$\varepsilon Nd_{(i)}$	n.d.	-5.89	n.d.	n.d.	n.d.	-7.24	n.d.	-6.58	n.d.	n.d.	-8.15
$^{206}Pb/^{204}Pb_{(i)}$	n.d.	18.737	n.d.	n.d.	n.d.	18.723	n.d.	18.737	n.d.	n.d.	n.d.
$^{207}Pb/^{204}Pb_{(i)}$	n.d.	15.710	n.d.	n.d.	n.d.	15.692	n.d.	15.714	n.d.	n.d	n.d
$^{208}Pb/^{204}Pb_{(i)}$	n.d.	39.232	n.d.	n.d	n.d.	39.131	n.d.	39.187	n.d.	n.d.	n.d.

Table C-2 XRF, ICP-MS, Sr, Nd and Pb isotope data for northern Tibetan samples

series	shoshonite	shoshonite	shoshonite	shoshonite	shoshonite	shoshonite	shoshonite	shoshonite	shoshonite	shoshonite	shoshonite
subgroup	Yongbocuo	Yongbocuo	Yongbocuo	Kunlun (VII)	Kunlun (VII)	Kunlun (VII)	Kunlun (VII)	Kunlun (VII)	Kunlun (VII)	Kunlun (VII)	Kunlun (VII)
sample	Bq142	Bq140	Bq141	K9024*	K9026*	K9027*	K9028*	K9029*	K9031*	K9032*	K9038
notes	b	b	b	c	e	c	d	f	c	e	c
age	12-14	12-14	12-14	13.0	12.9	12.7	18.5	11-19	11 8	11.9	9.6
XRF											
MgO	0.7	1.2	0.7	3.2	2.8	2.9	2.8	2.8	3.4	2.9	2.5
SiO_2	68	69	68	57	58	57	55	56	56	58	55
TiO_2	0 8	0.8	0.8	1.6	1.7	1.7	1.5	1.6	1.6	1.6	1.6
Al_2O_3	15.6	14.5	14.4	15.4	16.0	16.0	14.9	15.6	15 2	15.8	15.6
Fe_2O_3	2.1	3.2	3.7	7.1	6.8	6.8	6.3	6.7	6.9	7.2	5.9
MnO	0.0	0.0	0.0	0.1	0.1	0.1	0.1	0.1	0.1	0.1	0.2
CaO	1.9	1.4	1.9	5.6	5.5	5.4	7.6	6.3	6.3	5.0	7.4
Na_2O	3.9	4.2	4.3	3.7	4.0	4.0	3.6	3.9	3.6	3.8	3.6
K_2O	5 3	5.2	4.3	3.8	4.2	4.1	3.6	4.1	3.8	4.0	3.7
P_2O_5	0.2	0.3	0.4	0.9	0.8	0.9	0.8	0.8	0.8	0.8	0.8
LOI	1.4	1.2	1.1	1.8	0.9	0.8	3.8	1.9	2.0	0.9	3.3
Total	99.2	100.0	98.3	99 8	100.3	100.0	99.6	99.9	99.6	99.9	99.9
(anhydrous)											
MgO	0.7	1.2	0.7	3.2	2.8	2.9	2.8	2.8	3.4	2.9	2.5
SiO_2	68	69	69	57	58	57	55	56	56	58	55
TiO_2	0.8	0.8	0.8	1.6	1.7	1.7	1.5	1.6	1.6	1.6	1.6
Al_2O_3	15.7	14.5	14.7	15 4	15.9	16.0	15.0	15.6	15.3	15.8	15.6
Fe_2O_3	2.2	3.2	3.7	7.1	6.8	6.8	6.4	6.7	6.9	7.2	5.9
MnO	0.0	0.0	0.0	0.1	0.1	0.1	0.1	0.1	0.1	0.1	0.2
CaO	1.9	1.4	1.9	5.7	5.4	5.4	7.7	6.3	6.3	5.0	7.4
Na_2O	3.9	4.2	4.3	3.7	3.9	3.9	3.6	3.9	3.6	3.8	3.6
K_2O	5.4	5.1	4.4	3.8	4.2	4.1	3.6	4.1	3.8	4.0	3.7
P_2O_5	0.2	0.3	0.4	0.9	0.8	0.8	0.8	0.8	0.8	0.8	0.8
LOI	1.4	1.2	1.1	1.8	0.9	0.8	3.8	1.9	2.0	0.9	3.3
Mg#	0.4	0.4	0.3	0.5	0.4	0.5	0.5	0.5	0.5	0.4	0.5
ICP-MS											
Rb	237	235	239	110	116	111	107	126	118	119	94
Sr	651	634	720	982	899	969	968	1078	1001	1057	1074
Y	7	8	10	24	24	23	23	25	25	26	23
Zr	240	269	639	412	432	426	401	462	440	444	324
Nb	11	11	14	41	45	43	41	47	44	44	39
Cs	5	7	7	4	3	3	5	4	5	3	5
Ba	1789	1768	1763	1606	1673	1610	1610	1701	1732	1816	1427
Hf	6.1	6.7	11.8	8.6	9.3	9.0	8.4	9.5	9.4	9.3	7.1
Ta	0.5	0.5	0.6	2.0	2.3	2.1	2.1	2.3	2.2	2.2	2.1
Pb	71.1	76.0	97.8	31.1	25.9	32.2	25.0	28.6	31.9	25.9	21.3
Th	61.6	60.7	68.2	19.6	21.3	20.5	19 4	21.7	21.1	20.9	11.6
U	5.9	9.3	11.1	3.5	3.4	3.3	3.4	3.6	3.4	3.5	2 3
La	138.1	137.9	151.4	113.6	122.7	118.4	108.7	119.7	120.7	123.4	81.9
Ce	238.9	242.6	262.7	214.3	231.3	224.5	204.8	225.1	229.1	235.2	163.7
Pr	24.4	24.3	26.5	23.5	25.9	24.6	22.8	24.9	25.3	26.1	19.0
Nd	79 1	79.6	85.5	84.4	90.4	87.6	81.0	88.3	90.7	89 9	70 5
Sm	10.1	10.1	11.0	11.8	12.8	12.2	11.3	12.4	12.8	13.2	10.4
Eu	2.0	1.8	2.1	2.6	2.8	2.7	2.5	2.8	2.8	2.8	2.4
Gd	6.1	6.2	6.9	8.7	9.2	8.7	8.3	9.1	9.1	8.7	7.7
Tb	0.6	0.6	0.7	1.0	1.0	1.0	1.0	1.0	1.0	1.0	0.9
Dy	1.8	1.9	2.4	4.7	4.9	4.8	4.5	4 8	4.9	5.0	4.6
Ho	0.2	0.3	0.3	0.8	0.8	0.8	0.8	0.8	0 8	0.8	0.8
Er	0.5	0.5	0.7	2.1	2.0	2.0	1.9	2 1	2.1	2.1	2.0
Tm	0.1	0.1	0.1	0.3	0.3	0.3	0.3	0.3	0.3	0.3	0.3
Yb	0.3	0.4	0.5	1.7	1.7	1.7	1.6	1.7	1.8	1.8	1.7
Lu	0.0	0.0	0.1	0.2	0.3	0.2	0.2	0.3	0.3	0.3	0.3
Ga	23	22	24	19	20	19	19	21	20	21	19
V	22	22	24	98	95	96	90	90	104	104	115
Sc	1	1	1	10	9	8	8	9	12	11	11
Co	3	3	2	18	15	15	14	16	18	17	19
Ni	2	4	1	35	22	22	21	23	36	36	41
Cu	7	5	6	24	20	17	19	21	24	23	25
Zn	72	94	72	98	98	94	94	103	101	99	123
Cr (XRF)	5	3	4	86	35	47	43	35	62	83	109
$^{87}Sr/^{86}Sr_{(t)}$	0.709811	n.d.	0.709630	0.708292	0.708123	0.708068	0.708092	0.708170	0.709079	0.707949	0.707896
$^{143}Nd/^{144}Nd_{(t)}$	0.512103	n.d	0.512095	0.512327	0.512337	0.512325	0.512337	0.512320	0.512336	0.512341	0.512296
$E\ Nd_{(t)}$	-10.08	n.d.	-10.23	-5.74	-5.55	-5.78	-5.41	-5.83	-5.59	-5.49	-6.38
$^{206}Pb/^{204}Pb_{(t)}$	n.d.	n.d.	n d.	18.649	n.d.	n.d.	18.715	n.d.	18.761	n.d.	18.694
$^{207}Pb/^{204}Pb_{(t)}$	n.d.	n.d.	n.d.	15.615	n.d.	n.d.	15.693	n.d.	15.717	n.d.	15.702
$^{208}Pb/^{204}Pb_{(t)}$	n.d.	n.d.	n.d.	38.859	n.d	n.d.	39.106	n.d.	39.280	n.d.	39.102

Table C-2 XRF, ICP-MS, Sr, Nd and Pb isotope data for northern Tibetan samples

series	shoshonite	shoshonite	shoshonite	shoshonite	shoshonite	shoshonite	shoshonite	shoshonite
subgroup	Kunlun (VII)	Kunlun (VII)	Quangringnoinza	Quangringnoinza	Quangringnoinza	Quangringnoinza	Quangringnoinza	Quangringnoinza
sample	K9039	K9041	11H7/1	11H7/2	11H7/3	11H7/4	11H7/5	11H7/6
notes	f	c	b	b	b	b	b	b
age	12.5	11-19	36	36	36	36	36	36
XRF								
MgO	1.2	0.9	1.6	2.4	3.9	2.3	1.8	4.6
SiO_2	57	66	69	65	61	60	68	59
TiO_2	1.7	0.8	0.5	0.5	0.7	0.6	0.6	0.7
Al_2O_3	16.3	15.2	14.3	14.7	14.7	14.0	14.5	14.2
Fe_2O_3	7.5	6.3	2.5	3.2	4.2	3.1	2.8	4.6
MnO	0.0	0.1	0.0	0.1	0.1	0.0	0.0	0.1
CaO	5.7	3.1	2.3	3.2	5.0	3.1	2.6	5.7
Na_2O	3.8	4.3	4.2	4.1	4.7	4.7	4.0	4.3
K_2O	3.7	3.0	5.1	4.6	4.2	4.7	5.0	4.9
P_2O_5	0.9	0.3	0.2	0.3	0.4	0.2	0.2	0.5
LOI	2.3	0.4	0.3	0.4	0.5	0.6	0.2	0.3
Total	99.6	100.7	100.1	98.9	100.2	94.0	99.9	99.4
(anhydrous)								
MgO	1.2	0.9	1.6	2.5	3.9	2.4	1.8	4.6
SiO_2	57	66	69	66	61	64	68	59
TiO_2	1.7	0.8	0.4	0.5	0.6	0.6	0.6	0.7
Al_2O_3	16.3	15.1	14.3	14.8	14.7	14.9	14.5	14.3
Fe_2O_3	7.5	6.2	2.5	3.2	4.2	3.3	2.8	4.6
MnO	0.0	0.1	0.0	0.1	0.1	0.0	0.0	0.1
CaO	5.8	3.1	2.3	3.2	5.0	3.3	2.6	5.8
Na_2O	3.8	4.3	4.2	4.2	4.7	5.0	4.0	4.3
K_2O	3.7	3.0	5.1	4.6	4.2	4.9	5.0	4.9
P_2O_5	0.9	0.3	0.2	0.3	0.4	0.2	0.2	0.5
LOI	2.3	0.4	0.3	0.4	0.5	0.6	0.2	0.3
Mg#	0.2	0.2	0.6	0.6	0.6	0.6	0.6	0.7
ICP-MS								
Rb	93	186	291	209	167	233	315	208
Sr	1003	234	647	1189	1585	1081	718	2029
Y	26	40	15	14	16	20	21	20
Zr	341	282	95	27	21	21	102	42
Nb	43	17	22	16	17	23	36	21
Cs	5	21	13	10	16	21	20	14
Ba	1577	594	1258	1689	2021	1660	1313	2604
Hf	7.5	6.8	3.1	1.1	1.0	1.1	3.1	1.6
Ta	2.3	1.8	1.9	1.3	1.3	2.2	2.9	1.6
Pb	22.4	20.9	27.6	36.0	36.7	17.5	29.8	47.7
Th	12.7	13.2	71.7	32.9	30.3	52.6	98.3	40.5
U	2.3	5.8	5.1	3.4	8.0	6.0	10.6	7.4
La	89.1	37.8	76.8	71.2	73.9	68.9	104.9	95.7
Ce	177.8	79.6	138.3	130.1	138.8	139.7	201.1	180.5
Pr	20.9	9.7	14.5	14.2	15.8	16.2	21.8	20.5
Nd	76.3	38.9	44.9	46.0	53.5	54.5	68.1	70.1
Sm	11.4	7.8	7.0	7.1	8.6	9.1	10.3	11.2
Eu	2.7	2.0	1.2	1.5	1.9	1.8	1.6	2.5
Gd	8.7	7.3	4.1	4.1	5.2	5.5	5.9	6.8
Tb	1.0	1.1	0.6	0.5	0.6	0.7	0.8	0.8
Dy	5.0	6.6	2.7	2.5	3.1	3.7	3.9	3.8
Ho	0.9	1.3	0.5	0.4	0.6	0.7	0.7	0.7
Er	2.2	3.7	1.2	1.1	1.4	1.8	1.8	1.6
Tm	0.3	0.6	0.2	0.2	0.2	0.3	0.3	0.2
Yb	1.9	3.5	1.2	1.0	1.2	1.5	1.7	1.4
Lu	0.3	0.5	0.2	0.1	0.2	0.2	0.2	0.2
Ga	20	21	21	20	19	20	22	19
V	117	25	38	50	76	56	49	99
Sc	12	14	10	9	12	8	5	12
Co	20	7	6	10	15	8	7	18
Ni	56	2	20	39	82	36	22	82
Cu	26	11	19	16	15	<2	28	47
Zn	85	107	63	63	88	50	44	86
Cr (XRF)	107	28	38	78	141	66	49	158
$^{87}Sr/^{86}Sr_{(i)}$	0.707814	0.715692	0.707673	0.707188	0.707030	0.707265	0.707567	0.707210
$^{143}Nd/^{144}Nd_{(i)}$	0.512329	0.512365	0.511958	0.511836	0.511769	0.512002	0.512101	0.512217
$\varepsilon Nd_{(i)}$	-5.74	-5.03	-12.38	-14.76	-16.08	-11.61	-9.60	-7.34
$^{206}Pb/^{204}Pb_{(i)}$	n.d.	n.d.	n.d.	n.d.	n.d.	n.d.	n.d.	n.d.
$^{207}Pb/^{204}Pb_{(i)}$	n.d.	n.d.	n.d.	n.d.	n.d.	n.d.	n.d.	n.d.
$^{208}Pb/^{204}Pb_{(i)}$	n.d.	n.d.	n.d.	n.d.	n.d.	n.d.	n.d.	n.d.

Table C-2 XRF, ICP-MS, Sr, Nd and Pb isotope data for northern Tibetan samp

series	shoshonite	shoshonite	shoshonite	shoshonite	shoshonite	shoshonite	shoshonite	shoshonite
subgroup	Quangringnoinza	Dogai Coring	Dogai Coring	Dogai Coring	Dogai Coring	Dogai Coring	Dogai Coring	Dogai Coring
sample	11H7/7	12K1	12K3	12615A	12615B	12615C	12H10-1	12H10-2
notes	b	b	b	b	b	b	b	b
age	36	3	3	3	3	3	3	3
XRF								
MgO	0.3	1.1	1.5	1 2	1.3	1.3	1 0	1.1
SiO_2	97	64	63	65	63	64	65	64
TiO_2	0.6	1.1	1.4	1.1	1.1	1.1	1.1	1.1
Al_2O_3	1.1	14.2	14.9	14.5	14.2	14.4	14.6	15.5
Fe_2O_3	0.2	4.3	5.5	4.4	4.3	4.3	4.5	4.6
MnO	<0.01	0.1	0.1	0.1	0.1	0.1	0.1	0.1
CaO	0.2	6.0	3.8	3.9	5.4	5.2	3.3	3.7
Na_2O	1.3	4.8	6.1	5.2	3.8	3.6	4.9	4.5
K_2O	0.2	5.0	4.7	5.2	4.9	5.0	5.2	5.2
P_2O_5	0.2	0.4	0.6	0.4	0.4	0.4	0.4	0.4
LOI	0.8	3.4	0.2	1.6	3.2	2.8	0.4	1.1
Total	101.6	104.4	102.0	103.2	102 3	102.4	100.7	101.8
(anhydrous)								
MgO	0.3	1.1	1.5	1.1	1.3	1.3	1.0	1.1
SiO_2	95	61	62	63	62	62	64	63
TiO_2	0.6	1.0	1.4	1.1	1.0	1.0	1.1	1.1
Al_2O_3	1.1	13.6	14.6	14.1	13.8	14.1	14.5	15.2
Fe_2O_3	0.1	4.1	5.3	4.3	4.2	4.2	4.4	4.5
MnO	<0.01	0.1	0.1	0.1	0.1	0.1	0.0	0.1
CaO	0 2	5.7	3.7	3.8	5.3	5.0	3.3	3.6
Na_2O	1.3	4.6	6.0	5.1	3.7	3.5	4.8	4.4
K_2O	0.2	4.8	4.6	5.0	4.8	4.8	5.1	5.1
P_2O_5	0.2	0.4	0.6	0.4	0.4	0.4	0.4	0.4
LOI	0.8	3.4	0.2	1.6	3.2	2.8	0.4	1.1
Mg#	0 8	0.3	0.3	0.3	0.4	0.4	0.3	0.3
ICP-MS								
Rb	3	278	274	263	245	244	265	278
Sr	832	562	521	483	507	494	535	562
Y	7	32	29	24	24	23	30	32
Zr	110	831	782	371	343	353	787	831
Nb	29	23	22	25	24	24	21	23
Cs	1	3	2	3	3	3	n.d.	n.d.
Ba	321	1764	1853	1804	1745	1783	1780	1771
Hf	3.3	8.7	15.7	9.4	8.7	9.0	n.d.	n.d.
Ta	2.1	1.0	1.5	1.1	1.0	1.0	n.d.	n.d.
Pb	243.5	44.0	41.7	45.3	44.6	44.0	55.0	67.0
Th	50.9	54.9	47.8	57.6	54.0	55.0	n.d.	n.d.
U	5.5	5.9	5.5	6.2	6.0	5.9	n.d.	n.d.
La	161.3	175.9	170.6	185.6	175.5	177.1	n.d.	n.d.
Ce	236.5	324.8	319.2	342.2	325.0	327.1	n.d.	n.d.
Pr	27.7	34.7	34.8	36.7	34 8	34.7	n.d.	n.d.
Nd	93.6	107.7	110.4	113.4	108.0	107.8	n.d.	n.d.
Sm	11.7	15.3	16.2	16.3	15.5	15.4	n.d.	n.d.
Eu	1.3	2.2	2.7	2.4	2.2	2.3	n.d.	n.d.
Gd	3.1	8.3	9.0	8.7	8.7	8.5	n.d.	n.d.
Tb	0.4	1.0	1.1	1.1	1.1	1.0	n.d.	n.d.
Dy	1.5	4.7	5.3	5.0	5.0	4.7	n.d.	n d.
Ho	0.2	0.8	0.9	0.8	0.8	0.8	n.d.	n.d.
Er	0.7	1.8	2.1	1.9	1.9	1.8	n.d.	n.d.
Tm	0.1	0.2	0.3	0.3	0.3	0.2	n.d.	n.d.
Yb	1.0	1.4	1.7	1.5	1.5	1.4	n.d.	n.d.
Lu	0.2	0.2	0 2	0.2	0.2	0.2	n.d.	n.d.
Ga	3	22	23	23	23	22	n.d.	n.d.
V	6	42	62	45	46	43	59	55
Sc	0	7	9	8	6	5	n.d.	n.d.
Co	0	5	8	5	6	6	n.d.	n.d.
Ni	0	2	4	1	3	3	5	15
Cu	<5	4	8	7	23	14	12	21
Zn	22	144	155	146	138	135	125	151
Cr (XRF)	16	18	10	10	18	17	7	12
$^{87}Sr/^{86}Sr_{(i)}$	0.707638	0.709549	0.707089	0.709558	0.709584	0 709570	0.709544	0.709639
$^{143}Nd/^{144}Nd_{(i)}$	0.511947	0.512047	0.511887	0.512051	0.512064	0.512010	0.512094	0.512029
E $Nd_{(i)}$	-12.61	-11.46	-14.58	-11.37	-11.11	-12.17	-10.54	-11.81
$^{208}Pb/^{204}Pb_{(i)}$	n.d.	n.d.	n.d.	n.d.	n.d.	n.d.	n.d.	n.d.
$^{207}Pb/^{204}Pb_{(i)}$	n.d.	n.d.	n.d.	n d	n.d.	n.d.	n.d.	n.d.
$^{206}Pb/^{204}Pb_{(i)}$	n d.	n.d.	n.d.	n.d.	n.d.	n.d.	n.d.	n.d.

Table C-2 XRF, ICP-MS, Sr, Nd and Pb isotope data for northern Tibetan samples

series	shoshonite	shoshonite	shoshonite	shoshonite	shoshonite	shoshonite	rhyolite	rhyolite	shoshonite
subgroup	Dogai Coring	Dogai Coring	Dogai Coring	Dogai Coring	Dogai Coring	Dogai Coring	Kunlun (VII)	Kunlun (VII)	Dogai Coring (VIII)
sample	12H10-3	12H10-4	12H9-1	12H9-2	12H9-4	15G15A2	K9001	K9002	K9006
notes	b	b	b	b	b	b	c	f	c
age	3	3	3	3	3	3	8-13	8-13	8.9
XRF									
MgO	1.1	1.1	1.0	1.0	1.1	3.1	1.4	1.5	1.8
SiO_2	65	65	65	66	65	62	74	71	62
TiO_2	1.1	1.1	1.1	1.1	1.1	0.7	0.6	0.6	1.6
Al_2O_3	15.2	15.2	14.8	14.7	14.7	15.3	12.7	13.8	15.2
Fe_2O_3	4.5	4.4	4.5	4.6	4.5	5.6	3.6	4.3	6.0
MnO	0.1	0.1	0.1	0.0	0.1	0.1	0.1	0.1	0.1
CaO	3.8	3.5	4.0	3.3	3.3	4.7	1.4	1.8	4.0
Na_2O	4.6	4.6	3.8	4.7	4.1	4.1	3.5	3.0	3.9
K_2O	5.2	5.1	5.2	5.1	5.2	3.2	1.9	2.3	4.1
P_2O_5	0.4	0.4	0.5	0.5	0.4	0.2	0.1	0.1	0.9
LOI	1.1	0.5	1.0	0.5	0.6	0.5	1.4	1.8	1.1
Total	102.2	101.1	100.9	101.5	100.8	99.9	100.6	100.8	100.9
(anhydrous)									
MgO	1.0	1.1	1.0	1.0	1.1	3.1	1.4	1.5	1.7
SiO_2	63	64	64	65	65	62	74	71	62
TiO_2	1.1	1.1	1.1	1.1	1.1	0.7	0.5	0.6	1.6
Al_2O_3	14.9	15.0	14.7	14.5	14.6	15.3	12.6	13.7	15.1
Fe_2O_3	4.4	4.4	4.4	4.5	4.5	5.6	3.5	4.2	6.0
MnO	0.0	0.1	0.0	0.0	0.1	0.1	0.0	0.1	0.1
CaO	3.7	3.5	3.9	3.2	3.3	4.7	1.4	1.8	3.9
Na_2O	4.5	4.6	3.7	4.6	4.0	4.1	3.4	3.0	3.8
K_2O	5.1	5.0	5.1	5.1	5.1	3.2	1.9	2.3	4.1
P_2O_5	0.4	0.4	0.5	0.5	0.4	0.2	0.1	0.1	0.9
LOI	1.1	0.5	1.0	0.5	0.6	0.5	1.4	1.8	1.1
Mg#	0.3	0.3	0.3	0.3	0.3	0.5	0.4	0.4	0.4
ICP-MS									
Rb	274	266	258	262	260	265	136	100	227
Sr	521	537	540	545	541	535	1086	198	755
Y	29	29	29	29	29	30	15	24	28
Zr	782	755	749	756	739	787	209	138	523
Nb	22	20	22	22	21	21	6	12	49
Cs	n.d.	n.d.	n.d.	n.d.	n.d.	n.d.	3	6	19
Ba	1760	1725	1767	1793	1764	1542	357	376	1640
Hf	n.d.	n.d.	n.d.	n.d.	n.d.	n.d.	3.2	3.8	11.0
Ta	n.d.	n.d.	n.d.	n.d.	n.d.	n.d.	0.8	0.8	2.7
Pb	47.0	43.0	38.0	103.0	51.0	27.0	8.9	12.7	41.7
Th	n.d.	n.d.	n.d.	n.d.	n.d.	n.d.	9.6	9.8	32.1
U	n.d.	n.d.	n.d.	n.d.	n.d.	n.d.	2.1	2.2	8.2
La	n.d.	n.d.	n.d.	n.d.	n.d.	n.d.	29.1	29.6	148.9
Ce	n.d.	n.d.	n.d.	n.d.	n.d.	n.d.	57.4	59.1	281.3
Pr	n.d.	n.d.	n.d.	n.d.	n.d.	n.d.	6.9	7.1	30.6
Nd	n.d.	n.d.	n.d.	n.d.	n.d.	n.d.	26.1	27.4	108.5
Sm	n.d.	n.d.	n.d.	n.d.	n.d.	n.d.	4.8	5.2	15.3
Eu	n.d.	n.d.	n.d.	n.d.	n.d.	n.d.	1.0	1.1	3.0
Gd	n.d.	n.d.	n.d.	n.d.	n.d.	n.d.	4.2	4.4	10.8
Tb	n.d.	n.d.	n.d.	n.d.	n.d.	n.d.	0.6	0.7	1.2
Dy	n.d.	n.d.	n.d.	n.d.	n.d.	n.d.	3.7	3.9	5.6
Ho	n.d.	n.d.	n.d.	n.d.	n.d.	n.d.	0.7	0.8	0.9
Er	n.d.	n.d.	n.d.	n.d.	n.d.	n.d.	2.1	2.2	2.2
Tm	n.d.	n.d.	n.d.	n.d.	n.d.	n.d.	0.3	0.3	0.3
Yb	n.d.	n.d.	n.d.	n.d.	n.d.	n.d.	2.2	2.2	1.8
Lu	n.d.	n.d.	n.d.	n.d.	n.d.	n.d.	0.3	0.3	0.3
Ga	n.d.	n.d.	n.d.	n.d.	n.d.	n.d.	13	15	25
V	59	52	52	57	48	87	59	68	85
Sc	n.d.	n.d.	n.d.	n.d.	n.d.	n.d.	7	8	7
Co	n.d.	n.d.	n.d.	n.d.	n.d.	n.d.	10	11	11
Ni	8	5	<3	3	6	104	20	24	7
Cu	21	14	12	19	20	21	21	8	19
Zn	121	141	131	156	118	80	80	44	122
Cr (XRF)	13	12	8	9	10	145	77	76	18
$^{87}Sr/^{86}Sr_{(i)}$	0.706607	0.709587	0.709635	0.709638	0.709639	n.d.	0.708125	0.714184	0.708118
$^{143}Nd/^{144}Nd_{(i)}$	0.512185	0.511995	0.510662	n.d.	0.512021	n.d	0.512224	0.511944	0.512255
$\varepsilon Nd_{(i)}$	-8.75	-12.46	-38.47	n.d.	-11.97	n.d.	-7.78	-13.54	-7.25
$^{208}Pb/^{204}Pb_{(i)}$	n.d.	n.d	n.d.	n.d.	n.d.	n.d.	n.d.	n.d.	n.d
$^{207}Pb/^{204}Pb_{(i)}$	n.d.	n.d.	n.d.	n.d.	n.d.	n.d.	n.d.	n.d.	n.d.
$^{206}Pb/^{204}Pb_{(i)}$	n.d.	n.d.	n.d.	n.d.	n.d.	n.d.	n.d.	n.d.	n.d.

Table C-2 XRF, ICP-MS, Sr, Nd and Pb isotope data for northern Tibetan samples

series	shoshonite	shoshonite	shoshonite	shoshonite	shoshonite	shoshonite	shoshonite
subgroup	Dogai Coring (VIII)	Dogai Coring (VIII)	Dogai Coring (VIII)	Dogai Coring (VIII)	Dogai Coring (VIII)	Dogai Coring (VIII)	Dogai Coring (VIII)
sample	K9007	K9008 av	K9016	K9017	K9018	K9019	K9021
notes	c	c	c	f	c	f	c
age	13.4	9.35	8.4	8-13	9.6	8-13	13
XRF							
MgO	1.9	1.2	1.6	1.7	1.8	1.8	1.8
SiO_2	59	61	63	62	61	60	62
TiO_2	1.5	1.6	1.5	1.6	1.6	1.6	1.6
Al_2O_3	15.3	15.2	15.1	15.3	15.1	15.0	15.1
Fe_2O_3	6.1	6.2	5.7	6.0	6.1	6.2	5.9
MnO	0.1	0.1	0.1	0.1	0.1	0.1	0.1
CaO	4.8	3.8	4.2	4.0	4.3	4.7	4.0
Na_2O	3.4	3.8	3.9	3.8	3.8	3.7	3.8
K_2O	3.9	4.2	4.2	4.2	4.2	4.0	4.1
P_2O_5	0.8	0.8	0.8	0.9	0.9	0.9	0.8
LOI	3.0	0.9	0.8	0.9	1.0	1.9	0.8
Total	100.2	99.2	100.3	100.5	100.2	100.1	100.0
(anhydrous)							
MgO	1.9	1.2	1.6	1.7	1.8	1.8	1.8
SiO_2	59	62	62	62	61	60	62
TiO_2	1.5	1.6	1.5	1.6	1.6	1.6	1.6
Al_2O_3	15.3	15.3	15.0	15.2	15.1	14.9	15.1
Fe_2O_3	6.1	6.3	5.7	5.9	6.1	6.2	5.9
MnO	0.1	0.1	0.1	0.1	0.1	0.1	0.1
CaO	4.7	3.8	4.2	4.0	4.3	4.6	4.0
Na_2O	3.4	3.8	3.9	3.7	3.8	3.7	3.8
K_2O	3.9	4.2	4.2	4.1	4.1	4.0	4.1
P_2O_5	0.8	0.8	0.8	0.8	0.8	0.9	0.8
LOI	3.0	0.9	0.8	0.9	1.0	1.9	0.8
Mg#	0.4	0.3	0.4	0.4	0.4	0.4	0.4
ICP-MS							
Rb	199	208	238	214	209	193	204
Sr	699	650	624	718	666	774	669
Y	27	25	24	26	27	26	25
Zr	492	481	407	486	492	485	486
Nb	44	45	43	45	46	46	43
Cs	18	10	18	12	15	11	14
Ba	1458	1507	1345	1461	1521	1542	1416
Hf	10.4	10.2	9.1	10.1	10.4	10.1	10.4
Ta	2.4	2.6	2.6	2.6	2.6	2.4	2.4
Pb	69.9	29.4	28.9	44.9	37.1	38.2	39.5
Th	30.5	30.1	29.3	30.4	30.9	28.6	30.1
U	6.6	7.4	8.4	7.7	7.5	6.9	7.5
La	138.6	136.7	131.4	139.6	145.0	140.1	136.8
Ce	263.1	253.9	251.4	263.6	262.1	265.6	257.6
Pr	28.9	29.8	27.6	28.9	30.6	28.9	28.1
Nd	101.9	102.8	97.4	100.9	105.6	102.1	99.5
Sm	14.7	14.7	13.8	14.5	15.1	14.8	14.0
Eu	2.8	2.9	2.6	2.8	2.9	2.9	2.8
Gd	10.2	10.5	9.6	10.1	10.8	10.5	9.8
Tb	1.2	1.2	1.1	1.2	1.2	1.2	1.1
Dy	5.4	5.3	4.9	5.3	5.5	5.3	5.1
Ho	0.9	0.8	0.8	0.9	0.9	0.9	0.8
Er	2.2	2.1	1.9	2.2	2.2	2.1	2.1
Tm	0.3	0.3	0.3	0.3	0.3	0.3	0.3
Yb	1.8	1.6	1.5	1.7	1.8	1.7	1.6
Lu	0.3	0.2	0.2	0.2	0.3	0.2	0.2
Ga	23	23	23	23	23	23	22
V	72	81	68	79	80	86	75
Sc	7	7	6	7	7	7	6
Co	11	10	10	9	11	12	10
Ni	11	8	7	6	8	10	7
Cu	23	13	19	16	21	21	17
Zn	115	110	111	97	124	115	111
Cr (XRF)	15	21	40	18	16	21	15
$^{87}Sr/^{86}Sr_{(i)}$	0.709001	0.708958	-0.000132	0.708818	-0.000124	0.708924	0.708970
$^{143}Nd/^{144}Nd_{(i)}$	0.512293	0.512269	0.512247	0.512288	0.512296	0.512273	0.512309
$\varepsilon Nd_{(i)}$	-6.40	-6.97	-7.41	-6.51	-6.44	-6.76	-6.09
$^{206}Pb/^{204}Pb_{(i)}$	18.761	18.789	18.795	n.d.	n.d.	n.d.	18.788
$^{207}Pb/^{204}Pb_{(i)}$	15.710	15.736	15.732	n.d.	n.d.	n.d.	15.729
$^{208}Pb/^{204}Pb_{(i)}$	39.269	39.362	39.319	n.d.	n.d.	n.d.	39.426

Table C-3 Repeat ICP-MS analyses

sample	K89G185#1	K89G185#2	2 s.d.	K89G186#1	K89G186#2	2 s.d.	K9001#1	K9001#2	2 s.d.	K9032#1	K9032#2	2 s.d.
Rb	132	133	1	121	123	2	67	72	7	118	119	0
Sr	2123	2118	7	1958	1978	29	215	230	21	1051	1064	18
Y	32.3	31.8	0.7	27.5	27.7	0.3	21.2	22.5	1.8	25.7	25.5	0.3
Zr	455.9	447.9	11.2	448.4	455.0	9.3	105.0	113.4	11.9	445.4	442.3	4.4
Nb	42.5	42.2	0.4	39.0	39.7	1.0	9.9	10.7	1.1	44.1	43.7	0.5
Cs	2.2	2.2	0.1	3.0	3.0	0.0	2.4	2.6	0.3	2.6	2.6	0.1
Ba	2907	2801	151	2670	2725	78	344	370	36	1848	1784	91
Hf	9.8	9.4	0.5	9.4	9.4	0.0	3.0	3.3	0.3	9.3	9.3	0.1
Ta	2.0	1.9	0.1	1.9	1.9	0.0	0.7	0.8	0.1	2.2	2.2	0.0
Pb	34.5	33.5	1.4	31.5	31.6	0.1	8.8	9.0	0.3	27.8	23.9	5.5
Th	29.9	29.0	1.3	27.4	27.7	0.5	9.4	9.8	0.6	21.2	20.7	0.8
U	4.2	4.1	0.2	4.4	4.4	0.0	2.0	2.1	0.2	3.5	3.4	0.1
La	194.5	186.0	12.1	177.6	179.5	2.6	27.9	30.3	3.4	125.5	121.4	5.7
Ce	380.2	366.6	19.3	347.9	350.0	3.0	55.1	59.6	6.4	238.4	232.1	8.9
Pr	44.4	42.8	2.3	40.5	40.2	0.4	6.6	7.1	0.8	26.2	26.0	0.3
Nd	167.4	160.1	10.4	150.4	150.1	0.4	25.4	26.8	2.1	93.7	86.1	10.8
Sm	23.7	22.8	1.2	21.4	21.4	0.0	4.6	4.9	0.4	13.1	13.2	0.1
Eu	5.2	5.0	0.3	4.7	4.7	0.0	1.0	1.1	0.1	2.8	2.8	0.1
Gd	15.8	15.4	0.5	14.1	14.2	0.1	4.0	4.4	0.5	9.4	8.1	1.7
Tb	1.7	1.6	0.1	1.5	1.5	0.0	0.6	0.7	0.1	1.1	1.0	0.1
Dy	7.1	6.8	0.4	6.2	6.1	0.1	3.6	3.8	0.2	5.1	4.9	0.2
Ho	1.1	1.0	0.1	0.9	0.9	0.0	0.7	0.8	0.0	0.9	0.8	0.0
Er	2.5	2.4	0.2	2.2	2.2	0.0	2.1	2.2	0.1	2.2	2.1	0.1
Tm	0.3	0.3	0.0	0.3	0.3	0.0	0.3	0.4	0.0	0.3	0.3	0.0
Yb	1.8	1.7	0.1	1.6	1.6	0.0	2.1	2.2	0.1	1.8	1.7	0.0
Lu	0.2	0.2	0.0	0.2	0.2	0.0	0.3	0.3	0.0	0.3	0.3	0.0
Ga	21.8	21.7	0.1	20.3	20.7	0.7	12.9	13.9	1.4	20.7	20.9	0.3
V	136.4	134.2	3.1	128.2	128.0	0.2	56.8	61.4	6.5	105.8	102.2	5.0
Sc	10.0	9.8	0.4	10.0	9.3	0.9	6.3	7.6	1.9	9.7	12.7	4.3
Co	31.2	30.9	0.4	32.1	31.6	0.7	9.2	9.9	1.0	17.1	16.7	0.6
Ni	69.5	68.3	1.7	69.7	68.7	1.4	19.4	21.3	2.8	37.2	35.4	2.5
Cu	31.7	31.7	0.0	29.0	29.5	0.8	6.6	7.2	0.8	23.2	23.2	0.0
Zn	120.1	119.4	1.0	106.6	115.6	12.8	28.3	30.0	2.3	98.6	98.6	0.0

2 s.d. = 2 standard deviation of the mean of the analyses

Table C-3 Repeat ICP-MS analyses

sample	11H7/3#1	11H7/3#2	2 s.d.	12615C#1	12615C#2	2 s.d.	12K1#1	12K1#2	2 s.d.	12K3#1	12K3#2	2 s.d.
Rb	165	169	6	241	247	10	252	250	2	217	211	9
Sr	1590	1579	16	488	499	15	508	513	6	677	658	26
Y	16.2	16.4	0.3	22.7	23.1	0.6	22.7	23.6	1.2	26.3	25.8	0.7
Zr	21.2	21.3	0.2	349.9	356.4	9.2	343.3	344.3	1.5	712.6	698.0	20 6
Nb	16.5	16.5	0.0	23.5	23.8	0.4	23.6	24.0	0.6	33.4	32 7	1.0
Cs	15.9	16.2	0.5	3.4	3.5	0.0	2.9	2.9	0.0	2.5	2.5	0.0
Ba	2016	2026	15	1781	1786	6	1784	1745	55	1875	1831	62
Hf	1.0	1.0	0.0	8.9	9.0	0.1	8.7	8.7	0.0	16.0	15.5	0.8
Ta	1.3	1.2	0.1	1.0	1.0	0.0	1.0	1.0	0.0	1.5	1.4	0.1
Pb	36.7	36.8	0.0	43.7	44.3	0.8	44.1	43.9	0.3	42.2	41.3	1.3
Th	30.8	29.8	1.4	54.6	55.4	1.1	54.9	54.9	0.1	48.2	47.4	1.0
U	8.0	8.0	0.0	5.9	6.0	0.1	5.9	5.9	0.1	5.5	5.5	0.1
La	74.6	73.2	1.9	176.0	178.1	2.9	176.1	175.7	0.4	172.5	168.8	5.2
Ce	139.9	137.8	2.9	325.0	329.2	6.0	323.2	326.4	4.4	322.3	316.2	8.6
Pr	15.9	15.7	0.3	34.4	34.9	0.7	34.4	35.0	0.8	35.3	34.3	1.4
Nd	53.6	53.4	0.2	107.5	108.2	1.1	106.5	108.9	3.3	111.6	109.1	3.5
Sm	8.6	8.6	0.1	15.3	15.4	0.2	15.0	15.5	0.7	16 3	16.1	0.3
Eu	1.9	1.9	0.0	2.2	2.3	0.0	2.2	2.2	0.0	2.7	2.7	0.1
Gd	5.2	5.2	0.0	8.6	8.7	0.1	8.2	8.3	0.1	9.0	8.9	0.2
Tb	0.6	0.6	0.0	1.0	1.0	0.0	1.0	1.0	0.0	1.1	1.1	0.0
Dy	3.1	3.1	0.1	4.7	4.7	0.0	4.6	4.8	0.2	5.3	5.2	0.2
Ho	0.5	0.6	0.0	0.8	0.8	0.0	0.8	0.8	0.0	0.9	0.9	0.0
Er	1.4	1.4	0.0	1.8	1.8	0.0	1.8	1.8	0.0	2.1	2.1	0.1
Tm	0.2	0.2	0.0	0.2	0.2	0.0	0.2	0.2	0.0	0.3	0.3	0.0
Yb	1.2	1.3	0.0	1.4	1.4	0.0	1.4	1.4	0.0	1.8	1.7	0.1
Lu	0.2	0.2	0.0	0.2	0.2	0.0	0.2	0.2	0.0	0.2	0.2	0.0
Ga	19.2	19.3	0.1	21.8	22.1	0.3	22.3	22.5	0.3	23.5	23.4	0.3
V	73.4	77.8	6.2	42.7	43.1	0.5	40.5	43.0	3.6	62.4	60.8	2.3
Sc	11.8	11.8	0.1	5.6	5.1	0.7	5.7	9.2	5.0	9.5	8.7	1.2
Co	14.3	15.3	1.3	5.7	5.8	0.2	5.5	5.4	0.1	8.4	8.3	0.1
Ni	80.0	84.0	5.6	2.9	3.2	0.3	2.4	2.2	0.2	4.2	4.2	0.0
Cu	n.d.	n.d.	n.d.	n.d.	n.d.	n.d.	n.d.	n.d.	n.d.	n.d.	n.d.	n.d.
Zn	n.d.	n.d.	n.d.	n.d.	n.d.	n.d.	n.d.	n.d.	n.d.	n.d.	n.d.	n.d.

Table C-3 Repeat ICP-MS analyses

sample	T3F#1	T3F#2	2 s.d.	T4A#1	T4A#2	T4A#3	2 s.d.	JPT14.1#1	JPT14.1#2	2 s.d.	JPT14.2#1	JPT14.2#2	2 s.d.
Rb	424	427	4	392	401	392	10	89	93	5	63	67	6
Sr	879	884	7	742	699	684	60	987	911	108	904	856	68
Y	32.1	32.0	0.2	25.5	27.0	26.3	1.5	10.9	11.5	0.9	8.6	9.2	0.8
Zr	196.3	197.3	1.4	462.4	484.5	478.1	22.8	106.3	112.0	8.2	121.1	130.4	13.3
Nb	10.7	10.7	0.0	22.4	23.8	23.4	1.5	8.8	9.3	0.7	5.5	5.9	0.6
Cs	3.6	3.7	0.1	4.1	4.3	4.3	0.3	2.3	2.4	0.2	2.3	2.4	0.3
Ba	3408	3470	88	2936	2737	2732	233	821	872	72	683	734	72
Hf	5.0	5.1	0.2	12.2	12.6	12.4	0.4	3.0	3.2	0.2	3.2	3.5	0.4
Ta	0.5	0.6	0.0	1.3	1.3	1.3	0.0	0.6	0.6	0.1	0.4	0.4	0.1
Pb	76.9	78.7	2.6	51.5	59.8	59.2	9.2	27.9	28.9	1.3	23.8	24.9	1.6
Th	*84.9*	*83.1*	*2.5*	*164.2*	*146.9*	*146.2*	*20.4*	*15.5*	*16.5*	*1.4*	*8.5*	*9.2*	*0.9*
U	9.1	9.2	0.2	20.5	21.3	21.0	0.8	2.6	2.8	0.3	1.9	2.0	0.2
La	82.6	79.0	5.1	128.5	133.7	135.3	7.1	33.1	35.1	2.8	25.0	26.8	2.6
Ce	182.9	176.6	8.9	291.3	284.1	270.8	20.8	63.6	67.1	5.0	49.9	53.2	4.7
Pr	22.7	22.2	0.8	39.5	40.5	40.5	1.2	7.6	8.1	0.8	6.0	6.5	0.6
Nd	86.0	85.1	1.3	152.2	164.9	164.7	14.6	29.4	30.8	2.0	23.6	25.0	2.0
Sm	16.9	16.8	0.1	27.3	27.2	27.2	0.1	4.7	5.1	0.4	3.9	4.2	0.4
Eu	3.3	3.3	0.0	4.4	4.6	4.6	0.3	1.1	1.2	0.1	1.0	1.1	0.1
Gd	10.6	10.7	0.1	13.4	15.5	16.3	3.0	3.6	3.7	0.2	2.9	3.1	0.2
Tb	1.3	1.3	0.0	1.4	1.5	1.5	0.2	0.4	0.4	0.0	0.3	0.4	0.0
Dy	6.2	6.2	0.1	5.6	5.9	5.9	0.4	2.1	2.1	0.1	1.7	1.7	0.1
Ho	1.1	1.1	0.0	0.8	0.9	0.9	0.0	0.4	0.4	0.0	0.3	0.3	0.0
Er	2.7	2.7	0.1	1.9	2.1	2.0	0.2	0.9	1.0	0.0	0.7	0.8	0.1
Tm	0.4	0.4	0.0	0.3	0.3	0.3	0.0	0.1	0.1	0.0	0.1	0.1	0.0
Yb	2.3	2.4	0.1	1.6	1.6	1.6	0.1	0.8	0.9	0.1	0.6	0.7	0.1
Lu	0.3	0.3	0.0	0.2	0.2	0.2	0.0	0.1	0.1	0.0	0.1	0.1	0.0
Ga	18.4	18.4	0.1	19.1	19.8	19.3	0.7	20.8	22.0	1.6	18.3	19.8	2.2
V	77.6	78.0	0.5	106.6	116.1	113.1	9.7	75.3	79.4	5.8	69.1	74.8	8.1
Sc	15.0	11.7	4.7	12.5	15.8	12.8	3.6	7.2	8.0	1.2	5.2	5.7	0.8
Co	12.8	12.6	0.4	24.0	25.8	25.0	1.9	14.0	14.8	1.2	11.2	12.3	1.5
Ni	41.8	42.2	0.5	142.7	152.1	147.2	9.4	49.4	53.2	5.3	20.2	23.1	4.1
Cu	n.d.	n.d.	n.d.	n.d.	62.5	62.3	0.3	15.6	15.8	0.3	16.5	17.4	1.3
Zn	n.d.	n.d.	n.d.	n.d.	70.2	67.9	3.2	63.2	67.3	5.9	61.6	67.5	8.5

Table C-3 Repeat ICP-MS analyses

sample	JPT3#1	JPT3#2	2 s.d.	JPT4#1	JPT4#2	2 s.d.	JPT8#1	JPT8#2	2 s.d.
Rb	117	116	1	126	167	58	325	315	15
Sr	811	794	24	589	714	176	161	158	4
Y	11.0	11.0	0.1	4.1	5.4	1.9	4.5	4.5	0.1
Zr	123.0	121.6	2.0	23.7	31.1	10.6	46.2	47.4	1.7
Nb	8.2	8.1	0.1	4.1	5.3	1.8	14.3	14.2	0.1
Cs	20.1	20.2	0.1	10.4	13.7	4.6	11.6	11.3	0.4
Ba	914	915	1	659	862	286	968	963	7
Hf	3.5	3.5	0.0	1.0	1.3	0.5	2.1	2.1	0.1
Ta	0.7	0.7	0.0	0.4	0.5	0.2	1.2	1.2	0.0
Pb	33.0	32.9	0.1	31.7	41.3	13.6	62.0	60.5	2.1
Th	19.2	19.3	0.2	14.7	18.2	5.1	55.4	56.2	1.2
U	3.7	3.7	0.1	3.2	4.2	1.4	8.1	8.1	0.0
La	30.7	31.2	0.7	21.7	24.0	3.2	22.7	22.3	0.7
Ce	63.5	63.6	0.2	38.4	44.9	9.3	90.2	88.9	1.9
Pr	7.8	7.9	0.1	4.3	5.3	1.4	3.6	3.5	0.1
Nd	30.9	31.2	0.4	15.2	18.8	5.1	11.8	11.4	0.7
Sm	5.3	5.3	0.0	2.3	2.9	0.9	1.6	1.6	0.1
Eu	1.2	1.2	0.0	0.5	0.7	0.2	0.4	0.4	0.0
Gd	3.7	3.7	0.1	1.6	2.0	0.5	1.3	1.1	0.2
Tb	0.4	0.4	0.0	0.2	0.2	0.1	0.1	0.1	0.0
Dy	2.1	2.1	0.0	0.8	1.1	0.4	0.7	0.7	0.0
Ho	0.4	0.4	0.0	0.1	0.2	0.1	0.1	0.1	0.0
Er	0.9	0.9	0.0	0.3	0.4	0.1	0.4	0.4	0.0
Tm	0.1	0.1	0.0	0.0	0.1	0.0	0.1	0.1	0.0
Yb	0.8	0.8	0.0	0.3	0.4	0.1	0.6	0.6	0.0
Lu	0.1	0.1	0.0	0.0	0.1	0.0	0.1	0.1	0.0
Ga	17.8	17.6	0.3	13.8	18.8	7.0	19.3	18.9	0.7
V	74.2	73.7	0.8	26.6	36.1	13.4	26.2	26.4	0.2
Sc	6.2	6.5	0.4	1.7	2.9	1.6	2.3	2.6	0.4
Co	11.3	11.4	0.1	3.1	4.3	1.7	3.7	3.7	0.1
Ni	15.0	15.3	0.4	3.9	5.7	2.5	9.5	9.9	0.6
Cu	30.9	30.9	0.0	9.3	12.0	3.9	8.9	8.4	0.8
Zn	47.6	50.0	3.4	28.8	38.2	13.3	39.7	39.6	0.2

Table C-4 Repeat Sr, Nd, Pb isotope analyses

calculated errors are bases on standard reprodicibility (2 s.d.) during period of analysis

sample	$^{87}Sr/^{86}Sr$	± 2 s.d.	$^{143}Nd/^{144}Nd$	± 2 s.d.	$^{206}Pb/^{204}Pb$	± 2 s.d.	$^{207}Pb/^{204}Pb$	± 2 s.d.	$^{208}Pb/^{204}Pb$	± 2 s.d.	$^{208}Pb/^{206}Pb$	± 2 s.d.	$^{207}Pb/^{206}Pb$	± 2 s.d.
Bb121#1			0.512060	±7[8]										
Bb121#2			0.512290	±9*										
K702#1	0.709605	±31[1]	0.512158	±4[7]										
K702#2	0.710180	±12[4]	0.511985	±7[8]										
K9008#1	0.709081	±16*	0.512275	±9*										
K9008#2	0.709006	±25[5]	0.511945	±4[7]										
K9008#3	0.708770	±31[1]												
K9026#1			0.512344	±9*										
K9026#2			0.512166	±7[8]										
K9026#3			0.512183	±7[8]										
K9029#1			0.512328	±9*	18.6863	±12[10]	15.655	±4[10]	38.995	±12[10]	2.0865	±6[10]	0.83771	±24[10]
K9029#2			0.512362	±4[7]	18.6852	±12[10]	15.655	±4[10]	38.993	±12[10]	2.0866	±6[10]	0.83779	±24[10]
K9032#1	0.708004	±16*	0.512348	±9*										
K9032#2	0.708233	±12[4]	0.512171	±7[8]										
K9039#1			0.512371	±4[7]										
K9039#2			0.512337	±9*										
JPT24A#1			0.512001	±4[7]	18.8777	±2[9]	15.759	±1[9]	39.537	±2[9]	2.0943	±1[9]	0.83480	±2[9]
JPT24A#2	0.715250	±25[5]	0.511955	±7[8]	18.8746	±2[9]	15.758	±1[9]	39.531	±2[9]	2.0942	±1[9]	0.83482	±2[9]
JPT24A#3	0.715271	±31[7]			18.8718	±2[9]	15.756	±1[9]	39.527	±2[9]	2.0943	±1[9]	0.83485	±2[9]
JPT24A#4					18.8592	±12[10]	15.736	±4[10]	39.467	±12[10]	2.0924	±6[10]	0.83435	±24[10]
T2A#1			0.511709	±4[7]										
T2A#2			0.511439	±7[8]	19.8278	±12[10]	15.854	±4[10]	41.515	±12[10]	2.0933	±6[10]	0.79950	±24[10]
T2A#3			0.511691	±7[8]	19.8385	±2[9]	15.843	±1[9]	41.504	±2[9]	2.0917	±1[9]	0.79853	±2[9]
T3B#1	0.712352	±31[1]	0.511941	±4[7]										
T3B#2	0.712353	±12[4]	0.511832	±7[8]										
T3F#1	0.709220	±8[6]												
T3F#2	0.714926	±31[1]												
T4A#1	0.712004	±56[2]	0.511980	±4[7]										
T4A#2	0.712017	±12[4]	0.511821	±7[8]										
T5A#1	0.716159	±8[6]	0.511914	±4[7]										
T5A#2	0.716194	±31[1]	0.512447	±4[7]										
JPT14.1#1	0.707216	±8[6]												
JPT14.1#2	0.707174	±25[5]												
JPT14.2#1	0.706997	±8[6]												
JPT14.2#2	0.706957	±31[7]												
T11A#1	0.707244	±31[1]												
T11A#2	0.707279	±31[1]												
JPT3#1	0.706694	±25[5]												
JPT3#2	0.706653	±67[3]												
JPT3#3	0.706686	±31[1]												
JPT4#2	0.706764	±8[6]	0.512431	±4[7]										
JPT4#1	0.706769	±31[1]	0.512313	±4[7]										
JPT4#3			0.512313	±4[7]										
JPT8#1	0.711317	±25[5]	0.512019	±4[7]										
JPT8#2	0.710848	±67[3]	0.512028	±4[7]										
JPT8#3			0.512172	±4[7]										
JPT8#4			0.511172	±4[7]										
20E39A#1	0.716287	±8[6]												
20E39A#2	0.706960	±31[1]												
JPT22#1			0.512121	±4[7]										
JPT22#2			0.511890	±4[7]										

* Turner et al., 1993, 1996

1 MC-ICP-MS, June 1999; NBS 987 0.71032±32 (n=14)

2 MC-ICP-MS, November 1999; NBS 987 0.710185±56 (n=20)

4 MC-ICP-MS, April 1999, NBS 987 0.710201 ± 67 (n=31)

3 CU TIMS, 2000, NBS 987 0.710258±12

5 TIMS, June 1998, NBS987 0.710286±25 (n=9)

6 TIMS, December 1998, TIMS, NBS987 0.710172±8 (n=30)

7 TIMS, Jan-June 1999, J+M Nd 0.511758±4 (n=36)

8 MC-ICP-MS, Oct-Nov 1999, J+M Nd 0.511788±7 (n=11)

9 MC-ICP-MS, April 1999, NBS 981

$^{208}Pb/^{206}Pb$	$^{207}Pb/^{204}Pb$	$^{206}Pb/^{204}Pb$	$^{208}Pb/^{206}Pb$	$^{207}Pb/^{206}Pb$
36.721	15.497	16.9403	2.1676	0.91480
±0.009	±0.004	±0.0012	±0.0006	±0.00002

10 MC-ICP-MS, June 2000, NBS 981

$^{208}Pb/^{206}Pb$	$^{207}Pb/^{204}Pb$	$^{206}Pb/^{204}Pb$	$^{208}Pb/^{206}Pb$	$^{207}Pb/^{206}Pb$
36.725	15.497	16.9391	2.1677	0.91476
±0.002	±0.001	±0.0002	±0.0001	±0.00024

Table C-5 Electron microprobe data: clinopyroxenes

pyroxene endmembers calculated after Lindsley (1983)

sample	notes	SiO_2	TiO_2	Al_2O_3	FeO*	MnO	MgO	CaO	Na_2O	Cr_2O_3	NiO	Total	Mg#	Wo	En	Fs	T°C (1atm)**	T° (1.4GPa)**
JPT24A	core	54	0.3	0.9	6.0	0.2	18.4	20.0	0.3	0.1	n.d.	99.9	84.5	0.4	0.5	0.1	1100	1100
JPT24A	core	52	0.1	1.9	11.1	0.4	11.5	21.6	1.0	0.0	n.d.	99.9	64.9	0.4	0.4	0.2	800	850
JPT24A	core	54	0.4	1.3	5.6	0.2	17.9	20.4	0.3	0.1	n.d.	99.9	85.1	0.4	0.5	0.1	1100	1100
JPT24A	core	54	0.5	1.5	5.8	0.2	18.8	20.5	0.4	0.1	n.d.	101.4	85.3	0.4	0.5	0.1	1100	1100
JPT24A	core	53	0.5	1.8	7.6	0.3	16.6	19.9	0.5	0.3	n.d.	100.2	79.5	0.4	0.5	0.1	1100	1100
JPT24A	core	52	0.0	3.5	4.9	0.2	14.8	23.8	0.4	0.1	n.d.	99.6	84.2	0.4	0.5	0.1	900	950
JPT24A	core	54	0.2	0.7	5.0	0.2	18.9	20.0	0.4	0.4	n.d.	99.9	87.0	0.4	0.5	0.1	1100	1125
JPT24A	core	54	0.3	1.1	5.2	0.2	18.9	19.8	0.3	0.2	n.d.	100.0	86.7	0.4	0.5	0.1	1100	1125
JPT24A	core	54	0.2	1.0	4.1	0.1	18.9	20.5	0.5	0.7	n.d.	100.1	89.1	0.4	0.5	0.1	1100	1130
JPT24A	core	54	0.2	0.9	4.0	0.1	18.4	21.9	0.3	0.1	n.d.	99.8	89.2	0.4	0.5	0.1	1100	1100
JPT24A	core	54	0.2	1.1	5.9	0.2	17.8	20.2	0.5	0.1	n.d.	99.8	84.4	0.4	0.5	0.1	1100	1100
JPT24A	core	51	0.6	2.3	9.9	0.3	12.7	22.2	0.6	0.0	n.d.	99.9	69.4	0.5	0.4	0.2	800	850
JPT24A	core	53	0.1	1.1	9.4	0.3	12.7	22.6	1.0	0.0	n.d.	100.2	70.7	0.5	0.4	0.2	800	850
JPT24A	core	53	0.1	1.2	9.4	0.3	12.9	22.2	1.0	0.0	n.d.	99.9	71.0	0.5	0.4	0.2	800	850
JPT24A	core	54	0.4	1.2	6.3	0.2	18.2	19.7	0.3	0.1	n.d.	100.2	83.6	0.4	0.5	0.1	1100	1100
JPT24A	core	53	0.3	1.3	4.5	0.1	16.6	20.6	0.3	0.4	n.d.	99.5	88.0	0.4	0.5	0.1	1100	1125
JPT24A	core	54	0.3	0.9	4.8	0.2	18.8	20.5	0.3	0.2	n.d.	99.8	87.5	0.4	0.5	0.1	1100	1125
JPT24A	core	54	0.4	1.2	5.5	0.2	18.4	20.0	0.3	0.1	n.d.	99.9	85.6	0.4	0.5	0.1	1100	1125
JPT24A	core	54	0.4	1.4	5.2	0.2	18.6	20.1	0.3	0.2	n.d.	100.0	86.4	0.4	0.5	0.1	1125	1150
JPT24A	core	54	0.3	1.1	4.6	0.1	19.3	19.8	0.4	0.5	n.d.	100.3	88.1	0.4	0.5	0.1	1125	1150
JPT24A	core	53	0.4	1.2	6.0	0.2	18.8	19.4	0.3	0.1	n.d.	99.8	84.9	0.4	0.5	0.1	1125	1150
JPT24A	core	52	0.5	1.9	8.5	0.3	15.8	19.9	0.4	0.1	n.d.	99.4	76.9	0.4	0.5	0.1	1100	1100
JPT24A	core	54	0.3	0.9	4.4	0.1	18.9	20.6	0.3	0.5	n.d.	99.8	88.4	0.4	0.5	0.1	1100	1125
JPT24A	core	54	0.2	0.9	4.2	0.2	19.0	20.4	0.4	0.5	n.d.	99.8	88.9	0.4	0.5	0.1	1100	1125
JPT24A	core	53	0.3	1.2	5.5	0.2	18.9	19.5	0.3	0.2	n.d.	99.5	86.1	0.4	0.5	0.1	1100	1125
JPT24A	core	52	0.4	2.7	6.7	0.2	16.4	19.7	0.6	0.2	n.d.	99.0	81.4	0.4	0.5	0.1	1100	1100
JPT24A	core	54	0.3	1.2	5.8	0.2	19.1	18.6	0.4	0.3	n.d.	100.0	85.4	0.4	0.5	0.1	1125	1150
JPT24A	core	53	0.4	2.1	6.2	0.2	17.2	19.6	0.5	0.3	n.d.	99.6	83.1	0.4	0.5	0.1	1125	1150
JPT24A	core	54	0.3	1.1	4.7	0.1	18.7	19.7	0.3	0.4	n.d.	99.7	87.7	0.4	0.5	0.1	1125	1150
JPT24A	core	54	0.3	0.9	5.9	0.2	17.9	19.8	0.3	0.1	n.d.	99.5	84.4	0.4	0.5	0.1	1125	1150
JPT24A	core	54	0.3	0.9	4.2	0.1	19.0	19.7	0.3	0.4	n.d.	99.3	89.0	0.4	0.6	0.1	1125	1150
JPT24A	core	54	0.3	1.1	4.6	0.2	18.2	19.9	0.4	0.4	n.d.	99.4	87.5	0.4	0.5	0.1	1125	1150
JPT24A	core	54	0.4	1.2	5.1	0.2	17.8	21.1	0.3	0.2	n.d.	99.8	86.2	0.4	0.5	0.1	1100	1100
JPT24A	core	54	0.3	1.2	4.5	0.1	16.8	22.7	0.3	0.0	n.d.	99.8	86.8	0.4	0.5	0.1	1100	1100
JPT24A	core	52	0.3	2.5	8.6	0.3	12.5	22.3	0.9	0.0	n.d.	99.3	72.3	0.5	0.4	0.2	1100	1100
JPT24A	core	53	0.3	1.6	6.9	0.2	15.0	21.6	0.7	0.1	n.d.	99.4	79.4	0.4	0.5	0.1	1100	1100
JPT24A	core	54	0.3	1.4	5.1	0.2	18.3	20.1	0.4	0.3	n.d.	99.9	86.4	0.4	0.5	0.1	1100	1125
JPT24A	core	54	0.2	1.1	4.8	0.2	18.9	20.3	0.3	0.2	n.d.	99.6	87.6	0.4	0.5	0.1	1100	1125
JPT24A	core	54	0.3	1.2	5.9	0.2	18.1	19.7	0.5	0.2	n.d	100.2	84.6	0.4	0.5	0.1	1100	1125
JPT24A	core	54	0.2	1.0	5.7	0.2	18.0	20.2	0.4	0.1	n.d.	100.1	84.9	0.4	0.5	0.1	1100	1100
JPT24A	core	54	0.3	1.0	4.9	0.2	17.8	21.8	0.3	0.1	n.d.	100.1	86.7	0.4	0.5	0.1	1100	1100
JPT24B	core	55	0.2	0.8	4.6	0.2	19.1	20.6	0.3	0.2	n.d.	100.5	88.2	0.4	0.5	0.1	1100	1125
JPT24B	core	53	0.4	2.2	6.3	0.2	17.4	20.0	0.5	0.3	n.d.	100.0	83.2	0.4	0.5	0.1	1100	1100
JPT24B	core	54	0.3	2.0	5.5	0.2	17.6	20.7	0.4	0.1	n.d.	100.4	85.0	0.4	0.5	0.1	1100	1100
JPT24B	core	53	0.3	0.8	5.2	0.2	18.6	20.7	0.3	0.1	n.d.	99.5	86.4	0.4	0.5	0.1	1100	1125
JPT24B	core	53	0.3	1.0	4.6	0.2	18.9	20.2	0.4	0.4	n.d.	99.5	88.0	0.4	0.5	0.1	1100	1125
JPT24B	core	53	0.3	1.9	5.5	0.1	16.9	21.8	0.4	0.2	n.d.	99.9	84.5	0.4	0.5	0.1	1100	1100
JPT24B	core	53	0.4	1.9	5.6	0.2	17.8	20.6	0.5	0.3	n.d.	99.8	85.1	0.4	0.5	0.1	1100	1100
JPT24B	core	53	0.4	1.2	6.5	0.2	16.6	21.7	0.3	0.0	n.d.	100.2	82.0	0.4	0.5	0.1	1000	1000
JPT24B	core	52	0.4	1.4	5.1	0.2	18.1	20.9	0.4	0.1	n.d.	98.9	86.2	0.4	0.5	0.1	1100	1100
JPT24B	core	52	0.4	2.2	4.6	0.1	17.2	21.7	0.5	0.2	n.d.	98.9	86.8	0.4	0.5	0.1	1100	1100
JPT24B	core	53	0.3	1.0	5.7	0.2	18.1	20.8	0.3	0.1	n.d.	99.9	85.0	0.4	0.5	0.1	1100	1100

all oxides as wt%

**all iron as FeO*

*** based on the graphical thermometer of Lindsley and Anderson (1983)*

Table C-5 Electron microprobe data: clinopyroxenes

pyroxene endmembers calculated after Lindsley (1983)

sample	notes	SiO_2	TiO_2	Al_2O_3	FeO*	MnO	MgO	CaO	Na_2O	Cr_2O_3	NiO	Total	Mg#	Wo	En	Fs	T°C (1atm)	T° (1.4GPa)
JPT24B	core	53	0.3	1.1	6.4	0.2	17.6	20.9	0.3	0.0	n.d.	100.2	83.1	0.4	0.5	0.1	1000	1025
JPT24B	core	54	0.0	0.9	6.4	0.4	15.2	23.5	0.4	0.1	n.d.	100.5	80.9	0.5	0.4	0.1	900	950
JPT24B	core	54	0.0	0.9	6.3	0.4	14.9	23.7	0.4	0.0	n.d.	100.2	80.7	0.5	0.4	0.1	900	950
JPT24B	core	49	0.3	0.8	4.9	0.2	16.9	23.9	0.3	0.1	n.d.	96.8	86.0	0.4	0.5	0.1	1000	1025
JPT24B	core	54	0.3	0.9	5.6	0.2	18.2	20.7	0.3	0.1	n.d.	100.2	85.3	0.4	0.5	0.1	1100	1100
JPT24A	core	54	0.3	0.9	4.8	0.2	18.8	20.5	0.3	0.2	n.d.	99.8	87.5	0.4	0.5	0.1	1100	1100
JPT24C	core	54	0.3	1.0	5.2	0.2	16.7	22.6	0.4	0.0	n.d.	100.4	85.1	0.4	0.5	0.1	1000	1025
JPT24C	core	54	0.3	0.9	4.2	0.1	18.9	21.3	0.3	0.3	n.d.	100.7	88.9	0.4	0.5	0.1	1100	1100
JPT24C	core	53	0.5	1.6	7.4	0.2	16.6	20.7	0.4	0.0	n.d.	100.5	80.0	0.4	0.5	0.1	950	1000
JPT24C	core	54	0.4	1.4	5.8	0.2	18.2	20.0	0.3	0.1	n.d.	100.4	84.7	0.4	0.5	0.1	1100	1100
JPT24C	core	54	0.4	1.4	5.7	0.2	18.2	20.2	0.3	0.1	n.d.	100.4	85.0	0.4	0.5	0.1	1100	1100
JPT24C	core	54	0.4	1.4	6.4	0.2	17.6	20.9	0.3	0.0	n.d.	100.7	83.1	0.4	0.5	0.1	1100	1100
JPT24C	core	54	0.3	1.3	5.9	0.2	17.6	20.1	0.5	0.3	n.d.	100.1	84.3	0.4	0.5	0.1	1000	1025
JPT24C	core	53	0.4	1.0	6.6	0.2	16.0	22.1	0.4	0.1	0.0	99.2	81.3	0.4	0.5	0.1	950	1000
JPT24C	core	54	0.3	0.8	4.1	0.1	18.9	20.6	0.3	0.3	0.0	99.4	89.1	0.4	0.5	0.1	1100	1100
JPT24C	core	54	0.3	1.0	4.4	0.1	18.5	20.9	0.3	0.3	0.0	99.5	88.1	0.4	0.5	0.1	1100	1100
JPT24C	core	53	0.1	0.0	6.3	0.2	16.5	22.3	0.3	0.0	0.0	99.3	82.3	0.4	0.5	0.1	950	1000
JPT24C	core	53	0.1	1.5	6.5	0.2	14.4	23.4	0.6	0.0	0.0	99.5	79.8	0.5	0.4	0.1	950	1000
JPT24C	xundm	53	0.4	1.1	6.0	0.2	17.5	20.4	0.2	0.2	0.0	99.0	83.8	0.4	0.5	0.1	1100	1100
JPT24C	xundm	53	0.4	1.0	7.8	0.3	15.3	21.8	0.4	0.0	0.0	99.8	77.7	0.4	0.4	0.1	850	900
JPT24C	xundm	53	0.4	1.1	7.2	0.2	17.3	19.9	0.2	0.1	0.0	99.2	81.2	0.4	0.5	0.1	1000	1025
JPT24C	core	54	0.3	1.0	4.7	0.2	18.5	20.6	0.3	0.3	0.0	99.8	87.6	0.4	0.5	0.1	1075	1110
JPT24C	core	54	0.3	1.2	4.8	0.1	18.4	20.8	0.4	0.3	0.0	100.1	87.2	0.4	0.5	0.1	1075	1100
JPT24C	core	54	0.3	0.9	4.1	0.1	19.0	20.7	0.3	0.4	0.1	100.2	89.3	0.4	0.5	0.1	1075	1110
T2A	core	54	0.3	0.4	4.3	0.1	16.8	22.4	0.2	0.1	n.d.	98.4	87.4	0.4	0.5	0.1	1000	1025
T2A	core	53	0.3	0.4	3.9	0.1	17.1	21.1	0.2	0.0	n.d.	95.6	88.8	0.4	0.5	0.1	1100	1100
T2A	core	53	0.3	0.4	4.2	0.2	16.7	22.0	0.2	0.0	n.d.	96.6	87.7	0.4	0.5	0.1	1100	1100
T4C	core	54	0.3	0.9	5.0	0.2	17.4	21.2	0.3	0.0	0.0	99.1	86.1	0.4	0.5	0.1	1100	1100
T4C	core	54	0.3	0.8	5.7	0.2	16.6	21.2	0.3	0.0	0.0	99.1	83.9	0.4	0.5	0.1	1100	1100
T4C	core	54	0.3	1.2	4.6	0.1	17.5	20.8	0.4	0.0	0.0	99.1	87.2	0.4	0.5	0.1	1075	1100
T4C	core	54	0.4	1.1	5.1	0.2	17.1	20.8	0.3	0.0	0.0	99.1	85.6	0.4	0.5	0.1	1075	1100
T4C	core	55	0.3	0.6	3.9	0.1	18.4	20.9	0.2	0.0	0.0	99.2	89.4	0.4	0.5	0.1	1110	1150
T4C	core	55	0.3	0.8	4.0	0.1	17.7	21.4	0.3	0.0	0.0	99.2	88.7	0.4	0.5	0.1	1110	1150
T4C	core	53	0.5	1.2	5.1	0.2	16.8	22.1	0.3	0.0	0.0	99.3	85.4	0.4	0.5	0.1	900	900
T4C	core	54	0.3	0.7	5.0	0.2	17.4	21.1	0.2	0.0	0.0	99.4	86.1	0.4	0.5	0.1	1100	1100
T4C	core	54	0.3	1.1	4.0	0.1	18.1	21.0	0.4	0.1	0.0	99.5	89.0	0.4	0.5	0.1	1110	1150
T4C	core	54	0.4	1.1	5.1	0.2	16.7	22.1	0.3	0.0	0.0	99.5	85.3	0.4	0.5	0.1	1100	1100
T4C	core	54	0.2	0.9	4.4	0.1	18.7	20.4	0.3	0.1	0.0	99.5	88.2	0.4	0.5	0.1	1100	1125
T4C	core	54	0.2	1.1	3.8	0.1	18.0	21.7	0.4	0.1	0.0	99.7	89.5	0.4	0.5	0.1	1110	1150
T4C	core	54	0.3	0.7	4.9	0.2	17.4	22.0	0.2	0.0	0.0	99.8	86.3	0.4	0.5	0.1	950	1000
T4C	core	54	0.4	1.8	4.7	0.1	17.4	21.0	0.5	0.1	0.0	99.9	87.0	0.4	0.5	0.1	1100	1100
T4C	core	54	0.4	0.7	5.3	0.2	17.0	22.2	0.3	0.0	0.0	100.2	85.1	0.4	0.5	0.1	950	1000
T4C	core	54	0.3	0.7	4.9	0.2	17.5	22.1	0.2	0.0	0.0	100.3	86.5	0.4	0.5	0.1	950	1000

all oxides as wt%

**all iron as FeO*

*** based on the graphical thermometer of Lindsley and Anderson (1983)*

Table C-6 Electron microprobe data: orthopyroxenes

pyroxene endmembers calculated after Lindsley (1983)

sample	notes	SiO_2	TiO_2	Al_2O_3	FeO*	MnO	MgO	CaO	Na_2O	Cr_2O_3	Total	Mg#	Wo	En	Fs	T°C (1atm)	T° (1.4GPa)
JPT24A	core	56	0.2	0.7	9.9	0.2	31.8	1.4	0.0	0.1	100.6	85	0.03	0.83	0.14	1100	1200
JPT24A	core	56	0.2	0.9	7.5	0.2	31.3	3.9	0.1	0.5	100.7	88	0.07	0.82	0.11	1275	1400
JPT24A	*core*	*56*	*0.2*	*0.8*	*9.4*	*0.2*	*32.1*	*1.5*	*0.1*	*0.2*	*100.8*	*86*	*0.03*	*0.83*	*0.14*	*1100*	*1200*
JPT24A	core	56	0.1	0.8	8.9	0.2	32.4	1.6	0.1	0.2	100.7	87	0.03	0.84	0.13	1100	1200
JPT24A	core	57	0.1	0.8	7.2	0.2	32.9	2.0	0.1	0.5	100.5	89	0.04	0.86	0.11	1250	1400
JPT24A	core	53	0.1	2.4	19.6	0.5	23.8	0.8	0.1	0.2	100.3	68	0.03	0.67	0.31	1100	1200
JPT24A	core	57	0.1	0.9	5.7	0.1	34.2	0.8	0.1	0.5	99.6	91	0.02	0.90	0.09	900	1100
JPT24A	core	57	0.2	1.2	6.0	0.1	34.0	0.9	0.1	0.8	100.3	91	0.02	0.89	0.09	900	1100
JPT24E	core	56	0.1	2.3	6.5	0.1	34.5	0.6	0.0	0.3	100.2	90	0.01	0.89	0.09	900	1100
JPT24E	core	56	0.1	0.8	7.5	0.2	33.8	1.0	0.0	0.4	100.1	89	0.02	0.87	0.11	900	1100
JPT24E	core	54	0.2	3.5	12.5	0.3	28.4	1.0	0.1	0.2	100.0	80	0.02	0.79	0.19	1100	1050
JPT24E	core	53	0.2	3.1	13.3	0.3	28.8	1.0	0.1	0.2	99.8	79	0.02	0.78	0.20	1100	1100
JPT24E	core	54	0.2	2.6	13.3	0.3	28.9	1.0	0.1	0.2	100.2	80	0.02	0.78	0.20	1100	1100
JPT24E	core	53	0.2	2.8	13.4	0.3	28.8	1.1	0.1	0.2	100.2	79	0.02	0.78	0.20	1100	1100
JPT24E	core	53	0.2	2.7	13.1	0.3	28.5	1.1	0.1	0.2	99.8	80	0.02	0.78	0.20	1100	1100
JPT24E	core	54	0.2	2.8	13.3	0.3	28.9	1.1	0.1	0.2	100.7	79	0.02	0.78	0.20	1100	1100
JPT24E	core	53	0.2	2.6	13.2	0.3	27.9	1.4	0.1	0.2	99.1	79	0.03	0.77	0.20	1050	1100
JPT24E	core	54	0.2	2.6	13.4	0.3	29.0	1.0	0.1	0.2	100.6	79	0.02	0.78	0.20	1100	1100
JPT24E	*core*	*53*	*0.2*	*3.1*	*13.5*	*0.3*	*28.7*	*1.0*	*0.1*	*0.2*	*100.2*	*79*	*0.02*	*0.78*	*0.20*	*1100*	*1100*
JPT24E	*core*	*53*	*0.2*	*3.0*	*13.4*	*0.3*	*28.8*	*1.0*	*0.1*	*0.2*	*100.2*	*79*	*0.02*	*0.78*	*0.20*	*1100*	*1100*
JPT24E	core	53	0.1	3.3	12.9	0.3	29.0	0.9	0.1	0.2	100.2	80	0.02	0.79	0.20	900	1100
JPT24E	core	54	0.1	2.9	11.4	0.2	30.7	0.9	0.0	0.2	100.3	83	0.02	0.81	0.17	900	1100
JPT24E	core	56	0.2	1.1	8.8	0.2	32.6	1.4	0.0	0.5	100.8	87	0.03	0.85	0.13	1100	1200
JPT24E	core	56	0.2	1.0	7.7	0.2	33.2	1.4	0.0	0.5	100.2	89	0.03	0.86	0.11	1150	1200

all oxides as wt%

**all iron as FeO*

*** based on the graphical thermometer of Lindsley and Anderson (1983)*

Table C-7 Electron microprobe data: amphiboles

sample	notes	SiO_2	TiO_2	Al_2O_3	FeO*	MnO	MgO	CaO	Na_2O	K_2O	Cr_2O_3	NiO	Total	P GPa [1]	P GPa [2]
T2A	core	53	3.3	0.6	18.1	0.5	11.1	2.4	7.2	n.d.	0.0	0.0	96.1	n/a	n/a
T2A	core	52	2.7	0.6	17.4	0.5	11.4	2.8	6.7	n.d.	0.0	0.0	94.3	n/a	n/a
T2A	core	52	2.2	0.5	16.4	0.4	12.0	2.5	6.8	n.d.	0.0	0.0	93.3	n/a	n/a
T2A	core	51	2.9	2.0	16.5	0.4	12.4	2.3	6.2	n.d.	0.0	0.0	93.3	n/a	n/a
T2A	core	52	3.1	0.6	16.4	0.4	11.9	2.5	7.1	n.d.	0.0	0.0	94.4	n/a	n/a
T2A	core	52	2.7	0.6	13.8	0.4	13.4	2.5	7.2	n.d.	0.1	0.1	93.0	n/a	n/a
T2A	core	53	3.3	0.8	18.6	0.4	11.7	2.4	7.2	n.d.	0.0	0.0	95.0	n/a	n/a
JPT14.2	core	43	2.7	12.0	12.8	0.1	13.8	11.4	2.3	0.8	0.0	0.0	98.6	0.5	0.7
JPT14.2	core	43	2.7	11.4	10.0	0.1	15.3	11.4	2.3	0.7	0.1	0.0	97.3	0.5	0.6
JPT14.2	core	43	2.8	12.7	10.1	0.1	15.1	11.1	2.5	0.8	0.1	0.0	98.2	0.6	0.7
JPT14.2	core	43	2.6	12.5	10.8	0.1	14.6	11.1	2.5	0.7	0.0	0.0	97.8	0.5	0.7
JPT14.2	core	43	2.8	12.2	10.7	0.1	14.4	11.5	2.4	0.8	0.1	0.0	97.6	0.5	0.7
JPT14.2	core	42	2.8	12.3	13.4	0.1	13.1	11.3	2.3	0.7	0.0	0.0	98.1	0.5	0.7
JPT14.2	core	45	1.1	8.3	16.3	0.4	12.3	11.7	1.6	1.0	0.0	0.0	98.1	0.3	0.4
JPT14.2	core	43	2.6	12.0	12.3	0.1	13.6	11.5	2.4	0.6	0.0	0.0	98.0	0.5	0.7
JPT14.2	core	44	2.8	10.7	11.9	0.1	14.4	11.3	2.2	0.6	0.0	0.0	97.7	0.4	0.6
JPT14.2	core	42	2.7	13.2	11.8	0.1	13.7	11.3	2.5	0.8	0.1	0.0	98.2	0.6	0.8
JPT14.2	core	42	2.8	11.7	12.7	0.1	13.9	11.1	2.3	0.8	0.0	0.0	97.7	0.5	0.7
JPT14.2	core	44	2.7	10.6	10.5	0.1	15.5	11.5	2.3	0.6	0.0	0.0	98.2	0.4	0.5
JPT14.2	core	44	2.5	11.1	10.1	0.1	15.6	11.3	2.3	0.7	0.1	0.0	98.4	0.4	0.6
JPT14.2	core	43	2.9	11.3	10.5	0.1	14.9	11.7	2.4	0.7	0.1	0.0	97.8	0.5	0.6
JPT14.2	core	44	2.9	10.5	12.3	0.2	14.2	11.2	2.2	0.7	0.0	0.0	98.0	0.4	0.6
JPT14.2	core	42	2.7	12.8	11.8	0.1	13.5	11.5	2.4	0.7	0.1	0.0	97.8	0.6	0.7
JPT14.2	core	43	2.8	12.3	13.2	0.2	13.7	11.5	2.5	0.7	0.0	0.0	99.7	0.5	0.7
JPT14.2	core	44	2.9	11.6	11.0	0.1	15.2	11.4	2.4	0.6	0.0	0.0	98.8	0.5	0.6
JPT14.2	core	43	2.6	11.5	13.0	0.2	13.6	11.4	2.2	0.7	0.0	0.0	97.8	0.5	0.6
JPT14.2	core	45	1.8	9.1	12.8	0.2	15.0	11.2	2.0	0.6	0.0	0.0	98.1	0.3	0.4
JPT14.2	core	44	2.7	11.3	10.5	0.1	15.3	11.3	2.3	0.7	0.1	0.0	97.9	0.5	0.6
JPT14.2	core	44	2.3	9.7	12.9	0.2	14.2	11.6	2.0	0.7	0.0	0.0	97.9	0.4	0.5
JPT14.2	core	45	2.6	10.5	9.5	0.1	16.3	11.1	2.3	0.6	0.2	0.0	97.7	0.4	0.5
JPT14.2	core	43	2.4	14.1	12.8	0.1	13.1	10.1	2.6	0.9	0.0	0.0	98.8	0.7	0.8
JPT14.2	core	42	2.8	13.2	12.1	0.1	13.5	11.2	2.5	0.8	0.0	0.0	98.4	0.6	0.8
JPT14.2	core	43	2.7	13.5	11.4	0.1	14.0	10.9	2.6	0.8	0.0	0.0	98.5	0.6	0.8
T11B	core	42	2.8	12.6	10.7	0.1	14.6	11.2	2.5	0.7	0.0	0.0	97.3	0.6	0.7
T11B	core	43	2.5	12.3	12.0	0.1	14.1	11.4	2.4	0.7	0.0	0.0	98.3	0.5	0.7
T11B	core	44	2.0	10.9	12.4	0.2	14.2	11.7	2.1	0.7	0.0	0.0	98.2	0.4	0.6
T11B	core	43	2.8	12.1	11.8	0.1	14.4	11.3	2.4	0.7	0.0	0.0	98.2	0.5	0.7
T11B	core	43	2.6	11.7	10.9	0.1	14.9	11.5	2.4	0.7	0.1	0.0	98.2	0.5	0.6
T11B	core	44	2.0	10.9	12.4	0.1	14.5	11.7	2.2	0.7	0.0	0.0	98.6	0.4	0.6
T11B	core	43	2.9	11.2	9.8	0.1	15.6	11.5	2.4	0.7	0.2	0.0	97.7	0.5	0.6
T11B	core	43	2.5	12.0	11.2	0.1	15.0	11.5	2.4	0.7	0.0	0.0	98.1	0.5	0.7
T11B	core	44	2.7	11.7	10.9	0.1	15.3	11.2	2.4	0.7	0.0	0.0	98.8	0.5	0.6
T11B	core	43	2.7	11.5	11.8	0.1	14.2	11.7	2.3	0.6	0.0	0.0	97.7	0.5	0.6
T11B	core	42	2.8	12.4	12.9	0.1	13.0	11.6	2.3	0.8	0.0	0.0	97.6	0.6	0.7
T11B	core	42	2.7	12.2	13.3	0.1	12.9	11.6	2.3	0.9	0.0	0.0	98.0	0.5	0.7
T11B	core	42	2.7	12.1	12.5	0.1	13.4	11.6	2.3	0.8	0.0	0.0	97.8	0.5	0.7
T11B	core	43	2.7	11.9	11.8	0.1	14.0	11.7	2.3	0.8	0.1	0.0	98.2	0.5	0.7
T11B	core	43	2.7	12.0	11.3	0.1	14.3	11.6	2.4	0.8	0.1	0.0	98.0	0.5	0.7
T11B	core	42	2.7	12.2	12.5	0.1	13.4	11.5	2.3	0.8	0.0	0.0	97.8	0.5	0.7
T11B	core	42	2.7	12.4	12.2	0.1	13.4	11.6	2.3	0.8	0.1	0.0	97.3	0.6	0.7
T11B	core	43	2.6	11.8	11.2	0.1	14.6	11.3	2.4	0.6	0.0	0.0	97.7	0.5	0.7
T11B	core	43	2.8	11.6	10.4	0.1	15.0	11.6	2.3	0.7	0.0	0.0	97.5	0.5	0.6
T11B	core	43	2.6	11.7	11.2	0.1	15.4	11.2	2.3	0.7	0.0	0.0	98.6	0.5	0.6
T11B	core	43	2.8	12.3	10.9	0.1	14.4	11.7	2.4	0.7	0.2	0.0	98.5	0.5	0.7

all oxides as wt%

[1] pressure calculated using the Al in hornblende calibration of Johnson and Rutherford (1989)

[2] pressure calculated using the Al in hornblende calibration of Schmidt et al. (1992)

Table C-8 Fe-Ti oxide microprobe data

sample	phase	SiO_2	TiO_2	Al_2O_3	Cr_2O_3	MgO	CaO	MnO	FeO*	NiO	ZnO	Total	temp °C**	$fO_{2\ (rel\ FMQ)}$**
JPT24C	magnetite	0.5	11.9	2.7	0.9	1.8	0.3	0.5	75.0	n.d.	0.4	93.8		
JPT24C	ilmenite	0.2	44.4	0.3	0.3	4.6	0.4	0.4	46.5	n.d.	0.1	97.2	1004	-0.39
JPT23-1	magnetite	0.2	6.2	1.4	0.0	0.5	0.1	1.1	82.2	n.d.	0.4	92.0		
JPT23-1	ilmenite	0.1	37.8	0.2	0.1	1.2	0.1	0.7	57.8	n.d.	0.0	98.0	867	0.42
JPT23-2	magnetite	0.3	5.6	1.3	0.0	0.3	0.1	1.0	82.8	n.d.	0.4	91.9		
JPT23-2	ilmenite	0.1	37.3	0.2	0.1	1.2	0.1	0.7	57.0	n.d.	0.1	96.7	845	0.40
JPT23-3	magnetite	0.2	5.4	1.4	0.0	0.5	0.0	0.9	83.8	n.d.	0.3	92.4		
JPT23-3	ilmenite	0.1	37.4	0.2	0.0	1.4	0.0	1.6	55.4	n.d.	0.1	96.3	833	0.54
T3B-1	magnetite	0.3	3.5	1.8	0.1	0.4	0.2	0.6	83.8	n.d.	0.2	90.7		
T3B-1	ilmenite	0.0	95.7	0.3	0.2	0.0	0.0	0.0	2.0	n.d.	0.0	98.2	951	9.67
T3B-2	magnetite	0.2	3.3	2.6	0.1	0.7	0.1	0.6	82.9	n.d.	0.2	90.6		
T3B-2	ilmenite	0.1	95.1	0.2	0.2	0.0	0.0	0.0	2.0	n.d.	0.0	97.6	950	9.67
T11B-1	magnetite	0.2	5.5	3.4	0.3	2.1	0.0	0.2	83.2	0.0	0.2	95.2		
T11B-1	ilmenite	0.1	40.4	0.3	0.0	2.9	0.1	0.4	51.6	0.0	0.1	95.9	826	2.25
T11B-2	magnetite	0.2	6.8	3.3	0.2	2.0	0.1	0.2	81.3	0.0	0.2	94.4		
T11B-2	ilmenite	0.3	39.4	0.4	0.1	2.9	0.0	0.3	54.1	0.0	0.1	97.6	904	2.93

all oxides as wt%

***temperatures and oxygen fugacities calculated after Giorso and Sack (1991)*
initial pressures assumed for the calculation are 0.65 GPa (T11B); and 2.7 GPa (JPT23, JPT24C and T3B)
these pressures are based on the Al-hornblende barometry (T11B)
and trace-element constraints (JPT23, JPT24C and T3B)

Table C-9 Electron microprobe data: phlogopites

oxides as wt%		H_2O calculations after Tindle and Webb (1990)																		
sample	notes	SiO_2	TiO_2	Al_2O_3	FeO*	MnO	MgO	CaO	Na_2O	K_2O	SrO	BaO	Rb_2O	F	Cl	Cr_2O_3	NiO	H2O*	O=F,Cl	Total	Mg#
JPT23	core	42	1.4	12.5	2.8	0.0	25.1	0.0	0.1	10.2	n.d.	0.4	n.d.	2.0	0.0	n.d.	0.3	3.3	0.8	99.3	94
JPT23	core	37	3.7	13.8	18.2	0.2	12.9	0.1	0.3	8.9	n.d.	0.5	n.d.	0.2	0.1	n.d.	0.0	3.8	0.1	99.7	56
JPT23	core	42	1.3	12.9	2.7	0.0	25.0	0.0	0.1	10.4	n.d.	0.3	n.d.	1.8	0.0	n.d.	0.4	3.4	0.8	99.5	94
JPT23	core	42	1.6	12.6	3.0	0.0	24.8	0.0	0.1	10.2	n.d.	0.4	n.d.	2.0	0.0	n.d.	0.3	3.3	0.8	98.9	94
JPT23	core	43	1.6	13.2	4.1	0.0	24.3	0.0	0.1	10.2	n.d.	0.2	n.d.	1.1	0.0	n.d.	0.2	3.8	0.5	101.0	91
JPT23	rim	41	2.9	11.9	5.3	0.0	23.3	0.0	0.2	9.7	n.d.	0.9	n.d.	2.5	0.0	n.d.	0.0	3.0	1.0	99.9	89
JPT23		41	2.9	11.9	5.3	0.0	23.3	0.0	0.2	9.7	n.d.	0.9	n.d.	2.5	0.0	n.d.	0.0	3.0	1.0	99.9	89
JPT23	(traverse)	42	1.5	12.5	3.1	0.0	25.0	0.0	0.1	10.2	n.d.	0.4	n.d.	2.5	0.0	n.d.	0.2	3.1	1.0	99.6	94
JPT23		42	1.5	12.5	3.1	0.0	24.9	0.0	0.1	10.3	n.d.	0.4	n.d.	2.2	0.0	n.d.	0.2	3.2	0.9	99.4	94
JPT23	core	42	1.6	12.6	3.3	0.0	24.7	0.0	0.1	10.0	n.d.	0.4	n.d.	2.4	0.0	n.d.	0.2	3.1	1.0	99.3	93
JPT23		42	1.5	12.7	3.2	0.0	25.0	0.0	0.1	10.1	n.d.	0.4	n.d.	2.3	0.0	n.d.	0.2	3.1	1.0	99.7	93
JPT23		42	1.6	12.6	3.3	0.0	24.8	0.0	0.1	10.3	n.d.	0.4	n.d.	2.4	0.0	n.d.	0.2	3.1	1.0	99.8	93
JPT23	rim	42	2.8	11.6	5.3	0.0	23.7	0.0	0.2	9.8	n.d.	0.8	n.d.	2.5	0.0	n.d.	0.1	3.0	1.0	100.2	89
JPT24A	core	40	3.1	13.7	5.7	0.0	21.9	0.0	0.2	10.0	n.d.	0.3	n.d.	1.2	0.0	n.d.	0.2	3.6	0.5	99.1	87
JPT24A	core	40	2.5	13.2	5.1	0.0	22.4	0.0	0.4	9.9	n.d.	0.3	n.d.	2.0	0.0	n.d.	0.2	3.2	0.9	98.6	89
JPT24A	core	40	2.9	13.9	5.8	0.0	22.0	0.0	0.2	9.9	n.d.	0.3	n.d.	1.3	0.0	n.d.	0.1	3.5	0.6	99.5	87
JPT24A	core	40	3.2	13.2	6.6	0.0	21.2	0.0	0.4	9.6	n.d.	0.4	n.d.	2.3	0.0	n.d.	0.1	3.1	1.0	98.8	85
JPT24A	core	41	2.5	12.8	6.8	0.0	21.8	0.1	0.3	9.8	n.d.	0.2	n.d.	1.8	0.0	n.d.	0.1	3.3	0.8	99.4	85
JPT24A	core	39	2.3	14.0	8.6	0.0	19.6	0.1	0.3	9.4	n.d.	0.3	n.d.	3.4	0.0	n.d.	0.1	2.5	1.4	98.6	80
JPT24A	core	38	6.1	14.7	9.8	0.0	17.4	0.0	0.5	9.4	n.d.	0.4	n.d.	1.0	0.0	n.d.	0.1	3.7	0.4	101.1	76
JPT24A	core	40	3.4	13.4	8.3	0.1	20.6	0.1	0.4	9.7	n.d.	0.5	n.d.	2.5	0.0	n.d.	0.1	3.0	1.1	100.6	81
JPT24A	core	40	3.3	13.5	7.0	0.0	21.2	0.1	0.2	9.9	n.d.	0.4	n.d.	3.5	0.0	n.d.	0.1	2.5	1.5	100.2	84
JPT24A	core	39	2.9	13.2	8.0	0.0	20.8	0.1	0.5	9.5	n.d.	0.4	n.d.	5.1	0.0	n.d.	0.1	1.7	2.1	99.4	82
JPT24A	core	40	2.9	13.4	5.7	0.0	22.1	0.1	0.5	9.5	n.d.	0.3	n.d.	5.2	0.0	n.d.	0.1	1.7	2.2	99.8	87
JPT24C	core	40	2.5	13.0	6.8	0.0	21.9	0.0	0.5	9.8	n.d.	0.2	n.d.	3.1	0.0	n.d.	0.1	2.7	1.3	99.7	85
JPT24C	core	41	2.8	13.4	5.0	0.0	23.2	0.0	0.3	10.0	n.d.	0.4	n.d.	1.7	0.0	n.d.	0.2	3.4	0.7	100.2	89
JPT24C	core	39	2.7	12.5	7.1	0.0	20.7	2.2	0.4	8.9	n.d.	0.3	n.d.	5.0	0.0	n.d.	0.1	1.7	2.1	98.3	84
JPT24C	core	37	6.4	14.9	10.8	0.0	15.6	0.0	0.3	9.8	n.d.	0.3	n.d.	0.6	0.1	n.d.	0.1	3.8	0.3	99.7	72
T3B	core	37	3.5	18.5	14.2	0.0	13.7	0.1	0.2	8.8	n.d.	0.2	n.d.	0.2	0.0	0.0	0.0	4.0	0.1	99.9	63
T3B	core	37	4.7	17.2	13.9	0.1	13.7	0.1	0.4	8.6	n.d.	0.4	n.d.	0.2	0.1	0.1	0.0	3.9	0.1	99.9	64
T3B	core	36	4.1	17.9	16.2	0.1	12.3	0.0	0.3	8.9	n.d.	0.2	n.d.	0.1	0.0	0.0	0.0	4.0	0.0	100.0	58
T3B	core	36	4.9	17.6	13.4	0.1	13.7	0.0	0.4	8.7	n.d.	0.4	n.d.	0.2	0.1	0.1	0.0	3.9	0.1	99.9	65
T3B	core	36	4.0	17.5	16.1	0.1	12.7	0.0	0.4	8.8	n.d.	0.2	n.d.	0.2	0.0	0.0	0.0	3.9	0.1	100.0	58
T3B	core	36	4.9	17.2	13.8	0.1	13.9	0.0	0.4	8.5	n.d.	0.5	n.d.	0.3	0.1	0.1	0.0	3.9	0.1	99.9	64
T3B	core	36	4.1	17.5	14.9	0.1	13.3	0.1	0.3	8.7	n.d.	0.3	n.d.	0.2	0.0	0.0	0.0	3.9	0.1	99.9	61
T3B	core	36	4.1	17.5	14.8	0.1	13.5	0.1	0.4	8.7	n.d.	0.2	n.d.	0.2	0.0	0.1	0.0	3.9	0.1	99.9	62
T3B	core	37	3.6	18.6	13.6	0.1	13.7	0.0	0.1	9.0	n.d.	0.2	n.d.	0.3	0.0	0.0	0.0	3.9	0.1	100.0	64
T3B	core	38	4.9	15.3	13.9	0.1	14.1	0.2	0.3	8.3	n.d.	0.8	n.d.	0.5	0.0	0.1	0.0	3.8	0.2	99.7	64
T3B	core	37	4.8	17.0	13.4	0.1	14.5	0.0	0.4	8.5	n.d.	0.5	n.d.	0.3	0.1	0.1	0.0	3.9	0.1	100.0	66
T3B	core	37	4.1	17.2	15.7	0.1	12.7	0.1	0.4	8.7	n.d.	0.3	n.d.	0.2	0.0	0.0	0.0	4.0	0.1	100.2	59
T3B	core	36	4.1	17.3	15.2	0.1	13.8	0.0	0.4	8.6	n.d.	0.4	n.d.	0.3	0.0	0.0	0.0	3.9	0.1	100.2	62
T3B	core	37	5.3	15.7	13.5	0.1	14.9	0.0	0.3	8.2	n.d.	0.8	n.d.	0.5	0.1	0.1	0.1	3.8	0.2	100.0	66
T3B	core	37	4.7	17.0	12.6	0.1	15.0	0.1	0.3	9.0	n.d.	0.2	n.d.	0.4	0.0	0.1	0.0	3.9	0.2	100.2	68
T3B	core	37	5.0	16.3	13.3	0.1	15.0	0.1	0.3	8.8	n.d.	0.3	n.d.	0.4	0.0	0.1	0.0	3.9	0.2	100.2	67
T3B	core	36	4.0	17.5	15.3	0.1	13.5	0.1	0.4	8.9	n.d.	0.2	n.d.	0.2	0.0	0.1	0.0	3.9	0.1	100.3	61
T3B	core	35	4.9	18.3	14.0	0.1	13.4	0.0	0.4	8.9	n.d.	0.8	n.d.	0.1	0.1	0.1	0.1	4.0	0.1	100.4	63
T3B	core	36	4.0	18.1	15.3	0.1	13.0	0.0	0.4	9.0	n.d.	0.2	n.d.	0.1	0.0	0.0	0.0	4.0	0.1	100.5	60
T3B	core	37	4.1	17.7	15.9	0.1	12.8	0.1	0.3	8.7	n.d.	0.2	n.d.	0.1	0.0	0.1	0.0	4.0	0.1	100.5	59
T3B	core	36	5.0	17.7	13.4	0.1	13.9	0.0	0.4	8.8	n.d.	0.4	n.d.	0.2	0.1	0.1	0.0	4.0	0.1	100.4	65
T3B	core	36	4.1	17.3	15.3	0.1	13.7	0.0	0.4	9.0	n.d.	0.2	n.d.	0.4	0.0	0.1	0.0	3.9	0.2	100.4	61
T3B	core	37	4.7	17.5	13.6	0.1	14.2	0.0	0.4	9.0	n.d.	0.2	n.d.	0.3	0.0	0.0	0.0	3.9	0.1	100.6	65
T3B	core	37	4.7	17.3	13.3	0.1	14.3	0.0	0.4	8.8	n.d.	0.4	n.d.	0.3	0.1	0.1	0.0	4.0	0.1	100.7	66
T3B	core	37	4.6	17.7	13.3	0.1	13.9	0.0	0.3	9.3	n.d.	0.2	n.d.	0.3	0.0	0.0	0.0	4.0	0.1	100.7	65
T3B	core	38	4.9	16.7	13.1	0.1	14.4	0.1	0.4	8.6	n.d.	0.5	n.d.	0.4	0.1	0.1	0.0	3.9	0.2	100.7	66
T3B	core	36	4.9	17.5	14.1	0.1	13.8	0.0	0.4	9.3	n.d.	0.2	n.d.	0.3	0.0	0.1	0.0	3.9	0.1	100.8	64
T3B	core	37	4.8	17.7	13.1	0.1	14.5	0.0	0.2	9.3	n.d.	0.2	n.d.	0.3	0.0	0.1	0.0	4.0	0.1	101.1	66
T3B	core	37	3.5	18.5	14.2	0.0	13.7	0.1	0.2	8.8	n.d.	0.2	n.d.	0.2	0.0	0.0	0.0	4.0	0.1	99.9	63
T3B	core	37	4.7	17.2	13.9	0.1	13.7	0.1	0.4	8.6	n.d.	0.4	n.d.	0.2	0.1	0.1	0.0	3.9	0.1	99.9	64
T3B	core	36	4.1	17.9	16.2	0.1	12.3	0.0	0.3	8.9	n.d.	0.2	n.d.	0.1	0.0	0.0	0.0	4.0	0.0	100.0	58
T3B	core	36	4.9	17.6	13.4	0.1	13.7	0.0	0.4	8.7	n.d.	0.4	n.d.	0.2	0.1	0.1	0.0	3.9	0.1	99.9	65
T3B	core	36	4.0	17.5	16.1	0.1	12.7	0.0	0.4	8.8	n.d.	0.2	n.d.	0.2	0.0	0.0	0.0	3.9	0.1	100.0	58
T3B	core	36	4.9	17.2	13.8	0.1	13.9	0.0	0.4	8.5	n.d.	0.5	n.d.	0.3	0.1	0.1	0.0	3.9	0.1	99.9	64
T3B	core	36	4.1	17.5	14.9	0.1	13.3	0.1	0.3	8.7	n.d.	0.3	n.d.	0.2	0.0	0.0	0.0	3.9	0.1	99.9	61

Table C-9 Electron microprobe data: phlogopites

oxides as wt%		H_2O calculations after Tindle and Webb (1990)																		
sample	notes	SiO_2	TiO_2	Al_2O_3	FeO*	MnO	MgO	CaO	Na_2O	K_2O	SrO	BaO	Rb_2O	F	Cl	Cr_2O_3	NiO	H2O*	O=F,Cl	Total	Mg#
T3B	core	36	4.1	17.5	14.8	0.1	13.5	0.1	0.4	8.7	n.d.	0.2	n.d.	0.2	0.0	0.1	0.0	3.9	0.1	99.9	62
T3B	core	37	3.6	18.6	13.6	0.1	13.7	0.0	0.1	9.0	n.d.	0.2	n.d.	0.3	0.0	0.0	0.0	3.9	0.1	100.0	64
T3B	core	38	4.9	15.3	13.9	0.1	14.1	0.2	0.3	8.3	n.d.	0.8	n.d.	0.5	0.0	0.1	0.0	3.8	0.2	99.7	64
T3B	core	37	4.8	17.0	13.4	0.1	14.5	0.0	0.4	8.5	n.d.	0.5	n.d.	0.3	0.1	0.1	0.0	3.9	0.1	100.0	66
T3B	core	37	4.1	17.2	15.7	0.1	12.7	0.1	0.4	8.7	n.d.	0.3	n.d.	0.2	0.0	0.0	0.0	4.0	0.1	100.2	59
T3B	core	36	4.1	17.3	15.2	0.1	13.8	0.0	0.4	8.6	n.d.	0.4	n.d.	0.3	0.0	0.0	0.0	3.9	0.1	100.2	62
T3B	core	37	5.3	15.7	13.5	0.1	14.9	0.0	0.3	8.2	n.d.	0.8	n.d.	0.5	0.1	0.1	0.1	3.8	0.2	100.0	66
T3B	core	37	4.7	17.0	12.6	0.1	15.0	0.1	0.3	9.0	n.d.	0.2	n.d.	0.4	0.0	0.1	0.0	3.9	0.2	100.2	68
T3B	core	37	5.0	16.3	13.3	0.1	15.0	0.1	0.3	8.8	n.d.	0.3	n.d.	0.4	0.0	0.1	0.0	3.9	0.2	100.2	67
T3B	core	36	4.0	17.5	15.3	0.1	13.5	0.1	0.4	8.9	n.d.	0.2	n.d.	0.2	0.0	0.1	0.0	3.9	0.1	100.3	61
T3B	core	35	4.9	18.3	14.0	0.1	13.4	0.0	0.4	8.9	n.d.	0.8	n.d.	0.1	0.1	0.1	0.1	4.0	0.1	100.4	63
T3B	core	36	4.0	18.1	15.3	0.1	13.0	0.0	0.4	9.0	n.d.	0.2	n.d.	0.1	0.0	0.0	0.0	4.0	0.1	100.5	60
T3B	core	37	4.1	17.7	15.9	0.1	12.8	0.1	0.3	8.7	n.d.	0.2	n.d.	0.1	0.0	0.1	0.0	4.0	0.1	100.5	59
T3B	core	36	5.0	17.7	13.4	0.1	13.9	0.0	0.4	8.8	n.d.	0.4	n.d.	0.2	0.1	0.1	0.0	4.0	0.1	100.4	65
T3B	core	36	4.1	17.3	15.3	0.1	13.7	0.0	0.4	9.0	n.d.	0.2	n.d.	0.4	0.0	0.1	0.0	3.9	0.2	100.4	61
T3B	core	37	4.7	17.5	13.6	0.1	14.2	0.0	0.4	9.0	n.d.	0.2	n.d.	0.3	0.0	0.0	0.0	3.9	0.1	100.6	65
T3B	core	37	4.7	17.3	13.3	0.1	14.3	0.0	0.4	8.8	n.d.	0.4	n.d.	0.3	0.1	0.1	0.0	4.0	0.1	100.7	66
T3B	core	37	4.6	17.7	13.3	0.1	13.9	0.0	0.3	9.3	n.d.	0.2	n.d.	0.3	0.0	0.0	0.0	4.0	0.1	100.7	65
T3B	core	38	4.9	16.7	13.1	0.1	14.4	0.1	0.4	8.6	n.d.	0.5	n.d.	0.4	0.1	0.1	0.0	3.9	0.2	100.7	66
T3B	core	36	4.9	17.5	14.1	0.1	13.8	0.0	0.4	9.3	n.d.	0.2	n.d.	0.3	0.0	0.1	0.0	3.9	0.1	100.8	64
T3B	core	37	4.8	17.7	13.1	0.1	14.5	0.0	0.2	9.3	n.d.	0.2	n.d.	0.3	0.0	0.1	0.0	4.0	0.1	101.1	66
T2A	core	41	1.0	12.3	2.9	0.0	24.9	0.1	0.1	10.4	0.0	0.3	2.4	n.d.	n.d.	n.d.	0.3	4.2	0.0	100.2	94
T2A	core	38	2.7	11.4	13.7	0.2	16.6	0.3	0.2	8.7	n.d.	0.7	n.d.	0.5	0.1	0.4	0.1	3.6	0.2	96.8	68
T2A	core	37	2.9	10.6	15.7	0.2	14.9	0.4	0.1	7.9	n.d.	0.6	n.d.	0.5	0.1	0.4	0.1	3.6	0.2	95.0	63
T2A	core	40	1.4	10.6	11.6	0.1	18.3	0.6	0.1	7.7	n.d.	0.3	n.d.	0.7	0.0	0.0	0.1	3.5	0.3	94.4	74
T2A	core	38	2.3	10.9	13.9	0.2	16.3	0.3	0.2	8.1	n.d.	0.6	n.d.	0.6	0.0	0.5	0.2	3.5	0.3	95.2	68
T2A	core	40	0.8	12.3	2.6	0.0	24.2	0.3	0.1	10.3	0.0	0.2	2.5	n.d.	n.d.	n.d.	0.0	4.1	0.0	97.2	94
T2A	core	40	0.8	12.0	2.6	0.0	24.3	0.4	0.1	10.3	0.0	0.2	2.5	n.d.	n.d.	n.d.	0.5	4.1	0.0	97.6	94
T2A	core	39	0.9	15.6	2.7	0.0	23.3	0.9	0.1	8.5	0.0	0.2	2.1	n.d.	n.d.	n.d.	0.4	4.1	0.0	97.7	94
T2A	core	40	0.9	12.5	2.8	0.0	23.9	0.1	0.2	10.4	0.0	0.3	2.5	n.d.	n.d.	n.d.	0.4	4.1	0.0	97.7	94
T2A	core	40	0.8	12.4	2.6	0.0	24.3	0.2	0.1	10.4	0.0	0.2	2.6	n.d.	n.d.	n.d.	0.5	4.1	0.0	98.1	94
T2A	core	40	0.8	12.1	2.7	0.0	24.5	0.3	0.2	10.3	0.0	0.2	2.7	n.d.	n.d.	n.d.	0.5	4.1	0.0	98.2	94
T2A	core	40	0.8	12.3	2.6	0.0	24.2	0.3	0.1	10.3	0.0	0.2	2.5	n.d.	n.d.	n.d.	0.0	4.1	0.0	97.2	94
T2A	core	37	2.7	10.7	12.6	0.2	17.5	0.4	0.1	8.6	0.0	0.6	2.5	n.d.	n.d.	n.d.	0.1	3.9	0.0	97.0	71
T2A	core	40	0.8	12.0	2.6	0.0	24.1	0.6	0.1	10.0	0.0	0.2	2.7	n.d.	n.d.	n.d.	0.4	4.0	0.0	97.4	94
T2A	core	40	0.9	12.0	2.9	0.0	24.2	0.4	0.1	10.1	0.0	0.2	2.4	n.d.	n.d.	n.d.	0.4	4.1	0.0	97.5	94
T2A	core	40	0.8	11.8	2.6	0.0	24.2	0.2	0.1	10.3	0.0	0.2	2.9	n.d.	n.d.	n.d.	0.5	4.0	0.0	97.5	94
T2A	core	40	0.8	12.0	2.6	0.0	24.3	0.4	0.1	10.3	0.0	0.2	2.5	n.d.	n.d.	n.d.	0.5	4.1	0.0	97.6	94
T2A	core	39	0.9	15.6	2.7	0.0	23.3	0.9	0.1	8.5	0.0	0.2	2.1	n.d.	n.d.	n.d.	0.4	4.1	0.0	97.7	94
T2A	core	40	0.9	12.5	2.8	0.0	23.9	0.1	0.2	10.4	0.0	0.3	2.5	n.d.	n.d.	n.d.	0.4	4.1	0.0	97.7	94
T2A	core	37	2.7	10.8	14.3	0.2	16.1	0.8	0.2	8.0	0.0	0.6	2.9	n.d.	n.d.	n.d.	0.1	3.8	0.0	97.7	67
T2A	core	39	0.8	12.4	2.6	0.0	24.2	0.5	0.1	10.2	0.0	0.2	2.8	n.d.	n.d.	n.d.	0.5	4.1	0.0	97.9	94
T2A	core	40	0.8	11.9	2.6	0.0	24.6	0.3	0.1	10.4	0.0	0.2	2.5	n.d.	n.d.	n.d.	0.4	4.1	0.0	97.9	94
T2A	core	40	0.8	12.2	2.6	0.0	24.3	0.3	0.1	10.1	0.0	0.2	2.8	n.d.	n.d.	n.d.	0.5	4.1	0.0	98.0	94
T2A	core	36	3.8	10.4	15.5	0.2	15.3	0.5	0.2	8.8	0.0	1.1	2.4	n.d.	n.d.	n.d.	0.1	3.8	0.0	97.7	64
T2A	core	40	0.8	12.4	2.6	0.0	24.3	0.2	0.1	10.4	0.0	0.2	2.6	n.d.	n.d.	n.d.	0.5	4.1	0.0	98.1	94
T2A	core	41	0.8	12.6	2.6	0.0	24.3	0.3	0.1	9.5	0.0	0.3	2.4	n.d.	n.d.	n.d.	0.4	4.1	0.0	98.2	94
T2A	core	40	0.8	12.1	2.7	0.0	24.5	0.3	0.2	10.3	0.0	0.2	2.7	n.d.	n.d.	n.d.	0.5	4.1	0.0	98.2	94
T2A	core	40	0.9	12.6	3.0	0.0	24.5	0.4	0.2	9.3	0.0	0.2	2.4	n.d.	n.d.	n.d.	0.4	4.1	0.0	98.4	94
T2A	core	41	0.9	12.4	2.9	0.0	24.6	0.4	0.2	9.3	0.0	0.2	2.2	n.d.	n.d.	n.d.	0.4	4.1	0.0	98.5	94
T2A	core	41	0.9	12.4	3.0	0.0	24.6	0.3	0.2	9.6	0.0	0.3	2.6	n.d.	n.d.	n.d.	0.4	4.1	0.0	99.0	94
T2A	core	41	0.8	12.2	2.6	0.0	24.8	0.3	0.1	10.2	0.0	0.2	2.9	n.d.	n.d.	n.d.	0.5	4.1	0.0	99.5	94
T2A	core	39	3.0	10.9	13.4	0.1	17.0	0.4	0.1	8.4	0.0	0.6	2.8	n.d.	n.d.	n.d.	0.1	3.9	0.0	99.4	69
T2A	core	41	0.8	12.4	2.7	0.0	25.2	0.3	0.1	9.8	0.0	0.2	2.3	n.d.	n.d.	n.d.	0.5	4.2	0.0	100.0	94
T2A	core	41	1.0	12.4	2.9	0.0	24.9	0.1	0.2	10.4	0.1	0.3	2.3	n.d.	n.d.	n.d.	0.4	4.2	0.0	99.9	94

D Analytical Techniques

D.1 Sample crushing

Each sample was split into two parts using a hydraulic splitter; a small piece of hand specimen size for reference and section making, and a larger piece for powdering. Any weathered edges not removed in the field were split away from the samples. The sample was then split into small centimeter sized fragments, of which a small proportion were passed through a stainless steel jaw-crusher and discarded, to pre-contaminate the apparatus before crushing the main proportion of the sample into millimeter sized fragments. An aliquot (> 300 g) of the crushate was retained for future use, and the separation of micas/amphiboles for Ar analysis if required. The remainder (~ 100 - 200 g) was ground to a fine powder in a pre-contaminated agate ball mill for ~ 20 minutes.

D.2 X-Ray Fluorescence Analysis (XRF)

D.2.1 Glass Disc Preparation

Whole-rock major element and trace element (Cr) analyses were performed on fused discs and powder pellets following standard techniques at the Open University (Potts et al., 1984). Aliquots of powder for analysis were dried in porcelain crucibles overnight at 100°C and were

allowed to cool. Approximately (the exact mass depended on the batch of flux) 3.5 g of lithium metaborate/tetraborate flux (Johnson Matthey Spetroflux 100B) was weighed into platinum crucibles, followed by 0.7 G of sample powder. The sample powder and flux were stirred using a polythene rod to ensure homogeneity. Samples were fused for ~ 15 minutes at 1100°C in a muffel furnace; the mixture was swirled every 5 minutes to allow gas bubbles to escape. The melt was poured into a pre-heated brass mould and compressed to form a glass disc, which was allowed to cool before analysis.

Using the same dried aliquots of sample powder, 1-2 g of powder was accurately weighed into alumina crucibles which had been pre-ignited at 1000°C for ~ 15 minutes. Samples were then ignited at 1000°C for ~ 30 – 45 minutes before re-weighing to determine the loss on ignition for each sample.

D.2.2 Pressed Pellet Preparation

Approximately 9 – 10 g of sample powder was weighed out into a small plastic bag and 0.7 – 0.9 of polyvinylpyrollidone (PVP) binder was added and mixed with the powder (Watson, 1996). The mixture was emptied into a hardened steel mould, and placed in a hydraulic press. The completed pellet was dried overnight at ~ 100°C prior to analysis to ensure durability.

D.2.3 Technical Specification and Quality Assurance

Analysis of the glass discs and pressed pellets was undertaken on an ARL 8420+ dual goniometer wavelength dispersive XRF spectrometer. The spectrometer is equipped with a 3kW Rh anode end-window X-ray tube, and uses fully collimated flow proportional and scintillation counters. The machine is equipped with 5 diffraction crystals: multilayer AXO6, PET, Ge111, LiF200 and LiF220. Within each run, elemental intensities are corrected for background and peak overlap interferences. Medium-term instrumental drift is corrected for using a drift normalisation monitor built into the software. Matrix corrections for major elements use the Traill-Lachance procedure, and trace element matrix corrections were achieved by ratioing with the Compton scattered tube lines, or in the case of elements with atomic numbers < 27, a Lucas-Tooth correction using iron and Compton scatter peak intensities were employed. Typical estimates of the precision of major element determination are $\sim 0.18 - 0.73$ %, for Cr determination precision is ~ 0.83 % (Ramsey et al., 1995). Monitor samples used routinely at the OU were regularly included within the sample batches to ensure that there were no problems with either sample preparation or analysis.

D.3 Inductively Coupled Plasma Mass Spectrometry (ICP-MS)

D.3.1 Sample preparation

ICP-MS was undertaken at the Department of Geological Sciences at Durham University with the help of C. Ottley and J. Pearce. Samples were prepared in the Open University Sr isotope lab. All acids used were either Quartz distilled (QD) or Teflon distilled (TD). 18.1 Mohm water was purified by reverse osmosis (RO) followed by ion exchange and activated carbon water. It is referred to in the following text as RO water for simplicity.

Teflon dissolution bombs were cleaned as outlined in section D.4.1. Samples were dried overnight at 105 °C before the weighing out of 0.1g +/- 0.0001g of sample powder into a Teflon beaker, using a five figure balance. The beakers were freed from electrostatic charge by use of an anti static gun. 1 ml of TD 15M HNO_3 was added to the sample, followed by 4 ml of TD HF (48%). The beakers were sealed tightly and left on a hotplate at approx. 80°C for over 36 hours. Samples were then placed under evaporating hoods until only a few μl of acid remained. 1ml of TD 14M HNO_3 was then added in order to diminish the chance of fluoride formation. The samples were returned to the hotplate overnight and then dried fully under the evaporating hoods. This process was repeated again. 2.5ml of TD 14M HNO_3 was then added to the dried residue. The resulting solution was then diluted by the addition of 10-15ml of RO H_2O and returned to the hot plate for half an hour before cooling and transferring

to a cleaned 50ml polypropylene flask. Samples were transported to Durham in such flasks, where 1.25ml of 1ppm Re and Rh spike was added using a pipette cleaned with 3.5% HNO_3. Solutions were made up to 50ml with some more distilled water, and shaken well to ensure mixing. To make up the final solution for analysis, 1ml of sample was pipetted out into a 12ml testube and 10ml of 3.5% HNO_3 was added using a large pipette. Pipette tips were cleaned by rinsing with RO water twice and then rinsing with sample.

D.3.2 Technical Specification and Quality Assurance

Solutions were analysed on a Perkin-Elmer-SCIEX Elan 6000 inductively coupled plasma mass spectrometer using a cross-flow nebuliser. Internal drift was corrected for by monitoring the (spiked) abundances of Rh, In and Bi during the individual runs. Matrix corrections were made using oxide/metal ratios measured on matrix-matched standard solutions; oxide interferences were minimal for most analyses.

Total Procedure blanks were in the order of 21 counts per second for ^{140}Ce, which is equivalent to approximately 0.1ppt of blank contribution. Blanks were therefore deemed negligible. At least three blanks were included per batch of samples prepared. Reproducibility, based on repeated analyses of samples and standards was between 1 and 3%, and analysed standard (BHVO-1, AGV) values deviated less than 2% (and generally less than 1 %) from published values. Repeat preparations of Tibetan samples are given in Table C-3, the reproducibility is generally much lower than that of BHVO-1 and AGV-1, this reflects problems of sample heterogeneity.

D.4 Sr, Nd and Pb isotopic analysis

Sr and Nd whole rock isotopic analyses were determined by Thermal Ionisation Mass Spectrometry (TIMS) on Finnigan MAT 261 and 262 machines and Inductively Coupled Plasma Multi Collector Mass Spectrometry (ICP-MC-MS) on a Nu Instruments machine at the Department of Earth Sciences at the Open University. Pb isotopic analyses was determined solely by IC-MC-MS on the Nu Plasma. Chemical separation procedures were undertaken in clean chemistry laboratories.

D.4.1 Beaker Cleaning

All acids used were Quartz distilled (QD) or Teflon distilled (TD), apart from concentrated HNO_3 – this is of Analar grade. Water was purified by reverse osmosis (RO) and quartz distillation. Teflon Savillex® beakers were initially rinsed with RO H_2O before the addition of ~ 3ml of QD 6M HCl (TD HNO_3 was used in the case of ICP-MS, to avoid chloride interferences). They were then stood on a hot plate for a minimum of 48 hours before being added to a large beaker of Analar conc. 70 % HNO_3 for 48 hours minimum. Subsequent to this they were rinsed with RO H_2O in a fume cupboard and the transferred to a large beaker of RO H_2O which was boiled for ~ 1 hour on a hotplate. This process was repeated at least 3 times, using fresh RO H_2O. The beakers were then rinsed again with RO H_2O, after which TD 6M HCl (TD HNO_3 for ICP-MS) was added, and the beakers stood on the hotplate overnight. The beakers were then replaced with fresh TD 6M HCL (TD HNO_3 for ICP-MS), and the process repeated. After a further rinsing with RO H_2O (TD in the case of Pb isotope

and ICP-MS analyses) the beakers were covered over with cellophane and left to dry on a laboratory tissue.

D.4.2 Sample Preparation for Sr and Nd isotopes

Approximately 150 mg of sample was weighed out into a 15 or 30 ml beaker using a top pan balance. The sample was wetted with a few drops of TD 15M HNO_3, and 4 ml of TD HF (48%) was added. Beakers were allowed to stand on a hotplate for 48 hours. HF was evaporated off under hoods until the mixture resembled a paste, and approx. 6mls of 6M TD HCl was then added. Beakers were left on the hotplate for 24-48 hours, before evaporation under hoods and the addition of 2mls of QD 2.5M HCl. Samples were then transferred to a centrifuge tube rinsed with QD 2.5M HCl and RO water, and centrifuged at 400rpm for 5 minutes. The empty dissolution beakers were rinsed with RO H_2O, half filled with QD 6M HCl and placed on the hot plate in order to clean them before collection of the Sr fraction (clean beakers were used to collect the REE fraction).

Sr and REE fractions were separated using cationic ion-exchange resin columns. The columns used consisted of 10ml of anionic ionic exchange resin 200-400 mesh, cleaned and preconditioned with QD 6M HCl, RO H_2O and QD 0.25M HCl. Care was taken when pipetting liquids onto the column, that the resin remained undisturbed. 1ml of sample in QD 2.5M HCl was loaded onto the top of the resin bed. Pipette tips were cleaned with QD 2.5M HCl, and new ones taken for each sample, to avoid contamination. 1ml of QD 2.5M HCl was added to rinse the sample into the column, followed by another 1ml of this acid. 36 mls was then added to elute the Rb fraction. Sr was collected into the rinsed dissolution beakers upon

the addition of 14mls of QD 2.5M HCl. 18mls of QD 3M HNO_3 was eluted before the collection of the Nd fraction in 18mls of QD 3M HNO_3. Columns were cleaned, and both Sr and Nd fractions dried down, before the Nd fraction was passed through a further set of columns. Nd was separated from the REE fraction using hydrogen-diethyl-hexyl-phosphate (HDEHP) columns (Richard et al., 1976). The Teflon columns for Nd separation were cleaned and preconditioned with QD 6M HCl, RO H_2O, and QD 0.25M HCl. The Nd fraction was added in 0.5ml of QD 0.25M HCl and washed onto the column with two successive additions of 1ml of QD 0.25M HCl. 13mls of 0.25M HCl were then eluted. The Nd fraction was collected in clean Savillex® beakers upon addition of 10 mls of 0.25M QD HCl, and was then dried under the evaporating hoods.

D.4.3 Sample Preparation for Pb isotopes

Approximately 150mg of sample was weighed into a 7ml beaker. 1ml of TD HNO_3 was added to wet the rock powder before the addition of 3mls of TD HF. They were then left for 48 hours on the hot plate. The sample was evaporated until most of the moisture had gone, and approx. 5mls of TD 15M HNO_3 was added. The sample was left on the hotplate overnight, before being evaporated to dryness. Approximately 5mls of TD 6M HCl was added and the samples were again left on the hotplate overnight, before evaporation. The addition of approximately 5mls of 15M HNO_3 and 6M HCl followed, and these steps were then repeated with only 2mls of acid, until a clear solution was obtained. Samples were evaporated to dryness and checked to see if any HCl remained. 1ml of TD 1M HBr was added and the solutions warmed for 20 minutes, before being left to cool overnight.

Columns were prepared from 1ml pipette tips. Polypropylene frits were placed inside them, and they were rinsed and left to soak in QD 6M HCl overnight. After further rinsing with water, approx. 100 µl of anionic resin 200-400 mesh was added to each column, and the resin washed with TD 6M HCl and TD H_2O successively. The columns were preconditioned with 0.5ml of TD 1M HBr. Samples were loaded onto the column in 1ml of TD 1M HBr using disposable pasteur pipettes, and were washed in with 0.5ml of TD 1M HBr. 1ml of TD 1M HBr was then added and eluted to waste, to remove the Sr and Nd fraction. The dissolution beakers were cleaned with RO H_2O, QD 6M HCl, RO H_2O and then TD H_2O, before being used for collection. The Pb was collected upon the addition of 2mls of TD 6M HCl. To the collected fraction a large drop (50 µl) of TD HNO_3 was added in order to remove the bromine and the sample was evaporated to dryness. The columns were cleaned up for the second pass, and the process repeated.

D.4.4 Sample loading (TIMS) and solution preparation (ICP-MC-MS)

Filament holders were tested to check that they conducted electricity and cleaned using a sandblaster, dentists drill and by boiling several times in RO H_2O. Re and Ta filaments were outgassed in a vacuum for 10 minutes at 4.5 A and 4 A, respectively. Slit and blank plates were cleaned by scraping with fibre glass rods and boiling with RO H_2O. For Sr analysis on the Finnigan MAT 261 mass spectrometer, each sample was loaded on to a Ta single filament using TD H_2O and 10% Phosphoric acid (H_3PO_4). The samples were dried on to the filaments by passing a voltage and current of 1.5V and 1.2A through them. The current was then increased to 2A for 3s in order to burn off the phosphoric acid. For Nd analyses on the Finnigan MAT 262 mass spectrometer, samples were loaded in 2µl of TD H_2O onto a Ta

double filament. A Re double filament was used to promote ionisation during Nd isotope analysis. They were dried down at 1.5V and 0.8A.

In the case of ICP-MC-MS the collected Sr and Nd fractions were evaporated and subsequently dissolved in 2 % HNO_3 to give solutions for analysis. A stepwise dilution in 2 % HNO_3 was used to give a solution with a concentration of ~ 0.5 ppm Sr or Nd (Based on the known concentrations of Sr and Nd in the samples, and assumption of a 95 % column yield). For Pb, the evaporated fractions were dissolved in a 2 % solution of HCl pre-spiked with 2 ppm Tl, the concentration of Pb in the final analytical solutions was ~ 0.2 ppm.

D.4.5 Thermal Ionisation Mass Spectrometry (TIMS): Machine Specification and Quality Assurance

Sr and Nd whole rock isotopic analyses were determined by Thermal Ionisation Mass Spectrometry (TIMS) on Finnigan MAT 261 and 262 multicollector machines, respectively, operating in static collection mode at the Open University. A batch of samples were run for Sr isotopes on the VG sector 54 multicollector mass spectrometer at the University of Cambridge Department of Earth Sciences. Samples and associated standards- NBS 981 and Johnson and Matthey Nd standards - were run manually at the Open University, and automatically at Cambridge.

For Sr, samples were normally collected for 100-120 ratios with a ^{87}Sr beam $\geq$ 1pA, which gave typical internal precision for each run $\pm$ 10-20 2σ in the sixth decimal place. Each sample was corrected for mass fractionation during the run to $^{86}Sr/^{88}Sr = 0.1194$. Nd isotope

analyses involved collection for 150 – 200 ratios with ^{143}Nd and ^{144}Nd beams ≥ 2pA. Samples were corrected for mass fractionation during the run to $^{144}Nd/^{146}Nd = 0.7219$. Internal precision for each run is ± 5 – 10 2σ in the sixth decimal place.

Analysis of NBS 987 and a 1:10 dilution of the Johnson and Matthey Nd (made up to have the same $^{143}Nd/^{144}Nd$ ratio as the La Jolla standard) standard allowed long term reproducibility to be monitored. All sample data presented in Appendix C are normalised to an NBS 987 of 0.71023 and a Johnson and Matthey Nd value of 0.51185. Samples were run in several periods, the values of NBS 987 and Johnson and Matthey Nd during these intervals is given with sample repeat data, for both TIMS and IC-MC-MS, in Table D-1. Total procedural blanks were monitored regularly and were typically ≤ 1 ng Sr, and 200pg Nd.

D.4.6 Inductively Coupled Plasma Multi Collector Mass Spectrometry (ICP-MC-MS): Machine Specification and Quality Assurance

Sample solutions (section D.4.4) were nebulised and using a Cetac Aridus desolvating nebuliser and introduced into the plasma torch of the Nu Instruments ICP-MC-MS. Ions are extracted from the plasma through sampling and skimmer cones, which have aperture diameters of 1.0 mm and 0.6 mm, respectively. For Sr and Nd analyses, the nebuliser and torch setup was cleaned between subsequent analyses by alternately aspirating 2% HNO_3 and IPA (isopropyl alcohol) through the nebuliser for a period of approximately 15 minutes. For

Pb analyses, HNO_3 was found to have an affinity for Hg, resulting in significant interference of ^{204}Hg with ^{204}Pb, so 2 % HCl was used in the sample and cleaning solutions.

The Nu Plasma detector array consists of 12 Faraday cups and 3 ion counters in fixed positions; beams are directed into the collectors by varying the dispersion of the instrument using an electrostatic zoom lens. We measured masses 88, 87, 86, 85, and 84 simultaneously on Faraday cups 2, 4, 6, 8, 10, respectively for Sr analyses. For Nd, masses 150, 148, 147, 146, 145, 144, 143 and 142 were analysed on cups 1, 2, 3, 4, 5, 6, 7, and 8. For Pb, masses 208, 207, 206, 205, 204, 203, 202 and 200 were measured simultaneously on cups 1, 2, 3, 4, 5, 6, 7, 8 and 9. All analyses were carried out in static multi-collector mode. Peak integration times for 10 seconds for Sr, 8 seconds for Nd and and Pb. Baselines were collected for twice these integration times at half mass. 10 measurements were made per block of ratios; 20 blocks were collected for Sr, 10 for Nd and Pb.

During the period of sample analysis, the standards NBS 987, Johnson and Matthey Nd and NBS 981 were analysed, to assess i) reproducibility of isotope analyses and ii) the mass fractionation effects of the Nu Plasma. Samples were analysed in several periods for Sr, Nd and Pb, the corresponding values of the respective standards for these periods of analysis are given in Tables D-1 and D-2.

D.5 Electron Microprobe Analyses

Electron microprobe analyses were performed at the Open University using a wavelength dispersive cameca SX 100 microprobe, following techniques outlined in Reed (1995). Corrections for spectrometer angles, count times, crystal selection, specimen movement and on line PAP corrections (Pouchou and Pichoir, 1985) are performed automatically.

Polished thin sections were made of a thickness of ~ 30 μm. Phlogopites separated from samples were mounted within resin blocks, so that the *(001)* plane was perpendicular to the block, and approximately parallel to the incident electron beam. This prevents early volatilisation of elements, particularly Na, from the basal plane during analysis, which can compromise the data obtained. Sections and mounted blocks were carbon coated to provide a conductive layer and to minimise charge build-up under the electron beam. An accelerating potential of 20 kV and a beam current of 20 nA were used. The electron beam was defocussed to about 10 μm to reduce the possibility of sample decomposition.

Primary standards used were feldspar (Si, K, Al), bustamite (Mn, Ca), willemite (Zn), hematite (Fe), forsterite (Mg), rutile (Ti), jadeite (Na), synthetic potassium chloride (Cl) and synthetic LiF (F). The calibration was checked against a secondary standard, KKA (a kaersutitic amphibole). If any element fell outside the expected range for KKA, than a recalibration of that element was attempted on the primary standard until a satisfactory value was obtained. Reproducibility of KKA major element abundances was generally better than 2% (2 σ). The H_2O contents of phlogopites were calculated offline following (Tindle and Webb, 1990).

E Miscellaneous Calculations and Notes

E.1 Calculation of Mg#

Mg# is calculated using the following equation

$$Mg\# = (Mg^{2+}/(Mg^{2+} + Fe^{2+})) \times 100$$

using the molecular weights of MgO and FeO, 40.32 and 71.85, respectively, to calculate Mg^{2+} and Fe^{2+}.

E.2 Assimilation and Fractional Crystallisation (AFC) equations

The AFC equations used in this thesis are those given in (DePaulo, 1981). They are given here for reference. The equation for elemental concentrations during AFC is as follows:

Equation E-1

$$C_m = C_m^o \left\{ F^{-z} + \left(\frac{r}{r-1} \right) \frac{C_a}{zC_m^o} \left(1 - F^{-z} \right) \right\}$$

where C^{o}_{m} is the initial concentration of the element of interest in the magma, Ca is the concentration of the element in the assimilant, r is the ratio of the mass of crust assimilated to the mass of magma crystallised, F is the mass of magma remaining, and z is defined as follows:

Equation E-2

$$Z = \frac{r + D - 1}{r - 1}$$

where D is the bulk partition coefficient for the element of interest between the crystallising assemblage and the magma.

E.3 Partial melting Equations

The simple models of partial melting in this thesis use the non-modal fractional partial melting equation as given in (Shaw, 1970). This is shown in Equation E-3, where C_L is the concentration of the element of interest in the melt, C_o is the concentration of the element in the source, F is the weight fraction of melt formed, D is the bulk partition coefficient for the element of interest, and P is a proportionality factor which describes the relative contributions of the different mineral phases to the melt.

Equation E-3

$$\frac{C_l}{C_o} = \frac{1}{D}\left(1 - \frac{PF}{D}\right)^{\left(\frac{1}{P}-1\right)}$$

The proportionality factor, P is defined in Equation E-4, where p_n is the amount of mineral n entering the melt and Kd_n^i is the partition coefficient of the element *i* between phase n and the melt.

Equation E-4

$$P = p_1 Kd_1^i + p_2 Kd_2^i + ... + p_n Kd_n^i$$

E.4 Partition Coefficients used in modelling melting and AFC processes

Table E-1 Partition coefficients used in melt modelling

	pargasitic amphibole	phlogopite	clinopyroxene	orthopyroxene	olivine	garnet	rutile
Rb	0.22	1.34	0.0004	0.002	0.003	0.0002	0.0076
Ba	0.278	1.067	6.00E-06	6.00E-06	5.00E-06	7.00E-12	0.0043
Th	0.001*	0.0002	0.0021	0.0021	7.00E-06	0.0021	0
U	0.0012*	0.0002	0.001	4.00E-05	9.00E-06	0.011	0
Nb	0.05	0.0853	8.90E-03	0.003	5.00E-05	0.01	52.6
Ta	0.074	0.1069	as Nb	as Nb	as Nb	as Nb	99.5
K	1.36	1.5	0.001	2.00E-06	2.00E-05	0.013	0
La	0.039	0.00002	0.054	3.10E-03	2.00E-04	0.0007	0.0055
Ce	0.067	0.00002	0.086	0.0021	7.00E-05	0.11	8.70E-02
Pr	0.105	as Ce	0.15	0.0026	0.0003	0.005	0.0512
Pb	0.019*	0.032	0.0075	0.0014	0.0003	0.0003	0.0154
Sr	0.376	0.0372	0.091	0.0007	4.00E-05	0.0007	0.036
Nd	0.142	0.00003	0.19	0.0023	0.0003	0.027	0.0085
Sm	0.188	0.00003	0.27	0.0037	0.0009	0.22	0.00164
Zr	0.124	0.0126	0.26	0.012	0.001	0.2	3.07
Hf	0.331	0.19	0.33	0.019	0.0029	0.23	4.61
Eu	0.351	0.031	0.43	0.009	0.0005	0.61	0.0037
Ti	0.717	0.872	0.4	0.086	0.015	0.6	20
Gd	0.368	0.0082	0.44	0.0065	0.0011	1.2	0.0037
Tb	0.281	0.2541	0.44	0.00875	0.0019	1.6	0.0069
Dy	0.406	0.5	0.44	0.011	0.0027	2	0.0101
Y	0.333	0.03	0.47	15	0.0082	2	0.007
Ho	0.35	0.03	0.4	0.016	0.01	2.5	as Ho
Er	0.362	0.03	0.39	0.021	0.009	3.3	as Ho
Tm	0.281	as Er, Yb	0.41	0.0295	0.0165	4.85	as Ho
Yb	0.349	0.03	0.43	0.038	0.024	6.4	0.0093
Lu	0.246	as Yb	as Yb	as Yb	as Yb	as Yb	0.016

Pargasitic amphibole, data from Dalpe and Baker, 1994; Th, U and Pb taken from the compilation of Halliday et al., 1995

Phlogopite: data from Scmidt et al., 1999, Nb and Ta from Foley et al., 1996; K from compilation of Halliday et al., 1995, Hf from LaTourette et al., 1995, Eu and Gd to Yb, Halliday et al., 1995, Tb interpolated

Olivine, clinopyroxene, orthopyroxene, garnet from compilation of Halliday 1995, values for Tb and Tm interpolated

Rutile, data of Foley et al., 2000; Nb, Ta from Jenner et al., 1994, Ti calculated after Ryerson and Watson 1987 using compositional data from the most magnesian samples

E.5 Age correction of isotopic data

Age corrections for measured Sr, Nd and Pb used ^{40}Ar-^{39}Ar ages from the literature or obtained in the course of this study. $^{87}Rb/^{86}Sr$ and $^{147}Sm/^{144}Nd$ were calculated for each sample using the elemental abundances determined by ICP-MS (Appendix C) using the equations below:

Equation E-5

$$^{87}Rb/^{86}Sr = 2.891 \times Rb/Sr_{sample}$$

Equation E-6

$$^{147}Sm/^{144}Nd = 0.602 \times Sm/Nd_{sample}$$

Age corrections were calculated as below, where λ_1 ($1.428 \times 10^{-11} yr^{-1}$) and λ_2 ($6.54 \times 10^{-12} yr^{-1}$) are the decay constants for ^{87}Rb and ^{147}Sm, and t is the age of the sample in years.

Equation E-7

$$^{87}Sr/^{86}Sr_{initial} = {}^{87}Sr/^{86}Sr_{meas} - \left(^{87}Rb/^{86}Sr \times e^{\lambda 1 t} - 1\right)$$

Equation E-8

$$^{143}Nd/^{144}Nd_{initial} = {}^{143}Nd/^{144}Nd_{meas} - \left(^{147}Sm/^{144}Nd \times e^{\lambda 2 t} - 1\right)$$

Pb isotope data was corrected for the decay of U and Th as follows, where λ_3 (1.55125 x $10^{-10}yr^{-1}$), λ_4 (9.8485 x $10^{-10}yr^{-1}$) and λ_5 (4.9475 x $10^{-11}yr^{-1}$) are the decay constants for ^{238}U, ^{235}U and ^{232}Th, respectively; t is the age of the sample in years:

Equation E-9

$$^{206}Pb/^{204}Pb_{initial} = ^{206}Pb/^{204}Pb_{meas} - \left(^{238}U/^{204}Pb \times e^{\lambda 3t} - 1\right)$$

Equation E-10

$$^{207}Pb/^{204}Pb_{initial} = ^{207}Pb/^{204}Pb_{meas} - \left(^{235}U/^{204}Pb \times e^{\lambda 4t} - 1\right)$$

Equation E-11

$$^{208}Pb/^{204}Pb_{initial} = ^{208}Pb/^{204}Pb_{meas} - \left(^{232}Th/^{204}Pb \times e^{\lambda 5t} - 1\right)$$

The ratios of $^{238}U/^{204}Pb$, $^{235}U/^{204}Pb$ and $^{232}Th/^{204}Pb$ were calculated using the following equations:

Equation E-12

$$^{238}U/^{204}Pb = \left(U/Pb \times M_r Pb/238.08\right) \times \left(99.27\% \times ^{204}Pb\right)$$

where 238.03 is the atomic weight of U and 99.27 is the percentage of ^{238}U, ^{204}Pb is the concentration of this isotope in the sample and M_r is the atomic mass of Pb. Both ^{204}Pb and M_r were determined individually for each sample.

Equation E-13

$$^{235}U/^{204}Pb = \left(\frac{1}{137.88}\right) \times ^{238}U/^{204}Pb$$

Equation E-14

$$^{232}Th/^{204}Pb = (Th/Pb \times M_r Pb/232.08) \times (100\% \times ^{204}Pb)$$

where 232.08 is the atomic weight of Th and 100 is the percentage of ^{232}Th. M_r and ^{204}Pb as for equation E-12.

E.6 Isotope Model Age Calculations

Isotope model ages were calculated using age-corrected whole rock isotope ratios (Section E.5) and trace element abundances determined by ICP-MS (whole rock elemental and isotopic data is given in Appendix C).

Nd depleted mantle model ages (T_{DM}) were calculated assuming extraction from an upper mantle reservoir with present day $^{143}Nd/^{144}Nd$ and $^{147}Sm/^{144}Nd$ of 0.513114 and 0.222, respectively (Michard, 1985). The $^{143}Nd/^{144}Nd$ of the depleted mantle was corrected to the age of the sample by substituting the present day values of $^{143}Nd/^{144}Nd$ and $^{147}Sm/^{144}Nd$ into equation E-8 assuming linear isotopic evolution of the depleted mantle reservoir. The $^{147}Sm/^{144}Nd$ of the sample is calculated as in equation E-6. The initial depleted mantle model age was calculated as follows, where λ_2 (6.54 x 10-^{12}yr^{-1}) is the decay constant of ^{147}Sm (note

that while post sample and $^{143}Nd/^{144}Nd_{DM}$ are corrected to their values at the timing of the rock's emplacement, their present day values could also be used):

Equation E-15

$$T_{DM}^{Nd} = \frac{1}{\lambda_2} \ln \left\{ \frac{\left({}^{143}Nd/{}^{144}Nd_{sample} - {}^{143}Nd/{}^{144}Nd_{DM} \right)}{\left({}^{147}Sm/{}^{144}Nd_{sample} - {}^{147}Sm/{}^{144}Nd_{DM} \right)} + 1 \right\}$$

Depleted mantle Sr isotope model ages are calculated similarly, using equation E-5 to convert the measured sample abundances of Rb and Sr into a working value of $^{87}Rb/^{86}Sr$, and equation E-7 to calculate the initial Sr isotope ratio of the sample at the time of eruption or emplacement. The depleted mantle values of $^{87}Sr/^{86}Sr$ and $^{87}Rb/^{86}Sr$ are 0.7026 and 0.052, respectively (taken from McCulloch and Black, 1984) and λ_1 is the decay constant for ^{87}Rb and has a value of $1.428 \times 10^{-11} yr^{-1}$.

Equation E-16

$$T_{DM}^{Sr} = \frac{1}{\lambda_1} \ln \left\{ \frac{\left({}^{87}Sr/{}^{86}Sr_{sample} - {}^{87}Sr/{}^{86}Sr_{DM} \right)}{\left({}^{87}Rb/{}^{86}Sr_{sample} - {}^{87}Rb/{}^{86}Sr_{DM} \right)} + 1 \right\}$$

In the case of Pb, model ages are calculated by using the following expression where λ_3 ($1.55125 \times 10^{-10} yr^{-1}$) and λ_4 ($9.8485 \times 10^{-10} yr^{-1}$) are the decay constants for ^{238}U and ^{235}U, respectively and t is the time in years. The initial Pb isotope ratios used in the equation are calculated in equations E-9 and E-10.

Equation E-17

$$\frac{\frac{^{207}Pb}{^{204}Pb} - \frac{^{207}Pb}{^{204}Pb_{DM}}}{\frac{^{206}Pb}{^{204}Pb} - \frac{^{206}Pb}{^{204}Pb_{DM}}} = \frac{^{235}U}{^{238}U}\left[\frac{e^{\lambda 4t} - 1}{e^{\lambda 3t} - 1}\right] = \frac{1}{137.88}\left[\frac{e^{\lambda 4t} - 1}{e^{\lambda 3t} - 1}\right]$$

where the value of t is interpolated from a table constructed of the values of $^{207}Pb/^{206}Pb^*$ calculated for selected values of t. The values of $^{207}Pb/^{204}Pb_{DM}$ and $^{206}Pb/^{204}Pb_{DM}$ were calculated from the intersection of the geochron with the NHRL (Hart, 1984) after Silver et al. (1988).

F Conference Abstracts

Parts of this thesis have been presented at various conferences during the course of this study, as listed below:

Williams, H.M., Turner, S.P., Kelley, S.P. and Harris, N.B.W. (2000). Low degree mantle melting beneath Tibet: signals of heterogeneous lithosphere erosion. Goldschmidt 2000, Journal of Conference Abstracts **5**, 2, p. 1095

Williams, H.M., Turner, S.P., Kelley, S.P. and Harris, N.B.W. (2000). Small-degree mantle melting beneath Tibet: constraints on source region and petrogenesis. *VMSG Annual Meeting 2000.*

Williams, H.M., Kelley, S.P., Turner, S.P. and Harris, N.B.W. (1999). Post-collisional volcanism in North and South Tibet: implications for tectonic processes and late orogenic extension. *AGU Fall Meeting 1999.*

Prince, C., Williams, H.M., Kelley, S. and Harris, N. (1999). Cooling and Exhumation of the High Himalayan Crystalline Series: New Laser ^{40}Ar-^{39}Ar data from the Garhwal Himalaya. *AGU Fall Meeting 1999.*

Williams, H.M., Kelley, S.P., Turner, S.P. and Harris, N.B.W. (1999). New isotopic and geochronological results for volcanics in southern Tibet. *EUG 10. Strasbourg, 1999.*

Williams, H.M., Kelley, S.P., Turner, S.P. and Harris, N.B.W. (1999). Post-collisional, potassic volcanism in southern Tibet: Constraints on convective removal and related processes. *14th Himalayan-Karakorum-Tibet Workshop. Kloster-Ettal, Germany, 1999.*

Williams, H.M., Turner, S.P. and Kelley, S.P. (1999). Post-collision, potassic magmatism in S. Tibet: Sr-Nd-Pb isotope constraints on source region and petrogenesis. *VMSG Annual Meeting 1999*